SCIENCE & TECHNOLOGY

ARS JOURNAL

A PUBLICATION OF THE AMERICAN ROCKET SOCIETY

VOLUME 31 NUMBER 6 JUNE 1961

ANGELES PUBLIC LIBRARY

JUN 26 1961

IND

SURVEY ARTICLE

Recent Advances in Condensation and Evaporation . . . Welby G. Courtney 751

CONTRIBUTED ARTICLES

The Virtual Mass of Clustered Boosters . . Holt Ashley and Gifford W. Asher 757

Theory of Mixing and Chemical Reaction in the Opposed-Jet Diffusion Flame . . . . . D. B. Spalding 763

Verification of Nozzle Admittance Theory by Direct Measurement of the Admittance Parameter . . . . . Luigi Crocco, Rodolfo Monti and Jerry Grey 771

New Theory of the Aurora Polaris . . . . . S.-I. Akasofu and S. Chapman 775

Heat Sink Strand Bomb for Determining Ballistic Properties of Solid Propellants . . . . . E. K. Ives, J. Dominik and W. A. Proell 783

Selection of a Pressurization System for a Storable Liquid Propellant Rocket Engine . . . . . C. J. Kaplan 786

Gas Particle Flow in an Axisymmetric Nozzle . . . . . W. S. Bailey, E. N. Nilsen, R. A. Serra and T. F. Zupnik 793

Reactor Core Temperature Measurement . . L. H. Shinault and T. F. McGrath 799

Meteoroids vs. Space Vehicles . . . . . R. L. Bjork 803

Capabilities and Limitations of Reaction Spheres for Attitude Control . . . . . Ralph D. Ormsby and Mahlon C. Smith 806

Magnetorquer—a Satellite Orientation Device . . . . . L. J. Kamm 813

TECHNICAL NOTES

Application of Heat Flux Potentials to the Calculation of Convective Heat Transfer to Chemically Reacting Gases . . . . . Daniel E. Rosner 816

Measurement of Air Density at 430 Km by Sodium Resonance Cloud Techniques . . . . . J. Proudman and F. F. Marmo 819

Shock Wave Asymmetry for Cones and Sphere Cones at Angle of Attack . . . . . Robert A. Greenberg and Stephen C. Traugott 821

Convection Factor for Annular Nozzles . . . . . M. D. Vlachos 823

Unique Cross-Spin Control Concept for Fixed Fin Sounding Rockets . . . . Russell A. Nidey 824

Staging of Cruising Vehicles . . . . . M. Arens 824

"Pinhole Camera" for Determination of Plasma Arc Rotational Speed . . . . . E. A. Bunt and H. L. Olson 825

Contact Surface Tailoring in a Chemical Shock Tube . . Howard B. Palmer and Bruce E. Knox 826

Adiabatic Nozzle Flows . . . . . R. A. A. Bryant 826

Nonmatrix Formulation of an Eulerian Angle Vector Transformation . . Richard F. Leach 830

Simplified Sudden-Freezing Analysis for Nonequilibrium Nozzle Flows . . . K. N. C. Bray 831

Irradiation of a Lunar Satellite . . . . . W. Leon Francis 835

Energy Requirements for Satellite Stabilization of the Gravitational Gradient . . . . . Robert R. Wolfe, John M. Corgan and Peter B. Teets 836

Temperature Distribution in Couette Flow With Radiation . . .R. Viskanta and R. J. Grosh 839

Meteorological Analysis of Churchill Rocket Sounding Data . . . . . Sidney Teweles 841

Attitude Stabilization Using Focused Radiation Pressure . . . . . Robert R. Hibbard 844

Thermal Conductivity of Kerosine D. Eng. R. D. 2498 Between 18 and 326 C at Pressures up to 200 Atm. . . . . H. Ziebland and M. T. Dupree 845

DEPARTMENTS

Technical Comments 848

New Patents 851

Technical Literature Digest 853

New York Coliseum

October 9-15, 1961

AMERICAN ROCKET SOCIETY

SPACE FLIGHT REPORT

TO THE NATION

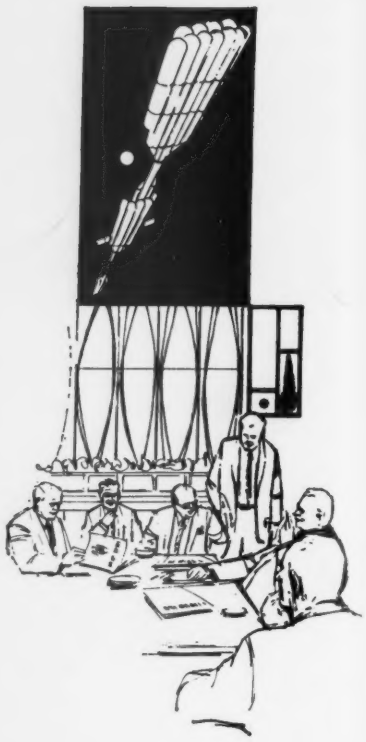

Through the medium of the ARS SPACE FLIGHT REPORT TO THE NATION, the American Rocket Society, during the week of October 9-15, 1961, in New York Coliseum, will present a thorough and comprehensive review of the U. S. space program.

The SPACE FLIGHT REPORT TO THE NATION will present for the first time under one roof a complete review of the most significant work being done in each of the major technical disciplines contributing to current progress in rocketry, missiles, and space flight, and one of the largest and most extensive technical exhibits ever undertaken in these fields.

More than 300 technical papers will detail major space projects; will explore problems that must be solved to insure further, faster progress; and will stimulate penetrating discussions by outstanding authorities in the audience.

There will be three floors of technical exhibits and displays by more than 350 manufacturers, suppliers, engineering organizations, and governmental agencies, disclosing latest achievements, concepts, products, and ideas.

ARS SPACE FLIGHT REPORT TO THE NATION will present:

- Under one roof, at one time, in one place the most comprehensive review of all the contributing technologies to the U. S. space effort.
- Forty-two specialized technical sessions, all on the same floor with comfortable lounge areas and conference rooms for informal discussions.
- Three unique Space Flight Report panels that will explore and interpret space missions, space vehicles, and the global impact of space events for the technical community at large.
- A new exhibiting technique called "Exhibiting in Depth", permitting for the first time 3-dimensional displays with the main aisle running *through* the booths instead of by them.
- Main exhibit organized by NASA and DOD, representing U. S. space capability, which will be 88′x50′ in floor area and will extend 60′ into the air.
- The history, purposes, and plans of ARS graphically displayed in a booth designed by Raymond Loewy.

For further information about reservations, program information or exhibit space contact

ARS SPACE FLIGHT REPORT TO THE NATION

American Rocket Society

500 Fifth Ave., New York 36, N. Y.

Honorary Committee

Wernher von Braun, Chairman

Harold Boyer
Detlev W. Bronk
Overton Brooks
Milton U. Clauser
James R. Dempsey
Gen. James H. Doolittle
C. Stark Draper
Hugh L. Dryden
Trevor Gardner
Mrs. Robert H. Goddard
Harry F. Guggenheim
Willis M. Hawkins
Rear Adm. John T. Hayward
Samuel K. Hoffman
Robert H. Jewett
Arthur Kantrowitz
Dan A. Kimball
Maj. Gen. John B. Medaris
George F. Metcalf
Maj. Gen. Don R. Ostrander
William H. Pickering
Richard W. Porter
Simon Ramo
Harold W. Ritchey
Lt. Gen. Bernard A. Schriever
Howard S. Seifert
Abe Silverstein
Col. John P. Stapp
George P. Sutton
Maj. Gen. Holger N. Toftoy
George S. Trimble, Jr.
Lt. Gen. Arthur G. Trudeau
Harold Urey
Theodore von Karman
Alan Waterman
Elmer P. Wheaton
Herbert F. York

ARS JOURNAL

A PUBLICATION OF THE AMERICAN ROCKET SOCIETY

EDITOR — Martin Summerfield
ASSOCIATE TECHNICAL EDITOR — Irvin Glassman
MANAGING EDITOR — Margaret Sherman
STAFF EDITOR — Barbara Nowak
ART EDITOR — John Culin

ASSOCIATE EDITORS

Igor Jurkevich, *G. E. Space Sciences Laboratory, Russian Supplement;* George F. McLaughlin, *Patents;* Charles J. Mundo Jr., *Raytheon Co., Guidance;* Bernard H. Paiewonsky, *Aeronautical Research Associates of Princeton, Flight Mechanics;* M. H. Smith, *Princeton University, Technical Literature Digest*

ASSISTANT EDITORS

Eleanor Rosman, Carol Rubenstein, Estelle Viertel

DIRECTOR OF MARKETING

Owen A. Kean

ADVERTISING PRODUCTION MANAGER

Walter Brunke

ADVERTISING REPRESENTATIVES

New York
D. C. Emery and Associates
400 Madison Ave., New York, N. Y.
Telephone: Plaza 9-7460

Los Angeles
James C. Galloway and Co.
6535 Wilshire Blvd., Los Angeles, Calif.
Telephone: Olive 3-3223

Chicago
Jim Summers and Associates
35 E. Wacker Dr., Chicago, Ill.
Telephone: Andover 3-1154

Detroit
R. F. Pickrell and Associates
318 Stephenson Bldg., Detroit, Mich.
Telephone: Trinity 1-0790

Atlanta
Joe H. Howell
1776 Peachtree Bldg., Atlanta 9, Ga.
Telephone: 873-2136

London
B. C. Nichols
151 Fleet St.
London E. C. 4, England

American Rocket Society

500 Fifth Avenue, New York 36, N. Y.

Founded 1930

OFFICERS

President — Harold W. Ritchey
Vice-President — William H. Pickering
Executive Secretary — James J. Harford
Treasurer — Robert M. Lawrence
General Counsel — Andrew G. Haley
Director of Publications — Irwin Hersey

BOARD OF DIRECTORS

Terms expiring on dates indicated

Ali B. Campbel	1962	Samuel Herrick	1963
Richard B. Canright	1962	Arthur Kantrowitz	1963
William J. Cecka Jr.	1963	A. K. Oppenheim	1961
J. R. Dempsey	1961	Simon Ramo	1963
Herbert Friedman	1962	David G. Simons	1961
George Gerard	1961	John L. Sloop	1961
Robert A. Gross	1962	Martin Summerfield	1962
		A. M. Zarem 1963	

TECHNICAL COMMITTEE CHAIRMEN

William H. Avery, Ramjets
R. M. L. Baker Jr., Astrodynamics
G. Daniel Brewer, Solid Propellant Rockets
Robert W. Bussard, Nuclear Propulsion
Bernhardt L. Dorman, Test, Operations and Support
William M. Duke, Missiles and Space Vehicles
William H. Dorrance, Hypersonics
James S. Farrior, Guidance and Control
Herbert Friedman, Physics of the Atmosphere and Space
George Gerard, Structures and Materials
Martin Goldsmith, Liquid Rockets
Andrew G. Haley, Space Law and Sociology
John H. Huth, Power Systems
Eugene B. Konecci, Human Factors and Bioastronautics
Frank W. Lehan, Communications and Instrumentation
Peter L. Nichols Jr., Propellants and Combustion
Milton M. Slawsky, Magnetohydrodynamics
Herman E. Sheets, Underwater Propulsion
Ernst Stuhlinger, Electric Propulsion

Scope of ARS JOURNAL

This Journal is devoted to the advancement of astronautics through the dissemination of original papers disclosing new scientific knowledge and basic applications of such knowledge. The sciences of astronautics are understood here to embrace selected aspects of jet and rocket propulsion spaceflight mechanics, high speed aerodynamics, flight guidance, space communications, atmospheric and outer space physics, materials and structures, human engineering, overall system analysis and possibly certain other scientific areas. The selection of papers to be printed will be governed by the pertinence of the topic to the field of astronautics, by the current or probable future significance of the research, and by the importance of distributing the information to the members of the Society and to the profession at large.

Information for Authors

Manuscripts must be as brief as the proper presentation of the ideas will allow. Exclusion of dispensable material and conciseness of expression will influence the Editors' acceptance of a manuscript. In terms of standard-size double-spaced typed pages, a typical maximum length is 22 pages of text (including equations), 1 page of references, 1 page of abstract and 12 illustrations. Fewer illustrations permit more text, and vice versa. Greater length will be acceptable only in exceptional cases.

Short manuscripts, not more than one quarter of the maximum length stated for full articles, may qualify for publication as Technical Notes or Technical Comments. They may be devoted to new developments requiring prompt disclosure or to comments on previously published papers. Such manuscripts are published within a few months of the date of receipt.

Sponsored manuscripts are published occasionally as an ARS service to the industry. A manuscript that does not qualify for publication, according to the above-stated requirements as to subject, scope or length, but which nevertheless deserves widespread distribution among jet propulsion engineers, may be printed as an extra part of the Journal or as a special supplement, if the author or his sponsor will reimburse the Society for actual publication costs. Estimates are available on request. Acknowledgment of such financial sponsorship appears as a footnote on the first page of the article. Publication is prompt since such papers are not in the ordinary backlog.

Manuscripts must be double spaced on one side of paper only with wide margins to allow for instructions to printer. Include a 100 to 200 word abstract. State the authors' positions and affiliations in a footnote on the first page. Equations and symbols may be handwritten or typewritten; clarity for the printer is essential. Greek letters and unusual symbols should be identified in the margin. If handwritten, distinguish between capital and lower case letters, and indicate subscripts and superscripts. References are to be grouped at the end of the manuscript and are to be given as follows. For journal articles: Authors first, then title, journal, volume, year, page numbers; for books: Authors first, then title, publisher, city, edition and page or chapter numbers. Line drawings must be clear and sharp to make clear engravings. Use black ink on white paper or tracing cloth. Lettering should be large enough to be legible after reduction. Photographs should be glossy prints, not matte or semi-matte. Each illustration must have a legend; legends should be listed in order on a separate sheet.

Manuscripts must be accompanied by written assurance as to security clearance in the event the subject matter lies in a classified area or if the paper originates under government sponsorship. Full responsibility rests with the author.

Preprints of papers presented at ARS meetings are automatically considered for publication.

Submit manuscripts in duplicate (original plus first carbon, with two sets of illustrations) to the Managing Editor, ARS JOURNAL, 500 Fifth Avenue, New York 36, N.Y.

ARS JOURNAL is published monthly by the American Rocket Society, Inc. and the American Interplanetary Society at 20th & Northampton Sts., Easton, Pa., U. S. A. Editorial offices: 500 Fifth Ave., New York 36, N. Y. Price: $18.00 per year, $3.00 per single copy. Second-class postage paid at Easton, Pa., with additional entry at New York, N. Y. This publication is authorized to be mailed at the special rates of postage prescribed by Section 132.122. Notice of change of address should be sent to the Secretary, ARS, at least 30 days prior to publication. Opinions expressed herein are the authors' and do not necessarily reflect the views of the Editors or of the Society.

© Copyright 1961 by the American Rocket Society, Inc.

Recent Advances in Condensation and Evaporation[1]

WELBY G. COURTNEY

Texaco Experiment Inc.
Richmond, Va.

CONDENSATION and evaporation may be included among the more difficult problems encountered by an engineer or chemist in, for example, the design of a wind tunnel or a propulsion system. These heterogeneous processes involve a number of phenomena, and it is quite difficult to predict on theoretical grounds which of these phenomena will be important in a particular case. It is even more difficult to investigate these processes experimentally. This article describes recent work on condensation and evaporation which is applicable to propulsion and high speed flow but includes other work in order to provide insight into these problems. The bibliography is, of course, only indicative of the voluminous literature on these subjects, although information directly relevant to propulsion and flow is very limited. Condensation was recently reviewed by Stever (1)[2] and others (2–4). Evaporation was recently reviewed by Knacke and Stranski (5).

Condensation

Condensation is encountered in many practical situations, such as the formation of: metal oxide or carbon particles in a thrust chamber, an expansion nozzle or a Bunsen-type flame; mercury particles in heat exchangers; water particles during cloud formation or in vapor trailing by aircraft; and liquid nitrogen drops in a supersonic wind tunnel. For example, it is necessary to avoid condensation completely for most wind tunnel applications. It would be of considerable interest to predict condensation kinetics during expansion in a nozzle or to predict the burning velocity of a combustible vapor mixture that forms a condensed phase in the combustion products by combining condensation kinetics with, e.g., the Hirschfelder treatment of burning velocity of a homogeneous vapor mixture. Also, thermal and mechanical slippage of particles in a rocket nozzle and the plastering of particles onto the motor or nozzle wall or turbine blades are intimately related to the size of the particles and thus to condensation kinetics.

From a fundamental viewpoint, condensation may be divided into nucleation, growth and agglomeration. Nucleation is defined as the formation of the least stable (thermodynamically or kinetically) cluster or particle of the new phase. Nuclei contain less than 100 atoms (or molecules, ions, etc.) in almost all cases and perhaps less than 10 atoms in some cases. Growth is the atom-by-atom deposition of new material onto the nucleus or larger particle. Agglomeration is the coalescence of two colliding particles to form a larger particle, and it includes a particle plastering onto a wall surface. The rate of condensation and also the size distributions of the product particles therefore involve the simultaneous kinetics of a sequence of nucleation, growth and agglomeration reactions.

Experimentally, one observes that condensation from ordinary impure vapor often occurs readily, but condensation from the pure vapor usually takes place only after an appreciable and moderately critical supersaturation is imposed. Since condensation rapidly occurs if large particles of the new phase are already present, nucleation is often a bottleneck in condensation. Once condensation begins, a few large particles will be formed if nucleation is slow compared to growth or agglomeration, and many small particles are formed if nucleation is fast compared to growth and agglomeration. Residence times for condensation can be as low as 40 microsec in a supersonic wind tunnel (6), is perhaps several milliseconds in a laminar flame or rocket nozzle, and is several seconds in the conventional cloud chamber (4). The end-product particles from combustion vary from about 50 to 10,000 Å in diameter (7–11). Particle concentrations

Received April 27, 1961.
[1] Parts of this paper were taken from work supported by the Office of Naval Research under Contract NOnr-3141(00).
[2] Numbers in parentheses indicate References at end of paper.

The author received an A.B. from Oberlin in 1949 and a Ph.D. in physical chemistry from Iowa State in 1951. His thesis and subsequent postgraduate work were on complexes and reaction kinetics of metal ions in aqueous solution. In 1952 he joined Chemical Construction Corp. and later Freeport Sulphur Co. and conducted research on chemical reactions in solution, including the kinetics and thermodynamics of phase transformations, complexes and catalysis. In 1956 he joined Experiment Inc. (later Texaco Experiment Inc.) where he has been primarily engaged in high energy propellant chemistry, condensation phenomena, and the fundamental properties of combustion, including ignition and reaction efficiency. In 1958 he was a consultant to CIBA in Switzerland. Dr. Courtney is currently a research chemist at Texaco Experiment Inc.

are about 10^9 to 10^{11} particles per cm^3 in combustion (8,11) and about 1 to perhaps 10^5 particles per cm^3 in a cloud chamber (12).

Nucleation

Nucleation can be either homogeneous or heterogeneous. Heterogeneous nucleation occurs when the new phase initially deposits onto foreign impurities (e.g., dust, salt particles, ions) and thus bypasses the more difficult homogeneous nucleation step. Homogeneous nucleation occurs in the absence of such impurities. There is considerable uncertainity whether or not a truly homogeneous nucleation ever does occur, because the total absence of subtrace amounts of catalytic impurities is unlikely in nature and is difficult to prove even in a laboratory experiment.

Quantitative experimental data on the rate of nucleation from the vapor phase are very limited. Most data have been obtained with water and various organic vapors in an expansion-type cloud chamber (13,14) and these data can be adequately interpreted by the classical steady-state liquid-drop theory of nucleation (12,15). Some data with water and also nitrogen have been obtained in supersonic wind tunnels (1), but some of these data cannot be interpreted by the classical theory (16). There appear to be no quantitative data on nucleation in combustion systems.

Since the nucleus may contain up to about 100 atoms, nucleation involves a sequence of perhaps 100 chemical reactions in which a vapor atom (or molecule) combines with a cluster to form a larger cluster.[3] The kinetics of nucleation theoretically can be completely described by a series of 100 or so interdependent differential equations which relate the rate of formation of clusters ranging from a two-atom cluster to the 101-atom cluster to the corresponding specific rate constants. Even if these kinetic rate constants were known, the resulting mathematical problem obviously would be difficult. The various theoretical approaches to nucleation kinetics assume different approximations in order to simplify this mathematical problem.

Nucleation involves a sequence of reactions to form successively larger clusters, and any one of these reactions (or even a sequence of several reactions) could be a bottleneck in a nucleation process. There are five general theories of nucleation. First, most nucleation theories are formulated in terms of the classical liquid drop model (13), in which it is assumed that the equilibrium concentrations of clusters can be calculated a priori in terms of the macrosopic volume and surface free energies of the condensing material. This macroscopic thermodynamic technique is obviously incorrect when applied to small clusters (1,17) but is generally thought to be realistic when applied to clusters containing more than about 20 or 30 atoms. In the liquid drop theory it is predicted that the cluster concentration goes through a sharp minimum with increasing size, and that the cluster present in the smallest concentration is the nucleus. The size of the nucleus decreases with increasing supersaturation or temperature. The classical liquid drop calculation of cluster and nucleus concentration is incorrect in that it predicts a concentration too high by a factor equal to the supersaturation, but the correction is of minor practical significance, since experimental errors in determining nucleation kinetics are much greater than the supersaturation, which seldom exceeds 10 (18). Second, the less popular (19) excess energy model of nucleation assumes that the equilibrium concentrations of very small clusters are very low, since their free energies are very high because of bond distortion in the small clusters. This model usually assumes that the nucleus contains less than about 10 atoms and that the size of the nucleus is essentially independent of temperature and supersaturation. Third, statistical mechanical techniques have also been used to predict the equilibrium cluster concentration (20–24); for example, the Cahn-Hilliard theory (23) predicts that at high supersaturation the nucleus is larger than predicted by the classical liquid drop theory. Fourth, quantum mechanical techniques to predict cluster concentration were used by Taylor et al. [(25, see also (26)]. Fifth, it is possible in a nucleation to assume that the initial formation of a two-atom or three-atom cluster is the bottleneck in nucleation when mono-atomic species, such as lithium and fluorine radicals, are condensing because a third body probably is required to absorb the "recombination" energy. The recombination model does not appear to have been applied to nucleation, probably because there are no relevant experimental data.

Approximations to nucleation kinetics can be divided into the non steady-state and steady-state approximations for the concentration of the nucleus.

Interest in the non steady-state rate of nucleation was stimulated primarily by the problem of nucleation during high speed flow in wind tunnels. The non steady-state of nucleation is difficult to evaluate exactly because of the mathematical complexity of solving the 100 or so differential equations. Various approximations which are usually based upon the liquid drop model (6,27–32) suggest that steady-state is established rapidly and that non steady-state is unimportant for most systems of interest. For example, water vapor presumably establishes steady-state nucleation in about a microsecond, whereas the wind tunnel residence time is 40 microsec. However, the value of these treatments must remain uncertain because of the severity of their approximations. For example, Frisch (30) presumed that the equilibrium concentration of the two-molecule cluster in water vapor could be calculated from the conventional liquid drop macroscopic volume and surface free energies—a decidedly unrealistic approach. A serious limitation to the liquid drop approximations is that the time required for the surface energy to reach its steady-state value is neglected, although this time can be several milliseconds (33,34). The writer is currently conducting a theoretical investigation of nonsteady-state liquid drop nucleation using a high speed computer to solve the differential equations.

Most theories of condensation kinetics assume steady-state nucleation, where the concentration of the nucleus rapidly builds up to its steady-state value, remains essentially constant at its steady-state value for a period of time, and then abruptly decreases to zero when the parent phase becomes slightly depleted owing to growth on previously formed nuclei. Nucleation is thus considered to be "on-off," and the remaining problem is to predict the steady-state rate.

The classical theories of steady-state nucleation kinetics were developed primarily by Volmer (13), Becker and Döring (35), and Frenkel (36) and were based on the liquid drop thermodynamic model for predicting cluster concentration. Volmer assumed the nucleus was present in the equilibrium concentration; Becker and Döring and Frenkel derived a steady-state rate of nucleation by assuming that the kinetics involved a sequence of similarly slow reactions localized around the nucleus. These variations in the kinetic assumptions actually are small compared to the experimental errors in the determinations of nucleation rates. The success of these classical theories in interpreting vapor condensation in the cloud chamber has led various authors to apply the steady-state liquid drop methodology to binary systems (37), liquid-solid transitions (38), crystal growth (39), etc. The excess energy model of nucleation has been used to interpret condensation of nitrogen in a wind tunnel (16), but has primarily been applied to nucleation in aqueous solution (26,40–43). Nucleation which involved excess energy kinetics would be slower than that predicted by the liquid drop theory. It may be noted that the nucleation of liquid water drops is usually very much faster than the nucleation of solid ice

[3] The probability that a cluster is formed by the agglomeration of smaller clusters is remote, since the concentrations of clusters are much smaller than the concentration of vapor atoms.

particles [(44), however, see (45)] even though the water drops are themselves supercooled.

One limitation to the classical interpretation of condensation kinetics is the assumption that nucleation is "on-off" during condensation. Phase transformations in aqueous solution have been interpreted on the more realistic assumption that the nucleation rate gradually decreases as the parent phase is depleted, but other approximations have been introduced to simplify this more complex mathematical problem. The writer is currently investigating the steady-state kinetic problem without the "on-off" assumption using a computer to expedite the mathematics.

Heterogeneous nucleation from the vapor phase onto impurities has been widely investigated (occasionally inadvertently) but will not be reviewed here. It has been estimated that impurity concentrations of up to about 10^6 particles per cm^3 (1) occur in nature. These concentrations may be sufficient to catalyze condensation in a cloud chamber but are small compared to the 10^{10} particles per cm^3 formed in combustion processes. The situation obviously is obscure, but it seems likely that the formation of particles during many combustion processes probably involved homogeneous nucleation. The atom-by-atom deposition of combustion products onto the motor walls initially does involve heterogeneous nucleation.

Trace impurities can inhibit heterogeneous nucleation by poisoning the nucleation catalysts (46). However, it is impossible to poison homogeneous nucleation by trace amounts of impurities adsorbing onto the nuclei of the new phase because new nuclei would immediately form in the supersaturated vapor.

Growth

Once nucleation is finished, the condensing material deposits onto the various sized growing particles. The rate of condensation of vapor molecules owing to growth could be predicted at any time if the age of each particle and its instantaneous growth rate during its lifetime were known. The growth of a particle involves:

1 Bulk diffusion of vapor molecules up to the surface of the particle.
2 Adsorption.
3 Surface diffusion.
4 Chemical reaction, if any.
5 Incorporation into the liquid or solid lattice of the particle.
6 Desorption of any vapor products.
7 Diffusion of the heat evolved in condensation away from the particle.

The rate of growth of a particle depends upon the kinetics of this sequence of reactions, and one or several of these reactions may be rate limiting. The growth kinetics of a particle will vary with supersaturation and temperature and also may vary with particle size because of abnormal surface effects with very small particles.

Surface controlled growth kinetics leads to linear growth where the radius of the particle increases with time, and an accommodation coefficient is conventionally introduced into the kinetic equation to denote the probability that a molecule which hits the surface of the particle will stick and be incorporated into it (47). Diffusion controlled kinetics has no rigorous mathematical solution (48), but approximate analyses of the quasi steady-state problem (48–51) lead to linear growth kinetics with very small particles and give parabolic growth kinetics with larger particles, where the square of the radius is proportional to time. Oscillating growth rates could occur in diffusion controlled growth if transient currents in the bulk phase resulting from density or thermal gradients disrupt the quasi steady-state diffusion gradient in the bulk phase (52,53). The growth of a particle is fastest when limited by bulk diffusion which is disrupted by convection currents in the bulk phase (54), is slower when limited by the quasi steady-state diffusion gradient, and is slowest when limited by a surface reaction.

Experimentally, growth kinetics in the formation of an aerosol is usually thought to be limited by bulk diffusion or by bulk diffusion and a surface reaction, although heat diffusion away from the particle may also be important. These opinions are based largely on theoretical arguments because of the experimental problems associated with measuring growth rates of very small particles. Wilde (55) assumed diffusion controlled growth kinetics in a rocket nozzle and analyzed the effect of the steady decrease in vapor temperature (56,57). Hazen (58) found that the growth of 20-μ diameter water drops from the vapor corresponded to diffusion controlled growth, but this drop size is much larger than that which occurs in aerosols.

The growth of a hydrosol from a condensed phase, such as aqueous solution, often is interpreted on the basis of surface controlled growth, although diffusion controlled growth of massive particles has been directly observed by interferometric techniques on the bulk solution adjacent to the growing surfaces (59). Also, the particle radius raised to the third power vs. time has been proposed as an approximation (60), and a radius to the 4.4 power vs. time was observed in the growth of very small iron particles in mercury (61).

The rate of disappearance of vapor molecules can be obtained by adding up the contributions of each particle. The resulting mathematical problem for surface controlled growth has been investigated by Turkevich (42), Bransom and Dunning (62); and Doremus (63). With diffusion controlled growth, the mathematical problem is less straightforward, because the diffusion gradient around one particle may interfere with the gradients around others (49). It is often difficult to decide whether growth is surface or diffusion controlled; for example, the formation of $BaSO_4$ hydrosol from aqueous solution has been interpreted in terms of a mixed diffusion surface kinetics (64) and also in terms of surface kinetics only (63). The size and number distributions of the particles at any particular time are directly related to growth and nucleation kinetics and can serve as analytical techniques for measuring these kinetics (42,62).

The growth kinetics of a particle particularly depends upon the mechanism whereby new material deposits into its surface. The surface of a liquid drop in contact with its vapor [and perhaps a solid in contact with aqueous solution (65)] presumably is atomically rough or "melted," and a new molecule can deposit rapidly at almost any position on the surface. However, the surface of a solid particle in contact with its vapor is probably atomically smooth (44), and a new molecule would only deposit either very slowly by a two-dimensional nucleation of an "island" on the surface or rapidly at kinks in the spiral surface steps generated by a screw dislocation emerging from the surface of the imperfect particle (39). Theoretically, a solid particle which is bound by nondislocated close packed surfaces would not grow despite an appreciable supersaturation in the vapor phase. This has been experimentally observed in growth from aqueous solution (59,66).

The shape of a particle depends upon the growth kinetics, but the morphology of crystals is not well understood. The spherical shape of liquid drops is, of course, to be expected, and the familiar whisker growth of crystals presumably results from an axial dislocation [(67), however, see also (66)], but the often-observed growth of a crystalline sphere onto the tip of a whisker and numerous other phenomena have not yet been explained.

The effect of impurities on growth kinetics is well known (68), but there appears to be no experimental information obtained during the formation of aerosols.

The principal current problem in growth kinetics is the accommodation coefficient. When growth involves a chemi-

cal reaction (as in the growth of Al_2O_3 liquid or solid from Al_2O, AlO and O_2 vapor), the accommodation coefficient must involve the usual activation energy, and is likely to be less than one. Experimentally, the measurement of the accommodation coefficient is at best very difficult even with massive particles because of the difficulties of measuring the surface temperature, and any results with massive surfaces are of questionable usefulness when applied to aerosol particles because growth kinetics vary with particle size. Theoretically, the simple condensation of a material onto an infinite liquid surface has been interpreted (69) in terms of the "free angle of rotation" in the liquid phase (70). A vapor molecule must preserve its rotational energy during condensation, and an adsorbed molecule would tend to re-evaporate if it must lose some of this rotational energy in order to fit into a liquid lattice with restricted rotation. For example, the accommodation coefficient for water is 0.04 [(71), however, see (72)], whereas the coefficient for CCl_4 is 1 (69).

Experimental data on growth kinetics in combustion processes are limited or even contradictory. For example, the growth of solid Al_2O_3 is confused by the possible existence of an AlO solid phase at high temperature (73) and has been variously interpreted as: deposition of AlO vapor in the conventional atom-by-atom manner at the screw-dislocation growth steps followed by disproportionation to Al_2O_3 solid and Al liquid (74); the deposition of Al_2O vapor in the presence of H_2O diectly to form a large "polymeric" Al_2O_3 nucleus (75); and the initial formation of an amorphous solid which then converts to a "new" unstable crystalline form and then to stable α-Al_2O_3 (76). Qualitative data suggest that B_2O_3 vapor readily forms B_2O_3 solid when condensed at low temperature (77), that SiO vapor readily forms SiO solid when condensed at elevated temperature (78), and that SiO vapor and O_2 readily form SiO_2 solid at lower temperature (79).

Agglomeration

Agglomeration can be considered to be an ordinary bimolecular chemical reaction, where the net rate of agglomeration between particles of type A and particles of type B (or the wall) depends upon: the collision frequency between A and B; a thermodynamic potential energy barrier (activation energy) characteristic for the agglomeration reaction, which depends upon van der Waal's attractive forces and electrostatic repulsive forces; the kinetic energy of A and B; and a "sticking" coefficient which is the probability that an embryonic agglomerate will be torn apart before it has coalesced into a single droplet or has been cemented together.

Theoretically, (80–83) it is predicted that the agglomeration rate increases with increasing particle size and that there is a certain minimum particle size for appreciable agglomeration. The agglomeration rate will be increased markedly by increasing particle velocity (e.g., increasing turbulence) but decreased by very high particle velocities because of excessive shear on an embryonic agglomerate. Thus, tiny particles do not agglomerate, and large particles tend to scavenge small particles, but the degree of turbulence is very important in determining the rate of agglomeration in a system. Theories of the shape of the end-product agglomerate predict both linear (84) and spherical (85) types.

In practice, agglomeration between two particles or between a particle and a wall (86,87) is usually a yes-or-no affair in that either all collisions give agglomeration or no agglomeration occurs despite collision. Agglomeration between the very small particles formed in a combustion process usually seems to give linear chains of discrete particles, but agglomeration between micron-sized particles in aqueous solution have been observed to give agglomerates either irregularly shaped with low density, streamlined with low density, or spherical with high density (88).

Evaporation

Although the evaporation of a material is merely the reverse of growth, evaporation and growth kinetics may be quite different because of different rate limiting steps in the two processes. As with growth, surface controlled evaporation kinetics leads to linear kinetics where the radius of the particle varies with time. Diffusion controlled evaporation from a particle again has no rigorous practical mathematical solution (48), but approximate analyses of both the nonsteady-state (89) and quasi steady-state (90) problems give give a radius squared dependence upon time. Evaporation kinetics are conventionally discussed in terms of the evaporation coefficient which is the ratio of the actual evaporation rate to the theoretical rate calculated from the equilibrium collision frequency on the surface. Growth and evaporation coefficients may be different.

Evaporation coefficients are usually less than one if: there is restricted rotation in the liquid phase; the interatomic distance must increase upon evaporation; and a chemical reaction must occur (that is, if the lattice in the liquid or solid does not consist of the major vapor species weakly bonded together). Furthermore, Hirth and Pound (91) concluded that the evaporation coefficient for most solid materials undermost conditions will be about 0.3 because of a dislocation mechanism for evaporation.

Experimental work with particles is primarily limited to particle combustion which almost always follows diffusion controlled parabolic kinetics (9). Mead (92) discussed the relationships between the evaporation limited combustion of drops and flat surfaces. The evaporation of 1-mm diameter water drops also is limited by diffusion (93), but nonsteady-state kinetics may be important (33,34,94). In most experimental work massive particles have been used. As an example of the first case, polar liquids such as H_2O usually have a small evaporation coefficient (69). For the second case, NaCl and LiF evaporate from the solid with coefficients somewhat less than one, presumably because stretching the interatomic bond to form the vapor molecule involves an activation energy (95). Numerous examples of the third case are cited in (5). For example, carbon evaporates mainly as C_2, although the equilibrated vapor is mainly mono-atomic (96), and the evaporation of LiF solid gives slightly more $(LiF)_2$ than is present in the equilibrated vapor (95). The vaporization coefficient of Na_2CO_3 is small because of dissociation upon evaporation (97), whereas NH_4Cl also dissociates upon vaporization (98) and also probably has a small coefficient.

Information directly applicable to combustion phenomena is limited. NH_4ClO_4 evaporates without appreciable dissociation (99) and probably has an evaporation coefficient of about one. Silicon readily gives the equilibrated vapor on evaporation in a Knudsen cell (100), and the evaporation coefficient therefore must not be too small. There appears to be no information on the evaporation of Al or other metals of interest.

It is perhaps of interest to note that the evaporation of Al_2O_3 from the liquid perhaps has a coefficient of about 1 at 2300 C, but evaporation from the solid perhaps has a coefficient appreciably less than 1 at lower temperatures (101), although values of 1 (102) and 0.05 (103) have also been reported for the solid. If Al_2O_3 dissociates upon evaporation to form the equilibrated Al_2O, AlO, and O_2 vapors, the evaporation coefficient should be rather small. If it evaporates without dissociation to form an Al_2O_3 vapor molecule which then dissociates, the coefficient should perhaps be about one.

Equilibration in a Knudsen cell or flow system is readily obtained with BeO (104), BeO and H_2O (105), B_2O_3 (106,107), B_2O_3 and H_2O (108), B_2O_3 and B (107), Al and Al_2O_3 (102), Al and $AlCl_3$ (109), Al and AlF_3 (110), Li_2O (111), Li_2O and H_2O (112), SiO_2 (79), SiO_2 and H_2O (113), and MgO (114). However, a SiO_2-Si mixture (106) does not equilibrate readily in a Knudsen cell.

Summary

The subjects of condensation and evaporation involve a number of separate phenomena, and an understanding of these processes requires knowledge of diverse areas of chemistry and physics. Although the general natures of these complex processes are well understood, alternate theories (or mathematical approximations) have been developed to interpret the several aspects of condensation and evaporation. At the present time the usefulness of these theories remains uncertain or at least quite arguable; for example, it is difficult to decide which theory of nucleation would be applicable to a particular experimental system or even to a particular set of experimental conditions, and it is even more difficult to perform a definitive experiment. Progress in these areas will depend upon sophisticated mathematical arguments or experimental investigations.

References

1 Stever, H. G., "Condensation Phenomena in High Speed Flows," in *Fundamentals of Gas Dynamics*, H. W. Emmons, Ed., Princeton University Press, Princeton, vol. III, 1958, p. 526.

2 Bradley, R. S., "Nucleation in Phase Changes," *Quart. Revs.* London, vol. 5, 1951, p. 315.

3 Dunning, W. J., "Theory of Crystal Nucleation from Vapour, Liquid, and Solid Systems," in *Chemistry of the Solid State*, W. E. Garner, Ed., Butterworths Scientific Publications, London, 1955, p. 159.

4 Courtney, W. G., "Kinetics of Condensation from the Vapor Phase," Texaco Experiment Inc., TM-1202, Aug. 15, 1960.

5 Knacke, O. and Stranski, I. N., "The Mechanism of Evaporation," in *Progress in Metal Physics*, B. Chalmers and R. King, Eds., Pergamon Press, N. Y., 1956, vol. 6, p. 181.

6 Kantrowitz, A., "Nucleation in Very Rapid Vapor Expansions," *J. Chem. Phys.*, vol. 19, 1951, p. 1097.

7 Line, L. E., Jr., Texaco Experiment Inc., private communication.

8 Tesner, P. A., "Formation of Dispersed Carbon by Thermal Decomposition of Hydrocarbons," in *Seventh Symposium (International) on Combustion*, Butterworths Scientific Publications, London, 1959, p. 546.

9 Olson, W. T. and Setze, P. C., "Some Combustion Problems of High-Energy Fuels for Aircraft," in *Seventh Symposium (International) on Combustion*, Butterworths Scientific Publications, London, 1959, p. 883.

10 Cabot, G. L., Inc., "Aluminum Oxide," *Brit.* 691,769, May 20, 1953; *Chem. Abstr.*, vol. 47, p. 10,821.

11 Säuerfabrik Schweizerhall, "Preparation of Finely Divided Oxides From Chlorides," *Swiss* 295,398, March 1, 1954; *Chem. Abstr.*, vol. 49, p. 13,612.

12 Barnard, A. J., "The Theory of Condensation of Supersaturated Vapours in the Absence of Ions," *Proc. Roy. Soc.*, London, vol. 220, 1953, p. 132.

13 Volmer, M., *Kinetik der Phasenbildung*, Edwards Bros., Ann Arbor, 1945.

14 Pound, G. M., Madonna, L. A. and Sciulli, C. M., "Low Temperature Cloud Chamber Studies on Water Vapor," in *Proc. Conf. Interfacial Phenomena and Nucleation*, H. Reiss, Ed., Air Force Research Center, Cambridge, 1955, vol. 1, p. 85.

15 Turnbull, D., "Kinetics of Solidification of Supercooled Liquid Mercury Droplets," *J. Chem. Phys.*, vol. 20, 1952, p. 411.

16 Bogdonoff, S. M. and Lees, L., "Study of the Condensation of the Components of Air in Supersonic Wind Tunnels. Part 1. Absence of Condensation and Tentative Explanation," Princeton Univ., Aeronautical Eng. Lab., Rep. no. 146, May 25, 1949.

17 Reiss, H., "Theory of the Liquid Drop Model," *Ind. Engng. Chem.*, vol. 44, 1952, p. 1284.

18 Courtney, W. G., "Remarks on Homogeneous Nucleation," in preparation.

19 Turnbull, D., "The Kinetics of Precipitation of Barium Sulfate from Aqueous Solution," *Acta Met.*, vol. 1, 1953, p. 684.

20 Mayer, J. E., "The Statistical Mechanics of Condensing Systems. I," *J. Chem. Phys.*, vol. 5, 1937, p. 67.

21 Yang, C. N. and Lee, T. D., "Statistical Theory of Equations of State and Phase Transitions. I. Theory of Condensation," *Phys. Rev.*, vol. 87, 1952, p. 404.

22 Reiss, H., "The Statistical Mechanical Theory of Irreversible Condensation. I," *J. Chem. Phys.*, vol. 20, 1952, p. 1216.

23 Cahn, J. W. and Hilliard, J. E., "Free Energy of a Nonuniform System. III. Nucleation in a Two-Component Incompressible Fluid," *J. Chem. Phys.*, vol. 31, 1959, p. 688.

24 Hart, E. W., "Thermodynamics of Inhomogeneous Systems," *Phys. Rev.*, vol. 113, 1959, p. 412.

25 Taylor, H. S., Eyring, H. and Sherman, A., "Binding Energies in the Growth of Crystal Nuclei from Metallic Atoms," *J. Chem. Phys.*, vol. 1, 1933, p. 68.

26 Courtney, W. G., "Nucleation of Copper Metal from Aqueous Solution," *J. Phys. Chem.*, vol. 60, 1956, p. 1461.

27 Probstein, R. F., "Time Lag in the Self-Nucleation of a Supersaturated Vapor," *J. Chem. Phys.*, vol. 19, 1951, p. 619.

28 Wakeshima, H., "Time Lag in the Self-Nucleation," *J. Chem. Phys.*, vol. 22, 1954, p. 1614.

29 Collins, F. C., "Time Lag in Spontaneous Nucleation Due to Non-Steady State Effects," *Z. Elektrochem.*, vol. 59, 1955, p. 404.

30 Frisch, H. L., "Time Lag in Nucleation," *J. Chem. Phys.*, vol. 27, 1957, p. 90.

31 Turnbull, D., "Transient Nucleation," *Metals Technology*, June 1958, p. 774.

32 Christiansen, J. A., "On Attainment of the Stationary (Steady) State in Nucleation," *Acta Chem. Scand.*, vol. 8, 1954, p. 909.

33 Ward, A. F. H. and Tordai, L., "Time-Dependence of Boundary Tensions of Solutions. I. The Role of Diffusion in Time-Effects," *J. Chem. Phys.*, vol. 14, 1946, p. 453.

34 Göring, W., "The Dependence of Surface Tension on the Rate of Formation and of Aging of the Surface," *Z. Electrochem.*, vol. 63, 1959, p. 1069; *Chem. Abstr.*, vol. 54, p. 5199.

35 Becker, R. and Döring, W., "The Kinetic Treatment of Nuclear Formation in Supersaturated Vapors," *Ann. Physik*, vol. 24, 1935, p. 719.

36 Frenkel, J., *Kinetic Theory of Liquids*, Clarendon Press, Oxford, 1946, chap. 7.

37 Reiss, H., "The Kinetics of Phase Transitions in Binary Systems," *J. Chem. Phys.*, vol. 18, 1950, p. 840.

38 Turnbull, D. and Fisher, J. C., "Rate of Nucleation in Condensed Systems," *J. Chem. Phys.*, vol. 17, 1949, p. 71.

39 Burton, W. K., Cabrera, N. and Frank, F. C., "The Growth of Crystals and Equilibrium Structure of Their Surfaces," *Phil. Trans. Roy. Soc.*, London, vol. A243, 1951, p. 299.

40 Christiansen, J. A. and Nielsen, A. E., "On the Kinetics of Formation of Precipitates of Sparingly Soluble Salts," *Acta Chem. Scand.*, vol. 5, 1951, p. 673.

41 Duke, F. R. and Brown, L. M., "Crystal Nucleation from Supersaturated Aqueous Solution. Tetraphenylarsonium Perchlorate and Nickel Nioxime," *J. Amer. Chem. Soc.*, vol. 76, 1954, p. 1443.

42 Turkevich, J., Stevenson, P. C. and Hillier, J., "A Study of the Nucleation and Growth Processes in the Synthesis of Colloidal Gold," *Discussions Faraday Soc.*, vol. 11, 1951, p. 55.

43 La Mer, V. K., "Nucleation in Phase Transitions," *Ind. Engng. Chem.*, vol. 44, 1952, p. 1270.

44 Cwilong, B. M., "Sublimation in a Wilson Chamber," *Proc. Roy. Soc.*, London, vol. A190, 1947, p. 137.

45 Hörbe, R., Knacke, O. and Prescher, K. E., "Condensation of a Stream of Vapor (Nucleus Formation and Diffusion)," *Z. Erzbergbau u. Metallhüttenw.*, vol. 11, 1958, p. 383; *Chem. Abstr.*, vol. 52, pp. 19, 270.

46 Birstein, S. J., "Studies on the Effect of Chemisorbed Impurities on Heterogeneous Nucleation," in *Physics of Precipitation*, H. Weickmann, Ed., American Geophysical Union, Washington, Geophysical Monograph no. 5, 1960, p. 247.

47 Erikson, T. A., "Mass Accommodation Coefficients at a Liquid-Vapor Boundary," *J. Phys. Chem.*, vol. 64, 1960, p. 820.

48 Kirklady, J. S., "The Time-Dependent Diffusion Theory for Condensation on Spherical and Plane Surfaces," *Canadian J. Phys.*, vol. 36, 1958, p. 446.

49 Frisch, H. L. and Collins, F. C., "Diffusional Processes in the Growth of Aerosol Particles. II," *J. Chem. Phys.*, vol. 21, 1953, p. 2158.

50 Ham, F. S., "Diffusion-Limited Growth of Precipitate Particles," *J. Appl. Phys.*, vol. 30, 1959, p. 1518.

51 Morrison, J. A. and Frisch, H. L., "Bounds on the Nonlinear Diffusion Controlled Growth Rate of Spherical Precipitates," *J. Appl. Phys.*, vol. 31, 1960, p. 1621.

52 Laitinen, H. A. and Kolthoff, I. M., "A Study of Diffusion Processes by Electrolysis with Microelectrodes," *J. Amer. Chem. Soc.*, vol. 61, 1939, p. 3344.

53 Wagner, C., "Theoretical Analysis of Diffusion of Solutes During the Solidification of Alloys," *J. Metals*, 1954, p. 154.

54 Nielsen, A. E., "Diffusion Controlled Growth of a Moving Sphere. The Kinetics of Crystal Growth in Potassium Perchlorate Precipitation," *J. Phys. Chem.*, vol. 65, 1961, p. 46.

55 Wilde, K. A., "Condensation in Nozzles," *J. Appl. Phys.*, vol. 30, 1959, p. 577.

56 Wegener, P. P. and Mack, L. M., "Comments on Condensation in Nozzles," *J. Appl. Phys.*, vol. 30, 1959, p. 1624.

57 Corner, J., "The Formation of an Aerosol by Condensation of a Dilute Vapor in a Carrier Gas," *Proc. Roy. Soc.*, London, vol. 211, 1952 p. 417.

58 Hazen, W. E., "Some Operating Characteristics of the Wilson Cloud Chamber," *Rev. Sci. Instr.*, vol. 13, 1942, p. 247.

59 Krueger, G. C. and Miller, C. W., "A Study in the Mechanics of Crystal Growth from a Supersaturated Solution," *J. Chem. Phys.*, vol. 21, 1953 p. 2018.

60 Greenwood, G. W., "Growth of Dispersed Precipitates in Solutions," *Acta Met.*, vol. 4, 1956, p. 243.

61 Luborsky, F. E., "The Kinetics of Growth of Spherical Iron Crystallites in Mercury," *J. Phys. Chem.*, vol. 61, 1957, p. 77.

62 Bransom, S. H. and Dunning, W. J., "Crystal Growth. Kinetics of Crystallization. Part II," *Discussions Faraday Soc.*, vol. 5, 1949, p. 96.

63 Doremus, R. H., "Precipitation Kinetics of Ionic Salts from Solution," *J. Phys. Chem.*, vol. 62, 1958, p. 1068.

64 Collins, F. C. and Leineweber, J. P., "The Kinetics of the Homogeneous Precipitation of Barium Sulfate," *J. Phys. Chem.*, vol. 60, 1956, p. 389.

65 Vermilyea, D. A., "On the Theory of Electrolytic Crystal Growth," *J. Chem. Phys.*, vol. 25, 1956, p. 1254.

66 Courtney, W. G., "Crystal Growth of Silver Metal. Mechanism and Kinetics," *J. Chem. Phys.*, vol. 27, 1957, p. 1349.

67 Nabarro, F. R. N. and Jackson, P. J., "Growth of Crystal Whiskers," in *Growth and Perfection of Crystals*. Doremus, Roberts, and Turnbull, Eds., John Wiley and Sons, Inc., N. Y., 1958.

68 Michaels, A. S. and Colville, A. R., Jr., "The Effect of Surface Active Agents on Crystal Growth Rate and Crystal Habit," *J. Phys. Chem.*, vol. 64, 1960, p. 13.

69 Wyllie, G., "Evaporation and Surface Structure of Liquids," *Proc. Roy. Soc.*, London, vol. A197, 1949, p. 383.

70 Mortensen, E. M. and Eyring, H., "Transmission Coefficients for Evaporation and Condensation," *J. Phys. Chem.*, vol. 64, 1960, p. 846.

71 Alty, T. and Mackay, C. A., "The Accommodation Coefficient and the Evaporation Coefficient of Water," *Proc. Roy. Soc.*, London, vol. A149, 1935, p. 104.

72 Littlewood, R. and Rideal, E., "On the Evaporation Coefficient," *Trans. Faraday Soc.*, vol. 52, 1956, p. 1598.

73 National Bureau of Standards, "Preliminary Report on the Thermodynamic Properties of Lithium, Beryllium, Magnesium, Aluminum and Their Compounds with Hydrogen, Oxygen, Nitrogen, Fluorine, and Chlorine," Rep. 6484, July 1, 1959.

74 Webb, W. W. and Forgeng, W. D., "Growth and Defect Structure of Sapphire Microcrystals," *J. Chem. Phys.*, vol. 28, 1957, p. 1449.

75 Sears, G. W. and DeVries, R. C., "Nucleation of Alumina at High Supersaturations and Subsequent Recrystallization," *J. Chem. Phys.*, vol. 32, 1960, p. 93.

76 v. Wartenberg, H., "Alumina," *Z. anorg. u. allgem. Chem.*, vol. 269, 1952, p. 76; *Chem. Abstr.*, vol. 47, p. 934.

77 Speiser, R., Naiditch, S. and Johnston, H. L., "The Vapor Pressure of Inorganic Substances. II. B_2O_3," *J. Amer. Chem. Soc.*, vol. 72, 1950, p. 2578.

78 Brewer, L. and Edwards, R. K., "The Stability of SiO Solid and Gas," *J. Phys. Chem.*, vol. 58, 1954, p. 351.

79 Brewer, L. and Mastick, D. F., "The Stability of Gaseous Diatomic Oxides," *J. Chem. Phys.*, vol. 19, 1951, p. 834.

80 Overbeek, J. Th. G., "Kinetics of Flocculation," in *Colloid Science*, H. R. Kruyt, Ed., Elsevier Publishing Co., N. Y., 1952, vol. 1, p. 278.

81 Elton, G. A. H., Mason, B. J. and Picknett, R. G., "The Relative Importance of Condensation and Coalescence Processes on the Stability of a Water Fog," *Trans. Faraday Soc.*, vol. 54, 1958, p. 1724.

82 Prokhorov, P. S., "The Effects of Humidity Deficit on Coagulation Processes and the Coalescence of Liquid Drops," *Discussions Faraday Soc.*, vol. 18, 1954, p. 41.

83 Gunn, R., "Droplet-Electrification Processes and Coagulation in Stable and Unstable Clouds," *J. Meteorology*, vol. 12, 1955, p. 511.

84 Rees, A. L. G., "Directed Aggregation in Colloidal Systems and the Formation of Protein Fibers," *J. Phys. and Colloid Chem.*, vol. 55, 1951, p. 1340.

85 Overbeek, J. Th. G., "Kinetics of Flocculation," in *Colloid Science*, H. R. Kruyt, Ed., Elsevier Publishing Co., N. Y., 1953, vol. 1, p. 299.

86 Gallily, I. and LavMer, V. K., "On the Behavior of Liquid Drops After Impinging on Solid Surfaces," *J. Phys. Chem.*, vol. 62, 1958, p. 1295.

87 Nakaya, U., Hanajima, M. and Muguruma, J., "The Growth of Snow Crystals," *J. Fac. Sci., Hokkaido Univ. Ser. II*, vol. 5, 1958, p. 87. *Chem. Abstr.*, vol. 54, p. 10,440.

88 Courtney, W. G. and Schaufelberger, F. A., "Observations on the Kinetics of the Reduction of $NiSO_4$ in Aqueous Solution," in *Proc. International Symposium of Physical Chemistry of Process Metallurgy*, 1959, to be published.

89 Luchak, G. and Langstroth, G. O., "Aplications of Diffusion Theory to Evaporation from Droplets and Flat Surfaces," *Canadian J. Research*, vol. 28A, 1950, p. 574.

90 Johnson, J. C., "Measurement of the Surface Temperature of Evaporating Water Drops," *J. Appl. Phys.*, vol. 21, 1950, p. 22.

91 Hirth, J. P. and Pound, G. M., "Coefficients of Evaporation and Condensation," *J. Phys. Chem.*, vol. 64, 1960, p. 619.

92 Mead, G. A., "Relation of Droplet Consumption Rates to Liquid Strand Consumption Rates," ARS JOURNAL, vol. 29, 1959, p. 440.

93 Langstroth, G. O., Diehl, C. H. H. and Winhold, E. J., "The Evaporation of Droplets in Still Air," *Canadian J. Research*, vol. 28A, 1950, p. 580.

94 Tovbin, M. V. and Savinova, E. V., "Kinetics of the Nonsteady State of a Process at a Liquid-Gas Interface. I. Kinetics of the Nonsteady State of the Evaporation of Water," *Zhur. Fiz. Khim.*, vol. 31, 1957, p. 2445; *Chem. Abstr.*, vol. 52, p. 8702.

95 Rothberg, G. M., Eisenstadt, M. and Kusch, P., "Free Evaporation of Alkali Halide Crystals," *J. Chem. Phys.*, vol. 30, 1959, p. 517.

96 Brewer, L., "Recent Determinations of the Vapor Pressure of Graphite," *J. Chem. Phys.*, vol. 20, 1952, p. 758.

97 Motzfeldt, K., "The Thermal Decomposition of Sodium Carbonate by the Effusion Method," *J. Phys. Chem.*, vol. 59, 1955, p. 139.

98 Metzger, F., "Determination of the Molecular Weight of Freely Evaporating Particles," *Helv. Phys. Acta*, vol. 16, 1943, p. 323; *Chem. Abstr.*, vol. 39, p. 1791.

99 Cassel, H. M. and Liebman, I., "Note on the Sublimitation of Ammonium Perchlorate," *J. Chem. Phys.*, vol. 34, 1961, p. 343.

100 Honig, R. E., "Sublimation Studies of Silicon in the Mass Spectrometer," *J. Chem. Phys.*, vol. 22, 1954, p. 1610.

101 Walker, R. F., National Bureau of Standards, personal communication.

102 Drowart, J. et al., "Thermodynamic Study of Al_2O_3 Using a Mass Spectrometer," *J. Chem. Phys.*, vol. 32, 1960, p. 1366.

103 Sears, G. W. and Navias, L., "Evaporation of Aluminum Oxide," *J. Chem. Phys.*, vol. 30, 1959, p. 1111.

104 Chupka, W. A. et al., "Vaporization of Beryllium Oxide and Its Reaction with Tungsten," *J. Chem. Phys.*, vol. 30, 1959, p. 827.

105 Grossweiner, L. I. and Seifert, R. L., "The Reaction of Beryllium Oxide with Water Vapor," *J. Amer. Chem. Soc.*, vol. 74, 1952, p. 2701.

106 Günther, K. G., "Measurement of Vapor Pressure and Rate of Evaporation of Glass-Forming Materials," *Glastech. Ber.*, vol. 31, 1958, p. 9. *Chem. Abstr.*, vol. 52, p. 10,674.

107 Searcy, A. W. and Myers, C. E., "The Heat of Sublimation of Boron and the Gaseous Species of the Boron-Boric Oxide System," *J. Phys. Chem.*, vol. 61, 1957, p. 957.

108 Meschi, D. J., Chupka, W. A. and Berkowitz, J., "Heterogeneous Reactions Studied by Mass Spectrometry. I. Reaction of $B_2O_3(s)$ with $H_2O(g)$," *J. Chem. Phys.*, vol. 33, 1960, p. 530.

109 Russell, A. S., et al., "Equilibrium and Rate of Aluminum Monochloride Formation from Aluminum Chloride and Aluminum," *J. Amer. Chem. Soc.*, vol. 73, 1951, p. 1466.

110 Witt, W. P. and Barrow, R. F., "The Heat of Sublimation of Aluminum Trifluoride and the Heat of Formation of Aluminum Monofluoride," *Trans. Faraday Soc.*, vol. 55, 1959, p. 730.

111 Berkowitz, J., et al., "Mass Spectrometric Study of the Sublimation of Lithium Oxide," *J. Phys. Chem.*, vol. 63, 1959, p. 644.

112 Schoonmaker, R. C. and Porter, R. F., "Mass Spectrometric Study of High Temperature Reactions of $H_2O(g)$ and $HCl(g)$ with Na_2O and Li_2O," *J. Phys. Chem.*, vol. 64, 1960, p. 457.

113 Wickert, K., "Deposits on Heating Surfaces in Steam Generators. II. Chemical Conversions in the Combustion Chamber and Measures Against Their Bad Effect," *Brennstoff-Warme-Kraft*, vol. 10, 1958, p. 101; *Chem. Abstr.*, vol. 52, p. 11,383.

114 Brewer, L. and Porter, R. F., "A Thermodynamic and Spectroscopic Study of Gaseous Magnesium Oxide," *J. Chem. Phys.*, vol. 22, 1954, p. 1867.

1961 ARS Meeting Schedule

Date	Meeting	Location	Abstract Deadline
June 13–16	National IAS-ARS Joint Meeting	Los Angeles, Calif.	Past
Aug. 7–9	Guidance and Control Conference	Palo Alto, Calif.	Past
Aug. 16–18	International Hypersonics Conference	Cambridge, Mass.	Past
Aug. 23–25	Biennial Gas Dynamics Symposium	Evanston, Ill.	Past
Oct. 2–7	XIIth International Astronautical Congress	Washington, D.C.	Past
Oct. 9–15	ARS SPACE FLIGHT REPORT TO THE NATION	New York, N.Y.	Past

Send all abstracts to Meetings Manager, ARS, 500 Fifth Ave., New York 36, N.Y.

The Virtual Mass of Clustered Boosters

HOLT ASHLEY[1]
Massachusetts Institute of Technology
Cambridge, Mass.

GIFFORD W. ASHER[2]
Boeing Airplane Co.
Seattle, Wash.

The need for estimating certain types of aerodynamic loadings on large boosters for space vehicles has generated a renewed interest in the problem of the virtual mass of two-dimensional shapes moving through constant-density fluid. One important example consists of pairs or clusters of parallel circular cylinders. A coordinated theoretical and experimental investigation of such configuration is described. Two complementary theories for unsteady flow over arrays of cylinders are described. The first deals approximately with an infinite row of equally spaced elements and provides limiting information on the influences of number and separation. The second involves systematic adaptation of the method of multiple imaged doublets. Considerable simplification is achieved through use of residues for calculating the fluid momentum. The application to a pair of cylinders is presented, and the method is capable of systematization on a high speed computer to determine the virtual masses for a rather general, finite aggregate of elements executing arbitrary translational motions. By measuring frequencies of oscillation in air and water the virtual mass is found for a pair of cylinders suspended by springs so as to translate either parallel or normal to the line between their centers. For several values of the ratio of radius to spacing, the theory is confirmed to within the experimental error of roughly ±6%. Sources of uncertainty, particular Reynolds number effect, are discussed.

WHEN calculating aerodynamic loads due to gust encounters or time-dependent lateral motions of slender configurations according to the crossflow theory of Munk, Jones et al., a very significant quantity is the virtual or apparent mass ρS (see, for instance, Section 7-6 of (1)[3] or Bryson (2)). The term ρS refers to the effective inertia, per unit length, of fluid carried along with a linear acceleration normal to the body axis; it varies with cross-sectional shape and with the direction of motion. In certain applications, ρS and similar two-dimensional inertia coefficients constitute the only information needed from the aerodynamicist.

One configuration which is likely to appear on spacecraft and large missile designs is the clustered booster stage, consisting of two or more circular cylindrical tanks in some sort of regular arrangement with parallel axes. While there is some doubt as to whether slender body theory is sufficiently accurate for estimating steady state aerodynamic derivatives of such shapes, except possibly in a narrow band of flight Mach numbers near unity, it can often be expected to yield reliable information on loads caused by unsteady or vibratory phenomena throughout the speed range that encompasses the maximum dynamic pressure.

Whereas the principles of virtual-mass calculation have been understood for a century (3), it would seem to be of interest to systematize the numerical process for the clustered-cylinder array and to apply an elementary experimental test to the results. The present paper describes a preliminary investigation along these lines. It is assumed in what follows that all booster elements are rigidly interconnected and accelerate rectilinearly as a unit. Vibrations of individual modules relative to one another and rotational motions can be analyzed by fairly direct extensions of the multiple image method used for the finite arrays.

Received Feb. 17, 1961.

[1] Professor of Aeronautics and Astronautics, Fluid Dynamics Research Laboratory.

[2] Chief, Dynamic Test and Direct Analog Unit, Aero. Space Div.

[3] Numbers in parentheses indicate References at end of paper.

Virtual Mass of Cylinders in an Infinite Row

While not having direct practical interest, the arrangement shown in Fig. 1 can be analyzed by an accurate closed-form approximation and provides a measure of the importance of interference effects on the virtual mass of a booster element centrally located in a row of three or more. One can proceed from the well-known solution given in Section 64 of Lamb (3) for an infinite row of point sources. The complex potential function reads

$$w(z) \equiv \varphi + i\psi = -C \ln \left[\sin h \frac{\pi z}{a} \right] \qquad [1]$$

Here $z = x + iy$, C is a real constant proportional to source strength, and φ and ψ are velocity potential and stream function according to the modern definitions (velocity vector $= +\text{grad } \varphi$). Differentiating Eq. 1 with respect to x, one obtains a row of doublets having axes parallel to x. With the uniform stream $w = -Uz$ added, the following complex potential is obtained

$$w = -Uz - C \coth \frac{\pi z}{a} \qquad [2]$$

To ascertain the form of the closed streamlines produced by the doublet row, note that the stream function deduced from Eq. 2 is

$$\psi = -Uy + \frac{C \sin \left(\frac{2\pi y}{a} \right)}{\cosh \left(\frac{2\pi x}{a} \right) - \cos \left(\frac{2\pi y}{a} \right)} \qquad [3]$$

If x is so small that $(2\pi x/a)^2 \ll 1$, Eq. 3 reduces to

$$\psi \cong -Uy\left[1 - \frac{b_0^2}{x^2 + y^2}\right] \qquad [4]$$

where $b_0 = \sqrt{a\,C/\pi U}$. This result implies that the flow, which obviously repeats itself whenever y is changed by an integral multiple of $\pm a$, reduces to that around a series of circular cylinders provided C is small enough to ensure the condition $(2\pi b/a)^2 \ll 1$. As observed in (3), moreover, the array of closed figures simulated by the doublets remains nearly a row of circles for much larger values of b/a. Thus the semi-axes x_1 and y_1 of the figure $\psi = 0$ from Eq. 3 are given by the implicit equations

$$\frac{xb_0}{a} = \sinh\frac{\pi x_1}{a} \qquad \frac{ay_1}{\pi b_0^2} = \cot\frac{\pi y_1}{a} \qquad [5]$$

Here b_0 might be described as a pseudo-radius, or limiting value of the semi-axes when the spacing becomes large.

Trial and error solution of Eqs. 5 yields the results shown in Table 1. These numbers, together with a more detailed study of the figure's shape, appear to justify the assumption that it is practically a circular cylinder up to diameters at least half as great as the spacing a.

In a similar fashion, streaming in the negative y-direction past the array of Fig. 1 is approximated by taking the derivative of Eq. 1 with respect to y and adding $w = iUz$

$$w = iUz + iC\coth\frac{\pi z}{a} \qquad [6]$$

The semi-axes x_2 and y_2 of the shapes thus produced now prove to be solutions of

$$\frac{ax_2}{\pi b_0^2} = \coth\frac{\pi x_2}{a} \qquad \frac{\pi b_0}{a} = \sin\frac{\pi y_2}{a} \qquad [7]$$

$b_0 = \sqrt{aC/\pi U}$ once more denoting a pseudo-radius. Table 2 again seems to verify the assumption of circularity up to about $b_0/a = 1/4$. But here the figures grow with decreasing spacing, until the final line represents a situation where each one just touches its neighbor.

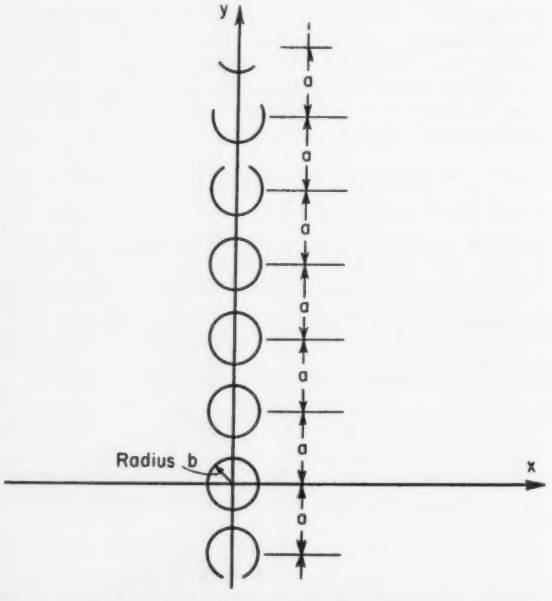

Fig. 1 Infinite row of identical circular cylinders with centers spaced at distances a along the y-axis

Table 1 Trial and error solution of Eqs. 5

b_0/a	x_1/b_0	y_1/b_0
0	1	1
$1/3\pi$	0.981	0.982
$1/2\pi$	0.962	0.960
$2/3\pi$	0.932	0.931
$1/\pi$	0.881	0.860

Table 2

b_0/a	x_2/b_0	y_2/b_0
0	1	1
$1/3\pi$	1.020	1.018
$1/2\pi$	1.045	1.049
$2/3\pi$	1.080	1.092
$1/\pi$	1.20	$\pi/2$

It can be checked without difficulty that, in the limit $b_0/a \to 0$, the virtual mass of any one cylinder in the foregoing arrays approaches

$$\rho S = \rho\pi b_0^2 \qquad [8]$$

regardless of the direction of motion. This is, of course, the same as if all other elements were absent and denotes vanishing interference effect. For closer spacings, one has recourse to the unsteady form of the Blasius theorem, as given on pp. 163–164 of Milne-Thompson (4)

$$X - iY = \frac{\rho}{2}\,i\oint\left(\frac{dw}{dz}\right)^2 dz + i\rho\frac{\partial}{\partial t}\oint \bar{w}\,d\bar{z} \qquad [9]$$

The contour in Eq. 9 is any suitable curve surrounding only those singularities which represent the body on which the force components X and Y are desired. In the absence of net circulation or yield, the first term on the right must always vanish.

When using Eq. 9 for an accelerated flow, the coordinate system must always be chosen to make the stream function constant at the body's surface, and this implies an accelerated *stream* $U(t)$. Since the present problem concerns an accelerated *body* in fluid at rest, a buoyant force equal to ρ times the displaced cross-sectional area must be subtracted from the apparent mass so obtained. For instance, one calculates from Eqs. 2 and 9

$$X = 2\rho\pi b_0^2\frac{dU}{dt} \qquad Y = 0 \qquad [10]$$

whence

$$\rho S_x = 2\rho\pi b_0^2 - \rho x(\text{area}) \qquad [11]$$

The area in question must be that of the actual slightly distorted figure. From Table 1 one sees that this is less than the area πb_0^2 based on the pseudo-radius, so that the effect of squeezing the cylinders together is to augment the mass associated with acceleration normal to the line of centers (as might have been expected on physical grounds). After some manipulation, the result can be put into the relatively simple form

$$\rho S_x = \rho 4\pi b_0^2\int_0^{y_1/b_0} \times \sqrt{\left(\frac{b_0}{a}\right)^2 + \frac{2b_0}{\pi a}\,q\cot\left(\frac{2\pi b_0 q}{a}\right) - \frac{q^2}{\pi^2}}\;dq \qquad [12]$$

In a parallel fashion, the virtual mass of an individual

cylinder due to motion along the line of centers is found from Eqs. 6 and 9 to be

$$\rho S_y = \rho 4\pi b_0^2 \int_0^{x_2/b_0} \times \sqrt{\frac{2b_0}{\pi a} q \coth\left(\frac{2\pi b_0 q}{a}\right) - \frac{q^2}{\pi^2} - \left(\frac{b_0}{a}\right)^2}\, dq \quad [13]$$

Closed-form expressions could not be discovered for the integrals appearing in Eqs. 12 and 13. Accordingly, they were calculated by quadrature for several values of the single parameter b_0/a on which they depend (the upper limit in each case corresponds to the value of the variable q where the integrand vanishes and is not an independent quantity). Fig. 2 plots the two virtual masses of the infinite row and compares them with those determined for a pair of cylinders in the section following. The symbol b employed in the abscissa and in the nondimensionalizing divisor $\rho\pi b^2$ denotes, in every instance, the best estimate of the actual radius and not the physically meaningless pseudo-radius b_0.

Pairs and Finite Arrays of Cylinders

Accelerated motion of a pair of circular cylinders through liquid can be analyzed by straightforward adaptation for two-dimensional flow of the multiple image method applied to double spheres in Sections 98–99 of Lamb (3).[4] The single booster element with horizontal velocity U is, of course, represented by a horizontal doublet, the complex potential being

$$w(z) = -\frac{Ub^2}{z} \equiv -\frac{H_0}{z} \quad [14]$$

A second, identical cylinder centered at $z = a$ would add the potential $-Ub^2/(z - a)$ in the absence of interference effects. The former doublet is known to possess an image in the latter's circle, however, located at $z = x_1 \equiv a - (b^2/a)$ and having strength

$$H_1 = -\frac{H_0 b^2}{a^2} \quad [15]$$

This image interferes with the boundary condition at the surface of the original cylinder, and by successive applications of the circle theorem (4) one constructs the system of doublets shown in Table 3. Similarly, the second cylinder's motion in the presence of the first is associated with another doublet system, shown in Table 4. (The two systems have been listed separately because relative motion U_r in the x-direction can be obtained by substituting $(U + U_r)$ for one of the U.)

With a uniform flow $U(t)$ added to make the circles instantaneous streamlines, one is thus led to the complex potential

$$w(z) = -Uz - Ub^2\left\{\frac{1}{z} - \frac{(b^2/a^2)}{z - x_1} + \frac{(b^4/a^2x_1^2)}{z - x_2} - \frac{b^6}{a^2x_1^2[a - x_2]^2}\left(\frac{1}{z - x_3}\right) + \frac{b^8}{a^2x_1^2[a - x_2]^2x_3^2}\left(\frac{1}{z - x_4}\right) - \cdots\right\} - Ub^2\left\{\frac{1}{z - a} - \frac{(b^2/a^2)}{z - x_1'} + \frac{b^4}{a^2[a - x_1']^2}\left(\frac{1}{z - x_2'}\right) - \cdots\right\} \quad [16]$$

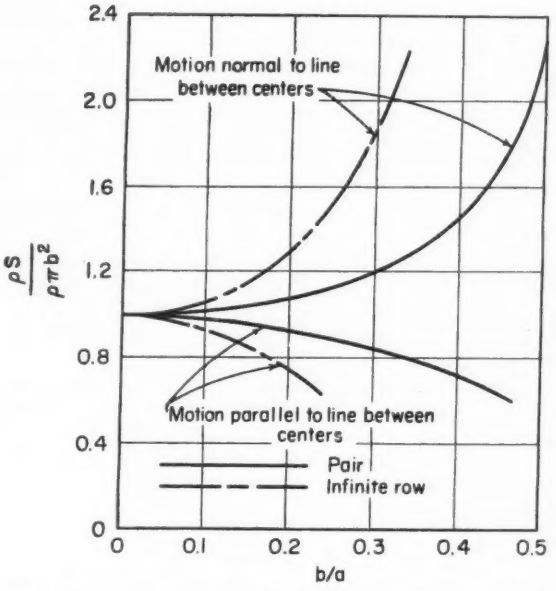

Fig. 2 Theoretical virtual masses of individual circular cylinders in a pair and an infinite row vs. the ratio of true radius b to spacing a

[4] This method has previously been used by Nechaev in a paper (6) which is difficult to obtain.

Table 3 Doublet system

Strength	Location z
$H_0 \equiv Ub^2$	0
$\frac{H_1}{H_0} = -\frac{b^2}{a^2}$	$a - \frac{b^2}{a} \equiv x_1$
$\frac{H_2}{H_1} = -\frac{b^2}{x_1^2}$	$\frac{b^2}{x_1} \equiv x_2$
$\frac{H_3}{H_2} = -\frac{b}{(a - x_2)^2}$	$a - \frac{b^2}{a - x_2} \equiv x_3$
$\frac{H_4}{H_3} = -\frac{b^2}{x_3^2}$	$\frac{b^2}{x_3} \equiv x_4$
$\frac{H_5}{H_4} = -\frac{b^2}{(a - x_4)^2}$	$a - \frac{b^2}{a - x_4}$
.	.
.	.
.	.

Table 4 Doublet system

Strength	Location z
$H_0' \equiv Ub^2$	a
$\frac{H_1'}{H_0'} = -\frac{b^2}{a^2}$	$\frac{b^2}{a} \equiv x_1'$
$\frac{H_2'}{H_1'} = -\frac{b^2}{(a - x_1')^2}$	$a - \frac{b^2}{a - x_1'} \equiv x_2'$
$\frac{H_3'}{H_2'} = -\frac{b^2}{(x_2')^2}$	$\frac{b^2}{x_2'} \equiv x_3'$
$\frac{H_4'}{H_2'} = -\frac{b^2}{(a - x_3')^2}$	$a - \frac{b^2}{a - x_3'} \equiv x_4'$
$\frac{H_5'}{H_4'} = -\frac{b^2}{(x_4')^2}$	$\frac{b^2}{x_4'}$
.	.
.	.
.	.

Once more the virtual mass is most efficiently worked out by means of Eq. 9. Evidently, the first integral vanishes; the second may be evaluated for an indefinitely large contour so that all doublets in Eq. 16 behave as if they were centered at the origin. The resulting virtual mass per cylinder, with the nonexistent buoyancy subtracted, proves to be

$$\frac{\rho S_y}{\rho \pi b^2} = 1 - 2R^2 + \frac{2R^4}{(1-R^2)^2} - \frac{2R^6}{(1-2R^2)^2} + \frac{2R^8}{(1-3R^2+R^4)^2} - \frac{2R^{10}}{(1-4R^2+3R^4)^2} + \cdots \quad [17]$$

Here $R = b/a$, and subscript y has been used with S to agree with earlier notation, the case being one of acceleration parallel to the line between the centers.

The doublet system describing motion perpendicular to the line of centers can be developed without difficulty. In this case all doublets are positive, with parallel axes, so that interference augments the disturbance. In fact, the virtual mass $\rho S_x/\rho\pi b^2$ is given by the same series as Eq. 17, except that all terms now have positive signs. Fig. 2 displays both sets of results graphically.

The calculations for Fig. 2 were made using only the terms in Eq. 17. Convergence appears to be excellent and can be tested by going to the extreme situation of tangent cylinders, $b/a = 0.5$, for which an exact solution may be found on pp. 174–175 of (4). Milne-Thompson shows that

$$w(z) = -b\pi U \coth \frac{b\pi}{z} \quad [18]$$

describes two cylinders in contact along the y-axis with a uniform stream $-U$ along x. From Eqs. 9 and 18 one computes the dimensionless virtual mass $(\pi^2/3) - 1 \equiv 2.29$, which may be compared with 1.98 from six terms of the series.

Indeed, these series may have inherent mathematical interest because of the repeated fractions that appear. Thus

$$\frac{\rho S_y}{\rho \pi b^2} = 1 + 2\sum_{n=1} (-1)^n \frac{R^{2n}}{D_n^2} \quad [19]$$

where

$$D_1 = 1 \qquad D_2 = 1 - R^2$$

$$D_n = D_{n-1} - R^2 D_{n-2} \text{ for } n > 2$$

The image method illustrated by the foregoing elementary examples is capable, in principle, of extension to arbitrary motion of an arbitrary array of circular cylinders. It is for this reason that the doublets were adopted for the two-cylinder case, which can be handled by more elegant application of conformal transformations that are unfortunately incapable of such a generalization.[5] The first step is to identify doublet potentials representing the disturbance produced by each of the elements in the absence of the others. Then each such potential is supplemented with a system of images that causes the other cylinders to be streamlines of its flow. This is an elaborate process, consisting of first reflecting the original doublet in each of the other cylinders, then reflecting each of the image doublets in all other cylinders including the original one. The images of the images are next constructed, and the process is continued until satisfactory convergence is achieved. When the various cylinders do not have all their centers along the same line, the following result from page 222 of Milne-Thompson (4) is worth restating: "The image of a doublet of strength μ at distance f from the center of a cylinder of radius b is a doublet at the inverse point

[5] See, for example, the rapidly convergent solution in bipolar coordinates developed on pp. 1211–1213 of Morse and Feshbach (7).

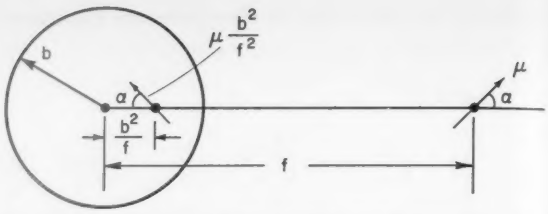

Fig. 3 Doublet of strength μ and its image in the circle $r = b$

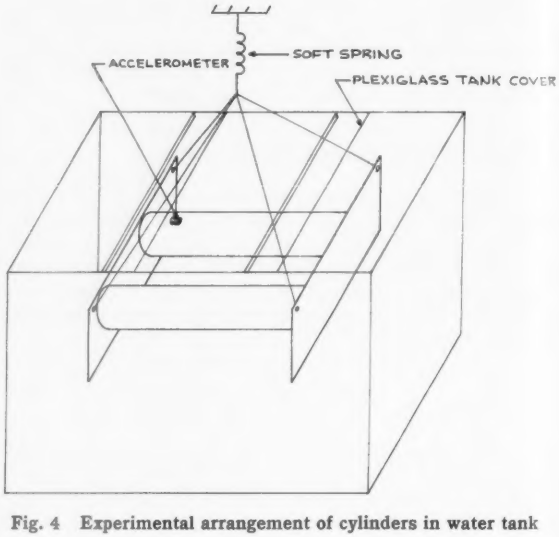

Fig. 4 Experimental arrangement of cylinders in water tank

(a) Configuration with 5×7 in. end plates

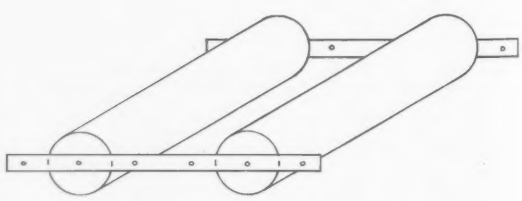

(b) Configuration without end plates

Fig. 5 Two basic arrangements of end plates

($r = b^2/f$) of strength $\mu b^2/f^2$, and the axes of the doublet and its image are equally inclined to the line joining them but are not parallel (antiparallel)." The relationship is shown in Fig. 3.

Given the locations, strengths and orientations of all the singularities, Eq. 9 together with the residue theorem will yield the virtual mass associated with any one booster element or the whole configuration translating in any stated direction. This calculation for the entire assemblage is facilitated by the fact that every doublet may be treated as if centered at the origin of coordinates.

A useful check on the results is provided by a formula for the kinetic energy of an incompressible flow in Section 46 of (3)

$$T = -\frac{\rho}{2}\int \varphi \frac{\partial \varphi}{\partial n}\, dS \qquad [20]$$

Here the surface integral is carried out over all the flow boundaries, including the one at infinity where it can be made to vanish, and the normal derivative is taken from the boundary into the fluid. The velocity potential is broken into a series of coefficients equal to the number of booster elements, each corresponding to unit velocity of one cylinder with all the others at rest. The kinetic energy expression then contains a symmetric matrix whose diagonal terms are the direct virtual masses for acceleration of individual cylinders, whereas the off-diagonal terms correspond to "cross-inertia" effects of the motion of one cylinder on the force experienced by another. Sections 98 and 99 of Lamb (3) give details of such a computation for two spheres.

No illustrations of the process are presented here, but it has been worked through by hand for three equally spaced cylinders, with equal radii, moving along the line between their centers. The object was to establish whether the operations can be systematized to the point that high speed machine computation becomes feasible. This appears to be definitely the case when only linear accelerations are involved. Although the programming has not yet been undertaken, a very high degree of mechanization will be possible if and when complicated configurations need to be analyzed. The rapidity of convergence should roughly equal that for the two-cylinder case with the same spacing-to-diameter ratio.

Measurements on Paired Circular Cylinders

Several simple experiments were undertaken to check the validity of the theory. In order to obtain a large virtual mass for measurement purposes cylinders were tested in water; the arrangement is shown in Figs. 4 and 5. Two cylinders were attached rigidly together and suspended from a soft spring. The cylinder pair was then displaced and allowed to oscillate in air. Frequency of oscillation was obtained from an accelerometer record. The cylinders were then immersed in water and the process repeated. From the difference in frequencies in water and air, the virtual mass can be found for one cylinder of the pair as

$$\frac{\rho S}{\rho \pi b^2} \cong \left[\left(\frac{f_{air}}{f_{H_2O}}\right)^2 - 1\right]\frac{M}{2\rho\pi b^2 L} \qquad [21]$$

where

ρS = virtual mass carried by the cylinder per unit length
b = cylinder radius
f_{air} = frequency in air
f_{H_2O} = frequency in water
M = total mass of the cylinders and end plates
L = length of the cylinders
ρ = density of water

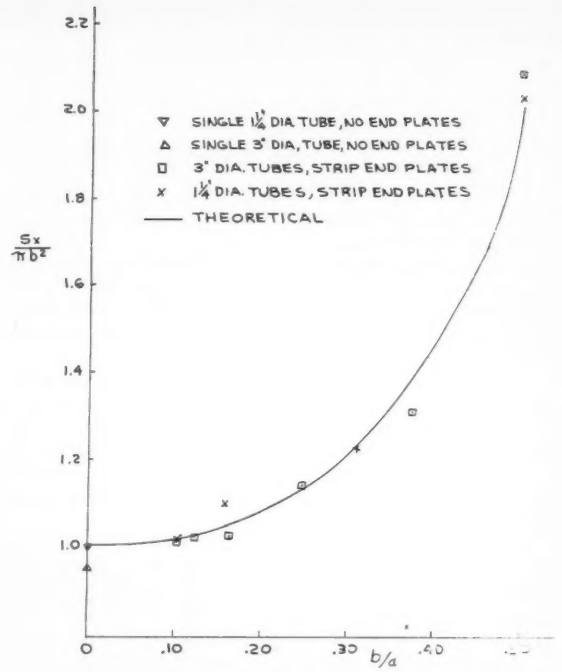

Fig. 6 Comparison of experimental and theoretical virtual mass, as a function of radius-to-spacing ratio b/a, for motion normal to the line of centers of two cylinders

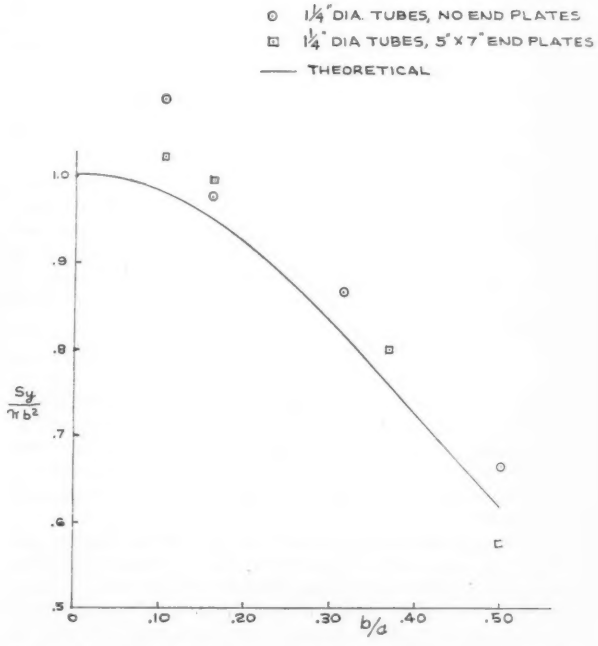

Fig. 7 Comparison of experimental and theoretical virtual mass, as a function of radius-to-spacing ratio b/a, for motion parallel to the line between the centers of two cylinders

Eq. 21 assumes that the virtual mass of the cylinder pair in air is negligible, and that the spring stiffness remains unchanged with the cylinders in air and in water.

Several model arrangements were employed. One series used two cylinders $1\frac{1}{4}$ in. in diameter and 10 in. long, which were tested with end plates 5 in. by 7 in. and with a thin strip connecting the cylinders (Figs. 5a and 5b). In motion parallel to the line between the centers little consistent difference could be found between the results with and without end plates, so all of the remaining tests with motion perpendicular to line of centers were made with thin strips connecting the cylinders.

Virtual masses of the $1\frac{1}{4}$ in. diameter cylinders were measured in a small tank 20 × 20 by 9 in. deep. A second series of measurements was made on two cylinders 3.0 in. in diameter and 30 in. long. These larger cylinders were tested in a tank 7 × 7 by 3 ft deep.

All of the experimental results are summarized and compared with the predicted virtual masses given in the previous section in Figs. 6 and 7. Nearly every data point falls within an expected scatter band of ±6% centered on the theoretical curves. The size of this probable error stems primarily from an uncertainty of about $\pm 1\frac{1}{2}\%$ in the frequency measurements.

Some comments are in order about other sources of experimental error. End effects and wall effects can be dismissed rather easily. The former may be estimated from the fact that an ellipsoid of revolution with 10:1 fineness ratio already has a virtual mass with respect to translation along a minor axis which is 96% of what would be computed by assuming two-dimensional flow at every cross section (3). Even in the absence of end plates, a 10:1 cylinder is expected to produce more nearly two-dimensional conditions than the ellipsoid.

The influence of vertical walls parallel to both the axes and the direction of oscillation, according to the concept of images, is roughly the same as that on an infinite row of cylinders in normal motion with spacing a equal to the tank's width. In the smaller tank the effective value of b/a is 1/32. Fig. 2 indicates about 0.1% difference from the virtual mass of a single, isolated cylinder.

Although no evidence of separation or wake formation was observed at the rather small ratios of amplitude to radius that characterized these tests, there is a question as to whether viscous stresses in the boundary layer may have affected the data. A clue is provided by the negligible difference between the damping ratios of vibrations in air and in water. But more quantitative estimates are possible by reference to the solution for an oscillating cylinder in slightly viscous liquid, pp. 194–197 of Schlichting (5). This theory indicates net forces due to viscous stresses both in phase and 90 deg out of phase with the cylinder's displacement. It is not difficult to determine that the ratio of the virtual-mass force to either viscous force component has an order of magnitude

$$\sqrt{(2\pi f_{H_2O})b^2/\nu}$$

ν being the kinematic viscosity of the liquid. Accordingly, the significant Reynolds number $(2\pi f_{H_2O})b^2/\nu$ for these experiments is based on a velocity equal to the circular frequency times the radius, and not on the maximum velocity of the oscillatory motion as the authors had originally believed.[6]

Taking a nominal value of 11×10^{-6} ft²/sec for the ν of water at laboratory temperature, one calculates Reynolds numbers which range from a minimum of 1690 on the smaller cylinders to 32,300 on the larger. Thus the conclusion that viscous effects are unimportant seems justified. To put the observation another way, although this same Reynolds number estimated for vibrations of large booster elements in air is of the order 10^6, a high enough value has been achieved in these experiments to permit safe extrapolation to the full-scale situation.

[6] This finding would have to be modified, of course, if the amplitude of oscillation became of the same order of magnitude as the diameter.

Discussion and Conclusions

The data summarized in Figs. 6 and 7 were obtained in an experimental situation which is believed to correspond quite closely to unsteady, two-dimensional translation of a cylinder pair through ideal, constant density fluid. That confirmation is indicated for the theoretical estimates to within the error of measurement, allows one to be optimistic about applying the theory to multiple cylinders and other, more complicated configurations and motions. One must, of course, extrapolate a long way on the Reynolds number scale when going from small tubes in a water tank to vibrations or gust encounters of full sized boosters. Nevertheless, if the angles of attack remain small and the time constants of the unsteady phenomena sufficiently short, one can find ample justification for overlooking viscous influences on aerodynamic loads.

Perhaps the major conclusion of the study is that interference effects among the elements in a cluster of cylinders are likely to be significant. These effects already amount to 12–14% on a pair separated by two diameters. With respect to loads normal to the line between centers they are unfavorable, in the sense that treating individual elements as if isolated will always yield an underestimate. When three or more cylinders are aligned, interference on the central members will be of the same order as that for an infinite row, which is about three times as great as for a pair.

The method of multiple imaged doublets offers a promising avenue for systematizing the theory to permit high speed digital computation of virtual masses on clustered arrangements not susceptible of analytical treatment. Any such elaborate programming effort should, of course, be backed up by additional tests. But the technique of oscillating small models in water provides a simple, inexpensive (albeit indirect) approach that can be implemented well in advance of costly wind tunnel and flight loads measurements.

Nomenclature

a	= distance between centers in equally spaced arrays of circular cylinders
b	= radius of circular cylinder
b_0	= $\sqrt{aC/\pi U}$ = pseudo-radius for infinite row of doublets in stream U
C	= strength of source or doublet
f	= frequency of oscillation, cycles/sec
H_n, H_n'	= strengths of doublets in image system (n = 0, 1, 2, ...)
i	= $\sqrt{-1}$
L	= length of cylinder
M	= total mass of experimental model
q	= dummy integration variable
r	= radial polar coordinate
R	= b/a
ρS	= virtual mass per unit length of two-dimensional cylindrical body in constant density fluid
S_x	= value of S for one element of a linear array of circular cylinders, corresponding to two-dimensional motion normal to the line between the centers
S_y	same as S_x, except corresponding to motion parallel to the line between the centers
t	= time
T	= kinetic energy of fluid
U	= velocity of uniform stream
$w(z)$	= $\phi + i\psi$ = complex potential function of two-dimensional, constant density flow
x, y	= rectangular Cartesian coordinates
x_n, x_n'	= locations of image doublets (n = 1, 2, 3, ...)
X, Y	= force components in x, y-directions

z = $x + iy$ = complex variable
ν = kinematic viscosity of water
ρ = fluid density
φ = velocity potential
ψ = stream function
$\overline{(\ )}$ = complex conjugate

References

1 Bisplinghoff, R. L., Ashley, H. and Halfman, R. L., "Aeroelasticity," Addison-Wesley, Cambridge, Mass., 1955.

2 Bryson, A. E., "Stability Derivatives for a Slender Missile with Application to a Wing-Body-Vertical-Tail Configuration," *J. Aero. Sci.*, vol. 20, no. 5, May 1953, pp. 297–308.

3 Lamb, Sir H., *Hydrodynamics*, Dover, N. Y., 1945, Sixth Edit.

4 Milne-Thompson, L. M., *Theoretical Hydrodynamics*, Macmillan, N. Y., 1960, Fourth Edit. (First Edit., 1950).

5 Schlichting, H., *Boundary Layer Theory*, McGraw-Hill, N. Y., 1955 (translated by J. Kestin from First German Edition, 1951).

6 Nechaev, S. V., "The Flow about Two Circles," (in Russian) *Trudi Kazansk. Aviats.* In-ta no. 35, pp. 21–35, 1957 (see *Appl. Mech. Rev.*, vol. 13, no. 6, June 1960, Review 2912).

7 Morse, P. M. and Feshbach, H., *Methods of Theoretical Physics*, Part II, McGraw-Hill, New York, 1953.

Theory of Mixing and Chemical Reaction in the Opposed-Jet Diffusion Flame

D. B. SPALDING[1]

Imperial College
London, England

An idealization of the flow system used by Potter and Butler is analyzed. The differential equation of mixing is solved exactly, to give the location of, and burning rate in, the flame. The solutions to the chemical kinetic differential equation are discussed, relations being derived between the jet flow rate at extinction, the chemical kinetic constants and the laminar flame speed in premixed gases. It is shown that the jet flow rate at extinction is independent of the transport properties. Comparison is made with the experimental data of Potter, Heimel and Butler. It is argued that experiments must be carried out at higher Reynolds numbers if the measurements are to be quantitatively analyzable.

EXPERIMENTS have been carried out by Potter and Butler (4)[2] on the extinction of the diffusion flame which forms between two opposed coaxial gas jets, one of which contains fuel and the other an oxidant. Further experimental data have been reported by Potter, Heimel and Butler (5).

The chief measurement made is of the highest mass flow rate in the jets at which the diffusion flame is unbroken on the axis of symmetry. Potter et al. call this the "apparent flame strength"; it has the units: lb_m/ft^2h.

Since the experimental technique promises to provide a simple and informative tool for investigating the reaction-rate constants of propellant substances, it is desirable to have a mathematical theory which links the experimental observations with the physical and chemical properties of the substances; for only then can quantitative conclusions be drawn.

The physical situation and the mathematical methods of analysis are also akin to those arising in the cooling of a missile stagnation point by a combustible gas. The solutions to be derived only apply in detail when the dimensionless mass transfer driving force is very large, so that combustion occurs at the outer edge of the boundary layer; however the actual boundary layer situation can be handled with only minor modifications to the techniques used herein.

The whole phenomenon has three main aspects involving: the flow pattern (velocity distribution); the mixing pattern (mixture ratio distribution); and the flame (distribution of departures from thermodynamic equilibrium). A complete theory will therefore involve three parts: a study of the fluid mechanics; a theory of mass transfer; and an appropriate application of chemical kinetic theory.

So far, none of these three theoretical problems has been adequately solved for the opposed-jet diffusion flame. Potter et al. have attempted to interpret their results in terms of the approximate chemical kinetic theories of Zeldovich (11) and Spalding (6). In order to do so, however, they have had to jump the gap left by the absence of fluid mechanical and mass

Received Jan. 23, 1961.

[1] Professor of Heat Transfer, Mechanical Engineering Department.

[2] Numbers in parentheses indicate References at end of paper.

transfer theories; consequently their tentative conclusions are subject to considerable doubt, and indeed, error, as will be shown.

The present paper is intended partially to fill this gap; it provides an exact theory for fluid mechanics and mixing in a situation which may be regarded as an idealization of that of Potter et al. Although the effects of variations in the fluid properties with composition and temperature are not fully accounted for in the theory, it is shown below that such an accounting would only cause minor modifications to the present conclusions.

The theory to be presented may also lead to experimental advances, for it indicates what conditions must be fulfilled by the apparatus dimensions if the experimental observations are to be used for the quantitative deduction of physical and chemical data.

The fluid mechanical part of the paper contains little more than a citation and interpretation of the work of Leclerc (1). This is contained in the next section. The mass-transfer theory, which has had to be developed *ab initio*, follows. Another section of the paper provides the chemical kinetic theory for a simple chemical reaction. No numerical computations are presented, these being reserved for a later paper; however, approximate solutions are presented by use of arguments akin to those of Zeldovich (11) and Spalding (6). These provide an adequate basis for the prediction or extinction phenomena, and for the comparisons with experiment.

Fluid Mechanical Theory of Opposed Jets

Although it is possible, and may be useful, to stabilize a diffusion flame between opposed fuel and oxygen jets of unequal diameters and unequal mass flow ratio, Potter and his co-workers have confined themselves to equal diameters and nearly equal velocities. It will therefore suffice, at present, to discuss the symmetrical case in which the diameters, densities and velocities of the two opposed streams are equal.

The symmetry of this system ensures that the flow pattern is identical with that of a single inviscid fluid jet impinging on a flat plate held normal to it. Fortunately, a solution to the equation of motion has been obtained for this case by Leclerc (1), by the use of an electrical resistance analog.

It is not necessary for us to do more here than to cite one of Leclerc's results, which is

$$\frac{u}{U} = \frac{x}{D} \qquad [1]$$

where

u = radial velocity in vicinity of the plate
x = radial distance from the axis of symmetry
U = velocity in the jet approaching the plate
D = diameter of the jet approaching the plate

This result holds for a layer whose thickness in the axial direction is about one-tenth of the jet diameter.

In the remainder of the present paper it will be assumed that Eq. [1] holds within a distance of $0.1D$ of the plane of symmetry when two equal jets impinge; this will be called the impingement region.

Mass Transfer in the Impingement Region

Differential Equations

The mass conservation principle applied to the impingement region implies the equation

$$\frac{1}{x}\frac{\partial}{\partial x}(x\rho u) + \frac{\partial(\rho v)}{\partial y} = 0 \qquad [2]$$

Hence, since

$$\partial\rho/\partial x = 0 \qquad [3]$$

as will soon become obvious owing to the fact that surfaces of constant fluid state are parallel to the $y = 0$ plane at a stagnation point, we may integrate Eq. 2 combined with Eq. 1 to yield

$$\rho v = -2\frac{U}{D}\int_0^y \rho dy \qquad [4]$$

Provided that the diffusion coefficients of all molecular species are equal in value at any particular point, the species conservation and flux equations reduce (9,10) to

$$\mathbf{G}(\nabla f) - \nabla[\gamma(\nabla f)] = 0 \qquad [5]$$

where f is the mass fraction of one of the two parent substances in the local mixture. In the context of the present stagnation point flow with zero x-wise gradients of fluid state, Eq. 5 becomes

$$\rho v\frac{df}{dy} - \frac{d}{dy}\left(\gamma\frac{df}{dy}\right) = 0 \qquad [6]$$

ρv can be eliminated from Eq. 6 by substitution from Eq. 4. If in addition the substitution is made

$$Y \equiv \int_0^y \frac{\rho}{\rho_\infty}dy \qquad [7]$$

there results

$$\frac{d}{dY}\left(\frac{\gamma\rho}{\rho_\infty}\frac{df}{dY}\right) + 2\rho_\infty\frac{UY}{D}\frac{df}{dY} = 0 \qquad [8]$$

The boundary conditions are

$$\begin{aligned} Y &= +\infty \qquad f = 1 \\ Y &= -\infty \qquad f = 0 \end{aligned} \qquad [9]$$

wherein Y and y have been defined as positive when measured toward the jet from which emerges the fluid of which f measures the mass fraction.

Eqs. 8 and 9 define the mathematical problem which must be solved.

Solution

If $\phi(f)$ is defined by

$$\phi \equiv \gamma\rho/\gamma_\infty\rho_\infty \qquad [10]$$

Eq. 9 may be written as

$$\frac{d}{dY}\left(\phi\frac{df}{dY}\right) + 2\rho_\infty\frac{U}{D\gamma_\infty}\cdot Y\frac{df}{dY} = 0 \qquad [11]$$

On integrating once

$$\phi\frac{df}{dY} = Ae^{-\frac{\rho_\infty U}{D\gamma_\infty}Y^2} \qquad [12]$$

where A is an integration constant.

Thereafter a further integration, coupled with insertion of the boundary conditions (Eq. 9), leads to the final solution

$$\int_0^f \phi df \Big/ \int_0^1 \phi df = 1/2[1 + \text{erf}\,(Y\sqrt{\rho_\infty U/\beta_\infty D})] \qquad [13]$$

Evaluation of the left-hand side of Eq. 13 is easy, since the property ratio ϕ depends on the local composition, measured by f, and on the local temperature, measured for example by the enthalpy h. h and f are easily related (9,10) by

$$f = (h - h_{-\infty})/(h_{\infty} - h_{-\infty}) \qquad [14]$$

provided that the Lewis number of the mixture is unity. However, since it is well known that the $\rho\gamma$ product of a gas mixture is much less influenced by composition or temperature than is either ρ or γ individually, and since we are here concerned with general effects rather than particular materials, it will suffice to take ϕ equal to unity throughout. Our solution is then

$$f = (1/2)[1 + \text{erf}\,(Y\sqrt{\rho_{\infty}U/\gamma_{\infty}D})] \qquad [15]$$

We shall also need, in the following discussion, the gradient of f. This is given by

$$\frac{df}{dY} = \frac{1}{\sqrt{\pi}}\sqrt{\frac{\rho_{\infty}U}{\gamma_{\infty}D}}\, e^{-\frac{\rho_{\infty}U}{\gamma_{\infty}D}Y^2} \qquad (16)$$

Flame Location and Burning Rate

We shall now suppose that one of the jets contains a mass fraction $m_{fu,\,\infty}$ of a fuel substance, and that the other contains a mass fraction $m_{ox,\,-\infty}$ of an oxidant substance; further it will be supposed that these two substances take part in a chemical reaction with a unique set of products, such that r lb_m of oxidant are consumed for every 1 lb_m of fuel.

It follows (9,10) that m_{fu}, m_{ox} and f are related by

$$f = \frac{(m_{fu} - m_{ox}/r) - (m_{fu} - m_{ox}/r)_{-\infty}}{(m_{fu} - m_{ox}/r)_{\infty} - (m_{fu} - m_{ox}/r)_{-\infty}} \qquad [17]$$

Since ordinarily $m_{ox,\,\infty}$ and $m_{fu,\,-\infty}$ are zero (i.e., equilibrium prevails in the entering streams), Eq. 17 reduces to

$$f = \frac{m_{fu} - m_{ox}/r + m_{ox,\,-\infty}/r}{m_{fu,\,\infty} + m_{ox,\,-\infty}/r} \qquad [18]$$

If, for the time being only, we make the assumption that chemical reaction rates are sufficiently fast for thermodynamic equilibrium to prevail at all points, we may insert in Eq. 18 the relations

$$m_{fu} > 0 \qquad m_{ox} = 0 \qquad [19]$$

$$m_{ox} > 0 \qquad m_{fu} = 0 \qquad [20]$$

We deduce

$$f \leqslant f_{stoich} \qquad f = -\frac{m_{ox}/r + m_{ox,\,-\infty}/r}{m_{fu,\,\infty} + m_{ox,\,-\infty}/r} \qquad [21]$$

$$f \geqslant f_{stoich} \qquad f = \frac{m_{fu} + m_{ox,\,-\infty}/r}{m_{fu,\,\infty} + m_{ox,\,-\infty}/r} \qquad [22]$$

where

$$f_{stoich} \equiv \frac{m_{ox,\,-\infty}/r}{m_{fu,\,\infty} + m_{ox,\,-\infty}/r} \qquad [23]$$

Flame location

Now the location of the reaction front in this case is that which gives both m_{ox} and $m_{fu} = 0$; i.e., it is that for which $f = f_{stoich}$. Although in practice equilibrium cannot prevail in the reaction zone, which therefore takes up a finite thickness, it is convenient still to regard $f = f_{stoich}$ as defining the flame location, Y_{stoich}. From Eqs. 15 and 23 there results

$$\frac{m_{ox,\,-\infty}/r}{m_{fu,\,\infty} + m_{ox,\,-\infty}/r} = \frac{1}{2}\,[1 + \text{erf}\,(Y_{stoich}\sqrt{\rho_{\infty}U/\gamma_{\infty}D})] \qquad [24]$$

This equation permits the flame location Y_{stoich} to be evaluated whenever the compositions of the jet streams are known.

Burning rate in the flame

By differentiating Eqs. 21 and 22 we obtain

$$f \leqslant f_{stoich} \qquad \frac{dm_{ox}}{dY} = -(rm_{fu,\,\infty} + m_{ox,\,-\infty})\frac{df}{dY} \qquad [25]$$

$$f \geqslant f_{stoich} \qquad \frac{dm_{fu}}{dY} = (m_{fu,\,\infty} + m_{ox,\,-\infty}/r)\frac{df}{dY} \qquad [26]$$

If the flame zone is thin, we can therefore deduce the rate of consumption of fuel per unit area of the flame, $\dot{m}''_{fu}$, from Eqs. 7, 16 and 26, to be

$$\dot{m}''_{fu} = (m_{fu,\,\infty} + m_{ox,\,-\infty}/r)\sqrt{\frac{\gamma_{\infty}\rho_{\infty}U}{\pi D}}\, e^{-\frac{\rho_{\infty}U}{\gamma_{\infty}}Y^2_{stoich}} \qquad [27]$$

A corresponding deduction for $\dot{m}''_{ox}$, based on Eqs. 25, 7 and 16, leads to a value r times as great as $\dot{m}''_{fu}$, as is to be expected.

Eq. 27 can conveniently be cast in a form involving dimensionless and physically understandable quantities. This is

$$\left\{\frac{\dot{m}''_{fu}}{m_{fu,\,\infty}\rho_{\infty}U}\right\}\sqrt{\frac{D\rho_{\infty}U}{\gamma_{\infty}}} = \frac{1}{\pi^{1/2}}\,\frac{e^{-\frac{\rho_{\infty}U}{\gamma_{\infty}D}Y^2_{stoich}}}{(1 - f_{stoich})} \equiv \Omega_{stoich} \qquad [28a]$$

say, where Ω is a function of f defined by Eq. 15 and by

$$\Omega \equiv \frac{e^{-\frac{\rho_{\infty}U}{\gamma_{\infty}D}Y^2}}{\pi^{1/2}(1 - f)} \qquad [28b]$$

The term in braces on the left-hand side of Eq. 28a is equal to the mass rate of fuel burned per unit area of diffusion flame divided by the mass rate of fuel flowing in unit area of the fuel-bearing jet. The term beneath the square root sign is a Peclet number for this jet.

Useful Functions

Fig. 1 contains curves of $Y\sqrt{\rho_{\infty}U/\gamma_{\infty}D}$, and of Ω vs. f, which have been derived from Eqs. 15 and 28b. It is seen that the former quantity increases from $-\infty$ to $+\infty$ as f_{stoich} increases from 0 to 1; it equals zero where $f = \frac{1}{2}$. The quantity Ω increases practically linearly with f at small values of this quantity; as f approaches unity however, Ω tends to infinity.

These curves will be helpful in the predictions of flame phenomena which are made herein.

Chemical Kinetic Theory

The Differential Equation

To know the position of the stoichiometric region and the mass burning rate is not enough: we need also to determine the temperature and composition distributions in the impingement zone and to establish whether a flame can exist stably there. These matters may be decided by solving the differential equation for the fuel concentration m_{fu}; this is

$$\rho v\frac{dm_{fu}}{dy} - \frac{d}{dy}\left(\gamma\frac{dm_{fu}}{dy}\right) = \dot{m}'''_{fu} \qquad [29]$$

Here we follow the notation of Spalding [10], in which $\dot{m}'''_{fu}$ is the mass rate of *generation* of fuel by chemical reaction per volume.

The boundary conditions appropriate to our problem are

$$\begin{aligned} y &= -\infty \qquad m_{fu} = 0 \\ y &= +\infty \qquad m_{fu} = m_{fu,\infty} \end{aligned} \qquad \ldots\ldots\ldots\ldots\ldots\ldots\ldots\ldots\ldots\ldots [30]$$

Transformation of the equation

It will be appropriate to use a transformation which is usually applicable to second-order equations like Eq. 29: a new independent variable is introduced which satisfies Eq. 29 when the right-hand side equals zero. Such a new variable is of course f. Replacing y by f, we obtain

$$\frac{d^2 m_{fu}}{df^2} = -\frac{\dot{m}'''_{fu}}{\gamma (df/dy)^2} \qquad [31]$$

which from Eq. 16 may be written

$$\frac{d^2 m_{fu}}{df^2} = -\frac{\dot{m}'''_{fu} e^{\frac{2\rho_\infty U}{\gamma_\infty D} Y^2}}{\phi \rho U/\pi D} \qquad [32]$$

wherein, of course, $(\rho_\infty U/\gamma_\infty D)Y^2$ is a function of f alone by reason of Eq. 15.[3]

The corresponding boundary conditions are

$$\begin{aligned} f &= 0 \qquad m_{fu} = 0 \\ f &= 1 \qquad m_{fu} = m_{fu,\infty} \end{aligned} \qquad \ldots\ldots\ldots\ldots\ldots\ldots\ldots\ldots\ldots\ldots [33]$$

The reaction rate expression

We assume that the volumetric reaction rate $\dot{m}'''_{fu}$ is a function only of the reactant specification, the pressure, the local temperature and the local mass fractions of fuel and oxidant; this is the case when the chemical reaction is single-step or when it proceeds by way of certain classes of chain reaction (8).

Now we have already seen how m_{ox} and h are related to m_{fu} and f in a given diffusion flame (Eqs. 14 and 18). It follows that the reaction rate can be expressed as a function of f and m_{fu} alone. It is convenient to incorporate the variations of $\dot{m}'''_{fu}$ and ρ into one function; thus

$$R(f, m_{fu}) \equiv -\dot{m}'''_{fu}\rho_\infty/\rho \qquad [34]$$

Substituting this and Eq. 28b in Eq. 32, there results

$$\frac{d^2 m_{fu}}{df^2} = \frac{DR}{\rho_\infty U(1-f)^2\Omega^2} \qquad [35]$$

The usual nature of the R function is indicated in Fig. 2 which shows lines of constant R on an $f - m_{fu}$ plane. It will be noted that these contours represent a mountain on a triangular base; its summit is at a point where f is approximately equal to f_{stoich}, and m_{fu} has much less than half its value in the fuel-bearing stream. These facts are consequences of the steep dependence of reaction rate on temperature, and of its less steep dependence on reactant concentration; they are easily verified in a particular case. It must be emphasized that the mapping of the "R-mountain" requires chemical kinetic knowledge (or assumptions) and cannot be derived from any of the considerations discussed in earlier sections of this paper.

The Mathematical Problem and Its Solution

If we define a nondimensional reaction rate function

$$\Psi \equiv R/R_{max} \qquad [36]$$

Eq. 35 can be written

$$\frac{d^2 m_{fu}}{df^2} = \Lambda \frac{\Psi}{(1-f)^2\Omega^2} \qquad [37]$$

where

$$\Lambda \equiv \frac{DR_{max}}{\rho_\infty U} \qquad [38]$$

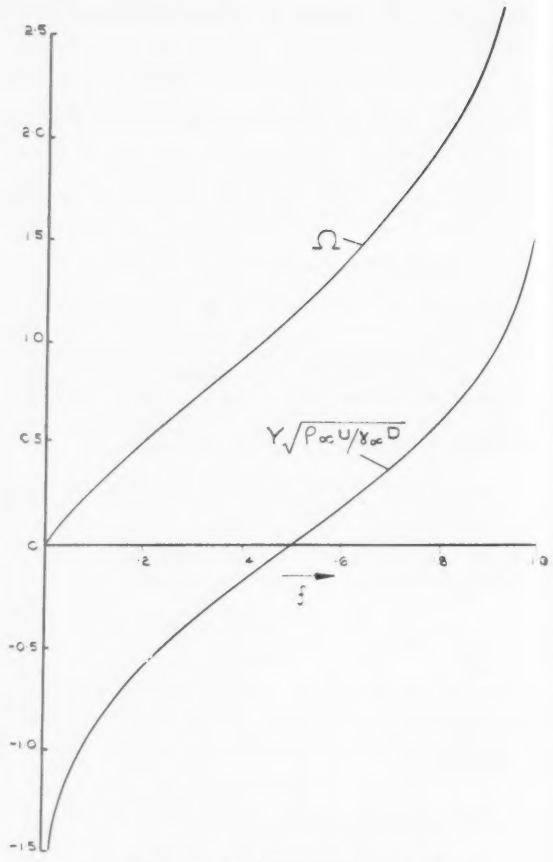

Fig. 1 Ω and $Y\sqrt{\rho_\infty U/\gamma_\infty D}$ plotted vs. f

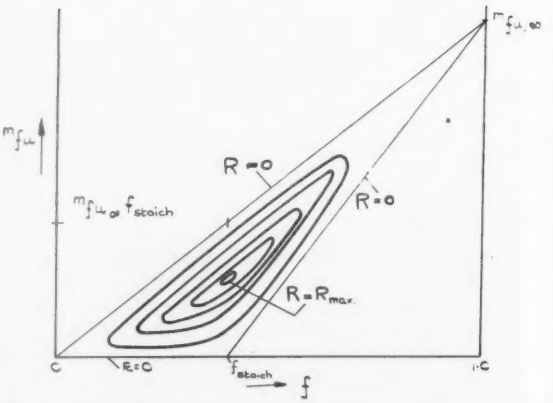

Fig. 2 The chemical kinetic function $R(m_{fu}, t)$ represented by means of a contour diagram

[3] We continue to take $\phi = 1$ here. There is no difficulty, but also no advantage for present purposes, in using any other $\phi(f)$ function.

and it will be remembered that Ψ is a function of f and m_{fu} whereas Ω is a function of f alone.

Eq. 37, together with the boundary conditions, Eq. 33, defines a family of curves on the $m_{fu} - f$ plane, with Λ as a parameter. The latter is a nondimensional quantity which measures the "reactivity" of the chemical substances in question as compared with the rate of convection; interestingly, it does not involve the transport property.

Fig. 3 is a sketch of a family of curves representing solutions to our problem, superimposed on the Ψ contours which correspond to the R contours of Fig. 2. These curves ordinarily would be deduced by numerical integration from one boundary, by iterative quadrature or by some other standard procedure of numerical analysis too prosaic to be discussed here. Each curve is valid for a different value of the quantity; the relation between Λ and the curve position may be perceived by examining the result of formal integration of Eq. 37 which is

$$\frac{1}{2}\left[\left(\frac{dm_{fu}}{df}\right)^2_{f=1} - \left(\frac{dm_{fu}}{df}\right)^2_{f=0}\right] = \Lambda \int_0^{m_{fu,\infty}} \frac{\Psi}{(1-f)^2\Omega^2}\, dm_{fu} \qquad [39]$$

Now the left-hand side is greater for the lower solutions of Fig. 3, i.e., those hugging the lower boundaries of the Ψ-mountain; it is smaller for the upper solution curves, and, indeed, is zero for the straight line forming the upper member of the family. The quadrature on the right-hand side of Eq. 39, by contrast, goes through a maximum as one proceeds from the lower curves to the higher: indeed, it equals zero for the very lowest curve of the family, and almost zero for the straight line; the intermediate curves, which run near the summit of the Ψ-mountain, must yield higher values of the quadrature.

These remarks suggest that, when Λ falls below a minimum value, the only possible solutions are those for which the $m_{fu}(f)$ curve is practically straight. These suggestions are borne out by integrations of the equations, provided that the activation energy of the reaction is high enough, as is commonly the case in practice. The minimum value of Λ is, of course, that corresponding to flame extinction; for, as Λ is lowered through this value, the peak temperature in the flame takes a sudden jump to a low value. This results from a concavity of the upper flank of the Ψ-mountain which is not easily shown in the sketch.

The behavior of the mathematical solution and its relation to the extinction phenomenon will not be described here in detail, firstly because these features are qualitatively similar to those pertaining to many other types of flame, and secondly because it is hoped to present numerical integrations in a later publication. Instead, attention will merely be directed to the following conclusions:

1 The extinction condition of the flame is found by numerical integration of Eq. 37 to determine the lowest value of Λ giving solution curves near the summit of the Ψ-mountain. This numerical value of Λ depends on activation energy, order of reaction, reactant concentrations at $\pm\infty$, etc.

2 Knowledge of Λ_{min} gives, from Eq. 38, the relation between the value of jet velocity at which extinction occurs U_{ext} and the value of R_{max}. Measurement of the former therefore leads directly to the latter.

3 The relation between U_{ext} and R_{max} just referred to does not involve transport properties. *We therefore have a system in which chemical properties can be deduced without any uncertainty being introduced by lack of transport data.*

The Zeldovich-Spalding Approximate Theory

Since Potter and co-workers have interpreted their results in terms of the theory developed independently by Zeldovich (11) and Spalding (6), it is as well to relate this to the foregoing discussion. The theory in question can be paraphrased as follows.

Determination of U_{ext} along the lines just indicated is rendered difficult on the one hand by the necessity to perform a time-consuming numerical computation and on the other by the fact that reaction rate data are scarce and uncertain.

Let us therefore imagine first that the Ψ-mountain is very steep (high activation energy) and has its summit near the point $m_{fu} = 0, f = f_{stoich}$. Then whenever Ψ is finite, $(1-f)^2\Omega^2$ has a value close to that for $f = f_{stoich}$. It follows that this quantity can be taken outside the integral of Eq. 39. Another consequence is that the two gradients appearing in the left-hand-side of Eq. 39 are respectively $m_{fu,\infty}/(1-f_{stoich})$ and 0. Eq. 39 therefore reduces to

$$\Lambda \approx m^2_{fu,\infty}\Omega^2_{stoich}/2\int_0^{m_{fu,\infty}} \Psi dm_{fu} \qquad [40]$$

It remains to evaluate the quadrature $\int_0^1 \Psi dm_{fu}$ for the path over the mountain corresponding to the lowest permissible value of Λ. Now, we do not know what this $m_{fu}(f)$ path is; however, a little thought about the shape of the Ψ-mountain, and about the positive curvature of the $m_{fu}(f)$ path, reveals that a good approximation will probably result from evaluating Ψ for $f = f_{stoich}$; i.e., a vertical section is taken through the hill, passing through the summit, and its cross-sectional area is measured. We may then write

$$\int_0^{m_{fu,\infty}} \Psi dm_{fu} \approx \bar{\Psi}_{stoich} m_{fu,\infty} \cdot f_{stoich} \qquad [41]$$

where $\bar{\Psi}_{stoich}$ is a number, smaller than unity, which is equal to the average height of the Ψ-mountain along the line $f = f_{stoich}$. Normally $\bar{\Psi}_{stoich}$ will have a value between $\frac{1}{3}$ and $\frac{1}{6}$.

First main result

Combination of Eqs. 38, 40 and 41 now yields an important result for the extinction condition. It is

$$\frac{\rho_\infty U_{ext}}{DR_{max}} \approx \frac{2\bar{\Psi}_{stoich} f_{stoich}}{\Omega^2_{stoich} m_{fu,\infty}} \qquad [42]$$

Second main result

Zeldovich (11) and Spalding (6) went beyond Eq. 42 because of the absence of data for R_{max} which could be inserted in the equation. They recalled that, according to the ap-

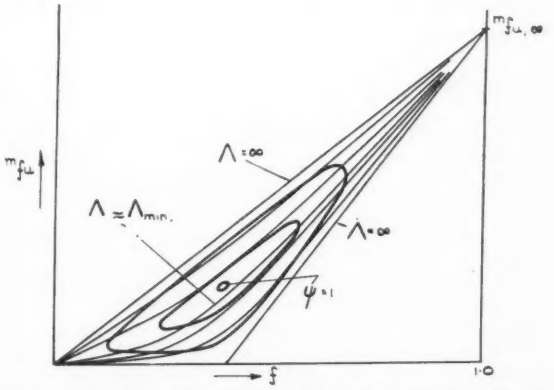

Fig. 3 Solution curves for various values of Λ superimposed on Ψ contours in the $m_{fu}(f)$ plane

proximate theory of laminar flame propagation developed by Zeldovich and Frank-Kamenetsky (12), it is possible to relate the reaction rate properties to the mass burning rate G in the stoichiometric mixture by a relation which, in the present notation, may be expressed as

$$m_{fu,\infty} f_{stoich} G \approx \sqrt{2 \int_0^{m_{fu,\infty} f_{stoich}} \gamma \dot{m}'''_{fu} dm_{fu}} \qquad [43]$$

thus

$$m_{fu,\infty} f_{stoich} G \approx \sqrt{2 \gamma_\infty m_{fu,\infty} f_{stoich} \bar{\Psi}_{stoich} R_{max}} \qquad [44]$$

This equation may now be used to eliminate the unknown $\bar{\Psi}_{stoich} R_{max}$ from Eq. 42 and replace it by G for which experimental data are often available. There results

$$\frac{\rho_\infty U_{ext} D}{\gamma_\infty} \Big/ \left(\frac{GD}{\gamma_\infty}\right)^2 \approx \frac{f_{stoich}^2}{\Omega_{stoich}^2} \qquad [45]$$

This is an important and useful relation which will be discussed.

Relation of burning rate in diffusion flame to burning rate in laminar premixed flame

Eq. 28 permits U and D to be eliminated from Eq. 45 and replaced by $\dot{m}''_{fu,ext}$, the burning rate of the fuel in the diffusion flame just before extinction; this is the quantity which was called the "flame strength" by Spalding (6). There results

$$\dot{m}''_{fu,ext} \approx m_{fu,\infty} f_{stoich} G \qquad [46]$$

This signifies that the flame strength is approximately equal to the burning rate of fuel per unit area of a laminar flame propagating through a stoichiometric mixture of the gases which comprise the oxidant- and fuel-bearing streams of the diffusion flame.

This result is a consequence of the approximations introduced by Zeldovich (11) and Spalding (6); it can easily be seen that, in the absence of these approximations, we would have

$$\frac{\dot{m}''_{fu,ext}}{m_{fu,\infty} f_{stoich} G} = \frac{\int_0^{m_{fu,\infty}} \{\Psi/(1-f)\Omega^2\} dm_{fu}}{\Psi_{stoich} m_{fu,\infty} f_{stoich}} \qquad [47]$$

where the right-hand-side is a number, of the order of unity, deduced from the path of the Λ_{min} curve over the Ψ-mountain.

Deductions From Theory and Comparison With Experiment

Flame Location

Fig. 1 permits the determination of the flame coordinate $Y_{stoich}\sqrt{\rho_\infty U/\gamma_\infty D}$ for any value of the stoichiometric mass fraction f_{stoich}. Thus for a propane-air jet pair, for which $f_{stoich} \approx 0.06$, $Y_{stoich}\sqrt{\rho_\infty U/\gamma_\infty D}$ is approximately equal to -1.0; for a hydrogen-air jet pair, $f_{stoich} = 0.0284$, and so $Y_{stoich}\sqrt{\rho_\infty U/\gamma_\infty D} = -1.3$.

The sign convention used implies that, since Y is negative in both cases, the flame lies well on the *oxidant* side of the stagnation point, particularly with the hydrogen jet.

This prediction has been confirmed qualitatively by Potter, Heimel and Butler (5); quantitative measurements of flame location relative to the stagnation point have not been made however.

Effect of D on "Apparent Flame Strength"

Eq. 38, with the subsequent discussion indicating that extinction occurs when Λ has a minimum value, implies that, for fixed jet composition, initial temperature and pressure

$$\rho_\infty U_{ext} \propto D \qquad [48]$$

The measurements of Potter et al., on the other hand, indicate that $\rho_\infty U$(called by these authors the "apparent flame strength") increases less rapidly with D than Eq. 48 predicts. This may have been due to the fact that the axial spacing of the jets was not altered simultaneously with the diameter; it almost certainly implies that the *real flow does not conform completely to the simple model postulated in the section, "Fluid Mechanical Theory of Opposed Jets."*

The latter conclusion is supported by the great influence of jet spacing on apparent flame strength reported by Potter and Butler (4), and by their eventual solution of this difficulty by the use of jets with pipe flow velocity profiles rather than uniform ones.

Absolute Magnitude of $\dot{m}''_{fu,max}$

By combining Eqs. 34 and 42, we obtain

$$\dot{m}'''_{fu,max} = \frac{\rho}{\rho_\infty} \frac{\rho_\infty U_{ext}}{D} \cdot \frac{m_{fu,\infty} \Omega_{st}^2}{2 \bar{\Psi}_{stoich} f_{stoich}} \qquad [49]$$

Taking Potter and Butler's measurement for a jet pair comprising propane and air at atmospheric conditions, for which the measurements were

$$\rho_\infty U_{ext} = 0.13 \text{ g/cm}^2 \text{ sec}$$
$$m_{fu,\infty} = 1$$
$$D = 0.46 \text{ cm}$$

and deduced quantities are

$$f_{stoich} = 0.06$$
$$\Omega_{st} = 0.175$$
$$\rho/\rho_\infty = 1/7$$

and assuming

$$\Psi_{stoich} = 0.25$$

substitution in Eq. 49 yields

$$\dot{m}'''_{fu,max} = 4.12 \times 10^{-2} \text{ g/cm}^3 \text{ sec} \qquad [50]$$

The corresponding volumetric heat release $\dot{q}'''_{max}$ is obtained by multiplying this quantity by 10^4 cal/g, which is a rough value for the heat of combustion of propane. There results

$$\dot{q}'''_{max} = 4.1 \times 10^2 \text{ cal/cm}^3 \text{ sec} \qquad [51]$$

This value should be compared with those deduced from other measurements, e.g., those of Longwell et al. (2). Such values are usually around 10^3 cal/cm^3 sec for the conditions in question (7). We may conclude that the Potter-Butler experiments, combined with the present theory, give results which agree as closely with those obtained by other methods as may be expected in the light of the discrepancies between the actual and the idealised flow patterns; in any case, the value of $\bar{\Psi}_{stoich}$ used in the foregoing will certainly have to be modified when exact numerical computations are available.

Influence of Transport Properties

Eq. 42 suggests that a change in the transport properties of the jet gases should not in itself influence the "apparent flame strength" $\rho_\infty U_{ext}$; for, γ_∞ is absent from the equation.

Potter and Butler have carried out experiments in which the fuel stream is propane and the oxidant stream consists of oxygen mixed either with argon or with helium. On the simplest

view, the change from argon to helium would not influence the temperatures achieved or the reaction rate function; it would, however, influence the transport properties. Potter and Butler found, in confirmation of the prediction in the previous paragraph, that the change from argon to helium brought only small changes in the apparent flame strength. Whereas this result appeared anomalous as represented by those authors, it is entirely in accordance with the present theory. Similarly, the onset of turbulence was not found by Potter and Butler to effect any change in the trend of the results.

It should be mentioned that secondary effects of the helium-argon substitution are to be expected. For example, we have assumed a unity Lewis number above; in fact, the Lewis number for the mixture with helium may be appreciably below unity, leading to reduced temperatures in the flame and so to a reduction in the value of $\rho_\infty U_{ext}$. A reduction of about 10% in apparent flame strength is indeed observed.

Effect of Pressure on Apparent Flame Strength

Eq. 38 and the subsequent discussion implied that, for fixed jet compositions and initial temperatures (which fix Λ) but varying pressure, the apparent flame strength is directly proportional to the volumetric reaction rate, i.e.

$$\rho_\infty U_{ext} \propto R_{max} \qquad [52]$$

Thus, if R_{max} is proportional to the nth power of pressure, $\rho_\infty U_{ext}$ will be proportional to the same power of pressure.

Potter (3) has reported that the apparent flame strength is proportional to pressure to the following powers: 1.2 for propane and a 50/50 O_2/N_2 mixture; 1.39 for propane and pure O_2; and 1.35 for propane and pure N_2O. We may deduce that R_{max} depends on pressure in a similar way.

The exponents just listed are rather low by comparison with that recommended for example by Longwell et al. (2), *viz.* 1.8. While there is still room for doubt as to what the exponent for R_{max} depends on, it appears likely that the low values of n reported by Potter are due in part to the existence of differences between the ideal and the actual flow patterns; they are almost certainly not due to approximations in the chemical kinetic theory.

Relation of Apparent Flame Strength to Laminar Flame Speed

Eq. 45, based on the Zeldovich-Spalding approximations, shows that, for a fixed jet diameter and provided that γ_∞ does not greatly vary, we may write

$$\rho_\infty U_{ext} \propto \frac{(m_{fu,\infty} f_{stoich} G)^2}{(m_{fu,\infty} \Omega_{stoich})^2} \qquad [53]$$

wherein, of course, $m_{fu,\infty} f_{stoich} G$ is the mass rate of burning of the fuel in a stoichiometric laminar flame.

Potter and Butler, knowing of the relation between the flame strength $\dot{m}''_{fu,ext}$ and the laminar flame speed derived by Zeldovich and Spalding (Eq. 46), plotted the *apparent* flame strength against $m_{fu,\infty} f_{stoich} G$. They found that these quantities were proportional to one another, and so deduced that the apparent flame strength was equal to $\dot{m}''_{fu}$ multiplied by a constant factor.

Eq. 53 contradicts this conclusion, for it implies a quadratic rather than linear relation between $\rho_\infty U_{ext}$ and $m_{fu,\infty} f_{stoich} G$. How is this contradiction to be explained? The solution may be found by noting that Potter and Butler varied $m_{fu,\infty} f_{stoich} G$ chiefly by varying the oxidant content of the oxidant-bearing stream. In this way they varied f_{stoich} and so Ω_{stoich}. Moreover the variation was such that Ω_{st} increased whenever G increased, so that the increase of G/Ω_{st} was less rapid than the increase of G.

This may be illustrated by Table 1, containing data abstracted from Potter and Butler's Fig. 3, together with deductions from these data.

Table 1

	Experiment 1	Experiment 2	Experiment 3
Fuel stream	propane	propane	propane
Oxidant stream	air	50/50 O_2/N_2	pure O_2
$\rho_\infty U_{ext}$, g/cm² sec	0.13	1.6	5.1
$m_{fu,\infty} f_{stoich} G$, g/cm² sec	2.8×10^{-3}	30×10^{-3}	100×10^{-3}
f_{stoich}	0.06	0.128	0.216
Ω_{st} (from Fig. 1)	0.175	0.335	0.53
$\rho_\infty U_{ext} (\Omega_{stoich}/f_{stoich} G)^2$	508	200	143

The quantity in the bottom row of this table would have the same value in each column if Eq. 53 were strictly obeyed. Evidently this quantity varied in value in the experiments reported; nevertheless, its variation is much less than that of $\rho_\infty U_{ext}$, for example. We may deduce that, when proper account is taken of the change in the stoichiometric mass fraction, the apparent flame strength depends more nearly on the second than on the first power of the fuel burning rate in a laminar flame.

Summarizing Remarks on the Comparison of Theory and Experiment

The foregoing discussion has shown that, both qualitatively and quantitatively, the predictions of the theory are roughly correct. However the closeness of correspondence is not yet sufficient to enable the opposed-jet diffusion flame to be used as a quantitative tool for the determination of chemical kinetic quantities.

It appears likely that the lack of correspondence, just referred to, may be eliminated by modifications to the apparatus, and to the theory. These possibilities are examined in the next section.

Possible Improvements to the Method

Experimental

Reynolds number

In a previous section it was noted that the flow field for which the differential equation is valid holds up to $y \approx 0.1\ D$. Now the diffusion flame may be situated at a distance from the central plane, given by $Y \sqrt{\rho_\infty U/\gamma_\infty D} = 1.5$. Taking Y as roughly $\frac{1}{2}y$, and putting these results together, we deduce that the theory can only be expected to hold if

$$\frac{\rho_\infty UD}{\gamma_\infty} > 1000 \qquad [54]$$

Indeed, a Peclet number (i.e., $\rho_\infty UD/\gamma_\infty$) of several thousand is desirable if the diffusion flame is to be well inside the region for which the flow can be predicted.

Now, most of the results reported by Potter and his coworkers were obtained with Peclet numbers appreciably below 1000. This fact is quite sufficient to explain the discrepancies between theory and experiment, for example in respect of the influences of D and pressure. It should be noted that the requirement expressed by Eq. 54 involves the use of bigger jet diameters, particularly at low pressure.

Flow pattern

In addition, if the theory is to be based on the flow pattern valid for impingement of an inviscid jet on a plate, special measures will probably have to be taken to ensure that the

flow is indeed of this character. In particular it must be ensured that no gas reaching the impingement zone has been contaminated by combustion products entrained by the jets.

Of course, other flow patterns may prove to be preferable. For example, the present author has used a pair of opposed porous disks, through one of which flows fuel, through the other oxygen, for the creation of a suitable flow pattern. If an annular gap is left at the disk edges, a very steady flat diffusion flame is formed between the disks.

Theoretical

Numerical computations

It has already been mentioned that a later report will be published containing exact solutions to Eq. 37, for various Ψ-functions. The use of these solutions will remove the Zeldovich-Spalding approximations as sources of uncertainty. However it should be recognized that many of the discrepancies noted above between theory and experiment, for example those regarding the pressure exponent, could not conceivably be reduced by improved computational methods. It is fair to say that an improvement in experimental technique is far more urgent.

Account for variable properties

Although the density and the exchange coefficient γ have been allowed to vary with temperature in the differential equations solved above, the fluid mechanical solution used (Eq. 1) was that for constant density flow. The error involved may be estimated as follows:

1 Along a plane normal to the jet axis at which the density is ρ instead of ρ_∞, the body forces which accelerate the bulk of the fluid at the rate U/D per unit length (Eq. 1) will accelerate the local fluid at the rate $(U/D)\sqrt{\rho_\infty/\rho}$ per unit length, provided that viscous forces are without effect.

2 In practice, viscous forces will prevent a thin layer of reduced density from being accelerated as fast as just indicated.

3 Therefore, and by reason of the known shape of temperature distributions in diffusion flames, an upper limit to the fluid dynamic effect of density differences may be obtained by multiplying U by $\sqrt{\rho_\infty/\rho_{\text{stoich}}}$ in all the formulas in the present paper; this factor will normally lie between 2 and 3.

4 Because of the action of viscous effects, and because the average velocity in the flame region will be less than the velocity of the hottest gas, the factor by which U should be multiplied to make the foregoing formulas conform with exact solutions will ordinarily be less than that mentioned in the foregoing paragraph 3; 1.5 is a more likely figure. However, this factor will depend on a number of conditions ($\rho_\infty/\rho_{\text{stoich}}$, f_{stoich}, etc.) and can only be determined for a particular case by solution of the variable-property equation of motion. Although interesting, and not particularly difficult, this problem nevertheless does not seem especially urgent.

Improvements to the chemical kinetic model

If the opposed-jet diffusion flame indeed becomes a widely used tool for chemical kinetic studies, it will soon be necessary to widen the area of theoretical inquiry. In particular, the extinction theory of diffusion flames proceeding by way of *chain reactions* will have to be studied. There is no essential difficulty about this: it merely means that Eq. 31 must be supplemented by other simultaneous equations, involving the concentrations of radicals, for example. Further simultaneous equations will also arise if non-unity Lewis numbers are considered.

In the author's view, investigation of such models will prove very much more rewarding than has been the case in the theory of laminar flame propagation; for the opposed-jet diffusion flame allows more independent variables to be altered than does the pre-mixed flame (e.g., fuel and oxidant temperatures can be varied independently). Intelligent exploitation of these possibilities should permit the diffusion flame to be used for the performance of *decisive* experiments; this has never been achieved by the use of the laminar flame.

Conclusions

1 A theory has been presented for the fluid mechanics, mixing and chemical kinetics in an opposed-jet diffusion flame. The Zeldovich-Spalding approximations were used in the final stages of this theory.

2 The experiments of Potter et al., agree only roughly with the predictions of the theory. The present case appears to be of the rare kind in which it is proper to recommend that the experiment should be altered rather than the theory. In particular, higher Reynolds numbers must be used if the full potentialities of the apparatus are to be exploited.

3 The most interesting direction for further theoretical work lies in the extension of the theory to chain reactions and more complex chemical kinetic models generally. No difficulties appear to lie in the way of this development.

Nomenclature

A = integration constant, ft^{-1}
D = jet diameter, ft
f = mass fraction of material derived from fuel-bearing stream which is present in the local mixture (−)
G = total mass flux vector, $\text{lb}_\text{m}/\text{ft}^2\text{h}$
G = mass flux normal to a laminar premixed flame propagating steadily through a stoichiometric mixture formed from the fuel-bearing and oxidant-bearing streams, $\text{lb}_\text{m}/\text{ft}^2\text{h}$.
h = specific enthalpy of mixture, $\text{Btu}/\text{lb}_\text{m}$
m_j = mass fraction of chemical compound j (−)
$\dot{m}_j''$ = mass burning rate of j per unit area of diffusion flame ($\text{lb}_\text{m}/\text{ft}^2\text{h}$), Eq. (27)
$\dot{m}_j'''$ = rate of creation, by chemical reaction, of chemical compound j per unit volume, $\text{lb}_\text{m}/\text{ft}^3\text{h}$
$\dot{q}'''$ = "volumetric heat release rate", $\text{Btu}/\text{ft}^3\text{h}$
r = mass of oxidant combining with unit mass of fuel in a simple chemical reaction (−)
R = modified volumetric consumption rate of fuel, $\text{lb}_\text{m}/\text{ft}^3\text{h}$
u = velocity of gas in x-direction, ft/h
U = velocity of jets far upstream of impingement region, ft/h
v = velocity of gas in y-direction, ft/h
x = distance from the axis of symmetry, ft
y = distance measured from plane of symmetry towards the fuel-bearing jet, ft
Y = distorted distance, ft
γ = exchange coefficient ($\equiv$ diffusion coefficient times mixture density; or thermal conductivity of mixture divided by specific heat at constant pressure), $\text{lb}_\text{m}/\text{ft h}$
Λ = dimensionless quantity measuring reactiveness of mixture relative to the convection rate (−)
ρ = density, $\text{lb}_\text{m}/\text{ft}^3$
ϕ = $\gamma\rho/\gamma_\infty\rho_\infty$ (−)
Ψ = dimensionless reaction rate (−)
Ψ = average reaction rate (−)
Ω = function of f indicative of burning rate in flame (−)

Subscripts

fu; ox = fuel; oxidant
$+\infty$; $-\infty$ = in fuel-bearing stream; oxidant-bearing stream
ext = at extinction
max; min = maximum; minimum
stoich = for stoichiometric mixture

References

1 Leclerc, A., "Déviation d'un Jet Liquide par une Plaque Normale à son Axe," *La Houille Blanche*, 1950, no. 6, pp. 3–8.

2 Longwell, J. P., Frost, E. E. and Weiss, M. A., "Flame Stability in Bluff-Body Recirculation," *Industr. Eng. Chem.*, vol. 45, 1953, p. 1629.

3 Potter, A. E., Jr., private communication, 1960.
4 Potter, A. E. and Butler, J. N., "A Novel Combustion Measurement Based on the Extinguishment of Diffusion Flames," ARS JOURNAL, vol. 29, 1959, pp. 54–56.
5 Potter, A. E., Jr., Heimel, S. and Butler, J. N., "Apparent Flame Strength: A Measure of Maximum Reaction Rate in Diffusion Flames," Eighth Symposium on Combustion, Pasadena, Calif., 1960.
6 Spalding, D. B., "A Theory of the Extinction of Diffusion Flames," *Fuel*, vol. 33, no. 3, 1954, pp. 255–273.
7 Spalding, D. B., *Some Fundamentals of Combustion*, Butterworth's, London, 1955, pp. 194–195.
8 Spalding, D. B., "One-Dimensional Laminar Flame Theory for Temperature-Explicit Reaction Rates," *Combustion and Flame*, vol. 1, no. 3, 1957, pp. 296–307.
9 Spalding, D. B., "Theory of Particle Combustion at High Pressure," ARS JOURNAL, vol. 29, 1959, pp. 828–835.
10 Spalding, D. B., "A Standard Formulation for the Steady Convective Mass Transfer Problem." *Int. J. of Heat and Mass Transfer*, vol. 1, 1960, pp. 192–207.
11 Zeldovich, Y. B., "On the Theory of Combustion of Initially Unmixed Gases," *J. Tech. Phys.*, Moscow, vol. 19, no. 1199, 1949; *NACA Tech. Transl.* 1296, 1951.
12 Zeldovich, Y. B. and Frank-Kamenetsky, D. A., *J. Phys. Chem.*, Moscow, vol. 12, 1938, p. 100.

Verification of Nozzle Admittance Theory by Direct Measurement of the Admittance Parameter[1]

LUIGI CROCCO,[2] RODOLFO MONTI[3] and JERRY GREY[4]

Princeton University
Princeton, N. J.

The nozzle boundary condition on a gas-filled chamber experiencing harmonic pressure oscillations can easily be expressed if the so-called admittance ratio of the nozzle is known. This quantity is defined as the ratio of velocity to density fluctuations expressed in complex representation. Direct experimental measurements of this parameter (sometimes referred to as the reciprocal of the impedance) have been made in order to check the theoretical predictions for choked nozzles (which are the most important for several applications). Fair agreement was found for the imaginary part of the admittance, which is not affected by temperature oscillations. Satisfactory agreement on the real part was obtained only after correcting for departures from the isentropic assumption.

NONSTEADY gas flow at the entrance to a choked nozzle was first studied by Tsien (1)[5] who calculated the response of a nozzle with linear axial velocity distribution to isothermal, harmonic, one-dimensional oscillations of very low or very high frequencies. Crocco (2) extended the solution to the general nonisothermal case and the entire frequency range, presenting his results in the form of the nozzle admittance parameter. According to Crocco's formulation, which appears in detail in (3), the admittance is a function of the nozzle subsonic axial velocity gradient, the frequency of the oscillations, the steady-state value of the Mach number at the nozzle entrance, and the length of the subsonic portion of the nozzle. Subsequently, results were also given for other velocity distributions (4), and for the more general case of transverse oscillations (5). In all cases the solutions are determined by the assumption that no singularity must arise at the sonic throat. Since doubts have been expressed about the validity of this fundamental assumption, the experimental verification of the theoretical solutions, even in the simplest one-dimensional case, has the important consequence of confirming the assumption, making valid the solutions obtained in the more complicated cases.

Previous measurements (6) have been successful in demonstrating that application of the theoretical nozzle admittance boundary condition to linearized one-dimensional equations for nonsteady flow in a constant section duct terminated by a nozzle provided satisfactory predictions of the duct behavior. These indirect measurements were not, however, of sufficient precision for a convincing demonstration of the validity of the nozzle admittance theory, since they depended on many other factors completely unrelated to the nozzle be-

Received Feb. 7, 1961.
[1] Sponsored by Project SQUID, Contract Nonr 1858(25) NR-098-038.
[2] Goddard Professor of Jet Propulsion.
[3] Assistant Professor, University of Naples; formerly, Assistant in Research, Department of Aeronautical Engineering.
[4] Associate Professor of Aeronautical Engineering.
[5] Numbers in parentheses indicate References at end of paper.

havior. The present paper describes a series of experiments in which the admittance parameter was determined directly by measuring the characteristics of the gas fluctuations at the entrance to a nozzle in an oscillating flow.

General Method

A hotwire anemometer and a diaphragm pressure transducer were installed in the entrance plane of a choked nozzle. Low Mach number air flow through a pipe feeding the nozzle was modulated by a siren to produce small longitudinal oscillations.

The forced oscillations were measured and found to be approximately sinusoidal in nature, and of less than 5% maximum amplitude. Fractional perturbations in pressure, density, temperature, and velocity may therefore be written

$$\frac{p'}{\bar{p}} \equiv \frac{p-\bar{p}}{\bar{p}} \equiv \varphi e^{i\omega t} \equiv \varphi_0 e^{i\omega t}$$

$$\frac{\rho'}{\bar{\rho}} \equiv \frac{\rho-\bar{\rho}}{\bar{\rho}} \equiv \sigma e^{i\omega t} \equiv \sigma_0 e^{i\omega t}$$

$$\frac{T'}{\bar{T}} \equiv \frac{T-\bar{T}}{\bar{T}} \equiv \theta e^{i\omega t} \equiv \theta_0 e^{i\omega}$$

$$\frac{V'}{\bar{V}} \equiv \frac{V-\bar{V}}{\bar{V}} \equiv \nu e^{i\omega t} \equiv \nu_0 e^{i(\omega t+\eta)} \qquad \ldots\ldots [1]$$

where steady state components are denoted by bars, and although φ, σ, θ, ν are generally complex, the time origin has been selected so that φ_0, σ_0, θ_0, and ν_0 are real. The admittance parameter α may therefore be defined (using the small perturbation isentropic relationship $\varphi = \gamma\sigma$, where γ = ratio of specific heats)

$$\alpha \equiv \frac{\nu}{\sigma} = \gamma\frac{\nu}{\varphi} = \gamma\frac{\nu_0}{\varphi_0}e^{i\eta}$$

$$= \gamma\frac{\nu_0}{\varphi_0}\cos\eta + i\gamma\frac{\nu_0}{\varphi_0}\sin\eta$$

$$\equiv \alpha_r + i\alpha_i \qquad \ldots\ldots [2]$$

Measurements of velocity and pressure perturbation amplitudes ν_0 and φ_0, and the phase angle η, are therefore necessary.

The oscillating pressure p is measured directly with a more or less conventional diaphragm-type transducer. In using a hotwire to measure velocity, however, some signal manipulation is necessary.

The rate of heat transfer to the stream from a hotwire of length L, diameter d, and temperature T_w may be written in the form (7)

$$q = I^2R_w = (T_w - T_0)L[k_1(pV)^{1/3} + K_2] + C(\pi d^2L)\frac{dT_w}{dt} \qquad [3]$$

where

T_0 = stagnation temperature (assumed equal to the recovery temperature, or temperature attained by an unheated wire in the stream)

$K_1 = 6.7\sqrt{d}$

$K_2 = 0.58\left[1 - \left(1.7 + 2\frac{T_w - T_0}{T_0}\right)M\right]$

M = Mach number ($M^2 \ll 1$)

q = ohmic heating in the wire

I = wire current (constant for the specific hotwire equipment used in these studies)

R_w = wire resistance

C = wire specific heat

L = wire length

For convenience in discussion,[6] we shall neglect K_2 (which is small compared to $K_1\sqrt{\bar{p}\bar{V}}$ for the pressures and velocities of interest here). Eq. 3 may then be perturbed under the usual assumptions associated with small perturbations, providing

$$\frac{(pV)'}{\bar{p}\bar{V}} = 2\left(\frac{f'}{\bar{f}} - \frac{T_w' - T_0'}{\bar{T}_w - \bar{T}_0}\right) \qquad [4]$$

where we have written

$$f \equiv \frac{I^2R_w}{LK_1} - \frac{C\pi d^2}{K_1}\frac{dT_w}{dt}$$

$$\bar{f} \equiv \frac{I^2\bar{R}_W}{LK_1}$$

$$f' \equiv \frac{I^2R_w'}{LK_1} - \frac{C\pi d^2}{K_1}\frac{dT_w'}{dt}$$

Considering a wire whose resistance is linearly dependent on the temperature

$$R_w = \bar{R}_0[1 + a(T_w - \bar{T}_0)] \qquad [5]$$

we obtain

$$\frac{T_W'}{\bar{T}_w - \bar{T}_0} = \frac{R_w'}{\bar{R}_w - \bar{R}_0} \qquad \frac{dT_w'}{dt} = \frac{1}{a}\frac{dR_w'}{dt}$$

where a = temperature coefficient of resistance.

Eq. 4 thus becomes

$$\frac{(pV)'}{\bar{p}\bar{V}} = 2\left[\frac{R_w'}{\bar{R}_w} - \frac{C\pi d^2L}{I^2\bar{R}_w a}\frac{dR_w'}{dt} - \frac{R_w'}{\bar{R}_w - \bar{R}_0}\right] + \frac{2T_0'}{\bar{T}_w - \bar{T}_0} \qquad [6]$$

The term in parentheses on the right-hand side of Eq. 6 depends only on the resistance perturbations R_w' of the hotwire, or, since the current I is maintained constant, on the voltage drop e

$$a_1R_w' + a_2\frac{dR_w'}{dt} = b_1e + b_2\frac{de}{dt}$$

Now, the amplifier is designed such that its output is proportional not to e but to the combination

$$e_1 = J_1e + J_2\frac{de}{dt}$$

with adjustable gains J_1 and J_2. If these are calibrated so as to match the coefficients b_1 and b_2, we may define

$$e_1 \equiv Be^{i\omega t} \equiv B_0e^{i\xi}e^{i\omega t} \qquad [7]$$

so that B_0 and ξ are the amplitude and phase (referred to φ_0) of the amplifier signal. Eq. 6 thus becomes, using Eqs. 7 and 1

$$\frac{pV'}{\bar{p}\bar{V}} = \dot{B}_0e^{i\xi}e^{i\omega t} + \frac{2\bar{T}\theta_0e^{i\omega t}}{\bar{T}_w - \bar{T}} \qquad [8]$$

where we have assumed that the flow Mach number is sufficiently small so that the difference between T_0 and T can be disregarded.

We may also use Eq. 1 to write

$$\frac{pV'}{\bar{p}\bar{V}} = \frac{p'}{\bar{p}} + \frac{V'}{\bar{V}} = (\varphi_0 + \nu_0e^{i\eta})e^{i\omega} \qquad [9]$$

[6] This assumption is not essential, and was not made in the complete study (8). It is valid, however, as shown by the experimental data of (8), and serves here to simplify the presentation considerably.

Using now the isentropic relation

$$\theta_0 = \frac{\gamma - 1}{\gamma} \varphi_0 \qquad [10]$$

and combining Eqs. 8 and 9, we obtain

$$1 + \frac{\nu_0}{\varphi_0} e^{i\eta} = \frac{B_0}{\varphi_0} e^{i\xi} + \frac{2(\gamma - 1)}{\gamma} \frac{\bar{T}}{\bar{T}_w - \bar{T}} \qquad [11]$$

Recalling the definition of the admittance ratio, we now write, using Eqs. 11 and 5

$$\alpha = \frac{\nu}{\sigma} = \frac{\nu_0 e^{i\eta}}{\sigma_0} = \frac{\gamma \nu_0 e^{i\eta}}{\varphi_0} = \gamma \left[\frac{B_0}{\varphi_0} e^{i\xi} + \frac{2\bar{T}}{\bar{T}_w - \bar{T}} \frac{(\gamma - 1)}{\gamma} - 1 \right]$$

or

$$\alpha_r = \gamma \left[\frac{B_0}{\varphi_0} \cos \xi + \frac{2(\gamma - 1)}{\gamma} \frac{a\bar{T}}{\left(\frac{\bar{R}_w}{\bar{R}} - 1 \right)} - 1 \right] \qquad [12a]$$

$$\alpha_i = \frac{B_0}{\varphi_0} \sin \xi \qquad [12b]$$

Resummarizing the notation

- B_0 = real amplitude of calibrated hotwire signal
- φ = real amplitude of pressure signal
- ξ = phase difference between hotwire and pressure signals (see definitions in Eqs. 7 and 1)
- a = wire coefficient of resistance at temperature $\bar{T}$
- $\bar{T}$ = steady state component of stream temperature
- $\bar{R}_w/\bar{R}$ = hotwire bridge sensitivity setting
- γ = ratio of specific heats

Experimental Technique

The equipment required for experimental measurement of the parameters in Eqs. 12 consisted of a long tube ½ in. in diameter on which was mounted the test nozzle; see Fig. 1 and (6 and 8). High pressure air flowed through the tube from a receiver tank. A U. S. Motors varidrive-powered siren mounted near the middle of the tube bled air at a nearly sinusoidal rate, measured under static conditions as described in (6), producing nearly sinusoidal pressure and velocity fluctuations at the nozzle entrance. The pressure transducer and hotwire elements were mounted at the entrance to the nozzle as shown in Fig. 1 for a set of three different linear velocity gradient nozzles and were mounted one inch upstream for an otherwise identical set of linear nozzles and a sharp edged orifice. The three nozzles were designed to provide data at two different entrance Mach numbers (0.1 and 0.2) and for two different convergent lengths (2 in. and 4 in.).

The pressure pickup was a strain-gage diaphragm type manufactured by Norwood. The final hotwire configuration consisted of three Flow Corporation W-2 probes[7] mounted in one transverse plane and connected in series to a Flow Corporation HWB constant-current compensating amplifier. Both signals were amplified and transmitted simultaneously to a multichannel FM Ampex tape recorder. Amplitudes were recorded during 20/1 reduced-speed filtered playback on a vacuum tube voltmeter, and phase between the signals was also observed simultaneously through continuously phase-corrected filters by means of a calibrated passive phase-shift network and an oscilloscope.

Steady state components of gas velocity, pressure, and temperature at the nozzle entrance plane were observed by a pitot probe and thermocouple, and were recorded on Leeds

[7] A number of different probe configurations were tested (8) in an effort to eliminate the "noise" due to turbulence, but none were fully successful. The three-probe configuration represents the best compromise, and provided reasonably good perturbation to turbulence ratios.

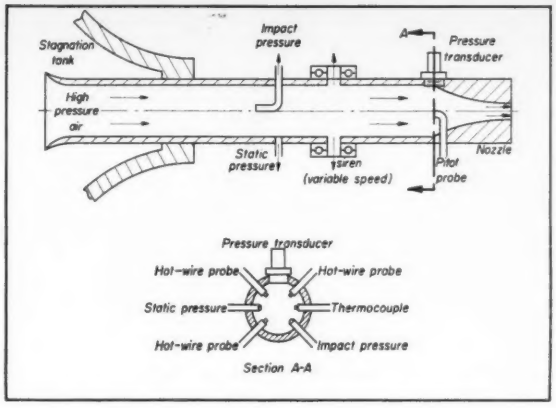

Fig. 1 Diagram of experimental equipment

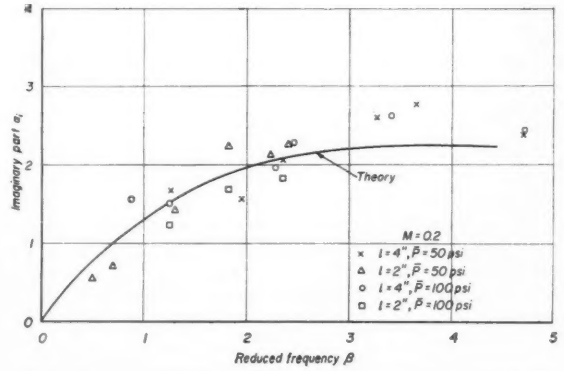

Fig. 2 Experimental-theoretical comparison of values for imaginary part α_i of linear nozzle admittance

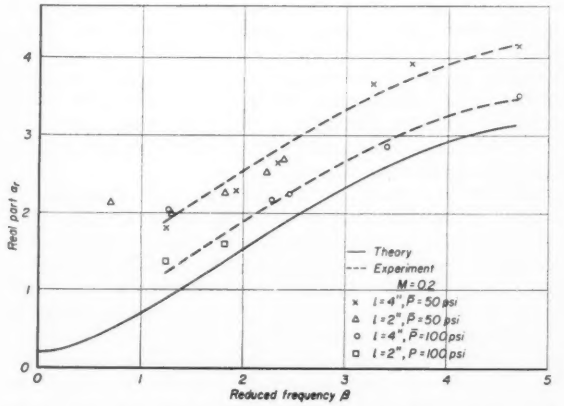

Fig. 3 Experimental-theoretical comparison of values for real part α_r of linear nozzle admittance assuming isentropic oscillations

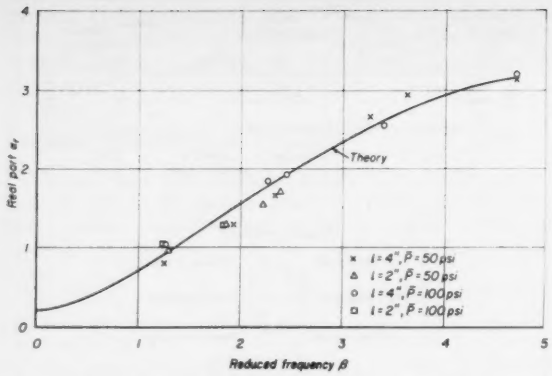

Fig. 4 Experimental-theoretical comparison of values for real part α_r of linear nozzle admittance—data are corrected for heat transfer by proper selection of polytropic exponent n

and Northrup strip-chart potentiometers. The modulating frequency, measured by a magnetic tachometer, was also observed on a recording potentiometer. Complete details of the apparatus, instrumentation, and measurement techniques appear in (8).

Results

Theoretical values of α_r and α_i, as calculated by the method of (3), are compared to the experimental values obtained from Eqs. 12 as shown in Figs. 2 and 3 for one of the test Mach numbers, both nozzle lengths, and both levels of chamber pressure tested. The other test Mach number gave similar results (8), omitted here for brevity. These figures are plotted against a reduced frequency defined by

$$\beta = \frac{\omega l_{sub}}{\bar{c}^* - \bar{V}_e}$$

where

ω = angular frequency of the induced oscillations
l_{sub} = length of the convergent (subsonic) section of the nozzle
$\bar{c}^*$ = sound velocity at the nozzle throat
$\bar{V}_e$ = gas velocity at the nozzle entrance

In discussing the results of these two figures, it is necessary to consider the physical nature of the admittance components α_r and α_i. The imaginary part α_i results from that part of the velocity which is out of phase with the pressure. Thus, since the temperature oscillations are also in phase with the pressure, neither pressure nor temperature oscillations (both of which can affect the hotwire signal) will affect the determination of α_i (see Eq. 12b). This independence results in reasonably good agreement[8] between the theoretical and experimental values for α_i.

On the other hand, the component α_r of the admittance is in phase with both pressure and temperature (see Eq. 12a), and is thus dependent in a major way on all three variables: pressure, temperature, and velocity fluctuations. Since we have three independent variables and only two measurements (hot wire and pressure pickup), an assumption is required. The assumption used in the analysis was that of isentropic oscillations (the temperature oscillation due to velocity changes is of second order for the low Mach numbers involved). The results of Fig. 3 indicate that, although the trend followed agrees qualitatively with that predicted by the theory, the vertical displacement of the experimental points requires some re-examination of the isentropic assumption.

The shifting of the α_r data is a function of pressure (as shown) and also of Mach number. Now, a lower Mach number means that the gas remains in the chamber longer and thus experiences a greater amount of heat exchange with the walls. This was experimentally verified (8). With regard to the pressure effect, the ratio of turbulent boundary layer heat transfer to stream heat capacity is decreased by increasing pressure (the heat capacity is proportional to the pressure, whereas the heat transfer varies as the pressure to the 0.8 power). Thus, at higher pressure levels, the isentropic assumption is more nearly valid. This trend is clear from Fig. 3.

In order to correct the data of Fig. 3 for the nonisentropic nature of the actual flow, we may assume a polytropic process; i.e., we replace the value of γ in Eqs. 12 by a polytropic exponent n, the value of which should be in the range $1 < n < \gamma$, tending to one (isothermal oscillations) as $M \to 0$ or $\bar{p} \to 0$. The proper value of n for each pressure level and Mach number condition was obtained by correcting the experimental data of Fig. 3; i.e., from Eq. 12a

$$n = \gamma\left[1 - \frac{\Delta}{2}\frac{\bar{R}_w - \bar{R}}{a\bar{T}}\right]$$

where Δ is the fractional difference between theoretical and experimental α_r and is constant for each set of $\bar{p}$ and $\bar{M}$.

Applying the above to the data of Fig. 3, we obtain the following results, which are in accord with the expected behavior as discussed above

$\bar{M}$	$\bar{p}$ psia	n
0.1	50	1.19
0.1	100	1.21
0.2	50	1.30
0.2	100	1.35

The corrected results for α_r are shown in Fig. 4, which now demonstrates agreement with theory to an even better degree of accuracy than α_i.

Results for the test condition in which the instrumentation was located one inch upstream of the linear nozzles, when analyzed by the methods presented here and in (6), provided almost identical results with those of Figs. 2, 3, and 4, as did results for the sharp edged orifice. These results, again, are omitted here for brevity, but appear in detail in (8).

Conclusions

1 Direct measurement of the imaginary part α_i of the complex nozzle admittance parameter α by means of a hotwire anemometer and a high response pressure transducer provided good confirmation of the theory in a set of linear-velocity-gradient nozzles.

2 In the case of the real part σ_r of the admittance, a consistent departure of the experimental measurements from the theoretical predictions was observed. This departure was traced to the inadequacy of the isentropic assumption used in the data reduction analysis for α_r (but not α_i). It was shown that the discrepancy can be eliminated by considering the process polytropic with an appropriate exponent somewhat smaller than γ.

3 Overall accuracies (indicated by the data-point scatter in all figures) were somewhat limited because of two basic experimental difficulties: (a) Distortion of the imposed harmonic oscillations at high forcing frequencies and pressure levels. (b) High hotwire turbulence "noise" relative to the small amplitude velocity oscillations.

4 Despite the limited accuracy of the experimental results, it seems possible to conclude that the basis for the theoretical calculation of the admittance ratio is fundament-

[8] Reasonably good in view of the signal to noise difficulties discussed in Footnote 7.

ally correct, and can be used for the treatment of more complicated cases.

References

1 Tsien, H. S., "The Transfer Functions of Rocket Nozzles," ARS JOURNAL, vol. 22, no. 3, May–June 1952, p. 139.

2 Crocco, L., "Supercritical Gaseous Discharge with High-Frequency Oscillations," *l'Aerotecnica*, vol. 33, 1953, p. 46.

3 Crocco, L. and Cheng, S. I., "Theory of Combustion Instability in Liquid Propellant Rocket Motors," AGARDograph no. 8, Butterworths Publications Ltd., London, England, 1958, Appendix C.

4 Crocco, L., Grey, J. and Harrje, D. T., "Theory of Liquid Propellant Rocket Combustion Instability and its Experimental Verification," ARS JOURNAL, vol. 30, no. 2, Feb. 1960, pp. 159–168.

5 Scala, S., "Transverse Wave and Entropy Wave Combustion Instability in Liquid Propellant Rockets," Princeton University Ph.D. Thesis, Aero Engineering Report no. 380, April 1, 1957.

6 Lambiris, S., "Experimental Verification of Nozzle Admittance Theory in a Simulated Rocket Chamber," Project SQUID Reprint PR-75, Sept. 1957.

7 "Selected Topics in Hot Wire Anemometer Theory," Bulletin no. 25, Flow Corporation, Arlington, Mass., 1958.

8 Crocco, L., Monti, R. and Grey, J., "Substantiation of Nozzle Admittance Theory by Direct Measurement of the Admittance Parameter," Project SQUID Report PR-102-R, Oct. 1958.

New Theory of the Aurora Polaris

S.-I. AKASOFU[1] and S. CHAPMAN[2]

Geophysical Institute College, Alaska

A new theory is given to explain why the aurora generally appears in the form of one or more long thin ribbons or bands of light, in the east-west direction, mainly in high latitudes; and why, after its initial quiet diffuse phase, it breaks up into rayed bands, folded and pleated, simultaneous with the appearance of strong electric currents along the auroral zone. During the magnetic storm, when Earth is enveloped in a stream of protons and electrons from the sun, part of the gas is trapped in Earth's vicinity. New electric currents and their magnetic fields develop around Earth during such a period, and they modify Earth's field in such a way as to produce neutral lines. We associate each auroral band with the presence of a particular *X* type of neutral line of the magnetic field in or near Earth's magnetic equatorial plane. For auroral bands in a customary latitude such as 66 deg the neutral line is about 6 Earth radii from Earth's center. The transition from the first to the second auroral phase is ascribed to the growth of an eastward electric field and current along the neutral lines.

THE AURORA polaris is an intermittent luminescence of the ionosphere, most often visible in geomagnetic[3] latitudes above 60 deg. Many hypotheses have been proposed to explain it. It is now generally believed, on good evidence, to be caused by gas ejected from time to time by the sun in the form of streams or clouds. Their dimensions may greatly exceed those of Earth. The gas is neutral but ionized; it consists mainly of protons and electrons. The speed is of order 1000 miles per sec and the time of travel is about one day. Auroras, magnetic storms and other phenomena occur when Earth becomes immersed in such a solar cloud or stream. The flow of gas may envelope the Earth for hours or days (1).[4]

Within a distance of order 10 Earth radii from Earth's center[5] the motions of the solar particles are much influenced by the geomagnetic field. Those whose line of approach is more distant from Earth proceed almost undisturbed. Many of the particles that approach most directly are turned backwards, or deflected away to one or other side, at a distance of several Earth radii. Thus a hollow is formed in the stream. Some of the particles, however, become "trapped" in the field. Some particles travel to high latitudes and there enter Earth's atmosphere. If they penetrate to sufficiently low levels they produce auroral light, and also in certain conditions electric ionospheric currents that may strongly disturb the geomagnetic field.

The US and USSR satellites and cosmic rockets have revealed the presence, nature and some of the changes of the inner and outer "radiation belts" that encircle Earth (2, 3).

Presented at the ARS 15th Annual Meeting, Washington, D.C., Dec. 5–8, 1960.

[1] Research Scientist, Physic Dept.

[2] Advisory Scientific Director. Also at High Altitude Observatory, Boulder, Colo., there engaged in research program jointly sponsored by National Bureau of Standards and Air Force Geophysical Directorate; and at Institute of Science and Technology, University of Michigan, Ann Arbor, Mich.

[3] The abbreviation *gm* will here often be used to denote *geomagnetic*. In this paper latitude, Equator, axis, equatorial plane will in general signify *gm* latitude, *gm* Equator, *gm* axis, *gm* equatorial plane—all referring to the field of Earth idealized as that of a point magnetic dipole (whose axis is inclined at 11½ deg to the geographical axis).

[4] Numbers in parentheses indicate References at end of paper.

[5] Distances from Earth's center will here generally be given in terms of the Earth's radius (a = 6370 km).

These belts, inner and outer, will here be referred to as V1 and V2 respectively. Both belts tend to decay, and are continually or intermittently renewed. For the V2 belt, the one of chief interest for the aurora, the rates of decay and renewal are decidedly variable. The energetic particles in the V2 belt, or at least the energetic protons, seem likely to come from the sun. Great changes in V2 have been observed during magnetic storms, when solar gas is flowing toward and past Earth.

The energetic particles of the belts circle around the lines of magnetic force. They also travel to and fro nearly along these lines, but with a sideways drift round Earth. The electrons drift eastward, the protons westward. These motions constitute an electric current encircling the Earth. This is commonly known as the (electric) ring current. Near Earth's surface it reduces the horizontal field component *H*.

In the early period of a magnetic storm *H* typically increases. This is ascribed to the relative motions of the solar particles near the surface of the hollow formed in the gas by the geomagnetic field. These relative motions constitute a distribution of electric current over the surface. The magnetic field of these currents may be denoted by *DCF* (*D* for disturbance, *CF* for corpuscular flux). The currents and the *DCF* field are strongest on the sunward side of Earth. They remain in being, doubtless with fluctuations, so long as the flow of solar gas toward Earth continues. The population and extent of the V2 belt vary during and after this onflow. We think that a third belt V3, outside the V2 belt, may be set up at such times (4). The energy of its particles may be below the limit of measurement with the instruments hitherto carried on the cosmic rockets. However this may be, the magnetic records taken at the Earth's surface show that the ring current is temporarily enhanced during magnetic storms. The additional field thus observed and produced may be denoted by *DR* (*D* for disturbance, *R* for ring current). After a few hours, at most, its growth overwhelms the *DCF* field at Earth's surface, so that during most of a magnetic storm the horizontal field *H* there is reduced. The *DR* field dies away in the course of days, after the maximum phase of the storm.

Thus when Earth lies in the path of a solar stream or cloud, conditions in the space within about 10 Earth radii around Earth are modified by the additional presence of solar particles, partly trapped and partly approaching and then passing away from Earth. Their motions influence the magnetic field in this large region—mainly by the addition of the *DCF* and *DR* field. Electric currents are also generated in the Earth's polar atmosphere, by the particles that produce auroras. Their magnetic field does not extend far outward in the space around Earth. It may be denoted by *DP* (*D* for disturbance and *P* for polar, because the currents appear to be generated in the polar regions).

Auroral Particles and Morphology

To understand the aurora polaris we need to know the nature, energy, flux and source of the solar particles that enter our atmosphere, and the details of how they produce the auroral light and the associated phenomena in the ionosphere. We need further to know why the solar particles enter the atmosphere in particular regions as observed, and why the inflow goes through cycles of change during auroral displays and magnetic storms. This last branch of auroral science may be called auroral morphology.

The Norwegian scientist Størmer, who made a lifelong study of the aurora, summarized his work and also in part the state of knowledge concerning it at the time (5). Chamberlain (17) is soon to publish a larger, more comprehensive treatise on the aurora and airglow. At a recent discussion on space science he remarked that only one attempt had been made to explain the morphology of the aurora. This attempt was made by Størmer, over a period of years of study of the motions of single-charged particles in the geomagnetic field. For the most part this field was treated, as is reasonable, as a dipole field. Many of his results seem encouraging and suggestive, but they cannot be regarded as explaining auroral morphology. One essential reason for this is that the auroral light and the associated magnetic disturbance require a flux of gas composed of charged particles in numbers far too great to permit their mutual electrostatic influence to be neglected.

Furthermore, recent rocket and spectroscopic observations suggest that most of the auroral light is produced by electrons whose energy is of order 30 to 100 kev (6). According to Størmer's theory, such electrons could enter Earth's atmosphere only within 4 deg from the geomagnetic poles.

We propose a new morphological theory of the aurora, which is different from Størmer's in several vital features. We do not claim to explain the full sequence of auroral causation by the solar streams and clouds. There remain gaps in our understanding of these events, and our theory involves one important ad hoc hypothesis, not yet independently established. In this respect the hypothesis parallels the inference—widely held over several decades, yet still not clearly proved or understood—that auroras and magnetic storms are caused by streams or clouds of solar gas.

Neutral Lines in the Magnetic Field

One of the most remarkable and distinctive features of the aurora is its typical form, an arc or "ribbon" of light (7). The ribbon at times extends for thousands of miles in a direction approximately normal to that of geomagnetic north, but its extent in height is measured in tens or at most hundreds of miles. Its thickness in the north-south direction is still less. The ribbon may be diffuse and quiet (8), or it may be marked by ray structure and folds, and be rapidly variable (9). The quiet diffuse form is about two or three miles thick; the rayed form is thinner, sometimes less than 500 yards thick.

An auroral arc may appear singly, or two or more may be visible at the same time. The transition from the quiet diffuse form to the actively changing rayed forms marks a definite stage in the course of an auroral display.

Two important phenomena of auroral morphology which pose problems are the ribbon appearance and the location of auroras, and the transition from the quiet to the active stage.

The auroral rays lie along the local lines of magnetic force. The quiet diffuse arc also conforms to the direction of these lines. The auroral particles clearly follow the magnetic lines as they enter our atmosphere. Suppose we were to travel outwards along a line of force, starting from a diffuse or rayed auroral arc. The line of force will curve downwards, approximately in a *gm* meridian plane, to the plane of the *gm* Equator. If it starts in a typical auroral latitude, e.g., 66 deg N, it will cross the Equator at a distance of $6\frac{1}{4}$ Earth radii (about 25,000 miles) from the Earth's center; thence it will proceed onward and reach the antarctic atmosphere at 66 deg *gm south* latitude. Such a line of force lies well beyond the main part of the normal V2 radiation belt, which extends to about 15,000 miles. But during strong magnetic disturbance this belt may extend outwards to or beyond this distance.

Consider next the course of *two* such lines of force associated with an auroral arc (66 deg *gm* latitude). Suppose one lies in the southerly "face" of the auroral arc or ribbon, and the other, in the same meridian, on the northerly face. The lines of force diverge, until the distance between them reaches a maximum in the plane of the magnetic Equator; then they converge to the same distance as at first, when they enter the antarctic atmosphere. For each mile or yard of thickness of the auroral ribbon, the distance between the lines at the equa-

torial plane is 29 miles or yards respectively. If the particles that produce the auroral ribbon travel along the lines of force, they must come from this very small "slice" of the V2 belt. But the total thickness of the belt is many thousands of miles. What can cause so striking a limitation of the source region of these auroral particles?

To this question we answer: the determining feature is the magnetic field. More particularly, we attribute the limitation to the presence of a certain type of *neutral line* in this field. A neutral *point* of a field of force is one at which the intensity vanishes; at such a point the field can have no direction. But neutral points are of two kinds, which we may call *O* points and *X* points (Fig. 1). By definition, an *O* neutral point is one at which the magnetic potential has a local maximum or minimum. At an *X* neutral point the potential declines outwards in some directions and increases in others. Lines of force can pass through an *X* point, where they will make a sharp change of direction. No line of force can pass through an *O* neutral point.

A neutral line is one of which every point is a neutral one. It may consist wholly of *O* neutral points: in that case it is called an *O* neutral line. Similarly it may be an *X* neutral line, consisting wholly of *X* neutral points. Or a neutral line may be partly *O* and partly *X*.

An *O* neutral line is *encircled* by lines of magnetic force, which shrink to zero radius as the line is approached. At any point *P* of an *X* neutral line, two lines of magnetic force approach it from opposite directions, and two other lines of force leave it in opposite directions. The tangents to these lines, at *P*, all lie in the plane through *P* normal to the neutral line. In free space, devoid of electric current, the angles between the tangents to the approaching lines of force and the receding lines of force are 90 deg; but if there is volume flow of electric current in the region of the *X* line, these angles may have other values.

A dipole field has no neutral lines (and consequently no such lines were involved in Størmer's attempts to explain auroral morphology). If neutral lines appear near Earth during periods of auroral and magnetic disturbance, they must be caused by the additional electric currents and magnetic fields then present. These flow partly near the surface of the hollow carved by the geomagnetic field in the flowing solar gas, partly in the whole volume of the radiation belts, and partly in the ionosphere. In addition the solar gas may carry within it a magnetic field (*DSM*)[6] transported away from the sun. The corresponding contributions to the magnetic field are those already denoted by *DCF*, *DR* and *DP*, together with *DSM* if present. The appearance of a neutral line or of neutral lines in the magnetic field near Earth we ascribe mainly to the *DR* field due to the ring current of the radiation belts. The *DCF* field makes a smaller contribution to the total field, but one to which we attribute considerable significance. The *DP* field, on the contrary, is likely to be too weak, at the distances of a few Earth radii where the neutral line(s) appear, to have any serious effect on their occurrence or form.

At times when no solar gas is flowing toward and past Earth, the radiation belts and the associated ring current distribution seem likely to be symmetrical about the geomagnetic axis. The *DR* field will in general have a direction different from that of the normal geomagnetic field—which for brevity we may call the *M* (main) field. Only in the equatorial plane, which is also the plane of the ring current, are the two fields parallel, namely normal to the plane. In this plane, outside the ring, the *DR* field has the same direction as the *M* field, because the ring current flow is westward. There the *DR* field strengthens the *M* field. Within the circular center line of the ring, it weakens the *M* field. Only there is it possible for the *DR* field to annul the *M* field and produce a neutral line of the combined field. For this to happen, the ring current electric flow must be sufficiently intense and suitably distributed over its cross section. The determining factors are the population and distribution of the energetic particles of the radiation belts.

A decrease of the total field intensity *F* below its normal main field value has been recorded by several cosmic rocket magnetometers, as follows: *R′* is the distance beyond which the field intensity was found to be reduced; *R* is the indicated radius of the ring current; both are expressed in Earth radii (see the table).

[6] *D* stands for disturbance, *SM* for solar magnetism.

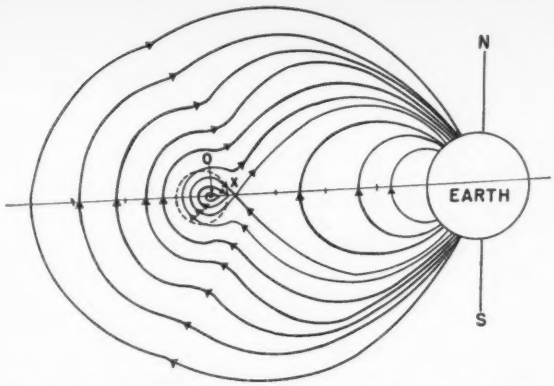

Fig. 1 Lines of force in geomagnetic meridian plane of Earth, when magnetic field is disturbed by a ring current. The circular cross section of this current is shown by broken line. Points *O* and *X* are the points where the resulting *O* and *X* neutral lines cross plane of diagram. Line *NS* is Earth's magnetic axis

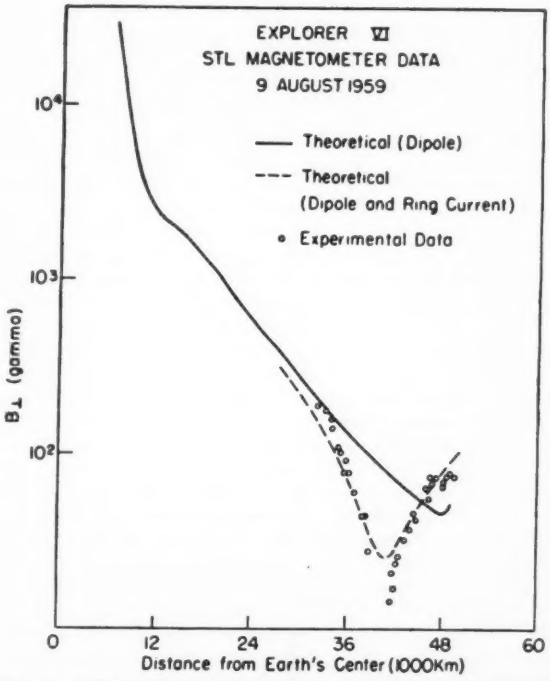

Fig. 2 Small circles indicate measurements made by US Satellite Explorer VI of magnetic field component perpendicular to its spin axis. At about 6 Earth radii they fall much below normal intensity of geomagnetic field (full line). Broken line indicates possible field reduced by presence of a ring current (courtesy of C. P. Sonett et al.)

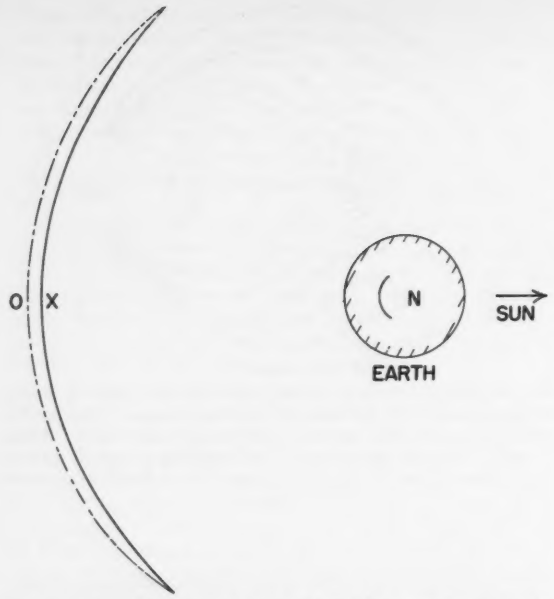

Fig. 3 Typical loop formed by an *O*- and *X*-type neutral line in geomagnetic equatorial plane, during magnetic storm. Radiation belt protons and electrons travel from vicinity of *X* neutral line and produce an auroral arc as shown on plan of Earth

Explorer VI recorded a deep minimum of *F* at about 6.4*a* (Fig. 2). All three US rockets indicated a region of severe fluctuations of *F* between 12 and 15*a* (10).

None of these observations has disclosed the presence of neutral points or lines. For several reasons this was not to be expected. Such presence is likely only during auroral displays, and in the magnetic equatorial plane, mainly on the side of Earth away from the sun. The rocket orbits did not lie in this plane, and the rockets were on the sunward side of Earth when they recorded the decrease of *F*. There a decrease was to be expected, but not a decrease to zero. It will not be easy to verify by rocket measurements that at times *F* sinks to zero along certain lines. To do so, the rocket orbit, if not in the magnetic equatorial plane, must intersect it at a point on the neutral line at just the time when this lines passes through that point. It should be possible, however, to detect exceptionally low values of *F* at points not too far from the neutral line or lines. Perhaps the best chance of neutral line detection would be given by a long-lived satellite with very elongated orbit, in or close to the plane of the geomagnetic Equator. The orbit should extend outwards to at least about 7*a*.

During a magnetic storm, the expected normal symmetry of the radiation belts and the ring current relative to the geomagnetic axis may be modified by the *DCF* field which is largest near the surface of the hollow in the day side. This asymmetry may distort the form of the ring current. It may cause the center to depart slightly from the *gm* axis, and may even slightly shift the plane from that of the *gm* Equator. The latter seems most likely to happen, if at all, when the sun's direction departs furthest from this plane. This will be at or near the solstice, at hours when the *gm* axis is tilted furthest from the sun's direction.

On the basis of present rocket observations of the radiation belt we cannot certainly predict that the observed growth of the *DR* field of the ring current will produce neutral lines. But there seems no inherent improbability in their appearance.

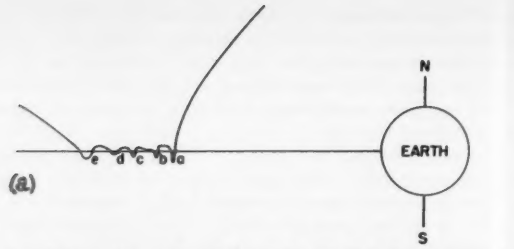

Fig. 4a Schematic graph of intensity of disturbed magnetic field along an equatorial radius from Earth, in midnight meridian plane, during magnetic storm. Marked points a, b, c, d and e are *X*-type neutral points; each is associated with an *O*-type neutral point on same equatorial radius

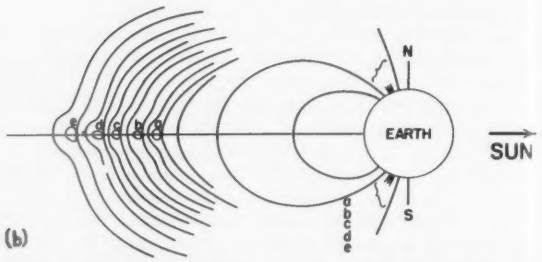

Fig. 4b Schematic diagram of magnetic field lines in midnight meridian plane of Fig. 4a. Protons and electrons travel along the lines from *X*-type neutral lines a, b, c, d and e and produce parallel auroral arcs in Earth's ionosphere, as indicated in diagram

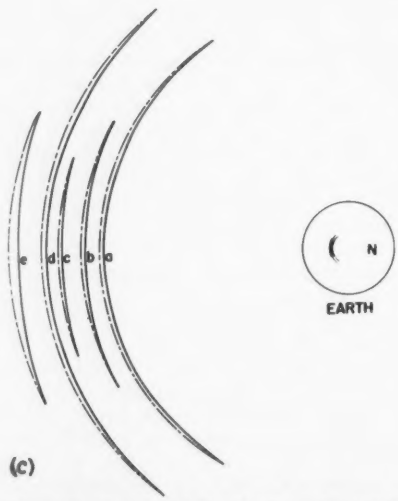

Fig. 4c Schematic diagram of the five loops formed by *X*-type neutral lines a, b, c, d and e of Figs. 4a and b, and by associated *O*-type neutral lines (broken lines). All these lines lie in or close to Earth's magnetic equatorial plane. Auroral arcs associated with the *X*-type neutral lines are indicated on Earth

Rocket	Launched	*R*	*R'*
USSR Mechta	1959 Jan. 2	2	3 or 4
US Pioneer I	1958 Oct. 11	5	9 or 10
US Explorer VI	1959 Aug. 7	5	9 or 10
US Pioneer V	1960 March 11	5	7 or 8

If they are present also at times when there is no solar stream, they are likely to be complete circles, surrounding the earth. If present only during the solar onflow, the neutral line may generally not completely encircle Earth. This is because of the *DCF* field in the equatorial plane, most intense on the sunward side. Thus storm conditions favor the presence of a neutral line on the dark side. Depending on the strengths of the *DCF* and *DR* fields, the neutral line may be confined to a small arc on the dark side, or extend over any larger angle up to complete encirclement of the Earth.

Fig. 3 shows a typical neutral line of limited angle, produced by a suitably intense toroidal ring current, symmetrical about the *gm* axis, in the presence of a *DCF* field of a certain intensity. The neutral line consists of a loop; the inner part, nearest Earth, is an *X* line, the remainder is an O line. Fig. 1 shows schematically the form of the lines of force of the combined field in the meridian plane that bisects this *OX* loop. Between the *O* and *X* lines the field direction is southward instead of northward (see Fig. 3).

The radiation belt is not toroidal, and the observed irregular distribution of its field beyond $10a$ implies an irregular distribution of the ring current. At such times it is natural to expect that in the region where the field intensity is low there may be more than one reversal of the field. Thus the *H* distribution along a radius in the equatorial plane, and the form of the field lines in the meridian plane, might instead be as in Figs. 4a and 4b. This shows five pairs instead of only one pair of neutral points (intersections with the neutral lines). Alternative simple typical forms of the whole set of neutral lines in (or near) the equatorial plane are shown in Fig. 4c. The pattern may at times be decidedly more complicated. The irregularities of the field may also distort some of the neutral lines slightly away from the equatorial plane. The pattern of these lines in or near this plane may be likened to the contour of the water surface on a lake, at its mean level, when the surface is slightly disturbed by winds or other influences. The rises or depressions of the surface, in this analogy, represent the northward and southward direction and intensity of the magnetic field in the equatorial plane. The pattern in the case of the neutral lines has a structure determined by the near symmetry of the electric current system around the *gm* axis. In the lake analogy, surface changes due to the throwing in of a stone would produce a circular pattern round the point of entry; wind might cause a less regular pattern.

Significance of the Neutral Lines for Auroral Morphology

The energetic particles of the radiation belts, as mentioned (1), circle around the local direction of the field intensity *F*. They also oscillate back and forth between northern and southern "mirror points." This oscillatory motion is along the *F* lines except for an additional sideways drift around Earth. The circular part of the motion causes the particles to modify the magnetic field as if they were small dipoles directed opposite to *F*. The equivalent dipole moment (μ) of a particle is proportional to Av, where A denotes the area of the circle it describes, and v the speed of motion round the circle. As the component motion along the field takes the particle into stronger or weaker parts of the field, A is respectively decreased or increased; the circle shrinks or expands. At the same time there is a compensating opposite change of the speed v, so that Av and the dipole moment μ remain invariant. But the total speed of the particle also remains constant. Hence the component speed along the field must decrease as the particle moves into a stronger part of the field. This retardation finally reduces this component speed to zero. The point where this happens is called a mirror point, because there the particle, still with the same dipole moment, turns back to return into regions of less intense field. This

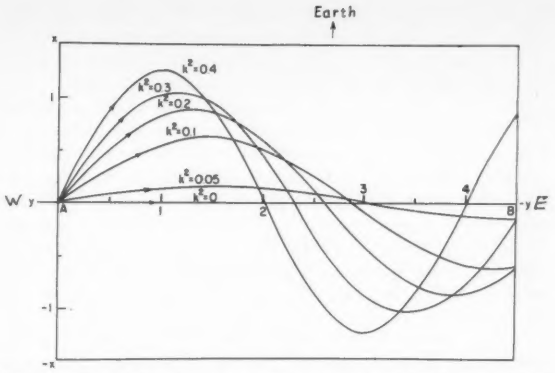

Fig. 5 Paths of protons near *X*-type neutral line in equatorial plane for various values of their inclination to neutral line at intersection. *AB* is part of neutral line; curvature of this line is too small to be shown here. Paths of electrons are similar but opposite in direction, with much smaller wave amplitude

description of the motion is valid anywhere in Earth's undisturbed magnetic field for protons of their energy less than 5 Mev and all the electrons observed so far, at about $6a$.

The tiny magnets are very little affected by hydromagnetic waves (fluctuations in the field) for any amplitudes and frequencies to be expected there. They are liable to change, however, if they come close to any neutral line that may develop in the field during the magnetic storm. There the invariance of the dipole moment ceases to hold. Indeed very close to a neutral point, where the field is zero, there is no question of circular motion and dipole moment. A particle with a certain magnetic moment that approaches a neutral line closely will have a different moment after it leaves the vicinity of the line. Hydromagnetic waves can play an important role during the passage of a particle through the neighborhood of the neutral line.

The change in the character of the motion will first be illustrated in a specially simple case, that of a particle initially moving in the *gm* equatorial field near a neutral line. Within a narrow strip of the plane, bordering the neutral line on each side, the motion is no longer trochoidal, with curvature always in the same sense. Instead the motion is as shown in Fig. 5 (11). If the particle is displaced slightly from the plane, it will continue to move away from it. But now the component speed along *F* is accelerated instead of retarded.

Consider the alternative fates of a particle which at a given time t is at a point *P* in the equatorial plane, and moving with given velocity v in the plane. Imagine alternative states of the magnetic field near *P*. In state 1 the field there is normal, for example, the undisturbed dipole field. In state 2, additional *DR* and *DFC* fields produce a neutral line close to *P*. If the particle is given a slight impulse and velocity normal to the equatorial plane, in state 1 this velocity will decrease as the particle moves away from the plane. The particle will soon reach a mirror point, and will thereafter oscillate between it and a corresponding point on the opposite side of the plane. In state 2, on the contrary, the motion away from the plane is accelerated, and the particle travels further along the line of force before reaching a mirror point.

Next suppose that the particle, instead of initially moving in the equatorial plane, reaches this plane with a significant fraction of its velocity along the normal to the plane. Such a particle, in state 1 of the field, will have come from a mirror point well away from the plane. Let h_1 denote the height of the mirror point above Earth. In state 2 of the field, however, if the particle at *P* has the same velocity v, inclined to the plane, it will be accelerated away from the plane, with decreasing dipole moment. It will reach a mirror point at a smaller height h_2 above Earth. This level might be deep in

the atmosphere, or even below the Earth's surface (h_2 negative). If so, when the air resistance becomes greater than the electromagnetic force on the moving particle, the motion will cease to conform to the equations valid for free space.

Thus the presence of the neutral line can enable a particle to contribute to auroral production, which in the undisturbed field would never approach auroral levels in the atmosphere.

This influence of the neutral line is confined to those particles that come close to it; the limiting distance for 30 kev electrons is about one-tenth of that for 130 kev protons. These energies are typical for the two kinds of particle as yet observed in the V2 belt. During a magnetic storm the *DCF* and, especially, the *DR* field may gradually change, so that the *X* neutral lines approach or recede from Earth. A particle that leaves the equatorial plane, moving northwards or southwards, from a "normal" point of the field may on its return find itself in the critical strip around a neutral line. Then it may travel into the auroral ionosphere, north or south, and be lost to the belt. A changing neutral line or lines may thus sweep up much of a certain region of the belt, with the flow to the auroral ionosphere at each moment confined to the thin space bounded by the magnetic field lines through the edges of the critical strip associated with the line or lines. If there is more than one *X* neutral line, as illustrated in Fig. 4, there will be a series of auroral ribbons, or arcs, as is often seen during displays.

Thus we interpret an auroral arc or arcs as indicating the presence, in the equatorial plane, of a neutral line or lines, linked with the auroral arc or arcs by field lines. The positions of the neutral line or lines in the equatorial plane can be inferred within narrow limits from the latitudes of the auroral arc or arcs, without taking into account the deviation of the lines of force of the disturbed magnetic field from those of the undisturbed dipole field.

The Auroral Breakup

A typical auroral display during a period of active *gm* disturbance has an initial quiet period followed by an active phase. In the former, the aurora is diffuse, and the arcs move slowly toward or away from the poles. Suddenly the display changes. Rays appear, the "ribbon" becomes thinner, and it becomes less regular and more mobile. Changing folds appear, forming "draperies" or "curtains." Superposed on these folds there is a finer corrugation or pleating of the "ribbon." The number of arcs, curtains or bands visible in the sky may increase. Evanescent rays may dart downwards, or ripples may flow eastward or westward along the bands. Viewed from a point on the ground, from which a line of force passed upwards *within* a great auroral fold, the rays in the curtain will be seen to converge toward the direction of that line of force. This convergence of rays may extend over a wide arc round this direction. Such a form is called a *corona*. It may cover a large part of the observer's sky, and be bordered by the edges and lower parts of more or less parallel auroral bands to north and south of the "observer's" fold.

At such times the bands are often tipped with red along their lower border, which extends deeper into the atmosphere than during the quiet phase.

We interpret this active phase of the aurora as indicating a change of conditions in and near the part of the equatorial plane where there are neutral lines. The particles still enter the auroral region from narrow strips or regions in this plane, bordering a neutral line or lines. But these strips are now narrower than before, and the neutral lines are wavy, corresponding to the folds in the auroral ribbons or bands. Like these folds, the waves in the neutral lines are quickly changing. New neutral lines may appear and disappear in a wide band of the plane, like new depressions on the surface of a lake dappled by breezes. The question naturally arises: what is the physical cause of this notable change of state in the equatorial band where the field intensity is low?

The explanation we offer is that weak electric currents flow eastward along the neutral line or lines during this phase. One consequence is to modify the field lines in the immediate vicinity of the neutral line or lines. Fig. 6a shows the form of the field lines near a neutral line, in the absence of such a current. Fig. 6b shows field lines of the additional field due to the current, and Fig. 6c shows the lines of the new compound field (12). The lines of force through the neutral line itself are no longer perpendicular. They become less inclined to the normal to the equatorial plane. Calculation shows that this narrows the strip centered on the neutral line, within which the circular motion of the particles can be partly converted into motion along the field, permitting the particles to penetrate the auroral ionosphere. Thus the auroral ribbons become notably thinner. They are reduced from two or three miles in thickness to only a few hundred yards.

The electric current implies the presence of an electric field along the neutral line. This accelerates the particles (especially the electrons) in the region near the line, increasing their energy. Consequently, when the accelerated particles leave the region to travel earthwards, their penetration into the auroral ionosphere is increased, as observed. The flux of electrons is enhanced, that of the protons is diminished. Slight changes in the distribution of other less energetic charged particles in the neighborhood keep net space charge densities to a low level.

The form of the magnetic field near the neutral line tends to confine the electric current toward this line. Constricted electric currents in a gas are known to be unstable; hence the wavy, changing structure of the current. This carries the neutral line with it in its fluctuations, thus explaining the folds in the auroral ribbon. However, these processes deserve further detailed study, for the conditions that obtain in the V2 or V3 belt during magnetic storms.

The finer corrugation or pleating of the auroral ribbon is explained as an instability of the thin curved sheets formed by the charged particles as they move from the vicinity of the neutral lines, along the magnetic field lines, into the auroral ionosphere. Instability of this kind in such sheets, due to the electrostatic forces between the particles, has been discussed by Webster (13) and demonstrated by his experiments.

Thus we explain the main features of the morphology of the aurora during its active phase by the hypothesis of an electric field along the neutral line or lines. At present this is a hypothesis ad hoc. It is somewhat on a par with the hypothesis, accepted over several decades, that magnetic storms and auroras are due to corpuscular streams and clouds from the sun.

As in the latter case, we cannot yet adequately explain how the electric field originates. But the one simple hypothesis accounts for several observed phenomena. These are not confined to the auroral features so far mentioned.

The difference between the flux densities of electrons and protons during the unstable phase produces a slight relative displacement of the two sets of charges in their overlapping curved regions of flow from the equatorial plane to the ionosphere. This produces an electric field in the ionosphere, usually directed equatorward. Because of the presence of the *gm* field, the electrical conductivity in the ionosphere at the auroral level is anisotropic (14). Hence this electric field associated with the influx of particles drives electric current *along* the auroral zone, usually westward. Strong magnetic disturbances (the *DP* field), which indicate the presence of such auroral electric currents, are a usual accompaniment of the active phase of auroral displays.

These *DP* fields and intense active auroras appear sporadically, and often suddenly, during magnetic storms. Their duration is only a fraction of that of the storm. More than one may appear in the course of a storm, at irregular intervals. We attribute both phenomena to the onset of an electric field along the neutral line or lines, due perhaps to the

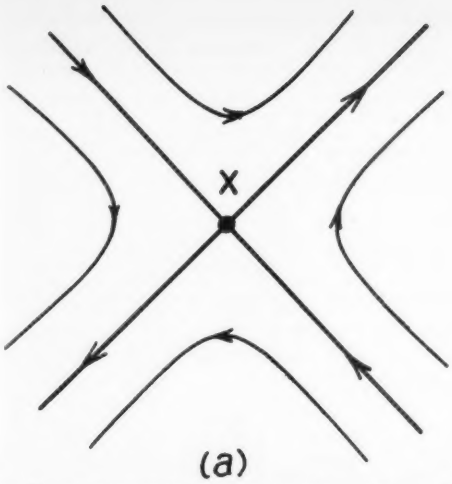

Fig. 6a **Lines of magnetic force (in empty space) near X-type neutral line in the disturbed field present during magnetic storm. Point X is on night side of Earth; Earth and sun are outside diagram, far to right. Reader's line of sight to diagram corresponds to westward direction round Earth**

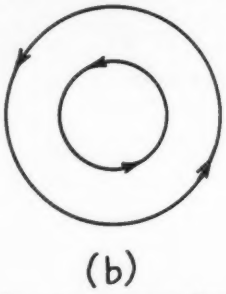

Fig. 6b **Lines of force due to current flowing eastwards (upwards from plane of diagram) along neutral line**

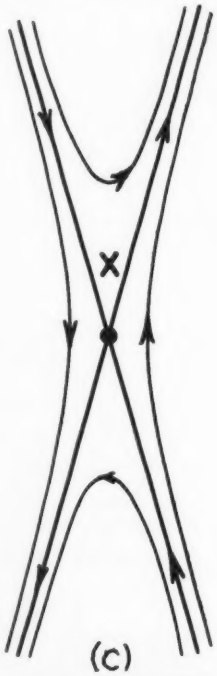

Fig. 6c **Lines of force, near neutral line, of combined field corresponding to main disturbed field (Fig. 6a) and the field (Fig. 6b) of eastward current along neutral line**

gensudden ulfing of a mass of solar gas in the V2 or V3 belt. This trapped mass, like the charged particles generated by the Argus nuclear explosions, will tend to spread all round the Earth, but during the spread, temporary electric fields in the belt region may be involved. The necessary electric field along the neutral line or lines is very small, of order 1 v per km.

During the development of a great magnetic storm and its associated auroral display, the ring current and its magnetic field *DR* increase to a maximum and then decline. As the *DR* field grows in intensity, the neutral line, mainly on the dark side of Earth, moves closer toward Earth. Correspondingly the northern and southern auroral arcs associated with it move toward lower latitudes.

The Final Auroral Phase

The final phase of a great auroral display is often fantastic. Isolated rays and pulsating patches of light appear and disappear over a large part of the sky, and there is no longer any arc structure. The field in the region of low intensity in or near the equatorial plane has lost its regularity of structure, owing to the instability of the electric currents along the neutral line or lines. To use the former metaphor, the dappling of the lake surface is entirely irregular, as might be caused by blustery eddying winds. Finally the influx of new solar gas trapped by the field becomes well distributed around the Earth. The electric field that is present while the gas is spreading from the trapping region dies away. The magnetic field settles down to regularity once more, with perhaps one neutral line present, with no electric field along it. The auroral cycle may begin anew, with a quiet diffuse arc. This may fade away if the *DR* field decays; or a new active display may later develop.

Concluding Remarks

Our theory is open to test in more than one way. It is desirable to try to check the presence and location of neutral lines in the field round Earth, by satellite measurements. Rocket magnetometers that can measure direction may be able to identify such regions of reversed field; they are, however, likely to be small, and the field is likely to be very weak there. Another check relates to the simultaneity and similarity of auroral appearance in the arctic and antarctic, at the ends of the same lines of force of the magnetic field. This check is possible only during the period when both regions are simultaneously in darkness. It requires observation, preferably by all-sky cameras, at northern stations linked by lines of force with one or more of the few available antarctic stations where all-sky photography is carried on.

If confirmed, our theory indicates that the occurrence of auroras is a fruitful source of information as to the magnetic and electric conditions in space near the *gm* equatorial plane, at distances of many Earth radii from Earth's center.

Appendix

This appendix gives tentative values of many quantities associated with our theory of auroral morphology. Some of these quantities are observed, many are inferred.

Solar streams and clouds

	Protons	Electrons
velocity	up to 2×10^8 cm/sec	up to 2×10^8 cm/sec
energy	up to 20 Kev[a]	$1 \backsimeq 2$ ev[b]
number density[c]	100/cm³	100/cm³
flux	up to 2×10^{10}/cm² sec	up to 2×10^{10}/cm² sec

DCF field

	Location of the stream front[d]			
	4a	5a	6a	∞
intensity[e]				
at the front of the stream	500 γ	260 γ	150 γ	0
at Earth's surface				
dayside	93 γ	44 γ	24 γ	0
nightside	44 γ	24 γ	15 γ	0

DR field

Intensity at Earth's surface: up to 400 γ. (The induction effect is subtracted.)

Intensity of the *DR* field at Earth's surface for the production of a neutral line at 6 Earth radii must be about 20 γ.

Trapped particles: illustrative data at 6 Earth radii

	Protons	Electrons
energy	500 kev	30 kev
speed	10^9 cm/sec	10^{10} cm/sec
maximum E-W[f] drift speed	W 250 km/sec	E 16 km/sec
oscillation time[f,g]	23 sec	2 sec
time of revolution round the Earth[f]	24 min	6 hr
Oscillations per revolution[f]	63	10,100

Radiation belts and particles (16)

	Protons	Electrons
	Observed	
	V1, inner belt, at 1.5*a*	
energy	40 mev	20 kev
flux	2×10^4/cm² sec	2×10^8/cm² sec
	V2 belt, at 3.5*a*	
energy	60 mev	20 kev
flux	10^2/cm² sec	10^{11}/cm² sec
	Inferred	
	V3 belt, ring current belt, beyond 6*a*, in outer part of V2	
energy	500 kev	20 kev
flux	(?)	10^9/cm² sec

Auroral zone

	Location	Corresponding location in the equatorial plane connected by lines of force
center of the auroral zone[h]	66°30′ *gm* lat	6.3*a*
low latitude aurora[i]	down to about 55°30′	3.1*a*

Auroral particles in the auroral zone

	Protons	Electrons
diffuse form		
energy	150 kev	30 kev
flux[j]	5×10^5/cm² sec	10^7/cm² sec
active form		
energy	150 Kev	30 kev ∽ 250 kev
flux[j]	5×10^3/cm² sec	10^{11}/cm² sec
lines and bands produced	Hα	5577 (OI), 3914 (N_2^+), etc.

Auroral particles in the equatorial plane; at 6 Earth radii

	Protons (100 kev)	Electrons (30 kev)
radius of gyration	180 km	1.7 km
period of gyration	0.26 sec	1.5×10^{-4} sec

Auroral curtains

length, at least 2000 km

thickness

	Proton layer (*Hα* layer)	Electron layer
diffuse form	30 km (700 km)[k]	3 km (70 km)
active form	30 km (?) (often invisible)	250 m (6 km)

rregularities

	Characteristic length	Cause
large scale irregularity (folded structure)	10 ∽ 500 km	instability of the neutral line
small scale irregularity (ray structure)	1 ∽ 4 km	instability of the thin electron beam-sheet

lifetime

diffuse form	1 ∽ 5 days (intense display)
active form	1 ∽ 2 hrs (intermittent)

Auroral ionosphere: Auroral electrojet

auroral electrojet

	Westward jet	Eastward jet
sense of the emf	Equatorward	poleward
emf	up to 60 v/km	20 v/km
current intensity	up to 3×10^6 amp	$<10^6$ amp
magnetic disturbing force at ground level	up to 1500 γ	< 500 γ

electron density in the aurora

diffuse aurora	up to 5×10^5/cm³
active form	up to 7×10^7/cm³

conductivity of the ionosphere

up to 1.2×10^{13} esu

emf along the neutral line

10^{-5} v/cm at about 6 Earth radii.

---

[a] On the basis of geomagnetic evidence, we think that the stream may at times contain protons of energy 500 kev or more confined by transported magnetic fields, perhaps tangled.

[b] Arnold et al. (15) observed a flux 10^7/cm² sec of 50 kev electrons in a solar stream.

[c] Possibly this may attain 1000/cm³.

[d] The distance from Earth's center; unit: a = 6380 km.

[e] Calculated using the image dipole approximation.

[f] The ratio of velocity along to that perpendicular to the lines of force in the equatorial plane is assumed to be about 30.

[g] Time for one complete oscillation between the two mirror points.

[h] The auroral zone is located between 65 and 70 deg *gm* latitude. More than 5 auroral curtains are often seen simultaneously in the belt.

[i] The curtain structure of auroras often appears there during great magnetic storms.

[j] Flux in the aurora: to obtain the corresponding flux at 6 Earth radii in the equatorial plane multiply the given number by 2.5×10^{-2}.

[k] The material in parentheses shows the corresponding thickness in the equatorial plane.

References

1 Chapman, S. and Bartels, J., *Geomagnetism* vol. I, p. 412; vol. II, p. 804, Oxford Univ. Press, Oxford, Eng.,1940.

2 Van Allen, J. A. and Frank, L. A., "Radiation Around the Earth to a Radial Distance of 107,400 km, "*Nature*, vol. 183, Feb., pp. 430–433.

3 Vernov, S. N., Chudakov, A. E., Vakulov, P. V. and Logachev, Yu. I., "The Study of the Terrestrial Corpuscular Radiation and Cosmic Rays

During the Flight of a Cosmic Rocket," *Soviet Physics, Doklady* (translation), vol. 4, Oct. 1959, pp. 338–342.
4 Akasofu, S. and Chapman, S., "The Ring Current, Geomagnetic Distance, and the Van Allen Radiation Belt", *J. Geophys. Res.*, vol. 66, May 1961".
5 Størmer, C., *The Polar Aurora*, Oxford Univ. Press, Oxford, Eng., 1955.
6 Bates, D. R., "The Auroral Spectrum and its Interpretation," *Physics of the Upper Atmosphere*, ed. by J. A. Ratcliffe, Academic Press, N. Y., 1960.
7 Størmer, C., *The Polar Aurora*, Oxford Univ. Press, 1955 (see Figs. 174 and 184).
8 *ibid.*, see Fig. 1.
9 *ibid.*, see Fig. 83.
10 Smith, E. J., Coleman, P. J., Judge, D. L. and Sonnett, C. P., "Characteristics of the Extraterrestrial Current System: Explorer VI and Pioneer V," *J. Geophys. Res.*, vol. 65, June 1960, pp. 1858–1861.
11 Parker, E. N., "Newtonian Development of the Dynamical Properties of Ionized Gases of Low Density," *Phys. Rev.*, vol. 107, 1957, pp. 924–933; *also see* Åström, E., "Electron Orbits in Hyperbolic Magnetic Fields," *Tellus*, vol. 8, Aug. 1956, pp. 206–267.
12 Dungey, J. W., "Conditions for the Occurrence of Electrical Discharges in Astrophysical Systems," *Phil. Mag.*, vol. 44, July 1953, pp. 725–738.
13 Webster, H. F., "Structure in Magnetically Confined Electron Beams," *J. Appl. Phys.*, vol. 28, Dec. 1957, pp. 1388–1397.
14 Baker, W. G. and Martyn, D. F., "Electric Currents in the Ionosphere," *Phil. Trans. Roy. Soc. A*, vol. 246, 1953, pp. 283–294.
15 Arnold, R. L., Hoffman, R. A. and Winckler, J. R., "Solar Cosmic Rays and Soft Radiation Observed at 5,000,000 km from Earth," *J. Geophys. Res.*, vol. 65, Sept. 1960, pp. 3004–3007.
16 Van Allen, J. A., "The Geomagnetically Trapped Corpuscular Radiation," *J. Geophys. Res.*, vol. 64, Nov. 1959, pp. 1683–1689.
17 Chamberlain, J. W., *Physics of the Aurora and Airglow*, Academic Press., N. Y., 1961.

Heat Sink Strand Bomb for Determining Ballistic Properties of Solid Propellants

E. K. IVES,[1] J. DOMINIK[2] and W. A. PROELL[3]

Amoco Chemicals Corp. Whiting, Ind.

A method is presented that allows quick and economical determination of certain ballistic parameters of solid propellants. Various data are presented comparing the results from the new heat sink method, regular Crawford bomb and motor firings. These results indicate that the new method is accurate and reproducible.

THE CRAWFORD bomb (1)[4] is a well-standardized device for measuring burning rates of propellants at various pressures. It is widely used as a means of controlling manufacturer products and as a research tool. The apparatus is most convenient for the measurement of burning rate at ambient temperatures and over a range of pressures. For advanced research and production control, the measurement of temperature coefficient of burning rate at constant pressure and at constant K_n is needed. The Crawford bomb has proved less versatile for these measurements, since accurate equilibration of the test strand with the bomb immersed in a bath of the required temperature is slow and inconvenient. As a result, relatively little research data have been gathered in this field.

Through research[5] a new apparatus has been developed and used for the measurement of temperature coefficient at constant pressure. This apparatus uses a conventional Crawford bomb as developed by Crawford and his co-workers (1) from the early apparatus of Muraour (2). Our apparatus includes a massive internal heat sink to maintain strand temperature without chilling or heating the entire apparatus. This heat sink bomb has proved accurate and reliable, and it has reduced the cost and time needed to obtain data on temperature coefficient, burning rate and pressure exponent over wide temperature ranges.

Received July 13, 1960.
[1] Assistant Project Chemist, Propellant Div.
[2] Test Foreman, Propellant Div.
[3] Director, Propellant Research, Propellant Div. Member ARS.
[4] Numbers in parentheses indicate References at end of paper.
[5] Funded by the Amoco Chemicals Corp., Whiting, Ind.

Existent Apparatus

The universally used type of Crawford strand bomb evaluates the linear burning rate of small propellant strands and involves the determination of time intervals between the burning out of wires embedded at predetermined locations in the strand. Burning rates are obtained at different pressures, which are kept constant by connecting the bomb with a nitrogen regulatory system. The closed bomb is similar (3), except that the pressure above a certain minimum amount is determined by the rate of gas evolution from the burning of the propellant itself.

The temperatures of this type of bomb may be controlled by having heating and/or cooling coils in the bomb itself (4,6) or by having the entire burning apparatus immersed in a temperature bath. A variation of this method is the immersion of the strand itself in a liquid which acts as a restrictor as well as a temperature control (5). These methods are time-consuming with regard to changing temperature and costly with respect to the apparatus necessary for this change; they involve various other inconveniences as well.

Another method to determine temperature dependent ballistic properties utilizes rocket motor firings, in which equal grains are burned at various temperatures. It is often difficult to choose the correct nozzle to give a desired pressure level, and rocket tests are expensive.

Development of the Heat Sink Bomb

It was conceived that a portable heat sink composed of a large piece of metal in which a strand could be conditioned and burned might keep a constant temperature without tempera-

ture equilibration of the bomb itself. If this heat sink were large enough, the strand and sink could be conditioned in standard heating and cooling units, charged to the bomb, and the propellant could be burned without the strand suffering a significant change in temperature from the conditioning temperature. The exterior electrical and pressure apparatus of a single Crawford bomb could be used while several heat sinks containing strands were being conditioned.

The apparatus developed is illustrated in Figs. 1 and 2. Modification of the standard bomb was confined to the internal strand carrier and removable head assembly; electrical, pressure, and bomb body details were not altered. This "heat sink" bomb essentially comprises a massive metallic strand carrier designed to shield the strand from radiation and convection. In use, a set comprising 6 to 8 such strand carriers is made up. A strand is loaded in each, the group is placed in an appropriate oven or cooler for 6 hr, and the carriers are individually removed and fired in the bomb as desired.

The removable head was patterned after that of a regular Crawford bomb, with flexible leads that could be attached to the heat sink. The head and sink were joined by a threaded pipe, which also contained a $\frac{3}{8}$ in. hole for a propellant gas outlet.

The heat sink itself is a two-piece machined cylinder (3-in. OD, $\frac{1}{2}$-in. ID) of metal held together with four screws. A hole was drilled into the center of the block where the strand is placed. Three small-diameter holes were drilled so that half the hole is in each half of the heat sink terminating at the cavity for the strand. Terminals are used to complete the electrical connection to the timing and igniter circuits.

Two metals (copper and stainless steel) were tested for the heat sink to compare reliability. Stainless steel was much easier to clean after use than copper and allowed more time between removal from the conditioning box and firing without the strand showing a change in rate.

A suitable restrictor for the strands (various LFT series ammonium nitrate propellants) was a 10% solution in 2-butanone (analytical grade) of methyl vinyl ether and maleic anhydride copolymer (General Aniline & Film Corp., PVM/-MA). The strands were dipped 4 to 6 times with 15 to 30 min drying intervals between each dipping, drying 1 hr after the final coat. The strands were then wrapped in a pressure sensitive tape (3M, Scotch Brand, 7MFS2, 1H 7p). Holes were drilled in the restricted strand at appropriate distances for the ignition wires and fuse wires; the latter were connected to an electrical timer.

Table 1 Burning rate of LFT series propellant as a function of the time between conditioning and firing of strands

Time interval, min	Initial conditions Time, hr	Temp, F	Burning rate at 1000 psi, ips	Heat sink material
1	6	170	0.065	stainless steel
2	6	170	0.064	stainless steel
4	6	170	0.065	stainless steel
6	6	170	0.064	stainless steel
8	6	170	0.063	stainless steel
10	6	170	0.060	stainless steel
1	6	170	0.064	copper
2	6	170	0.064	copper
4	6	170	0.064	copper
6	6	170	0.063	copper
8	6	170	0.060	copper
10	6	170	0.059	copper

Apparatus Tests

Demonstration of the following was necessary: adequacy of the heat sink; absolute accuracy of measurements; reproducibility; and comparison with motor data. The last item is of uncertain significance, since conventional Crawford strand data do not accurately correlate with motor data.

Adequacy of the heat sink was tested by varying the time needed to transfer the carrier to the bomb and run a determination, until a change in burning rate evidenced itself. The results are given in Table 1. It was found, therefore, that ample time was available for making the test, since normally the heat sink can be transferred from oven to bomb and fired in 2 to 3 min. Similar results were available from −65 F tests.

The finalized apparatus gave satisfactory results compared with motor results, especially in obtaining data for calculation of temperature coefficient of burning rate at constant pressure σ_p and the temperature coefficient at constant nozzle throat area π_k. The rates sometimes will be somewhat lower in the sinks as compared with motor firings, but after determination of burning rate in a regular Crawford bomb, the

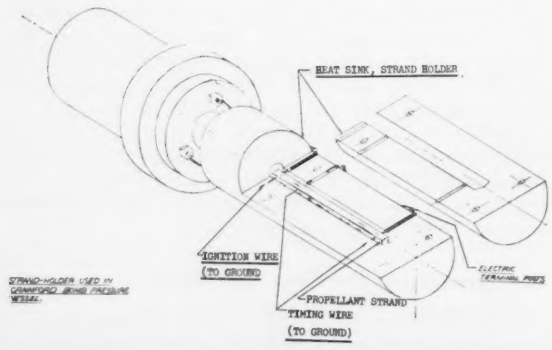

Fig. 1 Strand holder used in Crawford bomb pressure vessel

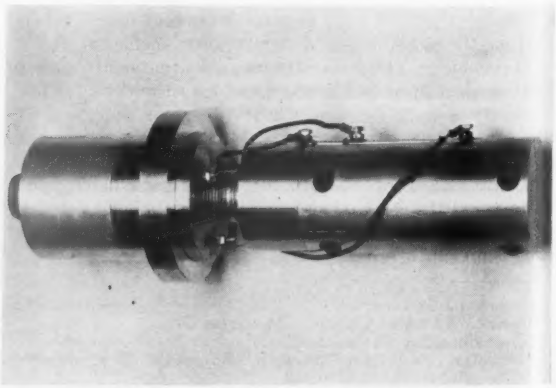

Fig. 2 Assembled apparatus ready for insertion in a Crawford bomb

nozzle size for desired pressure level can be accurately determined from the sink data. The difference in rates of strands between the heat sink and a regular Crawford bomb are due to changes in restrictors; the heavier restrictor used in the heat sink tests gives the same results when used in the usual bomb.

Two of the parameters used in describing the burning characteristics of solid propellants are temperature sensitivity π_k at constant K_n expressed in per cent and the change of rate with temperature at constant pressure in per cent σ_p. The value π_k is defined as

$$\pi_k = \frac{1}{P_{av}} \left(\frac{P_2 - P_1}{T_2 - T_1} \right) K_n \, (100) \qquad K_n = \text{constant}$$

where K_n is chosen so that $P_{av} = 1000$ psi at a propellant temperature of 70 F. The value of σ_k is defined as

$$\sigma_p = \frac{1}{r} \left(\frac{\Delta r}{\Delta T} \right)_p (100)$$

where r is the rate of the propellant at 70 F and 1000 psi. For comparison purposes, σ_p and π_k are calculated from heat sink data (Fig. 3) and motor firing data and tabulated in Table 2.

Although some discrepancies exist between motor and strand data, it is our opinion that the basic accuracy of test motor firings is less than the strand, occasioning these differences.

Conclusion

The advantages expected in the sink system have been realized and are reliable with regard to the mentioned ballistic properties. The experience over the last year and a half provided us with an apparatus that has cut the time and cost of obtaining data to a fraction of that required in motor firings or in conditioned Crawford bomb techniques.

References

1 Crawford, B. L., Huggett, C., Daniels, F. and Wilfong, R. E., "Direct Determination of Burning Rates of Propellant Powders," *Anal. Chem.*, vol. 19, 147, pp. 630–633.

2 Muraour, H. and Schumacher, W., "Speed of Combustion of Colloidal Powders at Atmospheric Pressure," *Memorial des poudres*, Imprimerie nationale, Paris, France, vol. 27, 1937, pp. 87–97.

3 Sutton, G. P., *Rocket Propulsion Elements*, John Wiley and Sons, Inc., N. Y., 1956, 2nd ed., p. 351.

4 Carlton, C. H., "Strand-Burning Techniques for Evaluation of Propellants," NOTS 1090, NavOrd Rep. 3478, May 1955.

5 Sears, R. W., Browning, J. L. and Robey, W. W., "Strand-Burning-Rate Measurements Over a Wide Pressure Range in One Firing," NavOrd Rep. 3053, Dec. 1954.

6 Lindred, A. and Walbrecht, B., "Development of a Strand Burning Rate Apparatus," Picatinny Arsenal Tech. Rep. 1828, June 1951.

Table 2 Ballistic data for LFT series propellant

	Burning rate at 1000 psi, ips	Pressure exponent, n	π_k	σ_p
sink				
+170 F	0.064	0.50	0.291%/F	0.148%/F
+70 F	0.055	0.50		
−75 F	0.044	0.50		
motor				
+170 F	0.069	0.53	0.289%/F	0.147%/F
+70 F	0.058	0.53		
−75 F	0.049	0.53		
Crawford bomb				
+70 F strand	0.058	0.52	regular restriction	
	0.054	0.50	restricted and taped	

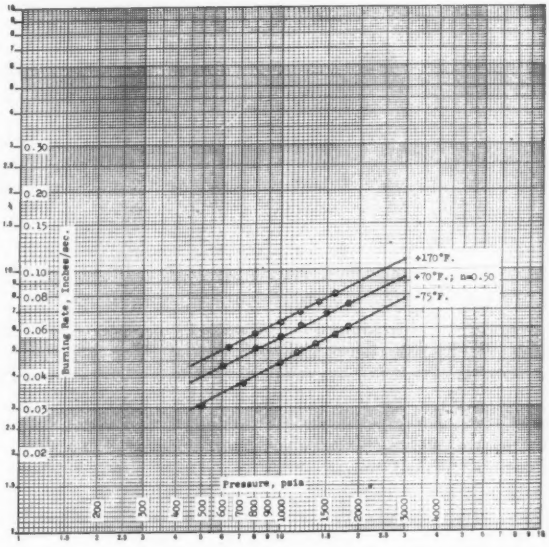

Fig. 3 LFT series propellant heat sink burning rate data, Standard Oil Co., Indiana

Selection of a Pressurization System for a Storable Liquid Propellant Rocket Engine[1]

C. J. KAPLAN[2]

Rocketdyne Div.,
North American Aviation, Inc.
Canoga Park, Calif.

A study was performed to select a propellant tank pressurization system for a high performance storable liquid propulsion system. Minimum weight and long term storability were desired. The systems proposed included four stored gas systems and eight generated gas types. The stored gas systems differ in the method of heating the gas. The generated gas systems differ in the generant employed and the method of controlling gas temperature. These systems are described and compared as to weight, component development problems, and performance characteristics. Compatibility between pressurizing gas and liquid propellant, and its effect on system selection, is discussed. Stored gas system weight is shown highly dependent on storage bottle material and safety factor assumptions. Selection was based primarily on minimum weight but tempered by considerations of degree of development required. Comparison leads to selection on a dual gas generator system.

A WIDE range of propellant tank pressurization systems were studied, both of the stored gas and generated gas types, in order to compare their suitability for use with a large, pressure-fed rocket engine using nitrogen tetroxide and UDMH. Principal requirements included light weight, long term storability, high reliability, and instant operational readiness. A tank pressure of approximately 450 psi was desired. Operating time was over one minute. Total propellant tank capacity was approximately 1000 ft³.

A survey of past work in this field revealed quite a number of pressurization systems which had been employed in other pressure fed rockets using storable propellants, and were potentially suitable for this application. Several other systems were proposed which, as far as is known, have not been used previously.

While the problem of pressurizing a propellant tank is not a new one, this project carried an increased emphasis on high mass ratio. Because of this and the availability of improved structural materials, a re-examination of past conclusions was believed to be warranted.

Stored Gas Systems

The weight of a stored gas pressurization system may be expressed, to a good approximation, as follows:

$$\text{weight} = \left[\frac{P_t V_t M}{R Z_t T_t}\left(\frac{P_0/T_0}{P_0/T_0 - P_f/T_f}\right)\right]\left[1 + \left(\frac{K_b R T_0 Z_0}{M}\right)\right]$$

T = temperature
P = pressure
R = universal gas constant
M = molecular weight
Z = compressibility of gas
K = ratio of gas bottle weight to product of its pressure and volume

and subscripts

0 = initial conditions in storage bottle
f = final conditions in storage bottle
t = final conditions in propellant tanks

This expression considers only the gas and its storage vessel, ignoring weight of valves, regulators, etc. In this case T, the ambient storage temperature, was beyond control of the designer. P_t was fixed, and P_f was P_t plus system flow losses. There was some leeway in selection of P_0, the storage pressure; however, previous studies have indicated that there is little to be gained by varying this parameter. Throughout this study, 4500 psi was employed; however, results would have been similar for higher pressures. The molecular weight is fixed by selection of the gas. Thus, if minimum weight is desired, the parameter K must be made as low as possible (by constructing the storage bottle of material with a high strength to weight ratio), and T_t and T_f must be made as high as possible. This requires that heat be applied to the gas delivered to the propellant tanks and also to the residual gas in the storage bottle. The various stored gas systems which were considered differ in their approach to the heating problem. These systems will now be described.

Selection of Stored Gas

The selection of chemically neutral stored gases is virtually limited to helium with a molecular weight of four and nitrogen with a molecular weight of 28. Neon with a molecular weight of 20 is lighter than nitrogen but prohibitively expensive.

Presented at the ARS Propellants, Combustion and Liquid Rockets Conference, Columbus, Ohio, July 18–19, 1960.
[1] This report is based upon work performed under Air Force Contract no. AF33(616)-6684.
[2] Research Specialist, Advanced Design Department.

As low molecular weight is to be desired, the choice obviously fell to helium and the stored gas phase of the study was confined to it. Weights of any of the helium systems would be approximately doubled if nitrogen were used.

Unheated Gas System

The unheated gas system is the simplest system possible and provides flow of gas directly from the storage bottle to the propellant tanks without heating. Disregarding heat pickup from the bottle, tank walls, and other components which cannot be relied upon to be of significant magnitude, the temperature in the bottle will drop 270 F, during the run, due to adiabatic expansion. The trend of temperature vs. time in the bottle and propellant tanks is shown in Fig. 1. This system was not expected to show attractive weight, but was analyzed to provide a basis of comparison for more sophisticated systems.

Thrust Chamber Heated Gas

In this system the gas flowing from the bottle is heated before entering the propellant tanks. In a turbopump engine the heat exchanger for this purpose is conventionally located in the turbine exhaust. However, as this study is concerned with a pressure fed engine, another source of heat had to be found. It consists of a heat exchanger in the form of a coil which forms an extension to the thrust chamber nozzle and transmits heat from the main rocket exhaust to the helium. No heating of the residual gas is provided. As the run proceeds, the helium entering the thrust chamber is progressively colder (its temperature increment received in the heat exchanger being almost independent of entering temperature) and is delivered to the tanks at a progressively colder state. Fig. 2 shows the estimated bottle and tank temperatures vs. time.

The remaining helium systems are all intended to heat the gas remaining in the bottle as well as the gas delivered.

Solid Propellant Injection Heating

The helium bottle in this system contains within it a solid propellant gas generator. This charge is ignited when enough gas has been delivered to deplete the stored gas pressure by about one third. The solid propellant burns at a pressure only slightly above the gas pressure in the bottle for the remainder of the run. For this reason, a lightweight propellant case may be used, and its gas ports are subsonic. Depending on the amount of heat supplied by the solid propellant products, the temperature in the bottle will either rise, remain constant or drop at a slower rate than for the unheated case. The charge selected was a relatively cool burning propellant with a weight ratio of 1.75 to the stored helium. As shown in Fig. 3, this results in a 400 F rise for the residual gas but a rise of only 140 F for the gas in the propellant tanks.

Solid Propellant Heating With Heat Exchanger

In this system (see Fig. 4) the solid propellant charge is contained in a case external to the gas bottle. The gas evolved as it burns is discharged through a heat exchanger within the bottle, after which it is injected into the helium delivery line. This system permits maintenance, throughout the run, of a constant temperature in the bottle, and also maintains the delivered gas at a constant temperature higher than that of the gas in the bottle. A helium bypass flow cools the solid propellant gases to a temperature low enough to avoid damaging the heat exchanger.

Injection Heating with Liquid Gas Generator

This system is analogous in its thermodynamics to the

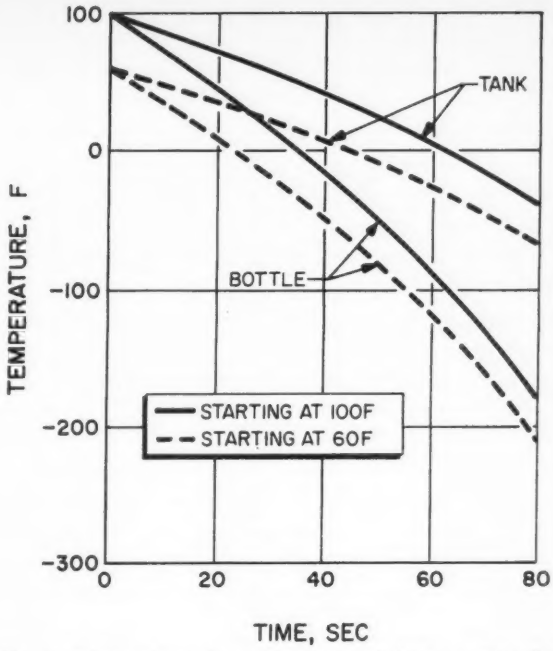

Fig. 1 Temperature of gas in bottle and tank vs. time for helium system with no heating

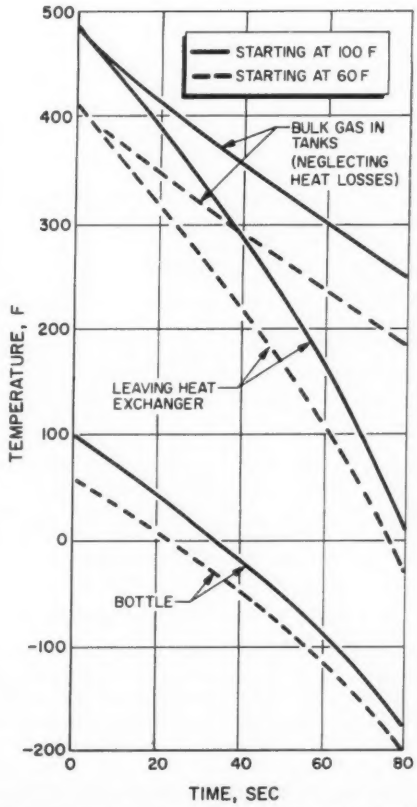

Fig. 2 Temperature vs. time for helium system with thrust chamber heating

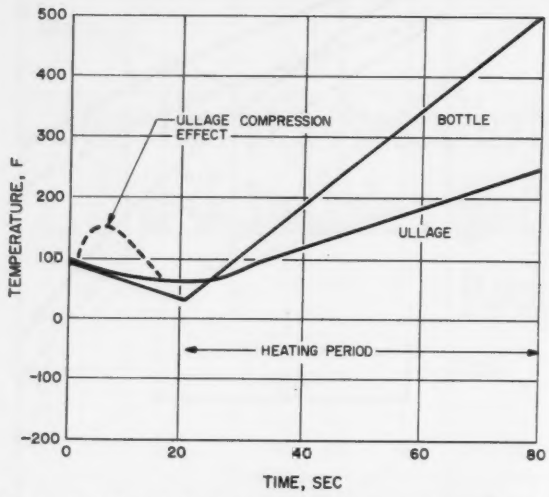

Fig. 3 Variation of storage bottle helium temperature and main propellant tanks ullage helium temperature with time for systems with helium heating inside bottle

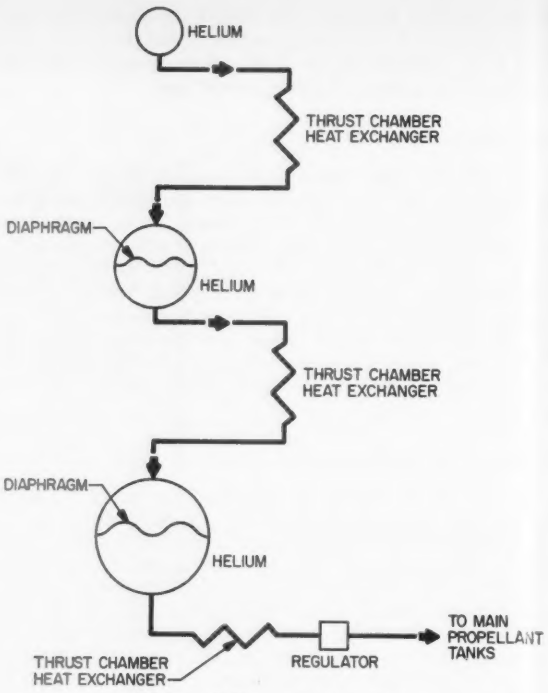

Fig. 5 Helium cascade system

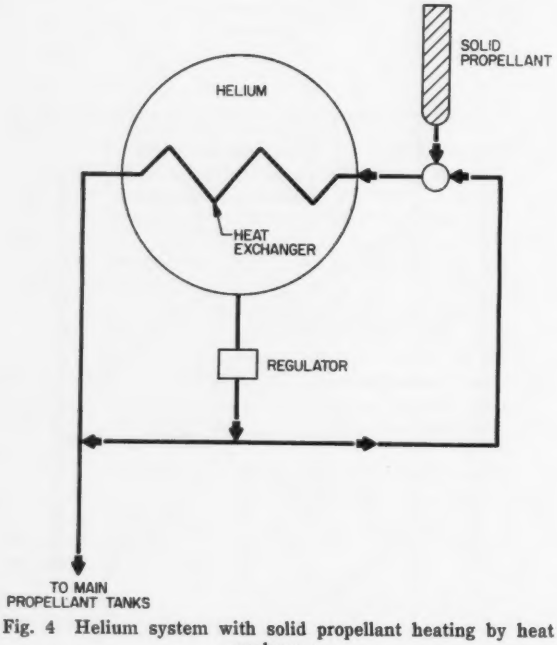

Fig. 4 Helium system with solid propellant heating by heat exchanger

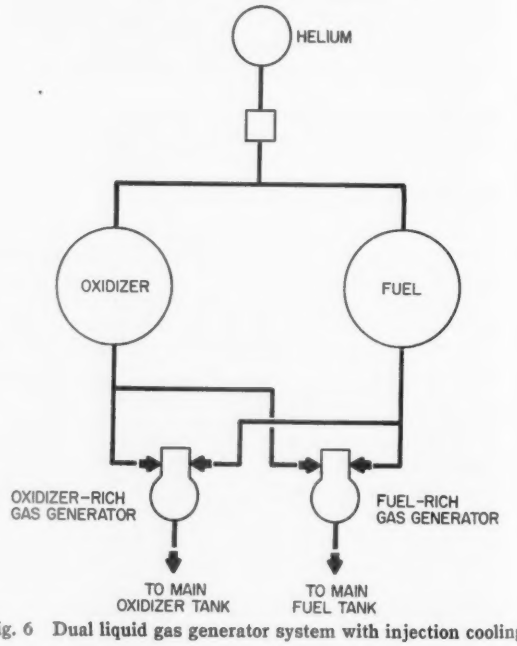

Fig. 6 Dual liquid gas generator system with injection cooling

solid propellant injection heating system but substitutes a liquid propellant hot gas source. The hypergolic fuel and oxidizer are contained in separate bottles within the helium tank. In each bottle is an ullage space charged with helium at the main bottle storage pressure. This furnishes the pressurization for feeding these propellants to a gas generator. When main bottle pressure has become depleted to a desired value, the delta pressure between the ullages and the main volume of gas automatically starts the system.

Cascade System

This system (see Fig. 5) uses thrust chamber heat exchangers but attempts to gain the advantage of high temperature for the residual gas by displacing the original gas with gas stored in a separate smaller bottle and heated by a separate heat exchanger. This secondary bottle in turn has its gas displaced by heated gas from a third still smaller bottle-heat exchanger combination. Thus, at the end of the run only the

final, smallest bottle contains low temperature helium. The total amount of stored helium required is only slightly greater than would be the case for a single bottle with the same residual temperature.

Generated Gas Systems

The systems described here all make use of one or more generants stored in solid or liquid form and converted to gas at the time of use. The storage volume is reduced greatly as compared to a stored gas system, and the pressure requirement for the containing vessel is also reduced, because the operating pressure need only be the desired propellant tank pressure plus system flow losses. With storage vessel weight thus reduced, the generant itself is, by far, the greatest portion of the system weight. Therefore, the prime desirable characteristics are that the generated gas has high temperature and low molecular weight in its final state in the propellant tanks. However, the temperatures produced in gas generation processes are inherently much higher than is believed practical for prolonged exposure to propellant tank walls. Therefore, all the gas generation systems to be described include a method of controlling the temperature of the gaseous output at a compromise temperature within the limits of the tank material.

The gas generants may be classified as solid and liquid types.

Solid Propellant Gas Generator With Subliming Coolant

A solid propellant charge is used as a gas source. The lowest flame temperature available in solid propellants is close to 2000 F. To reduce its temperature, the gas is passed through a bed of solid material which sublimes directly to a gas. This gas serves as a cooling diluent for the solid propellant gas as well as an additional pressurization contribution. A typical material of this type is oxalic acid. It has been found possible by this method to reduce solid propellant gas temperature to below 500 F. As it is not possible to throttle the burning rate of the propellant, regulation operates on the principle of dumping excess gas overboard. The inherent variation in burning rate of solid propellant with temperature requires that excess propellant be carried to provide sufficient gas flow at the low end of the temperature range.

Liquid Gas Generators

A number of monopropellants may be used to generate gas for pressurization. In addition almost any bipropellant combination may be used as a gas generant by using an off-stoichiometric mixture ratio to lower gas temperature. A single fuel-oxidizer combination may be used in both "fuel-rich" and "oxidizer-rich" gas generators to produce compatible gases for both the fuel and oxidizer.

Gas Generator System With Injection Cooling

One way to control the temperature of a bipropellant gas generator is to inject a sufficient excess of the rich component to cool by evaporation. The limit on this process is that if the propellant has a high molecular weight, heat of combustion serves to "crack" the excess into components of lower molecular weight; if too low a temperature is attempted the excess may evaporate without cracking, leaving an undesirable gas constituent which raises the average molecular weight of the gas, and may easily condense.

Ammonia is unique among storable liquid fuels in that it has a low enough molecular weight and low enough boiling point to be a desirable pressurization gas without cracking. It may therefore be used to carry injection cooling to a fairly low temperature.

Cooling may also be accomplished by injecting a separate liquid downstream of the gas generator. Water is good for this purpose if its dewpoint is not reached.

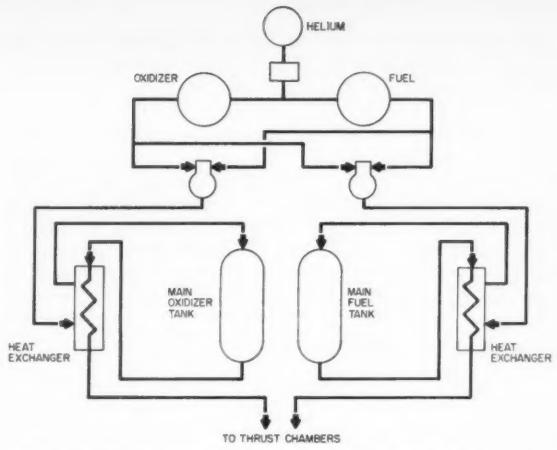

Fig. 7 Dual gas generation system with heat exchangers

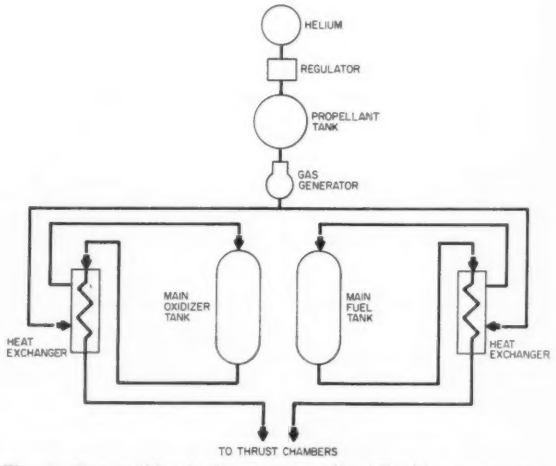

Fig. 8 Compatible single monopropellant liquid gas generator system

The system shown in Fig. 6 uses ammonia and nitrogen tetroxide as the generants. An ammonia-rich gas generator pressurizes the UDMH tank, and a tetroxide-rich gas generator pressurizes the tetroxide tank. The excess coolant in the output of the tetroxide gas generator is believed to be cracked at least partially into lighter gases including nitrogen, oxygen and nitrous oxide. In this case and for most propellant combinations considered, the molecular weight of the oxidizer-rich gas is considerably higher than that of the fuel-rich gas.

Liquid Gas Generator With Heat Exchanger

Another method of cooling gas generator products is by heat exchange with the liquid propellant. The system shown in Fig. 7 uses heat exchangers located in the lines from the propellant tanks to the thrust chamber. This type of cooling permits use of monopropellants such as hydrazine. Fig. 7 shows this type of cooling used with dual bipropellant gas generators. In Fig. 8 the heat exchanger-cooled products of a single hydrazine gas generator are used for both fuel and oxidizer pressurization.

Evaporated Ammonia System

Another system proposed for using ammonia and obtaining compatible gases is shown in Fig. 9, wherein a single oxidizer-rich gas generator discharges through a heat exchanger which evaporates liquid ammonia, the fuel pressurant.

The mass balance for this system is determined by the volumetric mixture ratio of the main propellant tanks. For a given mass balance, the heat balance may be adjusted over a fair range by adjusting the mixture ratio (hence the output temperature) of the gas generator. For the conditions of this study it was found that a gas generator temperature of 900 F will result in final generated gas and vaporized ammonia temperatures of 400 F and 200 F, respectively.

Hybrid Hydrazine-Helium System

It is possible to combine generated and stored gases, taking care of the temperature needs of both, by means of the system shown in Fig. 10, in which the helium flows en route to the oxidizer tank through a heat exchanger where it is heated by cooling the output of a hydrazine gas generator. The hydrazine products pressurize the fuel tanks. Again, the volumetric mixture ratio of the engine permits a favorable pressurant mass balance.

This completes the systems studied to the extent that is permissible in an unclassified presentation.

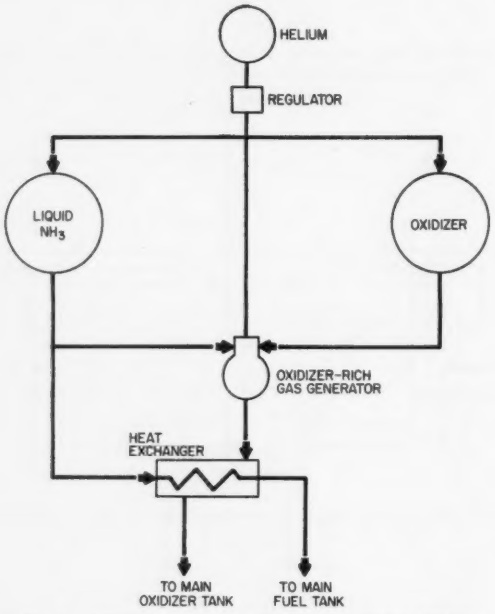

Fig. 9 Ammonia vapor - liquid gas generator system

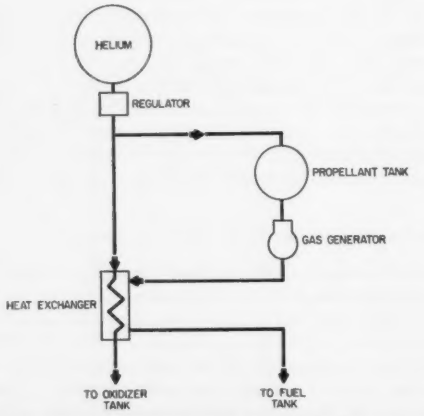

Fig. 10 Helium - monopropellant gas generator system with heat exchanger cooling

Estimation of Gas Changes of State

In making quantitative calculations of the amount of gas or generant required for the various systems, the study entered an area where theory is complex and little experimental data are available. A whole series of heat exchange and mass exchange effects may occur which may influence the final temperature, composition and molecular weight of the pressurizing gas. In both stored and generated gas systems, a gas temperature several hundred degrees above the ambient propellant temperature is desired. Heat transfer from the gas to the propellant is therefore to be expected. Loss of heat by the gas to the propellant tank walls may also take place. The heat transfer may produce evaporation at the propellant liquid surface, adding another component to the pressurizing gas. In a generated gas, additional effects are possible: products of the common bipropellant reactions include water which may condense if its dewpoint is reached. Ammonia may also condense if its partial pressure is high enough and the temperature low enough. Some of the generated gas constituents may be soluble in the propellant. In addition, there is some doubt as to the exact composition and molecular weight of the output when excess propellant is used to lower the temperature of generated gases. The rate at which most of these effects take place is dependent upon the rate and pattern of gas movement and wave action within the tank, a difficult problem to predict.

An exact solution for this formidable set of problems was not attempted. Reliance was placed upon available experimental data which indicate that it is possible to maintain a gas temperature at least 300 F above the propellant temperature under favorable conditions. All of the systems studied offered the possibility of varying the temperature at which the gas is supplied to the tanks over a range of several hundred degrees. Depending on the particular system, the temperature is adjusted by varying gas generator mixture ratio, heat exchanger area, solid propellant - subliming coolant ratio, etc. Making use of this flexibility, it was possible to select a final state temperature, say 400 F, and estimate only that the heat losses were such that a gas supply temperature somewhere within a wide range (say, 450 to 900 F) would yield this final temperature. If the system under consideration could be adjusted over this range, these broad assumptions furnish a satisfactory basis for calculations of the amount of gas or generant needed, which depends only upon the final temperature and molecular weight. In the case of injection or dilution cooled systems, the molecular weight would vary with the output temperature; however, the variation is small. Condensible gas constituents were treated by making certain that, throughout the assumed range of supply conditions, their dewpoint was below the assumed final temperature. Calculations indicate that mass transfer of soluble gases to the propellant should be a very slow process and a minor effect within the duration of the engine run.

Role of Compatibility in the Study

It may be seen that the systems presented do not all adhere to the rule of chemical compatibility between pressurizing gas and propellant, particularly the oxidizer. In the solid propellant - helium system, the helium contains about 13% by mole of fuel-rich solid propellant products. In the solid propellant - coolant system both oxidizer and fuel are pressurized by gas containing about 40-mole % of combustibles.

Table 1 Comparisons of pressurization systems

System	Stored gas and generants	Gas produced	Overall weight, lb	Overall volume, ft³
single gas generator with heat exchanger cooling	helium, hydrazine	hydrazine products[a]	1164	16.6
dual gas generator with heat exchanger cooling	hydrazine, N_2O_4, helium	hydrazine products on fuel, N_2O_4-rich gas generator products on oxidizer	1731	25
dual gas generator with injection cooling	helium, N_2O_4, ammonia	ammonia-rich gas generator products on fuel, N_2O_4-rich products on oxidizer,	1874	29.4
gas generator and evaporated fluid	helium, N_2O_4, ammonia	ammonia on fuel, N_2O_4-rich gas generator products on oxidizer	1925	33
solid propellant with subliming coolant	AN2011 solid propellant, oxalic acid pellets	solid propellant products,	2080	20
helium-gas generator hybrid	helium, hydrazine	helium on oxidizer, hydrazine products on fuel	2458	90.4
helium with liquid gas generator tank heating	helium, NTO, UDMH	helium, gas generator products	2740	113
helium with solid propellant tank heating	helium, solid propellant grain	helium, solid propellant products	2746	111.4
helium cascade	helium	helium	2754	119
helium with thrust chamber ing	helium	helium	3928	176
helium—no heating	helium	helium	6856	309

[a] Incompatible gas used on oxidizer.

The hydrazine monopropellant system pressurizes the oxidizer as well as the fuel with hydrazine decomposition products consisting largely of ammonia and hydrogen.

These systems were considered because limited experimental data indicate that incompatible gas-propellant combinations may be used without adverse reaction taking place. However, the state-of-the-art in use of incompatible gas was regarded as inadequate. Extrapolation of existing work to the size, duration and accurate pressure control required for this application was regarded as a major development task. This was an important factor in comparing the development problems of the various systems.

For generated gases there is a strong connection between compatibility and system weight: Oxidizer-rich gases consisting largely of O_2, N_2, CO_2 and oxides of nitrogen have approximately twice the molecular weight of fuel-rich gases which may contain ammonia, hydrogen and the lighter hydrocarbons. If a fuel-rich gas may be used to pressurize both the fuel and oxidizer tanks, a minimum system weight should result.

Comparison of System Weights

Table 1 compares the weights of the systems studied. These weights were calculated with consistent assumptions of stress level and material for pressure vessels. High strength steel was assumed used in all cases. It may be seen that each general type of system has an approximate weight level. In ascending order of weight, these categories rank as follows:

1 Incompatible single liquid gas generator (fuel-rich gas on both propellants).
2 Compatible dual liquid gas generator.
3 Solid propellant gas generator.
4 Generated-stored gas hybrid.
5 Stored gas with heating in storage bottle.
6 Stored gas with thrust chamber heating.
7 Unheated stored gas.

Influence of Safety Factor and Gas Bottle Material

The storage sphere constitutes the largest item of weight in all of the stored gas systems. Two structural materials were examined for this application: high strength steel with a stress-to-weight ratio of 0.8×10^6 and filament-wound fiberglass with a ratio of 1.5×10^6. (A thin, gas-impervious aluminum liner is used with the fiberglass.) There were two safety factors involved because of the necessity for considering two alternative conditions of engine use: 1 If the gas bottle

Table 2 Effect of helium sphere safety factor and material on system weights

Pressurization system	Optimum weight design; proof pressure = 1.1 × operating, 1.25 safety factor based on ultimate strength		Personnel-safe design per MIL-T-5208A; proof pressure = 1.5 × operating, 1.33 safety factor based on ultimate strength	
	Fiberglass[a]	Steel	Fiberglass[a]	Steel
dual gas generator ammonia - NTO injection cooled	1818	1874	1907	1956
helium with thrust chamber heating	2868	3928	3468	5478
helium heating inside the bottle by solid propellant	2003	2666	2378	3526

[a] Fiberglass spheres include creep factor of 1.3 on operating pressure which may be combined redundantly with proof pressure factor

Table 3 Comparison of component requirements for pressurization systems

System	Storage vessel	Regulator	Heat exchanger	Gas generator	Other components
helium thrust chamber heating	large, high-pressure	large gas	thrust chamber	...	...
helium tank heating:					
solid propellant	large and thin solid propellant	large; solid particles, heat	...	solid propellant charge	filter, ignition timer, igniter
solid propellant and helium	large and solid propellant case	large gas	large; inside helium bottle	solid propellant charge	filter, ignition timer, igniter
liquid gas generator	large and propellant bottles	large gas	...	small, bipropellant hypergolic	...
cascade	three high-pressure: large, medium, small	large gas	thrust chamber, three sizes	...	tank diaphragms
liquid dual gas generator with heat exchanger cooling	one small, high-pressure, and two small low-pressure	small gas and on-off liquid	two small gas-liquid	bipropellant hypergolic and HZ monocatalytic	hot gas duct
liquid gas generator, vaporized NH_3	one small, high-pressure, and two small low-pressure	not determined	gas-liquid, small, incompatible, can cause start delay	bipropellant hypergolic	hot gas ducts
solid propellant, coolant	solid propellant, hot, low-pressure and coolant case	hot gas dump type	...	solid propellant charge and coolant pack	filter, hot gas ducts
liquid: NH_3-NTO, dual gas generator	small, high-pressure and two small low-pressure	small gas	...	two bipropellant hypergolic	...
single gas generator with heat exchanger cooling	small high-pressure and small low-pressure	small gas	small, gas-liquid	HZ mono-catalytic	hot gas ducts
helium-hydrazine hybrid	large high-pressure and small low-pressure	large gas	small, gas-gas	HZ monopropellant	hot gas ducts

could be kept remote from personnel while it is pressurized, a safety factor of 1.25 on ultimate strength and a proof pressure of 1.1 times the operating pressure would be required; 2 If the bottle were required to be charged in the presence of personnel, a proof pressure of 1.5 times the operating pressure and a safety factor of 1.33 on ultimate strength would be required for safety.

Table 2 shows how the weight of several stored gas systems is dependent upon the combination of structural material and safety requirements. It also shows how these factors affect a liquid gas generator system containing a liquid-pressurizing gas sphere.

Comparison of Component Development Problems

In addition to weight, a principal factor in making a selection among the various systems was the anticipated time and cost of developing them to the point of reliable performance. For the purpose of evaluating this factor, a component breakdown of each system was made as shown in Table 3. Most development difficulties were associated with the listed components. While a considerable amount of arbitrary judgment entered into this comparison, the various categories of components were ranked approximately as follows in decreasing order of the development effort they were believed to require:

1 Large, lightweight, high pressure gas storage bottles.
2 Solid propellant charges and coolant packs.
3 Gas-to-gas heat exchangers.
4 Gas-to-liquid heat exchangers.
5 Small, high pressure gas storage bottles (order of size required for pressurizing liquid generants).
6 Bipropellant gas generators.
7 Monopropellant gas generators.

Regulators and other control components were also evaluated as to the degree of development required. Of those listed, the large gas regulators required for helium systems, and the hot gas dumping type required with solid propellant were regarded as the most difficult. As already stated, gas-propellant chemical incompatibility was viewed as a major development problem.

Comparison of Storability

Storability of the gases and generants was also subject to comparison. The liquid gas generants considered in the study have all been demonstrated as storable for long periods in containers of proper material. A solid propellant with suitable storage characteristics for the systems using solid propellant was believed available. Storability of the subliming solid coolants required with solid propellant requires further investigation. Helium stored at high pressure for long periods may be subject to leakage losses; however, instances of successful storage have been reported. Helium cannot escape through homogeneous metal containers by diffusion.

Conclusion

Weight comparison of the systems presented (Table 1) showed that the single gas generator system using hydrazine decomposition products on both fuel and oxidizer was lightest in weight. The dual gas generator system with heat exchanger cooling ranked next lightest, and the dual gas genera-

tor system with injection cooling ranked third. The weight difference between the second and third ranking systems was small. If weight were the only consideration, the single gas generator system would have been the obvious selection. However, the selection process was strongly tempered by considerations of comparative difficulty of development. The incompatibility of hydrazine products with the oxidizer was regarded as an item entailing considerable development. In comparing the two dual gas generator systems, the one employing injection cooling was preferred as least encumbered with component development difficulties. The injection cooled system was therefore selected as the preferred system on the basis of a compromise between the criteria of light weight and least required development.

Disregarding the arbitrary ground rules which resulted in the above selection, the study indicates that the ultimate in lightweight pressurization may be achieved by use of a fuel-rich generated gas on both fuel and oxidizer.

Gas Particle Flow in an Axisymmetric Nozzle[1]

W. S. BAILEY,[2]
E. N. NILSON,[3]
R. A. SERRA[4]
and T. F. ZUPNIK[4]

Pratt & Whitney Aircraft
East Hartford, Conn.

Two closely related problems are studied which are associated with the presence of particles in the flow through thrust nozzles: the possibility of erosion due to particle impingement upon nozzle walls and the loss in thrust caused by velocity and thermal lag of the particles. As a first approximation to the solution of the impingement problem, particle trajectories are constructed in the flow field previously determined for the reacting gas in the nozzle. Subsonic and supersonic sections of the nozzle are taken into account in computing the resulting velocity lags. It is found that no significant impingement takes place when the perfect nozzles considered are truncated. The effect upon thrust is estimated by solving the equations for a one-dimensional, two-phase system using area distributions associated with the three-dimensional nozzle. For the propellant considered with particles of 2-μ radius, thrust losses of more than 5% appear to be possible. Lag may be reduced by lengthening the nozzle or increasing the nozzle throat radius. Weight and length penalties, however, will result.

THE USE of propellants with metal additives that produce nongaseous products of combustion has raised questions concerning the effect of particles on the design of thrust nozzles. In the rapid acceleration which takes place in the nozzle throat there are lags which develop in particle velocity and temperature relative to the corresponding gas properties. Two points are of particular interest. The particles may impinge upon the wall and cause erosion of the nozzle wall. The lags in velocity and temperature, moreover, may have such an effect upon the flow properties as to cause a loss in thrust.

Gilbert, Davis, and Altman (1)[5] have considered the development of particle velocity lag for one-dimensional flow by assuming that the gas velocity increases linearly with distance through the nozzle and have based an estimate of thrust loss upon this assumption. The effects of the lags upon the flow properties were not included in this analysis. Kliegel (2) discusses the equations of one-dimensional flow of a two-phase system as set forth by Carrier (3). The solution of this system is restricted to the case in which velocity and thermal lags are constant. Kliegel's work is concerned largely with a qualitative discussion of lag effects.

The purpose of the present paper is twofold. The impingement problem is examined by constructing particle trajectories in three-dimensional nozzles. Moreover, the

Received Oct. 28, 1960.

[1] The authors wish to acknowledge the contribution of Fred Landis of New York University through discussions of various thermodynamic problems involved. A. F. Schwantor and W. A. Carey of the United Aircraft Corporation Computation Laboratories have contributed significantly to the machine solutions of the problems.

[2] Assistant Project Engineer.

[3] Project Engineer.

[4] Analytical Engineer.

[5] Numbers in parentheses indicate References at end of paper.

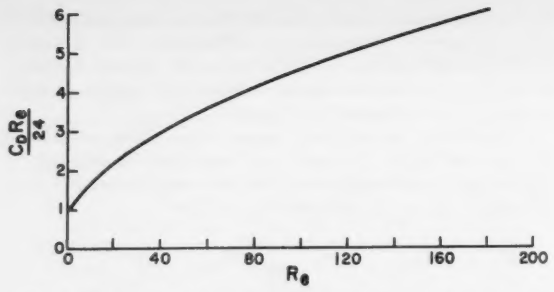

Fig. 1 Variation of drag coefficient with Reynolds number

thrust-loss problem is considered by carrying out solutions of the one-dimensional, two-phase system for area distributions associated with the three-dimensional nozzle. Because of the absence of scaling factors, it is necessary to consider the effects of a variety of parameters, such as particle diameter, throat radius or ratio of contour radius of curvature to throat radius.

Description of the Model

For the study of the trajectories, a representative solid propellant, Arcite, is used for which aluminum oxide droplets appear in the flow. As a first approximation to the three-dimensional model, the trajectories of the particles (i.e., droplets) are computed in the flow field previously determined for a contoured nozzle designed for this propellant using shifting equilibrium; that is, taking into account the changing chemical composition of the products of combustion. In this approximation, the effects of velocity and thermal lags upon the gas properties are not accounted for. The thermodynamic properties of the products of combustion upon which the construction of the flow field is based, moreover, are noticeably affected if there are significant lags in the particle velocity and temperature. The analysis leads to the conclusion, however, that the concentration of the particles is principally at the axis of the nozzle which is in agreement with experimental observation.

In order to estimate the magnitude of the effect of lag upon nozzle performance, the differential equations describing the two-phase system for one-dimensional flow are integrated and velocity and thermal lags computed. These are compared with the corresponding results for the situation in which the effects of lags upon thermodynamic properties are suppressed as in the three-dimensional case. This correlation is carried out for several area vs. length distributions, particle concentrations and throat radii. Quite apart from the relation to a specific nozzle, however, the effects of flow acceleration and concentration are of interest in themselves.

The fairly extensive computation involved in calculating thermodynamic properties simultaneously with solving the flow equations including lags is avoided by assuming constant gas properties but permitting energy exchange between particles and gas. The nozzle was designed using the products of combustion of Arcite as a uniform mixture. For the one-dimensional lag analysis, the mixture specific heats are fixed at the choking values. The properties of the gas phase of the two-phase system are fixed at the same point.

Trajectories in Three Dimensions

For the study of particle trajectories, it is assumed that the particles are spheres of constant and uniform size and do not collide. The relative volume occupied by the particles is negligible and no change in phase occurs in the nozzle. For determinination of the force exerted by the gas upon the particles, the variation in Reynolds number requires a knowledge of the dependence of drag coefficient upon Reynolds number. This variation is prescribed in accordance with the results of Langmuir and Blodgett (4). Forces on particles other than drag forces have been found to be negligible.

In view of the scarcity of reliable data on particle size, a range of particle radii was chosen from 2 to 10 μ. The effect of throat curvature is included by considering nozzles with radius ratio 2 (contour radius of curvature/throat radius) and with sharp corner at throat. Inasmuch as it has been shown that scaling is not possible here, throat radii of 1 in. and 5 in. were selected as typical. A perfect nozzle of area ratio 30 was chosen, and the impingement is studied as it relates to segments of this perfect nozzle.

The differential equation of particle motion is given by

$$\rho_p \frac{4}{3} \pi a^3 \frac{d\mathbf{V}}{dt} = C_D \pi a^2 \frac{1}{2} \rho_g |\mathbf{V}_g - \mathbf{V}_p| (\mathbf{V}_g - \mathbf{V}_p) \qquad [1]$$

where $\mathbf{V}_g$ and $\mathbf{V}_p$ are gas and particle velocity vectors; ρ_g and ρ_p are the corresponding densities; and a is the particle radius. The drag coefficient is represented in Fig. 1 as a function of Reynolds number Re in the form

$$\frac{C_D Re}{24} = f(Re) \qquad [2]$$

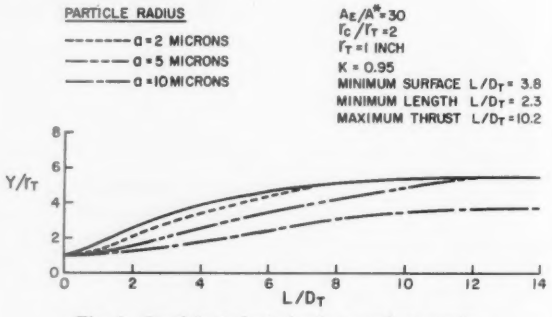

Fig. 2 Particle trajectories in a perfect nozzle

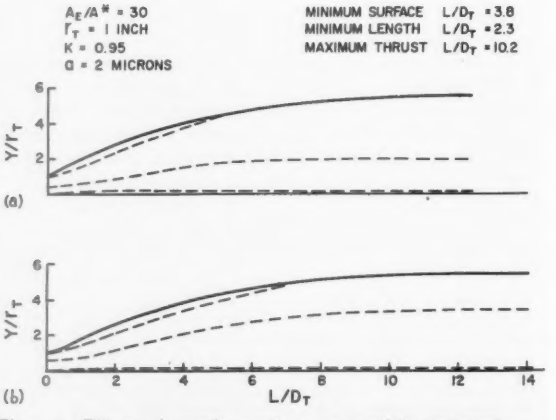

Figs. 3 Effect of nozzle contour on particle trajectories—a sharp corner perfect nozzle contour; b perfect nozzle contour with moderate turning $r_c/r_t = 2$

For Stokes flow, $f(Re) = 1$. Eq. 1 with velocity vector **V** separated into two components, u and v, becomes

$$u_p \frac{du_p}{dx} = \frac{9\mu_g f(Re)}{2\rho_p a^2} (u_g - u_p) \quad [3]$$

$$u_p \frac{dv_p}{dx} = \frac{9\mu_g f(Re)}{2\rho_p a^2} (v_g - v_p) \quad [4]$$

The trajectory analysis was carried out in two steps. The nozzle contours used were area ratio 30 perfect nozzles constructed for Arcite 372 as propellant with a sharp corner throat and with a throat radius ratio 2. Contours for throat radius $r_t = 1$ in. are shown in Figs. 2 and 3. A highly accurate flow field in the supersonic section of the nozzle was available from the nozzle construction in the form of a finely spaced characteristic net. Eqs. 3 and 4 were integrated in this field by an iterative numerical procedure. The trajectories were constructed from one down Mach line to the next by sending forward a tangent from the intersection with the first Mach line. Flow properties were thus obtained at a provisional point of intersection with the second Mach line. Average properties were then employed to correct this trajectory section much as in the construction of the characteristic mesh itself. In the first phase of this problem, trajectories were initiated from a set of radial positions uniformly distributed across the throat. The particle direction at this location was conservatively assumed to be axial and a range of initial velocities assigned.

Velocity lag is here defined with Kliegel to be

$$K = V_p/V_g \quad [5]$$

although perhaps the expression $(V_g - V_p)/V_g$ used by Altman et al. for velocity lag is more natural. Initial velocity lags (in the throat) are given a variety of values from 0.70 to 0.95. A subsequent consideration of the subsonic portion of the nozzle indicates that an interval of 0.70 to 0.95 covers the range to be expected.

In Fig. 2 is shown a typical set of trajectories starting in the nozzle throat at the wall. The ratio of nozzle contour radius of curvature to throat radius is 2, and the trajectories are for particle radii of 2, 5 and 10 μ. The effect of particle size is clearly considerable. It is significant that none of the trajectories intersects the wall ahead of the points where this nozzle would be truncated for minimum length or minimum surface (5).

It is shown in (5) that perfect nozzles may be truncated so as to optimize with respect to length, surface area, exit diameter or other parameter. In this optimization there is a segment of each nozzle in a family of perfect nozzles which is the minimum length nozzle for some value of the thrust coefficient. There is similarly a segment which is a minimum surface nozzle. It is important to ascertain the extent of the impingement problem for these common truncations.

The value of K in the throat was taken as 0.95. A similar calculation for $K = 0.70$ gives a particle trajectory for $a = 2$ μ only slightly different from that shown because the values of K associated with an initial $K = 0.70$ return almost immediately to the lag distribution found in the previous case.

The effect of throat curvature is exhibited in Figs. 3 for $a = 2$ μ. Here several trajectories are shown starting from various radial positions. The more rapid acceleration of gas flow in the throat region leads to more substantial lags both in the initial divergence from the axial direction and in the subsequent correction toward axial flow. The net effect of the increased throat curvature is to move the impingement point upstream. The minimum surface and minimum length nozzles, however, are still not intercepted.

Figs. 4 indicate the location of the wall impingement point as a function of particle size for throat radii r_t of 1 in. and 5 in. In contrast to the case of 1-in. throat radius where particles of radius greater than 5 μ fail to impinge upon the wall, considerably larger particles reach the wall for the 5 in. throat radius. It should be noted again that both curves lie above the truncation lengths for the minimum length and minimum surface nozzles.

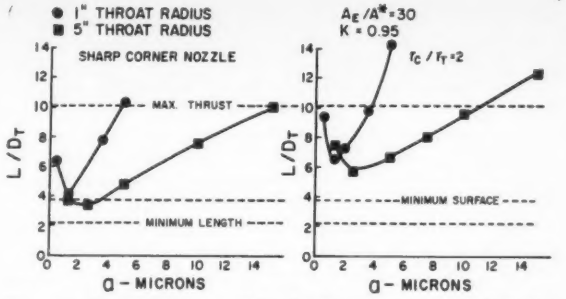

Figs. 4 Location of particle impingement for trajectories starting at wall

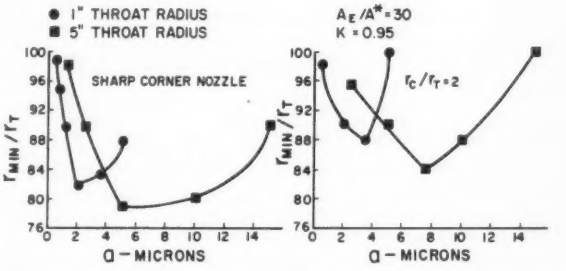

Figs. 5 Required particle position at throat for subsequent wall impingement (full nozzle)

The fact that the trajectory initiated at the throat wall intersects the nozzle contour does not, however, imply that there is an impingement problem. Analysis has shown that the particles are concentrated at the nozzle axis and for this particle size range do not appear in the throat at a distance more than 75 to 80% of the throat radius. Figs. 5 indicate the lowest radial position at the throat for which any impingement occurs. For nozzles with throat radius less than 5 in., there is effectively no wall interception. By reference to Figs. 4, the impingement which can occur for nozzles of larger throats is seen to be usually beyond the cutoff point.

In order to determine realistic values for lags and radial distribution of particle mass in the throat, it is necessary to perform trajectory calculations in the convergent portion of the nozzle. Here the flow properties are determined by a numerical three-dimensional streamline calculation procedure. The throat contour with $r_c/r_t = 2$ was carried back toward the combustion chamber. The trajectories of the particles chosen were initiated at a subsonic area ratio of about 2. Particle velocities were assumed to coincide with gas velocity at this location, and particles were taken to be uniformly distributed over this section. Integration of the trajectory equations yields the corresponding distribution of particles at the throat as it depends upon particle radius and throat radius. It was found that the 2-μ particles were contained within a distance of 0.80 r_t of the axis and that the velocity lag was of the order of 0.70. The trajectories were slightly inclined toward the axis at this point so that the above estimates of impingement are conservative in this respect. The 10-μ particles were contained within a radial dis-

tance of 0.5 r_t. The larger particles were concentrated very close to the axis. Some of the trajectories of these heavier particles actually intersected the axis near the throat so that the assumption of no collisions is not completely satisfied. However, the angle of intersection was not so great as to introduce the possibility of hitting the opposite wall.

It is perhaps not inappropriate to indicate at this point the complexity of this problem if a complete analysis of the three-dimensional, two-phase system is undertaken. Here it is necessary to combine, in the supersonic portion of the nozzle, the method of characteristics for nonisentropic flow with the simultaneous determination of gas streamlines and particle trajectories. This in turn requires concurrent determination of the thermodynamic properties of the reacting gas, taking into account the proper transfer of kinetic and thermal energy between the gas and particle phases of the system. Such a calculation of properties necessitates inclusion of either extensive tabulations of the gas properties such as density, entropy, specific heat, viscosity, conductivity, sound speed, etc., as functions of pressure and temperature, or, alternatively, the thermodynamic calculation procedure for determining these quantities directly from basic properties of constituents.

One-Dimensional Analysis

In order to obtain a reliable measure of the magnitude of thrust loss due to the velocity and temperature lags, it is necessary to include the effect of lag in the two-phase system. The one-dimensional, two-phase analysis, which includes the proper energy exchange based upon the lags as they develop, suffices to give a fairly reliable estimate of the loss. Even here, however, the solution is quite involved unless a restricted thermodynamic model is chosen for the gas phase. Accordingly, it is assumed that the gas phase of the products of combustion of Arcite has properties c_{p_g} and R_g fixed at the choking temperature and pressure attained in the isentropic expansion which was used in the three-dimensional nozzle design.

The following assumptions concerning the one-dimensional model are essentially those made by Kliegel. In addition to the requirements listed earlier in connection with the trajectory computations, it is assumed that the total energy of the two-phase system is fixed, that the gas is nonviscous except insofar as it exerts a drag force upon the particles, that the transmission of heat between particles and surroundings is via convection to the gas, and that the particles have uniform temperature. The specific heat of the aluminum oxide is also assumed constant. The differential equations are then

Continuity:

$$\text{gas} \qquad \rho_g u_g A = (1 - \lambda) W \tag{6}$$

$$\text{particles} \qquad \rho_s u_p A = \lambda W \tag{7}$$

where λ is the fraction of total mass flow rate W in particle form. Since the relative volume occupied by the particles is negligible, ρ_g and ρ_s are the mass of gas and solid, respectively, per unit volume of gas. The quantity ρ_p will be used as previously to refer to the density of a particle; the gravitational constant is denoted by g_0.

Momentum:

$$\rho_g u_g \frac{du_g}{dx} + \rho_s u_p \frac{du_p}{dx} + g_0 \frac{dP}{dx} = 0 \tag{8}$$

Energy:

$$(1 - \lambda) W \left[g_0 J c_{p_g} \frac{dT_g}{dx} + u_g \frac{du_g}{dx} \right] + \lambda W \left[g_0 J c_{p_p} \frac{dT_p}{dx} + u_p \frac{du_p}{dx} \right] = 0 \tag{9}$$

State:

$$P = R_g \rho_g T_g \tag{10}$$

The drag equation, 3, is repeated for convenience

$$u_p \frac{du_p}{dx} = \frac{9 \mu_g f(Re)}{2 \rho_p a^2} (u_g - u_p) \tag{11}$$

while the heat transfer is described by

$$\frac{4}{3} \pi a^3 \rho_p c_{p_p} \frac{dT_p}{dt} = 4 \pi a^2 h (T_p - T_g) \tag{12}$$

Here, the heat transfer coefficient h is obtained by assuming the Nusselt number $2ah/k_g = 2$ where k_g is the conductivity of the gas. Thus, the heat transfer equation takes the form

$$u_p \frac{dT_p}{dx} = - \frac{3 k_g}{\rho_p c_{p_p}} a^2 (T_p - T_g) \tag{13}$$

This system is brought into convenient form for integration by eliminating ρ_g, ρ_s and P from Eqs. 6, 7, 8 and 10

$$\left(u_g - \frac{g_0 R_g T_g}{u_g} \right) \frac{du_g}{dx} + \frac{\lambda}{1 - \lambda} u_g \frac{du_p}{dx} + g_0 R_g \frac{dT_g}{dx} = \frac{g_0 R_g T_g}{A} \frac{dA}{dx} \tag{14}$$

Eqs. 9 and 14 now give

$$\frac{du_g}{dx} = \frac{\dfrac{g_0 R_g T_g}{A} \dfrac{dA}{dx} - \dfrac{\lambda}{1 - \lambda} \left[u_g \dfrac{du_p}{dx} - g_0 R_g \dfrac{c_{p_p}}{c_{p_g}} \dfrac{dT_p}{dx} - \dfrac{R_g u_p}{J c_{p_g}} \dfrac{du_p}{dx} \right]}{u_g \left(1 - \dfrac{R_g}{J c_{p_g}} \right) - \dfrac{g_0 R_g T_g}{u_g}} \tag{15}$$

$$\frac{dT_g}{dx} = - \frac{1}{g_0 J c_{p_g}} \left[u_g \frac{du_g}{dx} + \frac{\lambda}{1 - \lambda} \left(g_0 J c_{p_p} \frac{dT_p}{dx} + u_p \frac{du_p}{dx} \right) \right] \tag{16}$$

which, together with Eqs. 11 and 13 constitute the system.

The constants have been determined as

$$c_{p_g} = 0.4981 \frac{\text{Btu}}{\text{lb}_{(\text{mass})}\,^\circ\text{R}} \qquad R_g = 87.96 \frac{\text{ft-lb}_{(\text{force})}}{\text{lb}_{(\text{mass})}\,^\circ\text{R}}$$

so that

$$\gamma_g = 1.294 \qquad c_{p_p} = 0.5371 \frac{\text{Btu}}{\text{lb}_{(\text{mass})}\,^\circ\text{R}}$$

The quantities μ_g (sec^{-1}) and k_g (Btu/ft °R sec) were entered into the calculation as functions of the gas temperature T_g. The pressure P is in lb (force)/ft^2, density ρ in lb (mass)/ft^3, temperature T in deg R, and u and v in fps.

The integration of the system of differential equations is complicated by the fact, pointed out by Kliegel, that $M < 1$

in the nozzle throat. The denominator of Eq. 15 is $[(M^2 - 1)/u_g]$ where M is the Mach number of the gas. When $dA/dx = 0$, the numerator of the right-hand member of Eq. 15 is negative since the bracketed term remains positive. For the case of constant lag K, to which Kliegel restricted his attention, the determination of the area $A(x)$ and the remaining dependent variables is immediate. In the present application, the area distribution associated with a particular three-dimensional nozzle is chosen and the lags determined. Since the location of the points where numerator and denominator vanish are not determinable in advance, either the initial conditions upstream or the cross-sectional area of the nozzle must be modified to bring these zeros into coincidence. In order to hold the mass flow fixed as a reference point upon which to compare thrusts, the cross-sectional area was corrected. This change in cross-sectional area proved to be quite small, and its effect was further diminished by plotting thrust vs. area ratio.

It is desirable to compare the dependence of thrust upon area ratio in the two-phase system containing lag with the thrust variation in the uniform mixture case in which no lags are assumed to occur. The equation system is integrated for the prescribed area distribution and vacuum thrusts computed

$$F = (1 - \lambda)Wu_g + \lambda Wu_p + PA \qquad [17]$$

Starting from the same initial conditions at a subsonic area ratio of about 4.5, the thrust distribution for the uniform mixture is obtained and values are compared. The total mass flow (0.186 slug/sec) is held fixed. The mixture properties are related to those of the gas phase and the particles by (6)

$$c_{pm} = \lambda c_{pp} + (1 - \lambda)c_{pg} \qquad R_m = (1 - \lambda)R_g$$

Here, λ is the weight fraction of particles 0.391 and the mixture specific heat ratio $\gamma_m = 1.154$.

Fig. 6a shows the comparison of thrusts for particle radii of 2 and 5 μ. The thrust shown has been referenced to the thrust for the uniform mixture and is expressed as a function of area ratio.

It is important to observe that while the thrust loss for the 2-μ particle is of the order of 5%, the thrust curve is very flat except in the immediate vicinity of the throat. This is the case in spite of the fact, shown in Figs. 6b and 6c, that the velocity and temperature lags approach unity rather quickly. (Temperature lag is defined as $L = (T_0 - T_p)/(T_0 - T_g)$.) Thus the thrust loss is not reduced simply by bringing K and L up to 1. Truncation of the nozzle for minimum surface or length involves no greater loss in thrust even though the lags may be significant. As shown in Fig. 6d, there is a decrease in the values of both u_p and u_g below the uniform mixture value. There is a corresponding increase in temperature of both gas and particles over that of the uniform mixture.

Figs. 6a and 7a indicate the effects of various parameters upon the relative thrust. While a particle radius of 2 μ is probably more realistic, the significantly greater thrust loss for a 5-μ particle size is also included. This effect of particle size on thrust should be considered when particles are added to solid propellants (e.g., to promote combustion stability). The effect of nozzle size is indicated by the thrust loss curve for $r_t = 5$ in. in Fig. 7b. Here the effective loss is of the order of 2%.

The effect upon thrust loss of elongating the nozzle is also indicated in Fig. 7a. Here the nozzle with $r_t = 1$ in. has been stretched to twice the original length. This elongation reduces the acceleration of the gas in the region of the throat. Consequently, the lags in velocity and temperature do not develop to the extent indicated for the shorter length nozzle. The thrust loss is correspondingly less, amounting now to 3%.

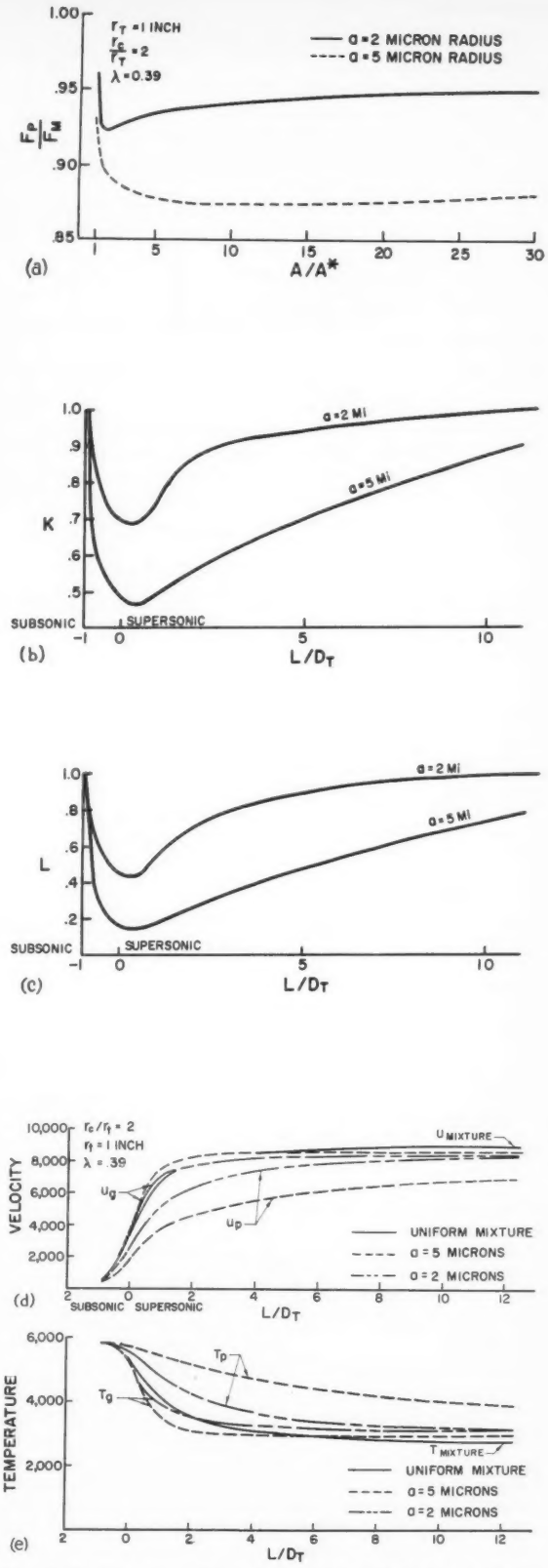

Figs. 6a through e—a Thrust loss due to particle lag; b velocity lag; c temperature lag; d particle and gas velocity; e particle and gas temperature

Conclusions

On the basis of the previous analysis the following conclusions are drawn:

1 For particle sizes likely to be encountered in the normal combustion of solid propellants, particle impingement upon the surface of axisymmetric nozzles truncated for either minimum length or minimum surface area is unlikely.

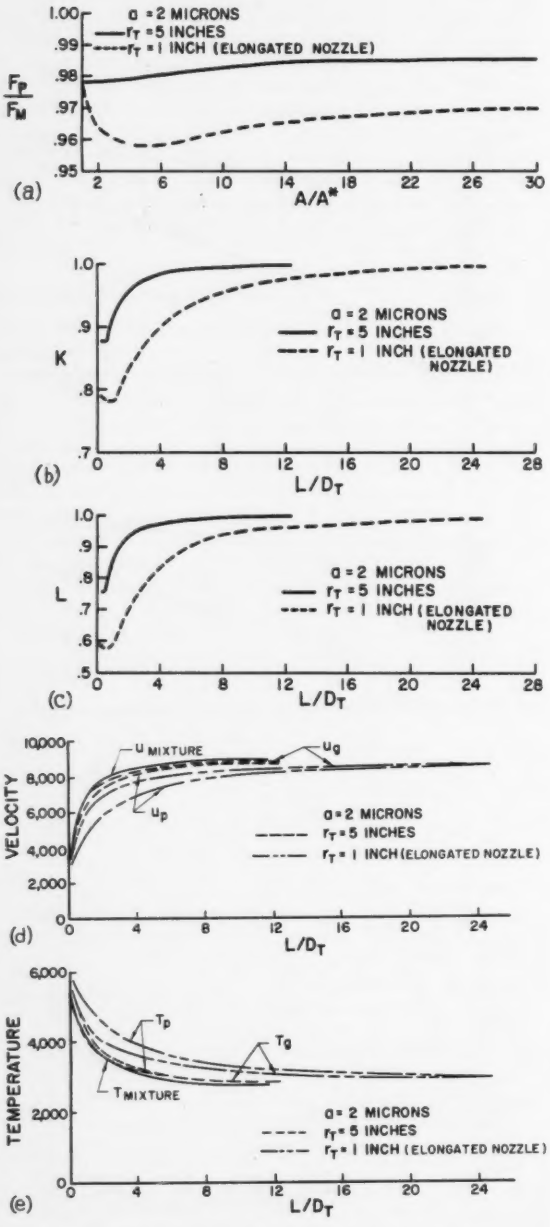

Figs. 7a through e—a Thrust loss due to particle lag; b velocity lag; c temperature lag; d particle and gas velocity; e particle and gas temperature

2 When particles are present in the flow, a thrust loss results due to the lag in velocity and temperature of the particle. This thrust loss increases significantly with particle size.

3 For a typical truncated nozzle of radius ratio 2, thrust losses of more than 5% may be encountered with a concentration of particle mass of the order of 40%.

4 Continuation of the truncated nozzle so as to reduce the exit velocity and temperature lags result in no appreciable recovery of this loss.

5 A more gradual acceleration of the flow in the neighborhood of throat results in a reduction of this thrust loss. Such a reduction, however, is achieved only at a corresponding increase of nozzle size and weight.

Nomenclature

A = nozzle cross-sectional area
C_D = drag coefficient
c_p = specific heat, constant pressure
c_v = specific heat, constant volume
J = Joule's constant
K = velocity lag, V_p/V_g
L = temperature lag, $(T_o - T_p)/(T_o - T_g)$
L/D = nozzle length/throat diameter
M = Mach number
R = gas constant
Re = Reynolds number
T = temperature, °R
V = velocity
W = mass flow
a = particle radius
g_0 = gravitational constant
h = convection coefficient
k = conductivity
P = pressure
r_c = radius of curvature of nozzle wall at throat
r_t = nozzle throat radius
F = thrust
u = axial component of velocity
v = radial component of velocity
y = radial distance
x = axial distance
γ = specific heat ratio
λ = particle concentration
μ = coefficient of viscosity
ρ = density

Subscripts

g = gas
m = mixture
0 = chamber
p = particle
s = solid

References

1 Gilbert, M., Davis, L. and Altman, D., "Velocity Lag of Particles in Linearly Accelerated Combustion Gases," JET PROPULSION, vol. 25, 1955, pp. 25–30.

2 Kliegel, J. R., "One-Dimensional Flow of a Gas Particle System," IAS Preprint no. 60-5, Jan. 25, 1960.

3 Carrier, G. F., "Shock Waves in a Dusty Gas," *Journal of Fluid Mechanics*, vol. 4, 1958, pp. 376 ff.

4 Langmuir, I. and Blodgett, K. B., "A Mathematical Investigation of Water Droplet Trajectories," Air Materiel Command, TR 5418 Feb. 19, 1946.

5 Ahlberg, J. H., Hamilton, S., Migdal, D. and Nilson, E. N., "The Use of Truncated Perfect Nozzles in Optimum Thrust Design," ARS JOURNAL, vol. 31, no. 5, May 1961, pp. 614–620.

6 Barrère, M., Jaumotte, A., de Veubeke, B. F. and Vandenkerckhove J., "Rocket Propulsion," Elsevier, Amsterdam, 1960, pp. 103 ff.

Reactor Core Temperature Measurement

L. H. SHINAULT[1] and
T. F. McGRATH[2]

Rocketdyne, Div. North American Aviation
Canoga Park, Calif.

This paper describes the design and development of a thermocouple suitable for the measurement of temperature in a nuclear reactor core. The thermocouple junction is formed by applying thin films of tungsten and rhenium on a ceramic rod and coating these films with a ceramic insulating film. The thermocouple is capable of operating over a temperature range of 100 to 5000 F and has a response time of 50 to 100 millisec or less. Discussions of manufacturing methods and test results are presented.

THE MEASUREMENT of temperature in the core of a reactor or of gas flowing through the nozzle is of prime importance to those involved in the design and development of nuclear rocket engines. The absolute value and time history of these temperatures have a very great influence on the design of the rocket engine:

1 Size, shape and placement of the fuel elements.
2 Reactor support structure.
3 Nozzle structure.
4 Cooling configuration of the nozzle and reactor shell.
5 Controls for the engine system.

The temperatures of interest are in the range of 4000 to 5000 F.

Our interest originally stemmed from the control problem. Since one of the objectives in the design of a control system for a nuclear rocket engine was to provide for close control of power, both to change the power level upon demand and to maintain constant steady state power, control of reactor temperature was investigated. Early in this investigation it was determined that a satisfactory method for measurement, with the accuracy and desired response characteristics, did not exist. Optical measurements, first considered, were bulky and complex, and the equipment was completely unsatisfactory for the environment; high temperature, high radiation flux and vibration were the principal problem areas.

Continuing investigations revealed that the most probable hope for success of measuring the reactor and nozzle temperatures, with the accuracy and reliability required, was by using thermocouples (1).[3] The experience of others at lower temperatures and lower radiation levels indicated that the thermoelectric properties of thermocouples are only slightly affected by neutron flux (5). Therefore, the problem is one of structural and thermoelectrical integrity at the high temperature level and of a fast response time.

Design Criteria

The design criteria which were established for the thermocouple are shown in Table 1

Table 1 Thermocouple design criteria

operating range	100 to 5000 F
accuracy	±25 F
radiation environment for internal reactor use	
response time to step change	50 to 100 millisec
thermoelectric characteristics	predictable and repeatable
electrical resistance	10 to 50 ohms
structural capabilities	to be able to withstand the forces generated by high velocity gas flow and thermal shock
calibration	must be capable of calibration external to the reactor
capable of operating in a reducing atmosphere and, if possible, in an oxidizing atmosphere	

Radiation Effects

The major effects of nuclear radiation on the materials of interest in a thermocouple assembly are twofold: the instantaneous effects of heating and ionization, and the long term structural damage due to integrated nuclear dosage. In electrical systems, heating and ionization contribute much the same problems: i.e., loss of electrical signal due to the breakdown of the insulation. Long term material damage and changes in crystalline structure will cause resistance changes in the metallic materials (6), or for a thermocouple, changes in the EMF output, since the homogeneity of the materials has changed.

With both metals and ceramics, long term damage effects are slowed or eliminated when these compounds or alloys are exposed to high temperatures, as the material is continuously annealed, and the crystalline structure reinstates itself. However, chemical changes still occur, especially under the potential induced by continuous gamma and neutron bombardment. For example, at elevated temperatures, tungsten in contact with hydrogen will form tungsten hydride. To determine the combined effect of total environment on the postulated thermocouples, an experimental program is necessary. All the effects cannot be determined on an analytical basis. If these effects are repeatable (4), con-

Presented at the ARS 15th Annual Meeting, Washington, D. C., Dec. 5–8, 1960.
[1] Group Leader, Dynamic Controls Components Engineering.
[2] Project Engineer, Nuclear Feed Systems. Member ARS.
[3] Numbers in parentheses indicate References at end of paper.

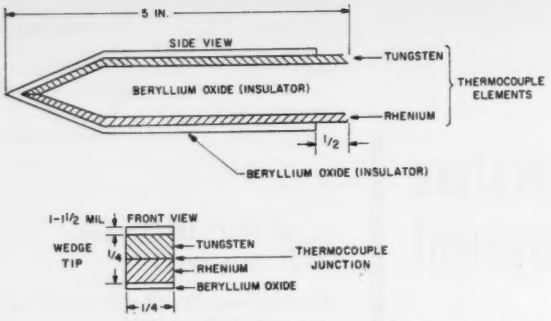

Fig. 1 Thin film thermocouple

tinuous compensation of a thermocouple may yet be possible to establish an electrical signal which is always indicative of the true temperature existing at the tip of the thermocouple.

Neutron collisions in the material allow the material to undergo n, α reaction. Isotopes of the material are formed, and if any of these isotopes are radioactive, beta particles are given off and new materials, impurities, are generated in the base material. Thus, inhomogeneities are formed in the thermocouple and the EMF generated changes with neutron bombardment.

Ceramics, in general, seem to be relatively stable under conditions of nuclear irradiation. However, in the combined radiation and high temperature environment, the electrical insulating value of most ceramic materials is materially reduced. Nevertheless, at this time, ceramics seem to offer the best potential as electrical insulators (3).

Thermocouple Design[4]

The preliminary design of the projected thermocouple was based on two factors:

1 To achieve the desired fast response with a reasonable degree of accuracy.

2 To get this response with the maximum possible mechanical strength and electrical insulating qualities.

An investigation of available high temperature thermocouple materials was conducted. Several promising materials arose, among them, molybdenum, rhenium, tungsten, iridium. Considerable work has been done on the Mo-W couple; and this couple has been used successfully up to 2200 C (7). The EMF of this couple is quite low, approximately 5.6 mv for a 2100 C range. Iridium is attacked by hydrogen at elevated temperatures, a situation which is quite undesirable for nuclear rocket engine use. Lachman (2) reported on rhenium-tungsten couples and displayed an EMF output for this couple of approximately 29 mv over a 4000 F range, much more satisfactory for a thermocouple which must supply input signals to a control system.

Since fast response is desired, the couple should be operated bare, out of a sheath, directly exposed to the gas stream. Initial investigations and tests disclosed that tungsten was not very satisfactory here, since it became very brittle after cycling through high temperatures. The couple goes to pieces under the gas flow and the vibration in the engine. Fig. 1 shows a design which was proposed to eliminate this particular difficulty, and some others which arose in the course of the investigation.

[4] Patent applied for.

To provide the necessary structural strength a central insulating rod is used as a support for the couple metals. A coat of rhenium is plated on one side of this rod and a coat of tungsten is plated on the other. The insulator is machined to a chisel tip and the junction is formed at the contact of the two platings. The whole assembly is to be coated with a thin ceramic film to enable the couple to be calibrated or used in air and to decrease thermionic shorting effects around the couple.

The first step in the development of this couple was to select an adequate central insulating rod. The primary requirements for this insulator were high melting point, stability at high temperatures, high thermal and mechanical shock resistance, and good electrical insulation value (see Table 2). In effect, however, the factors of melting point, conductivity and availability narrowed the choice to three ceramics: boron nitride, thorium oxide and beryllium oxide. Beryllia was included (although the melting point is below 5000 F) because of its excellent shock resistance and low electrical conductivity. Today various hydrides would be examined.

At high temperature there is considerable electrical leakage across the couple between the leads. This is reasonably uniform if good material quality is maintained; that is, control of insulator batches must be as precise as the control of the purity of the couple metals themselves.

Obviously, considerable attention must be paid to the measuring system as well as the couple in design. The couple should have reasonable low resistance in itself, and lead resistance is probably critical. The initial test leads were merely cemented to the plating.

The couple was analyzed from the thermodynamic point of view to estimate some preliminary response characteristics (8). The junction was analyzed as a segment of a cylindrical cross section.

M = resistance ratio, $k/r_m h$
n = position ratio, r/r_m
r_m = radius to point in body, ft
r = radius to point in surface, ft
k = thermal conductivity, Btu ft/hr ft², F
h = film coefficient, Btu/hr ft², F
Y = temperature difference ratio = $(t' - t)/(t' - t_b)$
t' = temperature of surroundings, F
t = temperature at distance r at time θ, F
t_b = original base temperature of solid, F
X = relative time ratio, $\alpha\theta/r_m^2$
α = thermal diffusity, $k/\rho C_p$, ft²/hr
θ = time, hr
C_p = specific heat of solid, Btu/lb, F
ρ = density, lb/ft³

For hydrogen, $h = 1721$ Btu/ft², F, hr.

For example, using approximations for the metal of interest

k = 32 Btu/hr ft², F/ft
Cp = 0.1450 Btu/lb, F
ρ = 555 lb/ft³
α = 0.39 ft²/hr

Table 2 Electrical resistivity and melting points of Beryllium oxide, boron nitride and thorium oxide

Electrical resistivity

Temp, F	BeO, ohm-cm	Temp, F	BN, ohm-cm	Temp, F	ThO_2, ohm-cm
1110	4×10^8	1830	3.1×10^4	1020	2.6×10^7
2010	5×10^6	2730	6×10^2	1470	8.0×10^5
3010	8×10^2			2190	1.5×10^4
melting point	4570 F ± 90		5430		5940 F

For a 63% response

$$Y = 0.37$$

For the cylindrical cross section and a position ratio

$$n = 0 \qquad m = 0 \qquad \text{then } X = 0.26$$

$$M = 0.26 = X\theta/r_m^2 = 0.39\theta/r_m^2$$

θ may be computed as a function of cylinder diameter.

For a value of

$$r_m = 0.0005 \qquad 0.001 \qquad 0.0015 \qquad \text{ft}$$

then

$$\theta = 0.045 \qquad 0.183 \qquad 0.411 \qquad m\text{ sec}$$

The thermal response of the metal film is so fast that it can be ignored as a design factor.

However, the effect of the insulating rod should be considered. For the rod in question, the response at $^1/_{64}$ in. from the tip is approximately 0.3 sec, and at 0.001 in. from the tip about 1.8 millisec. The system response is more than adequate for the purpose.

Fabrication Methods

Three methods for fabricating the thermocouple have been tried. The first method is one of plating from a solution. In this method one side of a boron nitride rod was coated with a solution of tungsten carbonyl in a resin-solvent combination, and the opposite side coated with a solution of rhenium carbonyl in a similar solution. The rod was baked at 250 F for 30 min, then fired in a helium atmosphere furnace at 1700 F and cooled to 300 F before removal. Several thermocouples were fabricated by this method and tested. In each case there was a good thermocouple junction; however, the resistance was too high, 3000 to 8000 ohms, for practical use and varied from thermocouple to thermocouple. A part of this variation was traced to discontinuities and oxidation of the deposited metal film.

The second method of fabrication is one of vacuum vapor deposition. In this method the plating material is boiled under a high vacuum and moderate temperature. The metallic vapor deposits in a thin film on the base material placed nearby. This method has been quite successful for depositing copper and gold films on ceramic, plastic and metallic bases but was not successful for the deposition of tungsten or rhenium on boron nitride or thorium oxide. Good adherence of the metallic particles was not obtained. This method was abandoned.

The third method of fabrication utilizes the principle of flame spraying. In this method a high temperature gas stream is used to carry the plating material in a finely divided form to the base material. Various ways are used to generate the hot gas stream and place the plating material in the stream, namely:

1 The plating material, in rod form, is fed into an electric arc.

2 An explosion process produces bursts of gas and plating material.

3 A plasmatron generates a gas stream with temperatures of 15,000 K and the plating material in powdered form is fed into the top of the gas stream.

The flame spray process produces a firm bond between the plating and the base since the plating impinges on the base material at a high velocity and high temperature. Also, this process can be used to apply ceramic insulating materials over the metallic thermocouple materials.

Test Program

The test program for the thermocouple consisted of calibration, response, accuracy and life tests.

The calibration tests were to be performed in an electric furnace to cover the range of temperatures up to 2400 F; then a solar furnace would be used for the higher temperatures.

The method planned to determine the response time of the thermocouple was the time lag between the temperature rise of a carbon block using an optical pyrometer and the temperature indicated by the thermocouple. The carbon block would be heated in a solar furnace.

The accuracy of the thermocouple was to be determined by using the solar furnace to heat the couple and an optical pyrometer to indicate the true temperature. The accuracy would then be found by comparing the curve of output vs. temperature in the unit obtained with the solar furnace to the curve of output vs. temperature of a bare wire couple of the same materials calibrated in an electric furnace. The repeatability between various determinations of the curve with the same couple and between different couples would also be determined.

The expected life would be evaluated only for a high temperature environment. The high temperature life was to be determined by heating the unit in an oven for varying periods and retesting for accuracy and response to detect any change.

Since the facilities at North American Aviation cannot provide high neutron and gamma flux densities to evaluate the thermocouple in a strong nuclear radiation field, it was planned to perform these tests at a later date at one of the test reactor facilities, assuming complete success at high temperature alone.

The first thermocouples were fabricated by the plating from a solution method, described above, on boron nitride rods. Although the resistance of the units was too high for practical usage, it was possible to perform calibration tests in the electric furnace in a reducing atmosphere. The results of one of these tests is shown in Fig. 2. It is noted that the thermocouple output is quite linear above 1200 F.

The next group of thermocouples were tungsten and rhenium on thorium oxide rods and these were fabricated by the flame spray method and had an electrical resistance of approximately 10 ohms. These thermocouples were also calibrated to 2300 F in a reducing atmosphere in the electric

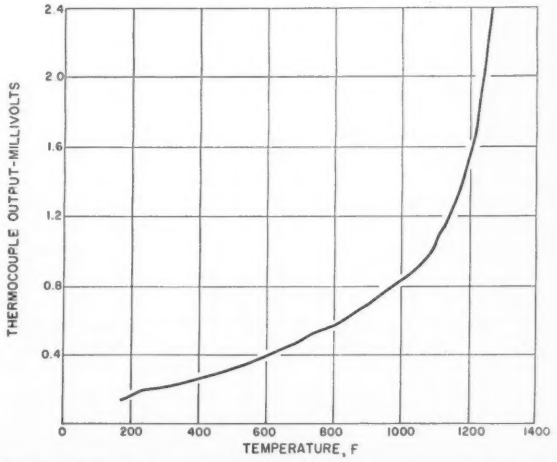

Fig. 2 Calibration of Re–W thermocouple on a boron nitride rod

furnace. The results of these tests are shown in Fig. 3. It is again noted that the thermocouple output is quite linear above 1200 F and that the magnitude of the output compares very favorably with the standard calibration curve of a wire-type tungsten-rhenium thermocouple.

This couple was then mounted in a bracket in the solar furnace so that calibration could be continued to 5000 F in an inert atmosphere. However, when the thermocouple was subjected to a thermal shock by opening the shutter on the furnace 50%, the thorium oxide rod cracked approximately $^3/_4$ inch from the tip. It is apparent from this result, which was duplicated with a second rod, that thorium oxide is unsatisfactory as an insulator support rod.

The next two thermocouples were made with tungsten and rhenium of beryllium oxide rods by the flame method; these units were overcoated with beryllium oxide by the same method. It was expected that the beryllium oxide would have considerably more resistance to thermal shock than the thorium oxide. However, the melting point of beryllium oxide is about 4500 F which limits the operating temperature.

Inasmuch as these thermocouples had the ceramic coating over the metal films, it was decided to take a big step and calibrate them in an oxidizing atmosphere. This was done in the electric furnace. The tests progressed well until a temperature of approximately 900 F was reached, at which time the thermocouple junctions opened. When the units were removed from the furnace, it was found that the tungsten had oxidized and had broken the ceramic coating. The cause for this action is unknown. The output voltage vs. temperature during these tests is shown in Fig. 4. The output is higher than that of the previously tested thermocouples and appears to be more nearly linear in the temperature range below 900 F. A photograph of one of the damaged units is shown in Fig. 5.

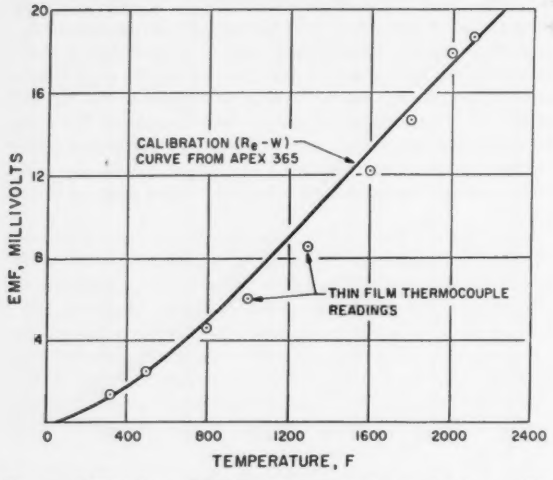

Fig. 3 Calibration of W–Re thermocouple on thorium oxide insulator in an inert atmosphere

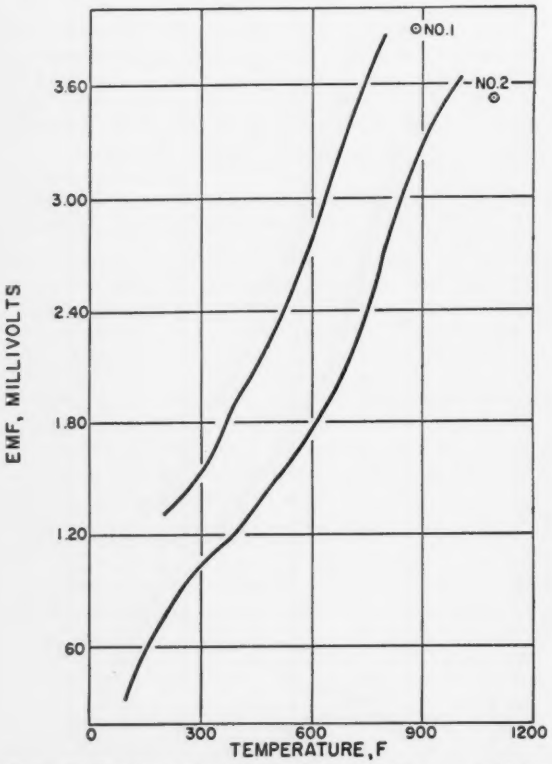

Fig. 4 Calibration of two W–Re thermocouples in an oxidizing atmosphere

Conclusions

It has been increasingly evident during the course of this program that the thermocouple design was a practical one, and that there were excellent possibilities that this type of couple would operate at the elevated temperatures. It is equally evident that a considerable amount of materials investigation is required. Precise control of materials is required to produce usable couples. Our work will continue.

Fig. 5 Oxidation damage to tungsten element

References

1 Ragent, B. and Samuel, A. H., "An Investigation of Temperature Measuring Techniques for Use in High Power Density Nuclear Reactors," Broadview Research and Development, Washington, D. C., Final Rep. (BRD-57-2C1), Feb. 1957.

2 Lachman, J. C., "Calibration of Rhenium-Molybdenum and Rhenium-Tungsten Thermocouples to 4000°F," (APEX-365), General Electric, Cincinnati, Ohio, April 30, 1958.

3 Moody, J. W., "The Effect of Nuclear Radiation on Electrical Insulating Materials," (REIC Memorandum 14), Radiation Effects Information Center, Battelle Memorial Institute, Columbus, Ohio, March 31, 1959.

4 Madsen, P. E., "The Calibration of Thermocouples under Irradiation in B.E.P.O.," A.E.R.E. Rep., Ministry of Supply, Harwell, Berkshire, Jan. 1951.

5 DeLorenzo, J. T., "Thermocouple Design and Test Program for Reactor Projects," (ORNL-26686), Oak Ridge National Lab., Oak Ridge, Tenn., May 6, 1959.

6 Calkins, V. P., "Radiation Damage to Non-Metallic Materials," Aircraft Nuclear Propulsion Dept., Atomic Products Div., General Electric, Aug. 1954.

7 Rudnitski, A. A., and Tyurin, I. I., translated by M. de O. Tollemache, "The Investigation and Choice of Alloys for High-Temperature Thermocouples," Atomic Energy Research Establishment, Harwell, Berkshire, 1958.

8 McAdams, W. H., *Heat Transmission*, McGraw-Hill Book Co., Inc., N.Y., 1942.

Meteoroids vs. Space Vehicles

R. L. BJORK[1]

The Rand Corp.
Santa Monica, Calif.

In order to assess the effects of meteoroids on vehicles in space, this paper summarizes current knowledge of the flux rate, mass, velocity and density of meteoroids, as well as that relative to the effects of an individual meteoroid impact. For aluminum and steel, the penetration rate as a function of armor thickness is derived. Weightwise, aluminum is found to give better protection than steel. The probability of meteoroid puncture as a function of vehicle area, exposure time and armor thickness is discussed, and the results are presented in analytical and graphical form. From them, one may derive the armor weight required to protect the vehicle to any confidence level. Two examples are given exhibiting typical armor weights and the masses of the important meteoroids. In cases of uncertainty, the conservative estimate is always chosen so that the armor weights presented may be regarded as upper limits. Areas of research are pointed out wherein more knowledge might lead to weight reduction in the future.

IT IS quite natural that people should be intensely interested in meteoroids now that the first rudimentary space vehicles have been launched and their more sophisticated successors are being designed. The object of this paper is to discuss the effects that meteoroids are expected to have on such vehicles. To this end, current knowledge of the meteoroid's flux rate, mass, velocity and density is summarized, as well as that regarding the impact effects of an individual meteoroid.

It will be shown that the meteoroid hazard will probably exert a definite influence on the design of certain space structures, but that the necessary protective measures are not extreme, imposing a weight penalty which in the cases investigated is only a fraction of the vehicle weight without the protective measures. However, the magnitude of the weight penalty is such that it would be beneficial to reduce it, and the analysis exhibits areas in which research toward this end appears most fruitful.

The problem is important to the design of a space power station, largely because such a station requires a large-area radiator. The station must rid itself of the waste heat associated with producing its useful electrical power, or else suffer the consequence of its temperature increasing steadily until intolerable levels are reached. If the electrical power is used in the station itself, the bulk of it will eventually appear as heat, which must also be disposed of. Since the vacuum of space is nearly a perfect insulator against heat transfer by conduction and convection, a radiator is required, which is a radiator in the true sense of the word.

Preliminary designs have indicated that the radiator is the component most vulnerable to meteoroids in the sense that it requires more additional weight to properly armor it than any other portion of the vehicle. For the higher power systems, this will probably constitute the predominant weight problem. Coombs(14)[2] has estimated that a 300 kw turbogenerator station, powered by a nuclear reactor, suffers about a

Presented at the ARS Semi-Annual Meeting, Los Angeles, Calif., May 9–12, 1960.

[1] Group Leader, Theoretical Analysis Group, Aero-Astronautics Dept.

[2] Numbers in parentheses indicate References at end of paper.

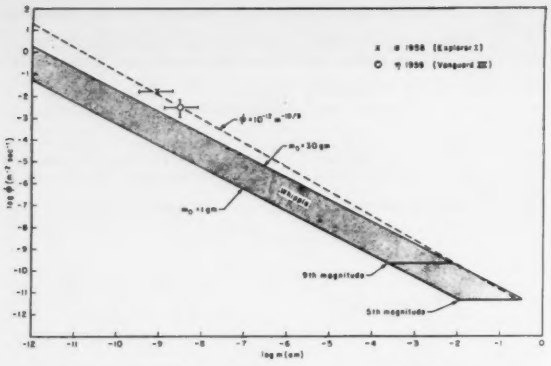

Fig. 1 Meteoroid flux vs. mass near Earth

40% weight penalty, and Zipkin and Schnetzer (1) estimate that a 1000 kw station, similarly powered, will suffer about a 60% weight penalty. Although these are gross estimates, and use different criteria for the acceptable damage level and armoring mechanism, they illustrate well the importance of an accurate assessment of the meteoroid hazard in the design of such stations.

Meteoroid Flux

Observations on the meteoroid flux in which Earth is bathed have been accumulated by photographic and radio-echo techniques from ground based stations and by various measuring devices carried in rockets and satellites. These measurements show that there are many more small meteoroids than large ones, but that a complete picture of the meteoroid flux as a function of mass has not yet been obtained. The results give scattered information throughout the mass spectrum with large gaps in between. The observational data is collected in Fig. 1, and it may be seen that the data can be fit by a simple curve which may be regarded as the best estimate available of the meteoroid flux as a function of mass. The total flux of all meteors having mass greater than m is ϕ. One important inference that may be drawn from Fig. 1 is the need for more measurements of the flux to fill in the large gaps.

Photographic and Radar Measurements

Thousands of photographs of meteors have been taken in the last two decades (2–4). Prominent among the work in this field is the Harvard Astronomical Observatory program, which has collected about 6000 pairs of meteor photographs taken simultaneously from two stations (15). These observations lead to the conclusion that photographic meteors have an extraordinarily low density, about 0.05 gm/cm^3. The photographic technique can record meteors down to about the fifth magnitude.

Thousands of observations have also been taken by the radio-echo technique (4–8) which can record meteors down to about the ninth or tenth magnitude. The magnitude of such small meteors, which cannot be detected by optical devices, is assigned by analogy. As commonly used, magnitude is really a measure of mass, according to the formula

$$M = 2.5 \log_{10} (m_0/m) \qquad [1]$$

where

M = magnitude
m_0 = mass of a zero-magnitude meteor
m = mass of the meteor under consideration

The direct data obtained by these techniques is meteor flux as a function of magnitude, and it is a major problem to translate magnitude into mass. The translation to be used here is due to Whipple, who has calculated that m_0 lies between 1 and 30 gm, with 25 gm the preferred value.

Noting that among the radio-echo and photographic data, the flux varied inversely as the mass, Whipple extrapolated this data to very small masses even before the satellite data was taken (9). His extrapolation is shown as the shaded region in Fig. 1. The width of the shaded region is due to the range in possible values of m_0, his preferred value lying near the top of the range. It is remarkable that his extrapolation falls so close to the satellite points subsequently taken.

Both the photographic and radio-echo measurements agree on the velocity range of meteors, namely 11 to 72 km/sec, and the physical interpretation of both limits is interesting (9). The lower limit is the escape velocity of a particle from Earth, and is just the velocity a particle would acquire if it started from rest with respect to Earth and then fell several Earth radii to the sensible atmosphere. The upper limit is the largest velocity a particle could have with respect to Earth if the particle were originally in a closed orbit about the sun. A meteor having a larger velocity than this must have originated outside our solar system, a fact which has caused careful scrutiny of the upper velocity limit. Apparently all meteors do originate within our solar system. The average velocity is about 30 km/sec for the photographic and radar meteors.

Rocket and Satellite Measurements

The photographic and radio-echo techniques are able to survey vast areas of the sky continuously, and so are able to measure the very small flux of particles large enough to produce phenomena detectable on the ground. The devices so far carried in a rocket or satellite vehicle, on the other hand, are able to detect only those meteoroids impinging on a small detector, whose area is limited to the order of a fraction of a square meter, and the operating times of these detectors is on the order of a few or tens of days. Only very small meteroids are present in sufficient quantities to strike these detectors during the operating period, and the detectors must be made very sensitive to record any hits at all. Thus, at the present time, rocket and satellite experiments are inherently limited to measuring the impacts of meteoroids having masses of about 10^{-8} gm or less. This limitation is responsible for the gap in information between the radio-echo and satellite data.

At the present, two sets of satellite data overshadow the rest in statistical significance. These are the Explorer I (alpha 1958) (10,11) and Vanguard III (eta 1959) data. In both cases the number of hits recorded in a 24-hr period varied by factors on the order of 10. This variation makes it apparent that information obtained from experiments operating for short time periods is liable to be wrong by a factor of 10 or so in predicting the average flux over a period of days, and that is exactly what one must do to assess the hazard to a space vehicle. For this reason only the two satellite experiments cited will be considered here.

The Explorer I point is based on 153 clear impacts recorded over a 12-day period, and the Vanguard III point on a preliminary reduction of data taken over a 50-day period in which about 1500 impacts were registered.

The cited points are plotted in Fig. 1. As shown there, the photographic and radio data, as well as the satellite points, may be fitted by the curve

$$\phi = 10^{-12}\, m^{-10/9} \qquad [2]$$

where ϕ is given in particles/m² sec and m is given in gm. This curve is more conservative than Whipple's extrapolation, giving a larger value of the flux for each value of mass.

It should be noted that the satellite data was taken in the vicinity of Earth, so that the satellite is shielded by Earth from the meteoroid flux in one direction. For this reason it is expected that as one goes a few Earth radii into space, the flux should about double. This is also true of the radio and photographic meteoroids.

Effects of an Individual Meteoroid

To date it has not been possible to accelerate particles of well-defined mass and velocity to meteoric velocities in the laboratory. Hence, there is no direct experimental evidence relative to the effects of such high velocity particles on a target. One is forced to use estimates based purely on theory.

The estimate used in this paper is due to the author (12). The craters produced in thick steel and aluminum targets by projectiles of the same material at normal incidence were calculated for impact velocities of 5.5, 20 and 72 km/sec. It was found that the forces generated in the impact process far exceeded the strength of these materials, so that the strength was neglected in the calculation. Such a model may be expected to improve with increasing impact velocity. The calculations agreed in both size and shape with experimental craters produced in aluminum at 6.3 km/sec and iron at 6.8 km/sec.

The results are summarized by the equations

Al on Al

$$p = 1.09\ (mv)^{1/3}$$

Fe on Fe

$$p = 0.606\ (mv)^{1/3} \qquad \ldots\ldots [3]$$

where

p = penetration depth in cm
m = projectile mass in gm
v = impact velocity in km/sec

Both the calculated and experimental craters are hemispherical with radius p. In the range of pressures developed in the impact, iron and steel behave identically.

The calculations were made for thick targets, but enough information was obtained to deduce that if a projectile penetrates a depth p in a thick target, it will just penetrate a sheet of the same target material which is 1.5 p thick.

The impact data so far taken in laboratories indicate that among particles of the same mass and velocity, the one of greatest density gives the largest penetration. The most definitive set of experiments has been performed by Summers and Charters (13). They performed a series of tests at 7000 fps (2.13 km/sec) keeping the projectile mass constant and using the same target material. Using spherical projectiles of various metals, they covered the density range of 1.5 to 17.2 gm/cm³. For each of the target materials used, they found their results could be correlated with the density ratio between projectile and target material

Copper targets

$$p \sim (\rho_p/\rho_t)^{0.6}$$

Lead targets

$$p \sim (\rho_p/\rho_t)^{0.3} \qquad \ldots\ldots [4]$$

where ρ_p and ρ_t are the projectile and target densities, respectively.

It seems too optimistic to expect that the same relation would hold at velocities several times higher than that used in obtaining the empirical fit, or at densities many times lower. But it does seem plausible to expect that the general trend would be the same, so that overestimating the projectile density results in overestimating the penetration. On this basis, it is conservative to use the results of Eq. 3 directly to predict the penetration. These equations will almost certainly overestimate the meteoroid damage considerably in the photographic meteor range, where there is a good indication that the meteors have a low density. On the other hand, the meteors of such great mass are very infrequent, and it will be seen that for all practical purposes, their presence may be neglected in designing something like a radiator required to operate in space for a year with a 90% probability of suffering no damage at all from meteroids.

It is reasonable to expect that the smaller meteoroids will not have the lacy, porous structure needed to give a specific gravity of 0.05, but that their density will increase as one goes down the mass scale, eventually approaching the specific gravity of stone, the basic component, as very small sizes are reached. To the knowledge of the author, there is no evidence to indicate what the functional dependence of density upon mass will be. For this reason, the conservative Eq. 3 will be used here, and the possibility of smaller meteoroids having the same low density as the photographic ones will be regarded as a safety factor for the present, and a possible bonus to be realized in the future when more is learned of the small particle structure.

The specific gravities of stone, aluminum, and steel are 2.8, 2.7 and 7.9, respectively. Thus, for stony density particles, Eq. 3 may be expected to give a good approximation for meteoroids vs. aluminum, but still to overestimate slightly the effects of meteoroids vs. steel.

Penetrating Flux

Combining Eqs. 2 and 3, one obtains for the penetrating flux

$$\psi = 10^{-12} t^{-10/3} K^{10/3} v^{10/3} \qquad [5]$$

where ψ is the number of penetrations per m² per sec of a target t cm thick, if the meteoroid velocity is v km/sec

Aluminum targets

$$K = 1.5(1.09) = 1.64 \quad K^{10/3} = 5.20$$

Steel targets

$$K = 1.5(0.606) = 0.908 \quad K^{10/3} = 0.725$$

The estimate of ψ as a function of t for aluminum and steel is summarized in Table 1. To compute the visual magnitude, an m_0 of 25 gm was used. Column 3 gives Whipple's estimate of the average meteoroid velocity as a function of the mass. Columns 4 and 5 are calculated from Eq. 3, including the factor of 1.5 to account for the fact that thin targets are considered. Column 6 is calculated from Eq. 5. Columns 4, 5 and 6 are presented in Fig. 2.

Examples of Expected Meteoroid Effects

To illustrate the expected meteoroid damage and find the important range of meteoroid masses, two simple examples will be discussed: 1 a radiator; 2 a space vehicle about the size of a large airplane fuselage. Only the simplest design will be considered, namely, armoring the radiator tubes with aluminum so that the total armor and tube wall thickness is t, and providing the large vehicle with an aluminum skin of thickness t.

One may expect the meteoroid punctures to follow a Poisson distribution, so that

$$P(n) = [(\psi A\tau)^n \exp(-\psi A\tau)]/n! \qquad [6]$$

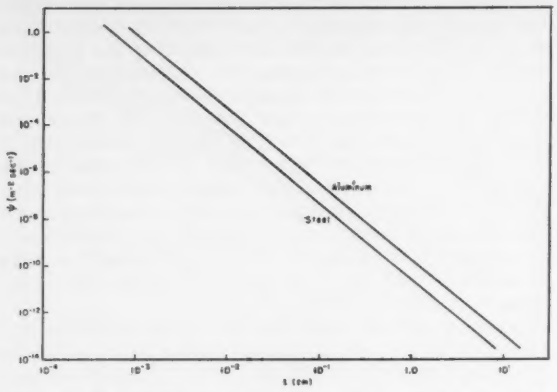

Fig. 2 Penetrating meteoroid flux near Earth vs. skin thickness

where $P(n)$ is the probability of n punctures of a sensitive area A exposed for a time period τ.

The general formula for skin thickness as a function of $P(0)$ and the other parameters may be obtained by combining Eqs. 5 and 6. The result is

$$t = \frac{2.5 \times 10^{-4} K v^{1/3} (A\tau)^{3/10}}{[-\ln P(0)]^{3/10}} \qquad [7]$$

The meteoroids which will puncture a skin of this thickness, from Eq. 3 have masses greater than

$$m = v^{-1}(t/K)^3 \qquad [8]$$

Other parameters being equal, it is seen that the required armor thickness is proportional to K. Since the mass per unit area is given by ρt, one sees that weightwise aluminum is a better armor than steel because $(\rho K)_{Fe}/(\rho K)_{Al} = 1.61$.

Example 1

Consider a radiator of area 40 m², which is exposed to the meteoroid flux for a period τ of about 1 year, or $\pi \times 10^7$ sec. Only the radiator tubes constitute the sensitive area, and these comprise about one-tenth of the total, so that $A = 4$ m². Such a radiator is about the size estimated by Coombs (14) for a 30 kw electrical turbogenerator, powered by a nuclear reactor. It is reasonable to demand that the tubes have a high probability remaining unpunctured, or that $P(0)$ is near unity. For $P(0) = 0.90$, one finds, using the forementioned figures

$A = 4$ m²
$\tau = \pi \times 10^7$ sec
$P(0) = 0.90$
$t = 0.66$ cm
$m = 0.0024$ gm

Example 2

As an approximation to the space vehicle, let us consider a cylindrical body 20 m long and 3 m in diameter (65.6 ft × 9.84 ft), having surface area 203 m². In this case, all of the surface area will be considered sensitive, and the operating period will again be $\pi \times 10^7$ sec. In this example, the crew will be put to work, as the vehicle will be designed with the expectation that a few punctures will occur. The value

Table 1 Penetrating flux for various thickness of aluminum and steel

Visual magnitude	Mass, gm	Velocity, km/sec	Aluminum thickness, cm	Steel thickness, cm	Penetrating flux, penetration/m² sec
0	25.0	28.0	15.5	8.06	2.80×10^{-14}
1	9.95	28.0	10.7	5.93	7.79×10^{-14}
2	3.96	28.0	7.85	4.36	2.17×10^{-13}
3	1.58	28.0	5.78	3.21	6.02×10^{-13}
4	0.628	28.0	4.25	2.36	1.68×10^{-12}
5	0.250	28.0	3.13	1.74	4.67×10^{-12}
6	9.95×10^{-2}	28.0	2.30	1.28	1.30×10^{-11}
7	3.96×10^{-2}	28.0	1.69	0.940	3.62×10^{-11}
8	1.58×10^{-2}	27.0	1.23	0.684	1.00×10^{-10}
9	6.28×10^{-3}	26.0	0.894	0.496	2.80×10^{-10}
10	2.50×10^{-3}	25.0	0.649	0.360	7.78×10^{-10}
11	9.95×10^{-4}	24.0	0.471	0.261	2.17×10^{-9}
12	3.96×10^{-4}	23.0	0.341	0.190	6.03×10^{-9}
13	1.58×10^{-4}	22.0	0.248	0.138	1.67×10^{-8}
14	6.28×10^{-5}	21.0	0.179	9.96×10^{-2}	4.67×10^{-8}
15	2.50×10^{-5}	20.0	0.130	7.21×10^{-2}	1.30×10^{-7}
16	9.95×10^{-6}	19.0	9.38×10^{-2}	5.21×10^{-2}	3.61×10^{-7}
17	3.96×10^{-6}	18.0	6.78×10^{-2}	3.76×10^{-2}	1.01×10^{-6}
18	1.58×10^{-6}	17.0	4.90×10^{-2}	2.72×10^{-2}	2.79×10^{-6}
19	6.28×10^{-7}	16.0	3.53×10^{-2}	1.96×10^{-2}	7.78×10^{-6}
20	2.50×10^{-7}	15.0	2.54×10^{-2}	1.41×10^{-2}	2.17×10^{-5}
21	9.95×10^{-8}	15.0	1.87×10^{-2}	1.04×10^{-2}	6.03×10^{-5}
22	3.96×10^{-8}	15.0	1.37×10^{-2}	7.63×10^{-3}	1.68×10^{-4}
23	1.58×10^{-8}	15.0	1.01×10^{-2}	5.62×10^{-3}	4.66×10^{-4}
24	6.28×10^{-9}	15.0	7.44×10^{-3}	4.13×10^{-3}	1.30×10^{-3}
25	2.50×10^{-9}	15.0	5.47×10^{-3}	3.04×10^{-3}	3.61×10^{-3}
26	9.95×10^{-10}	15.0	4.03×10^{-3}	2.24×10^{-3}	1.01×10^{-2}
27	3.96×10^{-10}	15.0	2.96×10^{-3}	1.64×10^{-3}	2.80×10^{-2}
28	1.58×10^{-10}	15.0	2.18×10^{-3}	1.21×10^{-3}	7.77×10^{-2}
29	6.28×10^{-11}	15.0	1.60×10^{-3}	8.90×10^{-4}	0.217
30	2.50×10^{-11}	15.0	1.18×10^{-3}	6.55×10^{-4}	0.603
31	9.95×10^{-12}	15.0	8.67×10^{-4}	4.82×10^{-4}	1.68

$\psi A\tau = 1$ will be chosen, so that the number of punctures and their associated probabilities will be

n	$P(n)$
0	0.3679
1	0.3679
2	0.1840
3	0.0613
4	0.0153
	0.9964

There is still some chance that no punctures will occur, but there is an equal likelihood that one will occur. Higher numbers of punctures become rapidly less probable. In this case, the values are

A	$= 203\ m^2$
τ	$= \pi \times 10^7$ sec
$P(0)$	$= 0.3679$
t	$= 1.1$ cm
m	$= 0.011$ gm
skin weight	$= 6.6$ tons

Using the same values of area and exposure time, but demanding that $P(0)$ be 0.90 increases the skin thickness to 2.2 cm and the skin weight to 13 tons. Thus it costs about 6.4 tons to increase $P(0)$ from 0.3679 to 0.90 for this vehicle.

Fig. 3 shows the skin thickness as a function of $A\tau$ for several values of $P(0)$.

Conclusions

The preliminary designs of space power station radiators, as well as the simple examples given herein, indicate that the weight penalty imposed by present best estimates of the meteoroid hazard is large enough to warrant considerable research aimed towards its reduction. The estimates given in this paper have purposely been kept conservative where uncertainties were felt to exist, and in this sense represent the design criteria forced upon the present-day designer. The analysis focuses attention on several promising areas where research might hopefully lead to lighter weight designs.

Investigating Meteor Mass as a Function of Magnitude

If m_0 the mass of a zero-magnitude meteor were found to fall at the lower limit of Whipple's estimate, the armor thicknesses would be reduced by about a factor of $(25)^{0.3}$ or 2.6. This assumes, of course, that the masses for all magnitudes are correspondingly lower.

The examples show that the important meteoroids have masses on the order of 10^{-2} to 10^{-3} gm, falling in the magnitude range of 8 to 11. These magnitudes lie toward the upper limit of radio-echo observations. The most satisfactory experiment would be to measure the masses as directly as possible through this technique. Next best would be better determinations of the mass through photographic observations and extrapolating in the present manner.

Investigating Meteoroid Density and Its Effect on Penetration

If the density of important meteoroids were found to be 0.05 gm/cm^3, and the density correction in the penetration law to be $(\rho_p/\rho_t)^{0.3}$, the armor thicknesses would be reduced by factors of 3.3 and 4.6 for aluminum and steel, respectively. If the penetration law varied as $(\rho_p/\rho_t)^{0.6}$, the reductions would be by factors of 11 and 21, respectively.

Experiments to determine the density are likely to be restricted to the radio-echo technique, as there seems to be no way to extrapolate from other observations.

It does not seem likely that projectiles of meteoric velocity will be obtained in the laboratory for the next several years, so that investigations of the density effects on penetration must be of a theoretical nature.

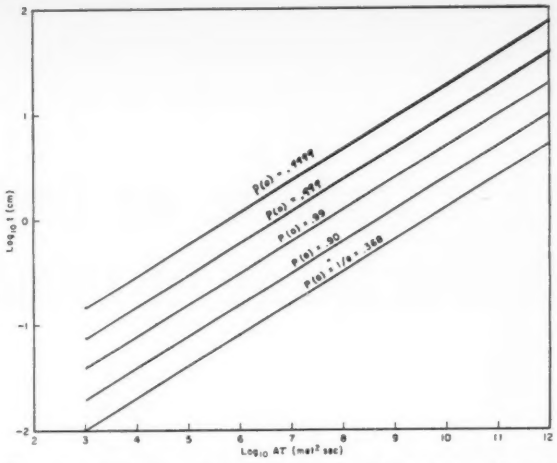

Fig. 3 Aluminum skin thickness required for meteoroid protection

Formulating More Sophisticated Armor Designs

The examples used only the simplest type of armor. Undoubtedly improvements can be made by using such devices as spaced thin sheets, laminated armor, and finding the optimum armor materials. To accomplish this, however, much more basic knowledge of the impact process must be obtained.

The foregoing research topics furnish only partial solutions to the problem, and the best experiment of all is undoubtedly the direct measurement of meteoroid effects by space vehicles. Present satellites have limitations in this respect, as outlined in the text. It is hard to overemphasize the payoff if these could somehow be circumvented.

The possible bonuses which might be realized from the first two investigations are so large that their realization would render the meteoroid hazard almost negligible. If these bonuses are not to be realized, future space vehicles will be heavy, but not impossibly so.

References

1 Zipkin, M. A. and Schnetzer, E., "Design Compromises in Space Power Systems," Tenth International Astronautical Congress, London, 1959. (Proceedings in publication.)

2 Whipple, F. L., "Photographic Meteor Orbits and Their Distribution in Space," *Astron. J.*, vol. 59, July 1954, p. 201.

3 Jacchia, L. G., "The Physical Theory of Meteors. VIII. Fragmentation as Cause of the Faint-Meteor Anomaly," *Astrophysical J.*, vol. 121, March 1955, p. 521.

4 Lovell, A. C. B., *Meteor Astronomy*, Oxford at the Clarendon Press, London, 1954.

5 McKinley, D. W. R., "Meteor Velocities Determined by Radio Observations," *Astron. J.*, vol. 113, March 1951, p. 225.

6 Hawkins, G. S., "A Radio Echo Survey of Sporadic Meteor Radiants," *Monthly Notices of the Royal Astronomical Society*, vol. 116, no. 1, 1956, p. 92.

7 Hawkins, G. S., "Variation in the Occurrence Rate of Meteors," *Astron. J.*, vol. 61, Nov. 1956, p. 386.

8 Manning, L. A. and Eshleman, V. R., "Meteors in the Ionosphere," *Proceedings of the I.R.E.*, vol. 47, 1959, p. 186.

9 Whipple, F. L., "The Meteoric Risk to Space Vehicles," *Vistas in Astronautics*, Pergamon Press, Los Angeles, Calif., 1958.

10 Dubin, M., "*Meteoric Dust Measured from Explorer I*, Air Force Cambridge Research Center, Cambridge, Mass. (undated)

11 Manring, E. R., "Micrometeorite Measurements from 1958 Alpha and Gamma Satellites," *Planetary and Space Science*, vol. 1, no. 1, 1959, p. 27.

12 Bjork, R. L., "Effects of a Meteoroid Impact on Steel and Aluminum," The Rand Corp. Paper P-1662, 1958; presented at the Tenth International Astronautical Congress, London, 1959, Springer-Verlag, Vienna.

13 Summers, J. L. and A. C. Charters, "High-Speed Impact of Metal Projectiles in Targets of Various Materials," *Proceedings of the Third Symposium on Hypervelocity Impact*, edited by F. Genevese, Armour Research Foundation of Illinois Institute of Technology, Chicago, Ill., 1959.

14 Coombs, M. G., personal communication; *also* Coombs, M. G., "A Design Procedure for a Minimum Weight Mercury Radiative Condenser" (unpublished paper), Atomics International, Canoga Park, Calif., 1959.

15 Whipple, F. L., personal communication.

Capabilities and Limitations of Reaction Spheres for Attitude Control

RALPH D. ORMSBY[1] and MAHLON C. SMITH[2]

The Bendix Corp.
Ann Arbor, Mich.

Some of the important characteristics of an electrically suspended reaction sphere for space vehicle attitude control are discussed, and data presented on the capabilities and limitations of the reaction sphere concept. Some of the factors which must be considered in determining the relative value of the reaction sphere are discussed with relation to a representative system application. Data which have resulted from experimental and analytical investigations are presented.

ATTITUDE control systems for space vehicles usually rely upon the principle of reaction to provide the control torques necessary to rotate the satellite axes to a preferred orientation. These control reaction torques are generated through the expulsion of gas to provide a thrust vector, or through the torque applied to a member free to rotate relative to the satellite vehicle.

An implementation of the latter is three single-axis reaction wheels mounted in the satellite so that their momentum vectors lie on orthogonal axes. By properly exciting each reaction wheel, a torque of the desired magnitude can be generated around any arbitrary satellite axis containing the satellite center of gravity.

A reaction wheel is essentially an electrical motor designed with a rotor having a large moment of inertia and an efficient torque producing capability over the entire operating speed range. The reaction wheel is a more efficient means for generating torque than reaction jets when the torque requirements are for a large number of cyclic torques (1).[3] The reason for the greater efficiency of the reaction wheels under these conditions is that energy for the reaction wheel can be obtained from solar energy. The reaction wheel also has an upper bound on the angular momentum which can be stored; hence, there is the limitation to cyclic disturbances. Reaction wheels are also efficient for controlling random disturbances.

The conventional reaction wheels described have the following problem areas: bearings, three wheels required (one for each axis), and gyroscopic cross coupling between axes.

The reaction wheel bearings must either be within a gas filled, sealed enclosure or they must be capable of operating in a vacuum environment. In either case, the bearings must be rugged to withstand the launch vibrations. Enclosing the reaction wheels in a pressure container will result in windage losses in addition to the bearing friction losses, both of which must be supplied by stator excitation.

The reaction sphere eliminates the forementioned problem areas for reaction wheels, but retains the reaction wheel advantages (2). A single reaction sphere can be designed with three induction motor stator winding in orthogonal planes to provide attitude control of the spacecraft around any axis.

Several schemes have been proposed for maintaining the reaction sphere position at the center of the torquing coils, and each scheme offers certain advantages and has particular disadvantages.

Factors which must be considered in the design of the positioning system include: reliability, efficiency and capability. In order to evaluate a particular positioning design, it is necessary to know the requirements on the reaction sphere control unit imposed by the application. Some of the design requirements which are important in determining the positioning concept are: spacecraft lifetime, torque requirements, angular momentum storage requirements and spacecraft normal accelerations. Several groups in the country have considered this problem, and have established answers which rather generally agree but which are biased by the individual experience of the evaluators. Three of the positioning concepts which have been considered are: gas bearing, magnetic field suspension and electric field suspension.

The gas bearing is perhaps the simplest positioning concept. An example of the work being done on gas bearings may be found in Jet Propulsion Laboratory reports such as (3).

Magnetic suspension has been proposed (4) and a theoretical paper has been published by Golay (5) on electrostatic suspension for gyroscopes.

Other groups have also investigated gas bearing and magnetic field positioning for the reaction sphere (6), and electric field rotor positioning techniques for the electrostatic gyro.

Electric field suspension is the only concept which does not provide drag torques on the spinning rotor from the positioning forces. Furthermore, large spheres can be suspended under moderate acceleration environments using energy which can be obtained from the spacecraft power supply. The major limitation of the electric field suspension concept is the maximum positioning force which can be generated. This bound is determined by the limit on the voltage gradient which can be maintained without voltage breakdown and the electrode area (2). Thus, the design of the reaction sphere will be determined by the system requirements.

Presented at the ARS 15th Annual Meeting, Washington, D. C., Dec. 5–8, 1960.

[1] Manager, Technical Planning Dept., Bendix Systems Div.

[2] Senior Engineer, Electronic Engineering Dept., Bendix Systems Division.

[3] Numbers in parentheses indicate References at end of paper.

Application

To illustrate the application of the electrically suspended free reaction sphere, a very simple yet practical control requirement will be considered.

When solar cells are used to provide electrical energy to the instruments in the satellite, maximum efficiency is obtained when the cells are oriented so that they always obtain the maximum sunlight.

For simplicity in the discussion, the cells are assumed to be rigidly attached to one half of a cylindrical satellite with the cylindrical axis of the satellite always aligned with Earth's radius vector. The satellite is assumed to be in a 24 hr equatorial orbit.

The attitude control system is required to rotate the satellite around the cylindrical axis to maintain the maximum possible incident sunlight on the solar cells. The importance of this problem in geometry is only really significant at 12 noon and 12 midnight. If the orbital plane were also the plane of the ecliptic, the satellite azimuth rotation rate would be zero, except at 12 noon and 12 midnight, where a positive and negative rate impulse would take place to keep the cells optimumly oriented. However, in a practical case, very little efficiency is lost if the satellite requires 20 min to rotate through 180 deg.

Assuming a triangular velocity increase and decrease over the 20 min period and a satellite moment of inertia of 1000 slug ft², a maximum torque of 0.01 ft lb and a peak angular momentum of 5.5 slug ft² per sec would be required from a free reaction sphere. This requirement can be met with a 5-in. diam, 1-in. thick wall, 410 stainless steel rotor capable of achieving a maximum speed of 10,000 rpm. From existing data, it is estimated that this free reaction sphere will require 5 w for suspension, 15 w peak and 0.27 w average per 24 hr cycle for the torque motor.

Fig. 1 is a chart of the rotor velocity and satellite velocity during the reorientation period. This example illustrates certain quantitative relationships which exist between rotor size, speed, torque level and power requirements for a particular satellite size and maneuvering requirement.

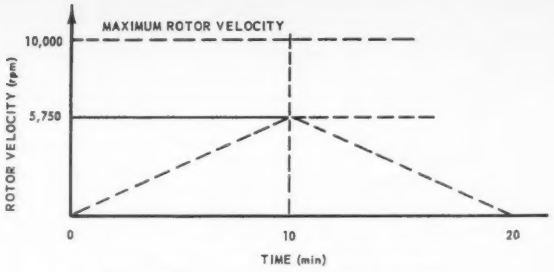

Fig. 1 Reorientation velocity schedule

Analysis

Suspension System

The three orthogonal motor stators cover the sphere as illustrated in Fig. 2; thus, there are eight areas available to locate the suspension electrodes. These eight areas quite naturally provide for four pairs of electrodes which can be paired to obtain four independent suspension forces. Four is the minimum number of independent suspension forces which can stably position the rotor.

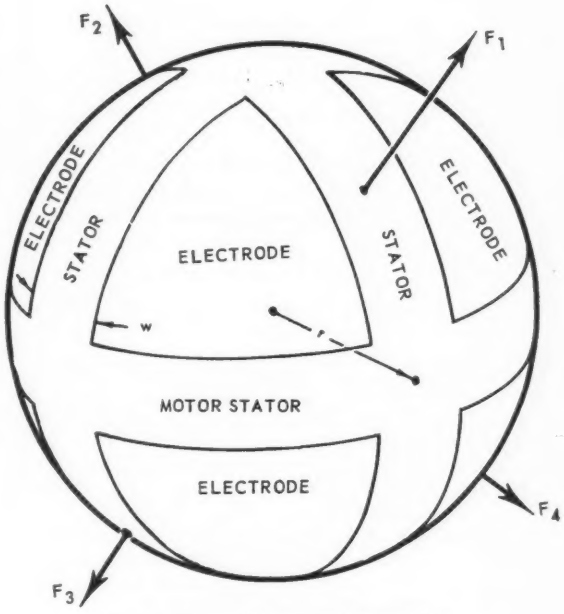

Fig. 2 Four-point suspension geometry

The electrodes will cover the sphere surface except for the areas needed for the motor stators. The area required for the motor stators is significant, and the effect of removing this area from the electrodes is shown in Fig. 3. The definition of w_1 is given in the figure, and the function $f(w_1)$ is the ratio of the lift force on the sphere with the stator area subtracted from the electrodes to the lift force that would exist if the electrodes covered the whole sphere. [$f(w_1)$ is an approximation.]

The total lift on the sphere can be obtained by multiplying the force shown in Fig. 4 by the factor $f(w_1)$ of Fig. 3. This is the force due to one hemisphere of electrodes.

It is noted that for checkout on the launch pad, in the gravitational field of Earth, it is desirable to have both hemispheres of electrodes operating. If both are operating at full voltage, it can be shown that about twice the sphere weight is necessary for the peak force of one hemisphere. Thus, for a sphere weight of 20 lb, a peak force would be desired of 40 lb, as given by Fig. 4. This requires about 1.4 times the potential gradient that would yield a lift force equal to the sphere weight.

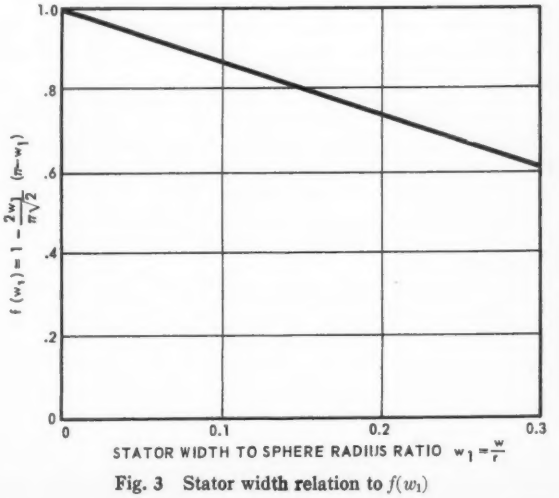

Fig. 3 Stator width relation to $f(w_1)$

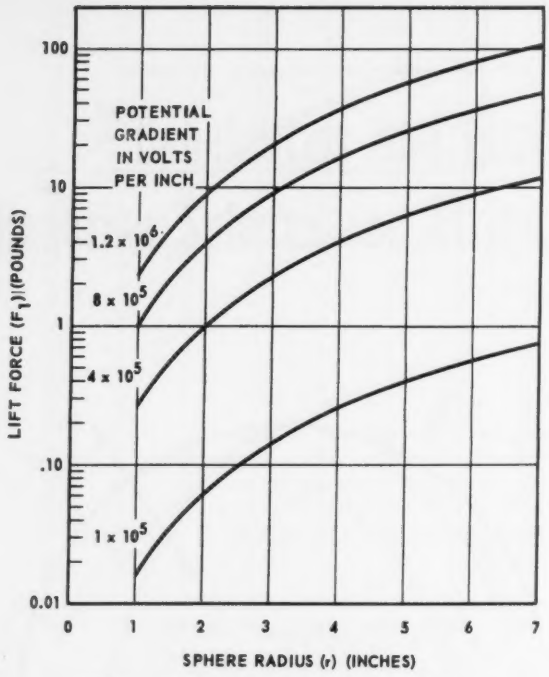

Fig. 4 Sphere lift force vs. sphere radius

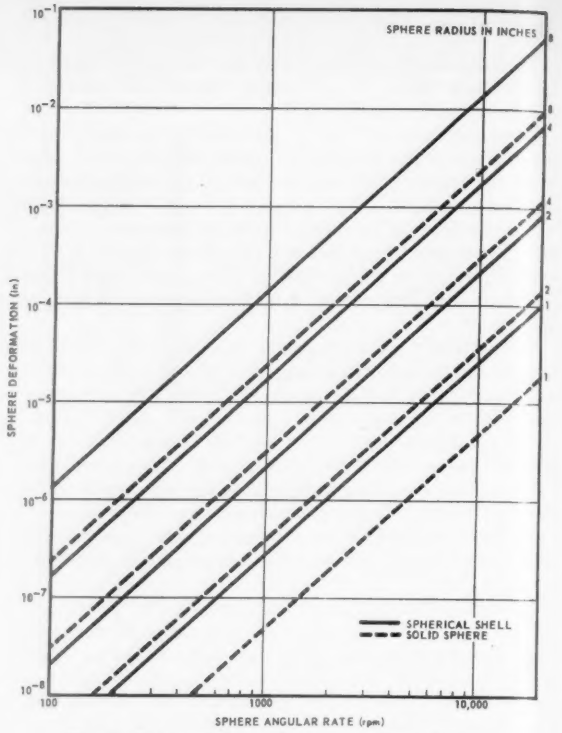

Fig. 5 Sphere deformation vs. angular velocity

The suspension system design must consider also three major factors associated with the spherical rotor characteristics. These are the deformation of the rotating sphere, variations in electrode-sphere gap distance due to sphere imbalance and sphericity, and the mass of the rotor which will determine the force requirements due to accelerations or vibrations of the satellite.

The rotating sphere will have a maximum deformation that is proportional to the square of the rotational rate and the cube of the radius. The magnitude of the deformation is shown in Fig. 5 for both thin wall and solid steel spheres.

The sphere will tend to rotate about its center of gravity, and if the center of gravity does not coincide with the center of geometry, then there will be a fluctuating sphere-electrode gap distance. In addition, a similar effect will result from the imperfections of sphericity due to manufacturing tolerances. These effects will introduce electrical oscillations into the suspension system, and will result in oscillating forces on the sphere. The displacement of the rotor will be determined by the suspension system damping characteristics and the magnitude of the sphere imbalance.

In the present case, it is desired to minimize the displacement of the sphere from its central position. The electrodes experience accelerations due to the motion and vibration of the vehicle. The suspension system must impose approximately the same accelerations on the sphere to maintain its central position. Also, the torquing stators will exert some side pull on the sphere which must be counteracted by the suspension forces.

The basic suspension system circuit can be represented as shown in Fig. 6. Analysis yields a natural spring constant for the resonant system of

for the case of no displacement of the sphere from the center of the cavity. In this equation, ϵ_0 is the permittivity of free space, r is the sphere radius, s is the gap distance and the angles α_a, α_b, β_a, and β_b are as shown in Fig. 7. The circuit parameters are

$$P_1 = 1 + 2C_0/C_1 \qquad P_2 = R_0/\omega L_0$$

$$P_3 = \omega^2 L_0 C_1 = \frac{X_{L_0}}{X_{C_1}} \qquad P_1^2 = \omega^2 I^2 M^2$$

Where the sphere has no displacement, the sphere-electrode capacitance, C_1 is representable by

$$C_1 = (\epsilon_0 r^2/s)(\alpha_b - \alpha_a)(\cos\beta_a - \cos\beta_b)$$

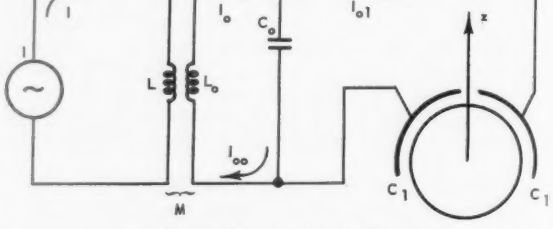

Fig. 6 Suspension circuit

$$k_1 = \left(\frac{\epsilon_0 P_4^2 r^2}{P_3^2 P_1^2 s^3}\right) \frac{(\alpha_b - \alpha_a)}{\left[P_3^2 + \left(1 - \frac{2}{P_1 P_3}\right)^2\right]} \left[\frac{P_2^2 + 1 - \frac{2}{P_1 P_3}(\cos^2\beta_a - \cos^2\beta_b + \cos\beta_a \cos\beta_b (\cos\beta_a - \cos\beta_b))}{4P_1\left[P_2^2 + \left(1 - \frac{2}{P_1 P_3}\right)^2\right] - \left(\frac{\cos^3\beta_a - \cos^3\beta_b}{3}\right)}\right]$$

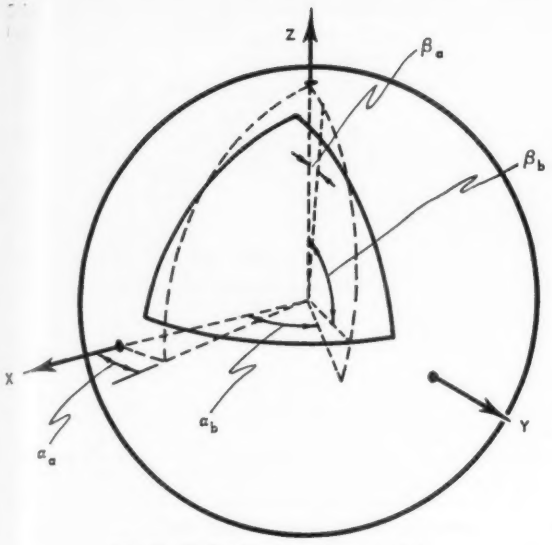

Fig. 7 Definition of angles α and β

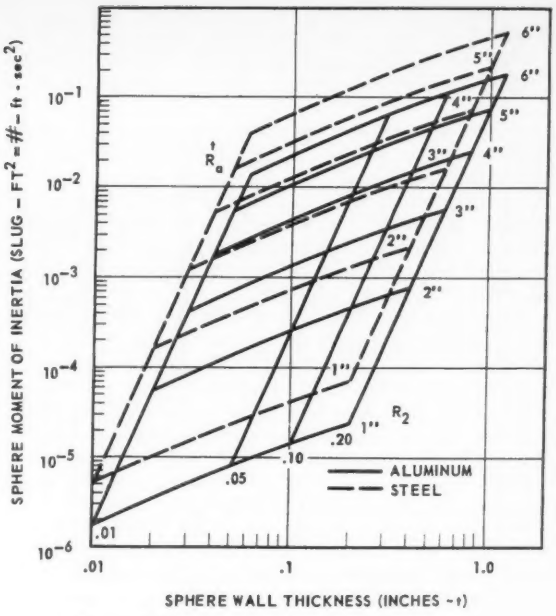

Fig. 8 Moment of inertia vs. wall thickness

The natural spring constant of the sphere in terms of the system characteristics can be calculated from these expressions. The desired damping constant will determine the compensation network.

Torque System

The torque system constitutes a set of three orthogonal stators, any one of which resembles a short electric induction motor stator in its electric and geometric characteristics. Electric motor theory applicable to solid rotor induction motors is valid for analyses of torque performance, except that the very short stators will result in appreciably different end effects. The torque cross coupling that may exist when the sphere spin vector lies at an angle with the normal to a stator provides a much more difficult analysis problem. Preliminary experimental investigations have shown that neither the generation of desired torque nor the minimizing of cross coupling will be major problems in the development of reaction sphere systems for space vehicles.

Reaction sphere torque is important from the points of view of maximum achievable torque, required power input, and torque resolution. Only the maximum achievable torque is considered here.

The factors determining torque performance will include: diameter, sphere material, sphere wall thickness, air gap, stator length, applied voltage, synchronous frequency, stator excitation frequency and stator windings and design. Each of these items will be discussed in the following paragraphs.

Diameter It is well known that the torque of a cylindrical induction motor is proportional to D^2L, where D is the rotor diameter and L is the rotor length. It is proposed that this is valid for a solid rotor machine. In the case of an electrostatically suspended spherical rotor, the maximum allowable length L is determined by the requirements for electrode surface between the stators. The suspension problem is expected to be easier for increasing diameter. Thus, if for a small sphere, a maximum allowable L is given by $L = k_L D$, then it would be conservative to assume $L \sim D$ for all larger systems. All this implies that the torque can be written as $T \sim D^3$. Thus, the problem of meeting a given torque requirement is eased by going to a larger diameter.

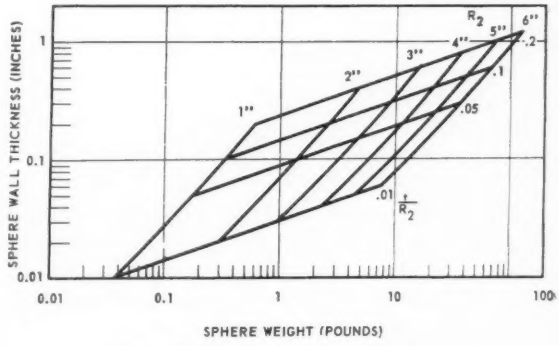

Fig. 9 Sphere weight vs. wall thickness

Sphere material Few facts have been assembled that describe the effect of the material of the sphere on the torque performance. Where induction causes most of the torque ("soft" rotors), the parameter $(\mu\rho)^{-1/2}$ is the significant variable, where μ = permeability and ρ = resistivity. This shows that as the permeability and resistivity decrease, the starting torque increases. With a "hard" rotor, i.e., a hysteresis motor, the variation of torque with rotor speed is relatively small. This is desirable from the point of view of the control system. However, the efficiency can be expected to be lower than for "soft" rotors.

Sphere wall thickness The effect of sphere wall thickness has not been precisely described nor tested. However, studies have indicated that there will be no appreciable effect for wall thicknesses on the order of $\frac{1}{30}$ of a radius, or greater.

Air gap The effect of the air gap in induction motors is to reduce the torque or torque efficiency by $1/s$ (one over

gap distance). A similar effect is expected for reaction spheres.

Stator length The torque will increase directly with the stator length, and thus the stator should be as long (wide) as the electrode requirements allow.

Applied voltage Induction motors experience torques proportional to the square of the applied voltage. This holds for the reaction sphere.

Synchronous frequency The synchronous frequency determines the possible operating region of sphere speed. The relation between the synchronous frequency and the rotor frequency (slip) influences the torque-speed relation and the efficiency of the motor.

Stator excitation frequency This influences some of the losses and construction practices of the system.

Stator windings and design These are considered to be comparable for cylindrical and spherical rotors.

The foregoing can be applied to the design problem of a reaction sphere. Variations in the design can be considered to improve the torque efficiency and the torque resolution.

Design Characteristics

Consider the following to be three primary requirements for a reaction sphere system: minimum system weight, maximum torque capability and maximum angular momentum capability. The suspension system design should be optimized around these three items, while satisfying all other requirements such as power and reliability.

The torque capability as a function of the sphere characteristics has been previously discussed. The sphere weight and the angular momentum capability are related to the sphere characteristics by the equations

$$\text{angular momentum} = I\omega = \omega(8\pi/15)\rho(R_2^5 - R_1^5)$$

where

I = moment of inertia
ω = angular speed
ρ = mass density of material
R_2 = outer radius
R_1 = inner radius

$$\text{sphere weight} = (4\pi/3)\rho(R_2^3 - R_1^3)$$

It is evident that if an upper limit on ω is fixed, there will be a lower limit on I for a given specified maximum angular momentum capability. The moment of inertia and mass of a spherical shell are plotted in Figs. 8 and 9.

For a preliminary design, it will be presumed that a given torque *force per unit area* of a stator coil can be achieved for a given system. Then it is assumed that for *geometrically similar stators*, this force density is not a function of absolute size. Thus, reference to the preceding discussions show that the torque can be written as

$$T = A(s, \tau, t)r^3$$

where

$\tau = (\mu\rho)^{-1/2}$
t = sphere wall thickness
A = is a functional relation

e.g., A equals $A_1\ \tau/s$. Again, from the previous discussions, the following equations and inequalities can be written

$$W = C\rho r^3[1 - (1 - t/r)^3]$$
$$(I\omega)_{\max} \leq B\rho r^5[1 - (1 - t/r)^5]\omega_{\max}$$
$$T_{\max} \leq Ar^2$$

$$(\delta/s)_{\max} \geq 1/s(\rho/Er^3\omega^2 k_{1\max} + k_2(\rho, E)r^2)$$

where $k_{2(\rho E)}$ depends upon manufacturing capabilities. Here E is the modulus of elasticity of the ball material, and A, B and C are constants. To these can be added the expression for the spring contsant; and note that the natural frequency of the sphere is

$$\omega_n = \sqrt{kg/W}$$

The mutual dependence of the various parts of the system in determining the motion of the sphere in the cavity makes the design procedure a trial and error process. A basic objective of this process is to minimize the system weight.

References

1 Adams, J. J. and Chilton, R. G., "A Weight Comparison of Several Attitude Controls for Satellites," NASA Memo 12-3-058L, Langley Research Center, Feb. 1959.

2 Ormsby, R. D., "A Free Reaction Sphere Satellite Attitude Control System," Proc. IAS National Specialists Meeting on Guidance of Aerospace Vehicles, Boston, Mass., May 1960, pp. 53–55.

3 Laub, J. H. and McGinness, H. D., "A Closed Cycle System for Gas Bearings," Astronautics, vol. 6, no. 3, March 1961, p. 70.

4 Spitzer, L., "Space Telescopes and Components," *Astron. J.*, June 1960.

5 Golay, M. J. E., "Gystats," Proc. IRE 1958 Conference, National Convention of Military Electronics, Washington, D. C., June 1958, pp. 286–289.

6 Hering, K. W. and Hufnagel, R. E., "An Inertial Sphere System for Complete Attitude Control of Earth Satellites," ARS preprint 1499-60, Dec. 1960.

Magnetorquer—a Satellite Orientation Device

L. J. KAMM[1]

General Dynamics/Astronautics
San Diego, Calif.

Satellite orientation torque is produced by the reaction of Earth's magnetic field on current carrying coils in the satellite. Components of the system are a magnetometer to measure the field, a computer and a set of coils. A torque command is assumed to be furnished from a guidance source. Adequate torque can be generated with reasonable weight and power at all altitudes up to 24 hr orbit. Torque cannot be produced about the instantaneous field axis, but since in general this axis varies with the position in orbit, any torque can be produced at some point in the orbit. The device may be used alone where this effect is permissible or it may be used to desaturate inertia wheels instead of using jets. The advantages of the system are simplicity, light weight, and zero propellant consumption.

THE MAGNETORQUER is an attitude control motor which generates torque by the action of Earth's magnetic field on electric currents in the satellite. No expendable propellant is used and energy is drawn from the satellite's electric power source, usually the sun.

The Magnetorquer consists of a set of three orthogonal coils to carry the current, a three-axis magnetometer to measure Earth's field, and a computer (see Fig. 1). It is a motor device only and requires that attitude error by separately sensed and a control torque command be supplied to its computer. It is recognized that in certain cases Earth's field may also be used as a reference in measuring error, but this discussion is limited to the generation of torque.

Torque Calculation

The torque on a current carrying coil in a magnetic field is

$$\bar{T} = \bar{M} \times \bar{B} \qquad [1]$$

where

$\bar{T}$ = torque in Newton meters
$\bar{M}$ = magnetic moment in ampere turns m²
$\bar{B}$ = flux density in Webers/m²

Earth's magnetic field is approximately that of a dipole located at the Earth's center and having a magnetic moment of 8.06×10^{25} cgs units. At any radius the flux density at the poles is twice that at the Equator. The magnitude of Earth's field is (1 and 2)[2]

$$\bar{B} = \frac{1.43 \times 10^6}{Ro^3} = \frac{1.43 \times 10^6}{(3444 \times h)^3} \qquad [2]$$

where

B = Earth field flux density in Webers/m² at the Equator
Ro = radius of orbit in nautical miles
h = height of orbit in nautical miles

The magnetic moment of a plane coil is

$$\bar{M} = NI\bar{A} \qquad [3]$$

where

N = number of turns
I = current in amperes
$\bar{A}$ = area in m²

A more useful set of parameters in computing M is power, size, shape and weight. Eq. 3 is transformed to these parameters as follows

$$R = \frac{N\rho p}{a} \qquad [4]$$

where

R = resistance of coil in ohms
ρ = resistivity of wire in ohm-meters
p = length of turn in meters, perimeter of coil
a = cross-sectional area of each turn in m²

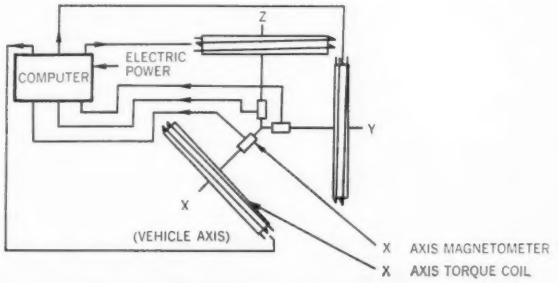

Fig. 1 Magnetorquer schematic diagram

Received July 25, 1960.
[1] Design Specialist. Member ARS.
[2] Numbers in parentheses indicate References at end of paper.

$$W = Npad \qquad [5]$$

where W is the mass of the coil in kilograms and d is the density of the conductor in kilograms/m³

$$P = I^2R \qquad [6]$$

where P is the power in watts. Combining Eqs. 3, 4, 5 and 6

$$\bar{M} = \sqrt{\frac{\overline{Pw}}{\rho d}}\,\frac{A}{p} \qquad [7]$$

M is a maximum when A/p is a maximum. This is the condition for a circular coil. For such a coil

$$A = \pi D^2/4 \qquad [8]$$

where D is the diameter in meters

$$p = \pi D \qquad [9]$$

$$\frac{A}{p} = \frac{D}{4} \qquad [10]$$

Substituting Eq. 10 into Eq. 7

$$M = \frac{D}{4}\sqrt{\frac{\overline{P\,W}}{\rho\,d}} \qquad [11]$$

Substituting Eqs. 2 and 11 into Eq. 1

$$T = \frac{1.43 \times 10^6\, D}{4(3444 + h)^3}\sqrt{\frac{\overline{PW}}{\rho d}} \qquad [12]$$

The expression ρd is characteristic of the wire material. Values for the three best conductors are shown in Table 1. Aluminum is the best material by a factor of 2.

Substituting the numbers for aluminum, Eq. 12 reduces to

$$T = 4.09 \times 10^7\,\frac{D\sqrt{PW}}{(3444 + h)^3} \qquad [13]$$

In Eq. 13 the units are T in Newton meters, D in meters, P in watts, W in kilograms, and h in nautical miles. A more convenient set of units are T in dyne cm, D in feet, P in watts, W in pounds (weight on Earth's surface), and h in nautical miles. In these units, Eq. 13 becomes

$$T = 8.42 \times 10^{13}\,\frac{D\sqrt{PW}}{(3444 + h)^3} \qquad [14]$$

Typical sets of parameters are

P = 1 watt	P = 10 watts
W = 1 lb	W = 10 lb
D = 5 ft	D = 10 ft
h = 300 nautical miles	h = 19,367 nautical miles (24 hr)
T = 8050 dyne cm	T = 708 dyne cm.

Since the steady state disturbing torque which the satellite torquer must balance is of the order of 200 dyne cm, the Magnetorquer is practical from the standpoint of weight and power.

Note that Eq. 14 is for a single coil in the best position to generate torque. In practice it is necessary to provide three orthogonal coils to generate magnetic moments on all three axis. Therefore, the coil weight computed by Eq. 14 should be multiplied by 3.

Table 1 Values for the three best conductors

Metal	ρ	d	ρd
copper	1.724×10^{-8}	8.89×10^3	1.53×10^{-4}
aluminum	2.828×10^{-8}	2.69×10^3	0.764×10^{-4}
silver	1.629×10^{-8}	10.60×10^3	1.73×10^{-4}

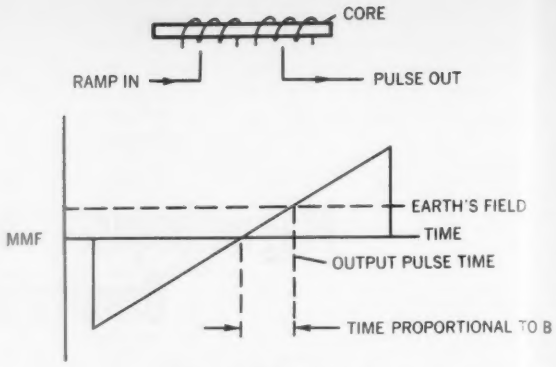

Fig. 2 Magnetometer

It can be shown that the power required for a given magnitude of $\bar{M}$ is independent of the direction of $\bar{M}$. Let

$$\bar{M} = \bar{\imath}M_x + \bar{j}M_y + \bar{k}M_z \qquad [15]$$

where M_x, M_y and M_z are the components of $\bar{M}$ produced by the three coils.

$$|M| = \sqrt{M_x^2 + M_y^2 + M_z^2} \qquad [16]$$

$$M = NAI_x \qquad M_y = NAI_y \qquad M_z = NAI_z \qquad [17]$$

Therefore

$$I_x^2 + I_y^2 + I_z^2 = |\bar{M}|^2/(NA)^2 \qquad [18]$$

Multiply by R, the resistance of each coil

$$I^2{}_xR + I_y{}^2R + I_z{}^2R = (|\bar{M}|^2R)/(NA)^2 \qquad [19]$$

Therefore, the total power in the three coils is a function of the magnitude of $\bar{M}$ only and is independent of its direction.

Magnetometer

The function of the magnetometer is to measure the magnitude and direction of Earth's magnetic field. The existing art is quite adequate for the purpose.

The principal type of magnetometer now used for mineral surveys and ASW detectors is the flux gate. Along each of three axes is a straight magnetic core of low hysteresis material. Two windings are on each core. The magnetic flux in the core is the sum of the fluxes due to currents in the windings and Earth's field flux.

One of the two windings carries a-c excitation. If there is a d-c component of flux in the core it causes current harmonics in the a-c circuit. These harmonics are used to control a d-c feedback current in the second coil to oppose and cancel Earth's field flux. The d-c feedback current is a measure of Earth's field component along the core.

The threshold sensitivity of these devices is about 0.5 gamma (0.5×10^{-5} gauss, or 0.5×10^{-9} Weber/m²). The flux density of Earth at the Equator is 3.5×10^4 gamma at sea level, 1.6×10^4 gamma at 1000 nautical mile altitude, and 130 gamma at 19,000 nautical mile altitude (24 hr orbit).

Such magnetometers for missile and space vehicle use have been made by Schoenstedt Engineering Co., Silver Spring, Md. A comparable device using a magnetron as a sensing element is made by Arnoux Co. of Los Angeles.

A modified flux gate magnetometer has been conceived whose output is in a more useful form for the computation needed; see Fig. 2. In this scheme a first coil on the core is periodically excited with a ramp function starting with a large negative current and rising uniformly through zero to a large positive current. When the ramp current MMF passes through the value of Earth's field MMF the core flux reverses and a pulse is generated in a second coil. The timing of this pulse is a measure of the earth's field strength component along the core axis. Magnetometer output as a time instead of a current is convenient for analog multiplication in the computer.

When the Earth field component is close to zero, the flux reversal occurs close to the point when the ramp crosses zero. If the threshold of each magnetometer is 0.5 gamma, then even at the 24 hr orbit, where the flux density at the Equator is 130 gamma, the threshold error in the measured direction of $\bar{B}$ is arc sin 0.5/130 or 4 milliradians.

Computer

The computer is given a command torque vector $\bar{T}$ as a function of attitude error and error rate and the Earth's field vector $\bar{B}$ from the magnetometer. It computes a magnetic moment vector $\bar{M}$ such that $\bar{T} = \bar{M} \times \bar{B}$ (Eq. 1). Eq. 1 may be solved for $\bar{M}$ as follows

$$\bar{B} \times \bar{T} = \bar{B} \times (\bar{M} \times \bar{B})$$

$$\bar{B} \times \bar{T} = \bar{M}(\bar{B} \cdot \bar{B}) - \bar{B}(\bar{B} \cdot \bar{M}) \qquad \ldots\ldots [20]$$

Since a component of $\bar{M}$ parallel to $\bar{B}$ would produce no torque, we can specify that such a component be zero and thereby minimize electric power. Thus

$$\bar{B} \cdot \bar{M} = 0 \qquad [21]$$

Substituting Eq. 21 into Eqs. 20

$$\bar{B} \times \bar{T} = B^2 \bar{M}$$

$$\bar{M} = \frac{\bar{B} \times \bar{T}}{B^2} \qquad \ldots\ldots [22]$$

Eqs. 22 may be simplified by the following reasoning: The magnitude of B for any altitude varies through a maximum of 2:1 (polar flux density:Equator flux density). Therefore, B^2 varies 4:1. Therefore, for a circular polar orbit, if we assume B^2 to be constant $\bar{M}$ would vary by 4:1 in magnitude but would not be influenced at all in direction. The assumption of constant B^2 would, therefore, only introduce a 4:1 variation in gain in a very low frequency feedback control system, which is harmless. The simplified equation is

$$\bar{M} = K(\bar{B} \times \bar{T}) \qquad [23]$$

where K is the gain constant of the system. This vector equation reduces to

$$I_x = \frac{1}{NA} M_x = \frac{1}{NA} K(B_y T_z - B_z Y_y) \qquad [19a]$$

$$I_y = \frac{1}{NA} M_y = \frac{1}{NA} K(B_z T_x - B_x T_z) \qquad [19b]$$

$$I_z = \frac{1}{NA} M_z = \frac{1}{NA} K(B_x T_y - B_y T_x) \qquad [19c]$$

where I_x, I_y, I_z are the currents in the three coils.

Thus the computation consists of two multiplications and one sum for each output current. If the time output magnetometer discussed is used, the multiplications are quite easily instrumented using ordinary analog computer concepts.

At this point it should be noted that the measurement of $\bar{B}$ cannot be made during the generation of $\bar{M}$ because the field produced by $\bar{M}$ would grossly distort the measurement of $\bar{B}$. Therefore, measurement and torquing must be time shared. Since in any satellite orbit significant variations in $\bar{B}$ will consume many minutes, the system should be designed to work with occasional brief interruptions for measuring $\bar{B}$ and computing $\bar{M}$ interlaced with relatively long periods of time for maintaining the computed value of $\bar{M}$.

Dynamics

It is impossible to generate a $\bar{T}$ competent parallel to $\bar{B}$ by the basic law describing the phenomenon $\bar{T} = \bar{M} \times \bar{B}$ (Eq. 1). Therefore, for any commanded torque, only the components normal to $\bar{B}$ are generated. In the case of a polar orbit or one with a large angle of inclination to the Equator this results only in delay in producing certain torques because the direction of Earth's field at the satellite is constantly varying relative to inertial space. In the case of an equatorial orbit the field direction varies about ± 12 deg because of the angle between Earth's spin axis and its magnetic axis.

In the case of 24 hr equatorial orbit the $\bar{B}$ direction is approximately horizontal and has zero variation. However, control of an Earth oriented satellite is still possible by rotating the vehicle around the local vertical until the error axis is rotated out of parallelism with $\bar{B}$.

For certain missions the Magnetorquer can be used alone as the sole torquing device. For precision control the Magnetorquer may be used to desaturate flywheels instead of the older practice of using rockets. Thus, the Magnetorquer is not a panacea but depends on the orbit and the acceptability of its control lags for a particular vehicle. In exchange it provides reliability, long life and zero propellant consumption.

References

1 Fleming, J. A., ed., *Physics of the Earth, Vol. 8: Terrestrial Magnetism and Electricity*, National Research Council, Committee on Physics of the Earth, McGraw-Hill Book Co., Inc., N. Y., first edition; see chap. VII by McNish, A. G.

2 Westphal, W. H. (Hrsg.), *Physikalisches Wortenbuch*, Springer-Verlag, Berlin, first edition; see p. 365, Erster Teil.

Technical Notes

Application of Heat Flux Potentials to the Calculation of Convective Heat Transfer in Chemically Reacting Gases[1]

DANIEL E. ROSNER[2]

AeroChem Research Laboratories, Inc., Princeton, N. J.

Langmuir (1)[3] and Hansen (2) have suggested that convective heat transfer rates in chemically reacting mixtures can be predicted by combining nonreactive heat transfer coefficients with heat flux potential differences. It is shown here that this coefficient-driving force combination will tend to systematically overestimate forced convection heat transfer rates in chemically reacting binary mixtures by a factor strongly dependent on (a) the departure of the Lewis-Semenov number Le_f from unity (when $Le_f > 1$); (b) the fraction of the total heat flux potential difference across the boundary layer attributable to chemical reaction; and weakly dependent on (c) the conditions of convection within the boundary layer. Numerical estimates are given of this correction factor using recent heat flux potential data (2) for equilibrium dissociated air at temperatures in the range of complete oxygen dissociation. For partially dissociated gases in general this effect is likely to be important when Lewis number conditions are favorable, and when boundary layer temperature ratios are near unity, provided the temperature level is in the range of maximum chemical contribution to the equilibrium heat conductivity.

A GAS MIXTURE in dissociation equilibrium behaves like a pure substance with an enhanced thermal conductivity and specific heat which depend strongly on the temperature and pressure level [see, e.g., (3)]. As a result, the prediction of convective heat transfer rates in such a system may fruitfully be regarded as a variable property problem (1,4,5).

In classical heat conduction theory, when the thermal conductivity λ is temperature dependent, it is convenient to define a new dependent variable φ by means of the Kirchoff transformation (6)

$$\varphi \equiv \int_0^T \lambda(T)dT \qquad [1]$$

This dependent variable has appropriately been called the *heat flux potential* since the heat flux vector J_Q at any point in the medium is simply related to the gradient of φ

$$J_Q = -\text{grad}\ \varphi \qquad [2]$$

Steady state heat fluxes in one-dimensional stagnant media (e.g., thermal conductivity cells) are therefore directly proportional to the potential difference $\Delta\varphi$ evaluated across the boundaries. From the defining equation [1] it is clear that the use of the dependent variable φ is equivalent to the introduction of the familiar temperature integrated average thermal conductivity (4)

$$\lambda_{avg} = \frac{1}{\Delta T}\int_{T_w}^{T_e} \lambda(T)dT \qquad [3]$$

In the case of chemically reacting gases, however, the thermal conductivity will be dependent on pressure as well as temperature so that, in general, $\varphi = \varphi(T; p)$.

Conjecture

Since low speed, nearly isothermal convective heat transfer rates in the absence of chemical reaction can be correlated in the Nusselt form (7)

$$\dot{q} = \text{Nu}(\text{Re}, \text{Pr}_\lambda)\lambda\Delta T/L \qquad [4]$$

it has been conjectured [see, e.g., (2)] that, in the presence of chemical reaction (and hence variable thermal conductivity) the heat flux should be calculable from

$$\dot{q} = \text{Nu}(\text{Re},\text{Pr}_\lambda)\Delta\varphi/L \qquad [5]$$

where the heat transfer coefficient $\text{Nu}_\lambda = \text{Nu}(\text{Re},\text{Pr}_\lambda)$ is, to a first approximation, unchanged by the thermochemical processes occurring within the boundary layer. If so, this generalization of Newton's "law" of cooling would constitute an extremely potent computational technique since, apart from the restriction to cases of local thermochemical equilibrium (8), the method can make use of a vast body of existing convective heat transfer data and is, *prima facie*, free of restrictions (2) as to the behavior of the Lewis-Semenov numbers in multi-component gas mixtures (9). One would require only tabular or graphical values of the heat flux potential $\varphi(T;p)$ which, for a given mixture, could be calculated once and for all using the methods outlined in (10).

Analysis

It would be desirable to gain a physical insight into the accuracy of the method as stated, as well as to obtain an *explicit* estimate of the dependence of the error upon known parameters of the problem. To this end the following procedure, based on a simplified analysis of the boundary layer energy equation, was adopted.

We consider a partially dissociated diatomic gas and make use of the fact that the enhancement of the thermal conductivity is related (10) to the thermochemical enhancement of the specific heat by an expression of the form

$$\lambda_{eq}/\lambda_f = 1 + (Le_f)[(c_{p,eq}/c_{p,f}) - 1] \qquad [6]$$

Since the thermal conductivity λ_{eq} may be regarded as being comprised of a chemically "frozen" contribution λ_f and a reactive contribution $\lambda_{chem} = \lambda_{eq} - \lambda_f$ a similar remark will

Received December 14, 1960; revised February 22, 1961.
[1] This research was supported by Wright Air Development Center Contract Number AF 33(616)-6216. Revised version of (12).
[2] Research Scientist. Member ARS.
[3] Numbers in parentheses indicate References at end of paper.

EDITOR'S NOTE: The Technical Notes and Technical Comments sections of ARS JOURNAL are open to short manuscripts describing new developments or offering comments on papers previously published. Such manuscripts are usually published without editorial review within a few months of the date of receipt. Requirements as to style are the same as for regular contributions (see masthead page).

apply to the heat flux potential. Thus we can write

$$\varphi = \varphi_f + \varphi_{chem} \quad [7]$$

where φ_f represents the integral of λ_f with respect to temperature and φ_{chem} is the contribution due to the dissociation-diffusion-gas phase recombination (Nernst-Langmuir) mechanism.

In order to write the energy equation for the laminar boundary layer in terms of the heat flux potential φ, we first make use of a differential relation readily derived from equation [6], i.e.

$$\frac{\mu}{Pr_{\lambda,f}}\,dh = d\varphi\left[1 - \left(1 - \frac{1}{Le_f}\right)\frac{d\varphi_{chem}}{d\varphi}\right] \quad [8]$$

The steady flow energy equation for the laminar boundary layer flow of a binary mixture of perfect gases may be written in terms of the static enthalpy h as follows (11)

$$\rho\left(u\frac{\partial h}{\partial x} + v\frac{\partial h}{\partial y}\right) = \frac{\partial}{\partial y}\left[\lambda_f\frac{\partial T}{\partial y}\right] + \frac{\partial}{\partial y}\left[\rho D_{12}(h_1 - h_2)\frac{\partial c_1}{\partial y}\right] + u\frac{dp}{dx} + \mu\left(\frac{\partial u}{\partial y}\right)^2 \quad [9]$$

Consider now the case of a flat plate ($dp/dx = 0$) with negligible viscous dissipation. When local thermochemical equilibrium is achieved in the gas phase, equation [9] may then be written

$$\rho\left(u\frac{\partial h}{\partial x} + v\frac{\partial h}{\partial y}\right) = \frac{\partial}{\partial y}\left[(\lambda_f + \lambda_{chem})\frac{\partial T}{\partial y}\right] = \frac{\partial^2\varphi}{\partial y^2} \quad [10]$$

Transforming the convective terms on the left-hand side of [9] with the use of equation [7] we obtain

$$\rho\left(u\frac{\partial \varphi}{\partial x} + v\frac{\partial \varphi}{\partial y}\right) = \frac{\mu}{Pr_{\lambda,f}}\frac{\partial^2\varphi}{\partial y^2}\left\{1 - \left(1 - \frac{1}{Le_f}\right)\frac{d\varphi_{chem}}{d\varphi}\right\}^{-1} \quad [11]$$

Inspection of this result reveals that, if an average value for the quantity in curly brackets is introduced, equation [11] reduces to the heat conduction equation for a pure (single) substance with a modified Prandtl number. A reasonable choice for this effective Prandtl number is seen to be

$$Pr_{\lambda,f}\left\{1 - \left(1 - \frac{1}{Le_f}\right)\frac{\Delta\varphi_{chem}}{\Delta\varphi}\right\} \quad [12]$$

where $\Delta\varphi_{chem}$ is the difference between φ_{chem} evaluated at the outer and inner edge of the boundary layer and $\Delta\varphi$ is the corresponding difference in the total heat flux potential across the boundary layer.

Thus the conjecture that the heat transfer coefficient Nu_λ in equation [5] is, to a first approximation, equal to $Nu(Re, Pr_{\lambda,f})$ is seen to be equivalent to neglecting the effect of thermochemically induced changes in the effective laminar Prandtl number on the boundary layer film conductance. Now, for many boundary layer flows, the Prandtl number dependence of the nondimensional heat transfer coefficient Nu_λ is adequately represented by a power law, i.e., $Nu_\lambda \propto (Pr_\lambda)^b$ where typical values of b range from $^1/_2$ to $^1/_3$ depending upon the magnitude of Pr_λ. We conclude therefore that the factor neglected when nonreactive heat transfer coefficients are combined with heat flux potential driving forces in chemically reacting binary mixtures will be approximately given by

$$\left\{1 - \left(1 - \frac{1}{Le_f}\right)\frac{\Delta\varphi_{chem}}{\Delta\varphi}\right\}^b \quad [13]$$

An alternate method of arriving at this conclusion may be of interest (12). This can be accomplished using a simple method paralleling that given in (13).[4] Thus, if the accuracy of equation [5] is dependent upon the power b of the ratio $(Pr_{\lambda,eq})_{avg}/(Pr_{\lambda,f})_{avg}$ then an explicit estimate of this factor in terms of boundary data should be possible by introducing the quantities

$$(\lambda_{eq})_{avg} = \Delta\varphi/\Delta T \quad [14a]$$

$$(\lambda_f)_{avg} = \Delta\varphi_f/\Delta T \quad [14b]$$

Use of equation [6] leads immediately to the result

$$(Pr_{\lambda,eq})_{avg} = (Pr_{\lambda,f})_{avg}\left\{1 - \left(1 - \frac{1}{Le_f}\right)\frac{\Delta\varphi_{chem}}{\Delta\varphi}\right\} \quad [15]$$

in agreement with [12] and the aforementioned conclusion [13].

Discussion

For weakly dissociated diatomic gases, the Lewis-Semenov number Le_f is appreciably greater than unity (11), reflecting the fact that atom diffusion is a more efficient energy transport mechanism than ordinary conduction through such mixtures. Thus the factor [13] should be less than unity for most cases in which energy is transferred from hot partially dissociated gases to cooled solids. Inspection of [13] reveals that, in general, the error will become negligible in three distinct circumstances

$$\text{if } Le_f \to 1 \quad [16a]$$

$$\text{if } \Delta\varphi_{chem}/\Delta\varphi \to 0 \quad [16b]$$

$$\text{if } b \to 0 \quad [16c]$$

Conditions (*a*) and (*b*) have parallels in evaluating the errors implicit in the use of total enthalpy as a driving force for energy transport (13). Condition (*c*) will not be encountered in the presence of convection.

Numerical Example

As a typical example of the magnitude of this correction factor we consider the laminar stagnation point flow of dissociated air, making use of the recent heat flux potential shock tube data reported by Hansen (2). Fig. 6 of (2) shows that φ/φ_f for equilibrium air is unity for temperatures below about 1000 K but rises to a plateau of about 2.5 at temperatures in the range of complete oxygen dissociation (5000 K in the case shown). Since φ_f behaves approximately as $T^{3/2}$ it is readily verified that

$$\frac{\Delta\varphi_{chem}}{\Delta\varphi} \cong \frac{[(\varphi/\varphi_f)_e - 1] - (T_w/T_e)^{3/2}[(\varphi/\varphi_f)_w - 1]}{(\varphi/\varphi_f)_e - (T_w/T_e)^{3/2}(\varphi/\varphi_f)_w} \quad [17]$$

Therefore, if $T_e = 5000$ K and $T_w = 1000$ K (say), equation [17] yields $\Delta\varphi_{chem}/\Delta\varphi \approx 0.62$. While the Lewis-Semenov number for atom diffusion in partially dissociated air is not accurately known, available estimates place it in the neighborhood of 1.4 (11,14). Finally, we take $b = 1 - 0.6 = 0.4$ for stagnation flow (15). The calculated value of the factor [13] for these conditions is 0.92. Thus, in this particular case, the use of the nonreactive heat transfer coefficient $Nu(Re, Pr_{\lambda,f})$ with $\Delta\varphi$ as the driving force should overestimate the stagnation point heat transfer rate by about 8 per cent. As is apparent from [17], the error will, in general, depend upon *each* of the chosen temperature levels, T_e and T_w. This is displayed in Fig. 1, constructed from Hansen's theoretical curve [see Fig. 6 of (2)] of φ/φ_f vs. T. The quantity $\Delta\varphi_{chem}/\Delta\varphi$ is shown as a function of the free stream static temperature T_e for several values of the temperature ratio T_w/T_e across the boundary layer.[5] Over the range of vari-

[4] Conversely, the foregoing analysis of the energy equation in terms of enthalpy can be used to derive the results of (13).

[5] Calculated as though the φ/φ_f data shown in Fig. 6 of (2) corresponded to a single pressure level.

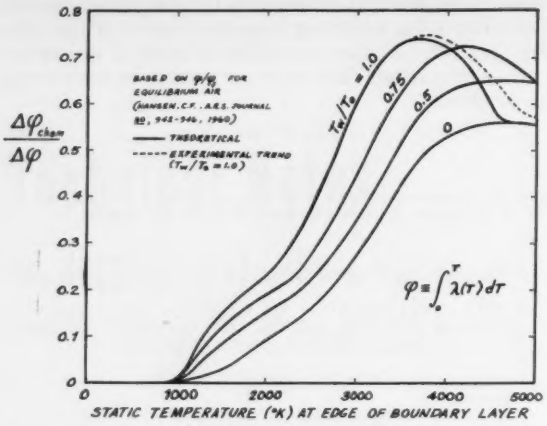

Fig. 1 Chemical contribution to the driving force for energy transport from partially dissociated air to solid surfaces

ables shown, $\Delta\varphi_{chem}/\Delta\varphi$ approaches values as large as 0.75 for free stream and surface temperatures in the neighborhood of 3600 K. Due to the effect of nonunity Lewis-Semenov number, this would correspond to about a 9% change in the stagnation point heat flux.

Note that if $\Delta\varphi_{chem}/\Delta\varphi \to 1$ the factor [13] would approach its minimum value of $(Le_f)^{-b}$ (or 0.87 for $Le_f = 1.4$). In this extreme we have the limiting law: $\dot{q} \propto Nu(Re,Pr_D)\Delta\varphi_{chem}$ where $Nu(Re,Pr_D) \equiv Nu_D$ will be recognized as the *mass* transfer coefficient (Sherwood number). Indeed, equation [6] reveals that the diffusional Prandtl number Pr_D may, alternatively, be interpreted as $Pr_{\lambda,chem} \equiv c_{p,chem}\mu/\lambda_{chem}$.

In high temperature (combustion) gases containing significant amounts of hydrogen atoms, values of the effective Lewis-Semenov number[6] can exceed 2.0 or 3.0 (16). As a result, convective heat fluxes (particularly to high temperature solids, i.e., solids not far removed from the flame gas temperature) are likely to be appreciably overestimated if the effect of dissociation on the laminar Prandtl number (and hence the heat transfer coefficient) is left unaccounted for in a correlation equation of the form $\dot{q} = Nu(Re,Pr)\Delta\varphi/L$.

Nomenclature

b	=	exponent on the Prandtl number in a correlation equation of the Nusselt form
c	=	mass fraction
c_p	=	specific heat at constant pressure
D_{12}	=	binary diffusion coefficient for atoms in the gas mixture
h	=	static enthalpy of the mixture (per gram) $= \sum c_i h_i$
J_Q	=	energy flux vector (relative to mass-averaged velocity)
L	=	characteristic physical length
Le_f	=	chemically "frozen" Lewis-Semenov number $= D_{12}/[\lambda_f/(\rho c_{p,f})]$
Nu	=	nondimensional transfer coefficient, Nusselt number
p	=	total pressure
Pr_λ	=	Prandtl number for heat conduction $= (\mu/\rho)/[\lambda_f/(\rho c_{p,f})]$
Pr_D	=	Prandtl number for diffusion (Schmidt number) $= (\mu/\rho)/D_{12}$
$\dot{q}$	=	heat flux at the surface
Re	=	Reynolds number
T	=	absolute temperature
u,v	=	x and y components, respectively, of the local gas velocity
x,y	=	physical coordinates parallel and perpendicular, respectively, to the gas/solid interface
λ	=	thermal conductivity of the mixture
μ	=	absolute viscosity of the mixture
ρ	=	mass density of the mixture
φ	=	heat flux potential, Eq. 1
φ_f	=	thermal (inert) contribution to the heat flux potential
grad	=	gradient operator
Δ	=	change in (across the boundary layer)

Subscripts

1	=	pertaining to the lighter constituent (atoms in the case of a partially dissociated diatomic gas)
2	=	pertaining to the heavier constituent
avg	=	average
chem	=	chemical
D	=	pertaining to diffusion
e	=	at the outer edge of the boundary layer
eq	=	equilibrium
f	=	chemically "frozen"
w	=	at the wall (surface of solid)
λ	=	pertaining to ordinary thermal conduction

[6] For hydrogen atom diffusion through the mixture.

References

1 Langmuir, I., "The Dissociation of Hydrogen into Atoms," *Journal of the American Chemical Society*, vol. 34, 1912, p. 860.

2 Hansen, C. F., "Heat Diffusion in Gases, Including Effects of Chemical Reaction," ARS JOURNAL, vol. 30, 1960, pp. 942–946; see also NASA TR R-27 and NASA TN D-687.

3 Coffin, K. P., and O'Neal, C. Jr., "Experimental Thermal Conductivities of the $N_2O_4 \rightleftarrows 2NO_2$ System," NACA TN 4209, Feb. 1958; see also *J. Chem. Phys.*, vol. 31, 1959, p. 1290.

4 Brokaw, R. S., "Correlation of Turbulent Heat Transfer in a Tube for the Dissociating System $N_2O_4 \rightleftarrows 2NO_2$," NACA RM E57K19a, March 1958.

5 Schotte, W., "Heat Transfer to a Gas Phase Chemical Reaction," *Industrial and Engineering Chemistry*, vol. 50, no. 4, 1958, pp. 683–690.

6 See, for example, Jakob, M., *Heat Transfer*, John Wiley and Sons, N. Y., 1949.

7 See, for example, Eckert, E. R. G., and Drake, R. M., *Heat and Mass Transfer*, McGraw-Hill Book Co., Inc., N. Y., 1959.

8 Rosner, D. E., "Recent Advances in Convective Heat Transfer With Dissociation and Atom Recombination," JET PROPULSION, vol. 28, 1958, pp. 445–451.

9 Lees, L., "Convective Heat Transfer with Mass Addition and Chemical Reactions," *Third AGARD Colloquium, Combustion and Propulsion*, Pergamon Press, New York, 1958, pp. 451–498.

10 Butler, J. N., and Brokaw, R. S., "Thermal Conductivity of Gas Mixtures in Chemical Equilibrium," *Journal of Chemical Physics*, vol. 26, No. 6, 1957, p. 636; see also, Brokaw, R. S., ibid., vol. 32, no. 4, 1960, pp. 1005–1006.

11 Lees, L., "Laminar Heat Transfer over Blunt-Nosed Bodies at Hypersonic Flight Speeds," JET PROPULSION, vol. 26, 1956, pp. 259–269.

12 Rosner, D. E., "Application of Heat Flux Potentials to the Calculation of Convective Heat Transfer in Chemically Reacting Gases," AeroChem Research Laboratories, Princeton, N. J., TP-20, December 14, 1960.

13 Rosner, D. E., "Effects of Diffusion and Chemical Reaction on Convective Heat Transfer," ARS JOURNAL, vol. 30, 1960, pp. 114–115.

14 Fay, J. A., and Riddell, F. R., "Theory of Stagnation Point Heat Transfer in Dissociated Air," *J. of the Aeronautical Sciences*, vol. 25, 1958, p. 73 ff.

15 Sibulkin, M., "Heat Transfer Near the Forward Stagnation Point of a Body of Revolution," *J. of the Aeronautical Sciences*, vol. 19, 1952, pp. 570–571.

16 Rosner, D. E., "Convective Heat Transfer With Chemical Reaction I. Theoretical Development of Correlation Formulae for the Prediction of Heat Fluxes in High Performance Rocket Motors and Related Systems," AeroChem Research Laboratories TP-22, Jan. 1961, WADC Rep. (in preparation).

Measurement of Air Density at 430 Km by Sodium Resonance Cloud Techniques[1]

J. PRESSMAN[2] and F. F. MARMO[3]

Geophysics Corp. of America, Bedford, Mass.

Some comments are made on Shklovskii and Kurt's evaluation of a Soviet high altitude release in 1958. It is shown by using the mean displacement for one dimension rather than two dimensions, as well as an inappropriate density distribution for their observations for $t > 270$ sec, that their calculated diffusion coefficient D is too large by a factor of 4. Remarks are also made on the lower limit of applicability of the resonant cloud techniques.

SHKLOVSKII and Kurt (1)[4] have recently measured the density at 430 km by means of a sodium release. Their motivation here was to provide an independent check on the satellite drag measurements of density in this region (2). This technique is a promising one that is capable of yielding valuable information throughout an extended region of the atmosphere.

The following remarks are directed, first, toward a critical evaluation of the density at 430 km as determined by Shklovskii and Kurt's data, and second, toward an understanding of the altitude capability of this technique. Our conclusions differ from those of the forementioned authors. It will be shown that the computed diffusion coefficients (D-values) that they used are too high by a factor of 4 for their first calculation because of the use of an incorrect equation for the mean square displacement. In addition, their second calculation of the D-value at 430 km is found to be in error. Specifically, this value is too high by a factor of 3 due to the use of a mathematical formulation which was inappropriate to the problem at hand. Finally, it is suggested that the conclusion they reached concerning the lower altitude limit for the performance of sodium cloud experiments is also in error. The discussion will involve constant reference to Shklovskii and Kurt's data which is not easily accessible. Therefore, the basic data are reproduced here in Figs. 1 through 3 for ready reference.

Our first remarks concern determination of D through considerations of the mean displacement.

For the squared mean displacement Shklovskii and Kurt give [see Eq. 3 in (1)]

$$(\bar{s})^2 = (1/3)v\bar{l}t \qquad [1]$$

where

v = mean velocity of particle
$\bar{l}$ = mean free path length

They point out that $(1/3)v\bar{l}$ is nearly equal to the coefficient of diffusion D. Thus, we gather that they have utilized the approximate relationship

$$(\bar{s})^2 = Dt \qquad [2]$$

It can be shown that the $(\bar{s})^2$ values for the one-, two- and three-dimensional cases for the distribution functions employed are $(4Dt/\pi$, πDt and $16(Dt/\pi)$, respectively. In addition, the corresponding values for the mean squared displacement $(\bar{s}^2)$ are $2Dt$, $4Dt$ and $6Dt$.

It is apparent that Shklovskii and Kurt's defining equation

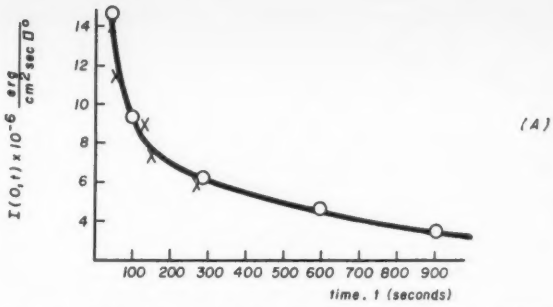

Fig. 1a Dependence of brightness of the center of sodium cloud vs. time; 0 = photographic observation, X = photoelectric observation

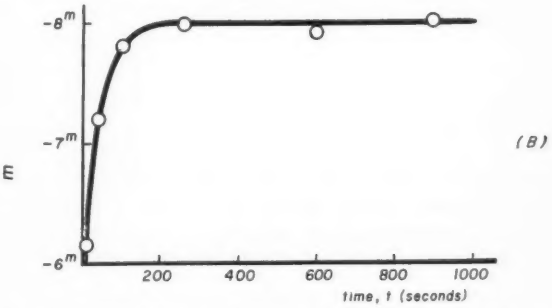

Fig. 1b Dependence of integral visual stellar magnitude vs. time

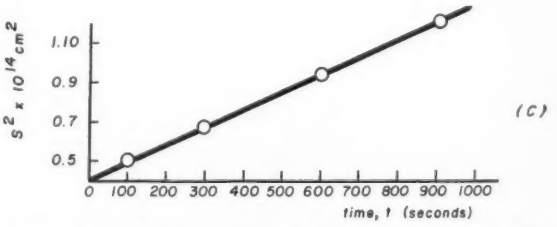

Fig. 1c Dependence of square of the effective radius of cloud vs. time

for D is close to, but is not equivalent to the mean displacement squared $(\bar{s})^2$ for one dimension. However, a sodium release in the atmosphere is a problem of diffusion in *three dimensions*. Moreover, the observed variable is brightness, which is obtained by integrating the number of particles along the line of sight, thus reducing the problem to that of diffusion in two dimensions. Then, their D-value of 8.5×10^{10} cm^2 sec^{-1}, as obtained from Fig. 1c, should be divided by π or 4 depending upon the nature of the operations involved in the observation.

This problem can be resolved by another independent analysis of Shklovskii and Kurt's data as noted in Fig. 1c. The graph depicts the observed time behavior of the square of the effective radius, which is defined as that distance from the cloud center to the isophote having one eth the brightness

Received March 22, 1961.

[1] Work performed under Contract AF 19(604)-7269 with Air Force Cambridge Research Labs.

[2] Manager, Atmospheric Physics Dept. Member ARS.

[3] Director, Space Sciences Lab. Member ARS.

[4] Numbers in parentheses indicate References at end of paper

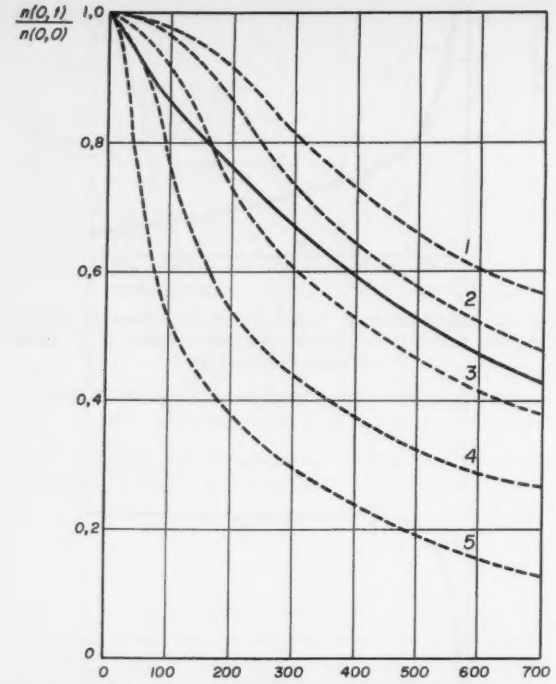

Fig. 2 Relative concentration of sodium atoms as a function of time for the center of cloud. Solid line = experimental curve; dashed lines = family of curves for various values of diffusion coefficient D. Curve 1, $D = 0.37410^{11}$; curve 2, $D = 0.45 \times 10^{11}$; curve 3, $D = 7.4 \times 10^{11}$; curve 4, $D = 1.47 \times 10^{11}$; curve 5, $D = 2.95 \times 10^{11}$

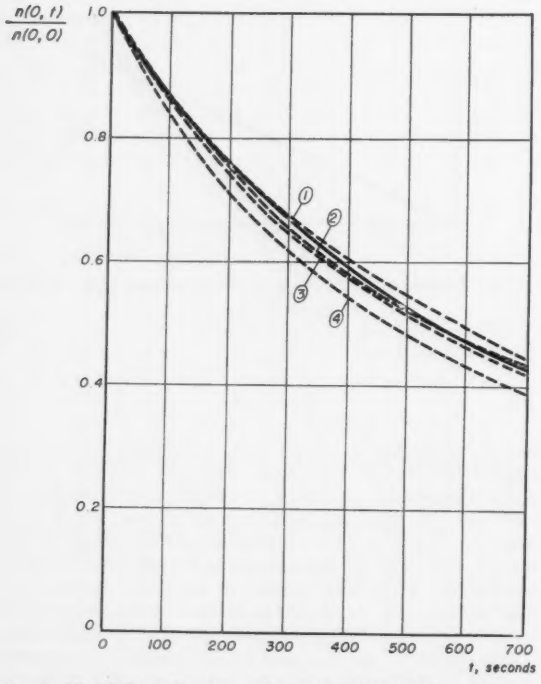

Fig. 3 Fit of Gaussian form of centerpoint density to observed centerpoint variation for: curve 1, $D = 1.6 \times 10^{10}$; curve 2, $D = 1.72 \times 10^{10}$; curve 3, $D = 1.8 \times 10^{10}$; curve 4, $D = 2 \times 10^{10}$ ($cm^2\ sec^{-1}$), equals experimental value

of the center. From Pressman et al. (3) a Gaussian distribution $S(r, t)$ can be expressed as

$$S(r, t) = \frac{N_T}{\pi(r_0^2 + 4Dt)} \exp - \frac{r^2}{(r_0^2 + 4Dt)} \qquad [3]$$

where

S = total number of atoms in line of sight (for the case of sodium S can be taken as surface brightness in photons/cm^2sec)
N_T = total number of resonant atoms in cloud
r_0 = half-width of Gaussian, at $t = 0$
D = diffusion coefficient

The effective radius can be defined here as

$$r_e^2 = r_0^2 + 4Dt \qquad [4]$$

For two values of time t_1 and t_2 (3)

$$D = \frac{r_e(t_2)^2 - r_e(t_1)^2}{4(t_2 - t_1)} \qquad [5]$$

and

$$r_0^2 = \frac{t_2 r_e(t_1)^2 - t_1 r_e(t_2)^2}{t_2 - t_1} \qquad [6]$$

This formulation points up the correction factor of four. Hence, the measurements shown in Fig. 1c now give a $D = 2.1 \times 10^{10}$ $cm^2 sec^{-1}$ for the present analysis. As pointed out by the two authors under discussion, the display of a high degree of linearity in Fig. 1c indicates a good Gaussian behavior; consequently, the present value of D as computed by the effective radius technique should have high validity. Comments on Shklovskii and Kurt's analysis of the centerpoint brightness follow.

They have also determined a D-value of 5.9×10^{10} cm^2 sec^{-1} from an analysis of the time variation of the centerpoint brightness as shown in Fig. 1a. In an additional analysis, they utilize the equation for the centerpoint density for a spherical cloud of initial *constant* density $n(0, 0)$ of radius r_0 at $t = 0$, namely

$$\frac{n(0, t)}{n(0, 0)} = \psi\left[\frac{r_0}{2(Dt)^{1/2}}\right] - \frac{r_0}{(4\pi 0t)^{1/2}} \exp\left(-\frac{r_0^2}{4Dt}\right) \qquad [7]$$

where

$$\psi(z) = \frac{2}{(\pi)^{1/2}} \int_0^z e^{-\xi^2} d\xi$$

Shklovskii and Kurt used the following approximation

$$\frac{n(0, t)}{n(0, 0)} = \left(\frac{S(0, t)}{S(0, 0)}\right)^{3/2} \qquad [8]$$

where $S(0,t)$ and $S(0,0)$ are observables [see Fig. 1a]. Fig. 2 represents their attempt to fit Eq. 8 by plotting the $n(0,t)/n(0, 0)$ ratios for various values of D (the dotted curves) from Eq. 7. The solid curve is generated from the approximation in Eq. 8. It is important to note that they compute an r_0 value for Eq. 7 at $t = 270$ sec (on the real time scale) by relating the total particle count of a *uniform* sphere to that of the observed *Gaussian* distribution at this time. This procedure for using the time variation of the centerpoint brightness leads to an error because of their use of a uniform distribution at a time when the distribution has already become Gaussian. Moreover, the Shklovskii-Kurt approximation of the square well model in Eq. 7 is true exactly only for a Gaussian. Thus, an inconsistency exists which is in contradiction with the stated observations. In order to be consistent and to obtain more valid results the Gaussian equivalent of Eq. 7 should be employed

$$\frac{n(0, t)}{n(0,0)} = \frac{r_0^3}{(r_0^2 + 4Dt)^{3/2}} \qquad [9]$$

A plot of this function is given in Fig. 3 where the zero time, as in Fig. 2, is at $t = 270$. It is seen that the shape of the computed curves is much more similar to the "actual" curve and that the best fit gives $D = 1.6$ to 1.8×10^{10} cm^{2}sec^{-1} suggested here rather than between 5.9 to 8.5×10^{10} cm^{2}sec^{-1} as suggested by Shklovskii and Kurt. Hence, density values they obtained should be increased proportionately.

Finally, it is appropriate to include here some remarks concerning their arguments for establishing altitude limits for the experiments. For example, the lower altitude for usefulness of the "sodium cloud" technique was set at 200 km. Experiments carried out by Marmo et al. (4) in "doping" artificial electron clouds have established the usefulness of this technique down as far as 100 km. The half-life for consumption of alkali atoms has also been computed (5) where at 100 km this is approximately 10^4 sec; this is not a deterrent to the use of the alkalies at this altitude for clouds lasting 10 to 15 min as is suggested by Shklovskii and Kurt. Moreover, Pressman et al. (3) have shown that even with chemical consumption occurring under certain conditions, the reduction of the optical data and the computation of the diffusion coefficient cannot be precluded. Indeed, the restriction against experimentation for altitudes below 100 km is more often due to the problem of the background and illumination under twilight conditions for small solar angles rather than the problem of chemical consumption.

References

1 Shklovskii, I. S. and Kurt, V. G., "Determination of Atmospheric Density at a Height of 430 Km by Means of the Diffusion of Sodium Vapors," ARS JOURNAL, vol. 30, no. 7, July 1960, pp. 662–667.

2 Harris and Jastrow, Naval Nuclear Research Laboratory, Washington, Fifth General Assembly of SC IGY 30, June 1958.

3 Pressman, J., Brown, H. K. and Marmo, F. F., "Chemical Release Studies VII; Resonance Clouds With Diffusion for Various Initial Release Geometries," Tech. Rep., AFCRL-207, Jan. 1960.

4 Marmo, F. F., Aschenbrand, L. and Pressman, J., *Planetary Space Sci.*, vol. I, 1959, p. 227.

5 Marmo, F. F., Aschenbrand, L. and Pressman, J., *Planetary Space Sci.*, vol. I, 1959, p. 291.

Shock Wave Asymmetry for Cones and Sphere Cones at Angle of Attack

ROBERT A. GREENBERG[1] and STEPHEN C. TRAUGOTT[2]

The Martin Company, Baltimore, Md.

IN A recent note Gonor (1)[3] points out that for supersonic or hypersonic flow about a right circular cone at angle of attack there exist conditions for which the shock layer on the windward side of the body is thicker than that on the shadow side instead of as in the opposite and more conventional case. He further points out that the shock can therefore also be a concentric cone just as for zero incidence. It is the purpose of this note to discuss this behavior in somewhat greater detail and to show that a similar phenomenon can exist for blunted cones.

As mentioned by Gonor, the situation is easily illustrated by supersonic flow over a wedge. Whether the shock layer on the wind and shadow sides grows or shrinks with angle of attack is simply described by the derivative of shock wave angle with respect to flow deflection angle. If this is less than unity the windward shock layer thins and the shadow side shock layer thickens with respect to zero incidence conditions. This will be called the normal case, following Gonor. When the derivative of shock wave angle with respect to deflection angle is greater than unity the windward shock layer thickens, and this is here designated as the reversed case. A boundary between normal and reversed conditions as a function of flight Mach number M_∞ and body semiapex angle θ is simply established on the basis of unity for this derivative; it is easily calculated, for instance, from (2). The resulting boundary (for $\gamma = 1.4$) is shown in Fig. 1 as line A.

The same procedure can be followed for conical flow at zero incidence using the charts from (2), ignoring the effects of cross flow which now complicate the situation. θ is now the cone semiapex angle. A similar boundary is found as before, shown in Fig. 1 as line B. This is not the real boundary between normal and reversed conditions; it is shown only to illustrate that except for the effect of cross flow, the axially symmetric and two-dimensional cases exhibit basically the same behavior.

To determine the extent of the cross-flow influence it is necessary to examine solutions for cones at angle of attack. For small angles of attack the solution of Stone as modified by Sims (3) has been used, together with some additional similar numerical computations, to establish line C in Fig. 1 as a boundary for normal and reversed conical shock layers. The solution of Gonor, valid for hypersonic flow, can be shown to lead to the boundary D in Fig. 1. It can be seen that these two solutions agree very well for $M_\infty > 4$ and give boundaries that are qualitatively similar to the others. For very large Mach numbers the difference between axially symmetric and

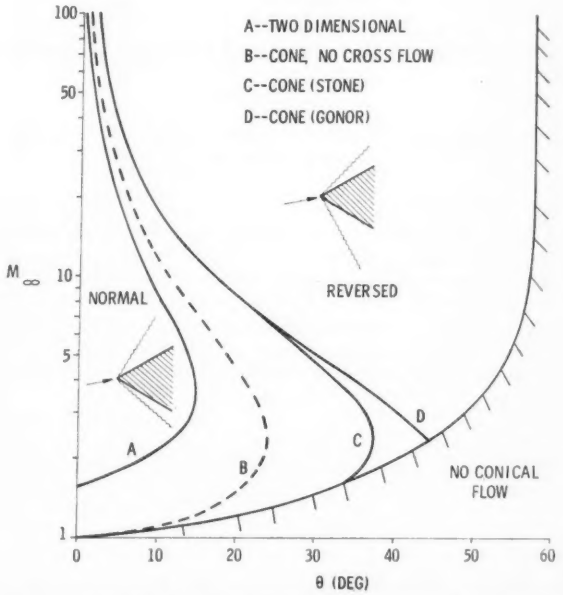

Fig. 1 Boundaries between normal and reversed shock layers, ratio of specific heats 1.4

Received Jan. 30, 1961.

[1] Senior Engineer, Aerophysics Research Staff.

[2] Chief, Aerophysics Research Staff.

[3] Numbers in parentheses indicate References at end of paper.

Fig. 2 Reversed regime, $M_\infty = 5.0$, 47.5 deg sphere cone, 7 deg angle of attack

two-dimensional flow disappears, and both wedges and cones of large semiapex angle will have a thicker shock layer on the windward side.

Blunting a cone leads to a layer of high entropy near the surface. It is known, however, that despite this layer both surface pressure and shock shape for a blunted cone at zero incidence approach asymptotically their conical values. If this is still true at angle of attack, then the same distinction between normal and reversed conditions regarding the shock layer should exist for blunted cones.

Zakkay (4) presents angle of attack shock shapes of a 20 deg semiapex angle cone blunted by a spherical cap at $M_\infty = 6.0$. These conditions fall to the left of the conical boundary in Fig. 1 in the normal regime, and an unblunted cone would have a thicker shock layer on the shadow side than on the windward side. The blunted cone shocks also have this behavior up to 15 deg angle of attack, the largest incidence shown in (4). A test recently performed[4] for a 47.5 deg sphere-cone at $M_\infty = 5.0$ and 7 deg angle of attack corresponds to the reversed regime and resulted in the shock shown in Fig. 2. It is seen that here the shock layer on the windward side is thicker than that on the shadow side. Thus the boundary between normal and reversed conditions established for cones can also be useful in predicting this phenomenon on blunted cones, at least for spherical blunting.

An interesting situation arises for a cone or wedge blunted by another cone or wedge. It can be seen that there will exist a range of M_∞ such that the forebody is in the reversed regime while the afterbody is in the normal regime.

References

1 Gonor, A. L., "Location of Frontal Wave in Asymmetrical Flow of Gas at High Supersonic Speed Over a Pointed Body," ARS JOURNAL, vol. 30, no. 9, Sept. 1960, pp. 841–842 (Russian Supplement).

2 Ames Research Staff, "Equations, Tables, and Charts for Compressible Flow," NACA TR 1135, 1953.

3 Sims, J. L., "Supersonic Flow Around Right Circular Cones, Tables for Small Angle of Attack," ABMA Rep. no. DA-TR-19-60, April 1960.

4 Zakkay, V., "Pressure and Laminar Heat Transfer Results in Three-Dimensional Hypersonic Flow," WADC TN 58-182, Polytechnic Institute of Bklyn., Sept. 1958.

[4] Through the courtesy of Dr. Joseph Sternberg, Ballistic Research Laboratories, Aberdeen Proving Ground, Aberdeen, Md.

Correction Factor for Annular Nozzles

N. D. VLACHOS[1]

Allegany Ballistics Laboratory, Hercules Powder Company, Cumberland, Md.

A CORRECTION factor for the thrust obtained from annular nozzles can be derived using a method similar to that of Malina and Tsien (1).[2] Such a factor accounts for the deviation in direction of the exhaust gases from the direction of the rocket centerline. What follows is based on the assumption that the nozzle surfaces are conical (as opposed to contoured) and that the exhaust velocity is constant (i.e., is the same at any point on the curvilinear exit surface shown in Fig. 1).

Analysis

The problem is to derive a coefficient λ for use in the thrust equation

$$F = \lambda \dot{m} V_e + (P_e - P_a) A_e \qquad [1]$$

when calculating thrust of an annular nozzle.

Referring to Fig. 1, the mass discharged from a rocket is the product of the gas density, gas velocity, and curvilinear area

$$\dot{m} = \rho V_e A_e \qquad [2]$$

The coefficient in question can be determined from the equation

$$\lambda \dot{m} V_e = \int_{A_p} V_{e_z} d\dot{m} \qquad [3]$$

Finding the area element

$$\Delta A_e = r \Delta\phi \Delta r$$

where

$$r = r_t + R \sin\theta \text{ and } \Delta r = R\Delta\theta$$

Then

$$\dot{m} V_e = \rho V_e^2 R \int_0^{2\pi} \int_{-\beta}^{\alpha} (r_t + R \sin\theta) d\theta d\phi$$
$$= 2\pi\rho V_e^2 R[r_t(\alpha + \beta) - R(\cos\alpha - \cos\beta)] \qquad [4]$$

Similarly, knowing that $V_{e_z} = V_e \cos\theta$

Received April 4, 1961.

[1] Supervisor, Mathematics Group. Now Senior Applications Engineer, Hercules Powder Company, Wilmington, Del. Member ARS.

[2] Numbers in parentheses indicate References at end of paper.

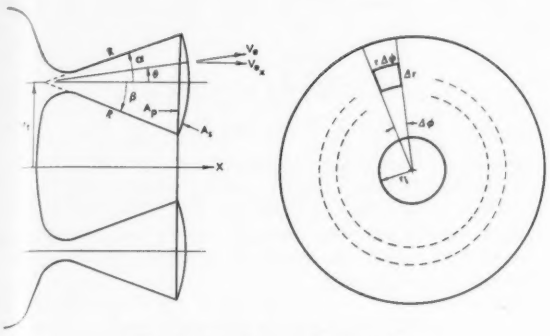

Fig. 1 Annular nozzle geometry

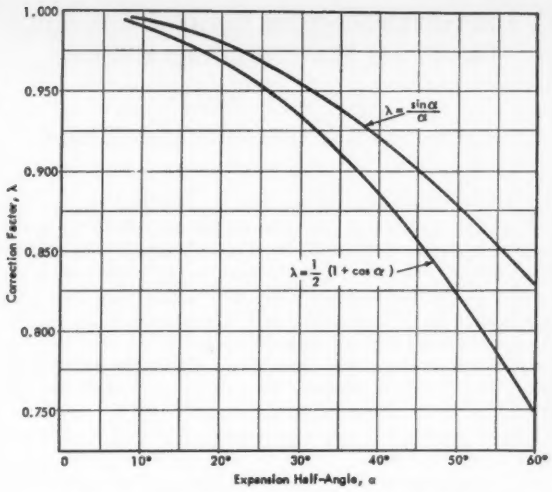

Fig. 2 Comparison of nozzle correction factors

$$\int_{A_p} V_{e_x} d\dot{m} = \rho V_e^2 R \int_0^{2\pi} \int_{-\beta}^{\alpha} \cos\theta (r_i + R\sin\theta) d\theta d\phi = 2\pi\rho V_e^2 R[r_i(\sin\alpha + \sin\beta) + R/2(\sin^2\alpha - \sin^2\beta)] \quad [5]$$

From Eqs. 3, 4, and 5

$$\lambda = \frac{r_i(\sin\alpha + \sin\beta) + R/2(\sin^2\alpha - \sin^2\beta)}{r_i(\alpha + \beta) - R(\cos\alpha - \cos\beta)} \quad [6]$$

Equation 6, admittedly cumbersome, can be simplified by letting $\alpha = \beta$; then

$$\lambda = \frac{\sin\alpha}{\alpha} \quad [7]$$

This is the simplest and probably most common case.

The significance of this result can be seen by considering the correction factor developed in (1) for conventional conical nozzles, namely

$$1/2(1 + \cos\alpha) \quad [8]$$

It is evident that

$$\frac{\sin\alpha}{\alpha} > 1/2(1 + \cos\alpha) \quad [9]$$

for values of α appropriate for nozzle design (the limiting case is $\lambda(0) = 1$), thus indicating a superiority of annular nozzles over conventional types. See Fig. 2.

There are certain restrictions to the use of Equation 7. Since $\alpha = \beta$, and remembering that R is constant, the areas formed at the exit by the outer and inner cones (for the latter it may be an apex only) must lie in the same plane. If $r_i = 0$ and, also, if the apex of the inner cone is upstream of the exit area, the slant height of the inner cone is less than R and the derivation is not applicable. However, as the center plug becomes shorter, r_i is decreasing and the configuration is approaching that of a conventional nozzle.

It is to be noted that Eq. 6 represents a general case. For a conventional nozzle, where $\beta = 0$ and $r_i = 0$, it reduces to the well-known expression [8].

This derivation resulting in Eq. 6 ignores the pressure and velocity differences between the plane and curvilinear exit areas. A further correction for these differences is given by Landsbaum (2), although he maintains the use of such a factor gives a negligible change in the resulting thrust.

Conclusion

The thrust of an annular nozzle, for which the expansion angles for the inner and outer cones are the same, α, and further, for which both cones terminate on the same plane, can be calculated from the equation

$$F = \frac{\sin\alpha}{\alpha}\dot{m}V_e + (P_e - P_a)A_e \quad [10]$$

Nomenclature

A	=	area
F	=	thrust
$\dot{m}$	=	mass rate of flow
P	=	pressure
R	=	slant height
r	=	radius
V	=	velocity
α, β	=	angles, fixed
θ, ϕ	=	angles, variable
λ	=	correction factor
ρ	=	density

Subscripts

a	=	ambient
e	=	exit
i	=	inner
p	=	plane
s	=	curvilinear
t	=	throat
x	=	x-direction

References

1 Malina, F. J., "Characteristics of the Rocket Motor Unit Based on the Theory of Perfect Gases," *J. Franklin Institute*, vol. 239, 1940, pp. 448–449.

2 Landsbaum, E. M., "Thrust of a Conical Nozzle," ARS JOURNAL, vol. 29, no. 3, March 1959, pp. 212–213.

Unique Cross-Spin Control Concept for Fixed Fin Sounding Rockets

RUSSELL A. NIDEY[1]

Kitt Peak National Observatory, Tucson, Ariz.[2]

THE CROSS spin (vector sum of yaw and pitch) of an axially symmetrical rigid body such as a fixed fin sounding rocket does not admit to direct control by body fixed jets, in the presence of spin, because of the precession of the vehicle. Furthermore, synchronous reinforcement of the cross spin by vehicle asymmetry during ascent (termed dynamic instability or, erroneously, coupling of roll into yaw) may result in inordinate cross spin. Excessive aerodynamic drag and disadvantageous "flat spin" over apogee are both produced by undue cross spin.

By articulating a pair of transverse jets such that the resulting control torque is continually opposed to the instantaneous cross spin, direct control of the cross spin is achieved independent of spin (1).[3] This propitious separation of variables is accomplished by the use of velocity coordinates rather than by the conventional body coordinates in Euler's equations of motion (2).

Let M_η, M_ξ and M_ζ be the components of the external torques in the frame of reference described by the orthogonal axes η, ξ and ζ, where η is in the direction of the cross spin and ζ is the axis of symmetry. Then Euler's equations of motion are as follows

$$M_\eta = I_\eta\dot{\omega}_\eta + (I_\zeta - I_\xi)\omega_\zeta\omega_\xi \qquad [1]$$

$$M_\xi = I_\xi\dot{\omega}_\xi + (I_\eta - I_\zeta)\omega_\eta\omega_\zeta \qquad [2]$$

$$M_\zeta = I_\zeta\dot{\omega}_\zeta + (I_\xi - I_\eta)\omega_\xi\omega_\eta \qquad [3]$$

where I_η, ξ, ζ and ω_η, ξ, ζ are the principal moments of inertia and corresponding components of angular velocity, respectively. Noting that ω_ξ is continuously zero by definition of the frame of reference, these equations simplify to the following

$$M_\eta = I_\eta\dot{\omega}_\eta \qquad [4]$$

$$M_\xi = I_\xi\dot{\omega}_\zeta + (I_\eta - I_\zeta)\omega_\eta\omega_\zeta \qquad [5]$$

$$M_\zeta = I_\zeta\dot{\omega}_\xi \qquad [6]$$

respectively. Hence, the cross spin and the spin are independently controllable, and the precessional nature of the motion is neatly confined to one equation, Eq. 5. It should, however, be noted that only because of the axial symmetry are we able to use the rotating (relative to the vehicle) transverse principal axes.

Fortuitously, the implementation of the cross-spin control system is equally elegant. An orthogonal pair of sensitive transverse rate gyros mounted with sensitive axes normal to the axis of symmetry provides transducers for both control loops: one gyro for the articulation servoloop and the second for the cross-spin servoloop. The former is a position servo and requires appropriate phase compensation, whereas the latter is a velocity servo and is therefore inherently stable. The articulation actuator would logically be an electrical motor, whereas the cross-spin actuator, an opposed pair of cold gas jets.

Articulated transverse control would be particularly valuable on sounding rockets both to stabilize the aspect of the vehicle and to thwart the dynamic instability during ascent.

References

1 Nidey, R. A., "Aspect Sensing, Astrostat Design and Orientation Control in Space Research," ARS preprint 1016-59, Nov. 1959.

2 Slater, J. C. and Frank, N. H., *Mechanics*, McGraw-Hill Book Co., Inc., N. Y., 1947, p. 105.

Received April 12, 1960.

[1] Systems Manager, Space Div. Member ARS.

[2] Operated by the Association of Universities for Research in Astronomy, Inc., under contract with the National Science Foundation.

[3] Numbers in parentheses indicate References at end of paper.

Staging of Cruising Vehicles[1]

M. ARENS[2]

Technion—Israel Institute of Technology, Technion City, Haifa, Israel

ALTHOUGH staging has been primarily considered for application to ballistic vehicles, it has also been applied to cruising vehicles, such as aircraft launching of standoff missiles. The purpose of this note is to define optimum staging requirements for cruising vehicles.

If the flight trajectory of each stage is broken down into

1 climb and/or acceleration to cruising speed and altitude

2 useful cruise to point of separation or destination

3 non-useful cruise after separation, if required

then the mass ratio of the ith stage during the useful cruise is

$$\frac{W_{1i}}{W_{2i}} = \frac{\mu_i}{\mu_{ai}} \qquad [1]$$

where μ_i denotes the mass ratio for climb and acceleration, and useful cruise, and μ_{ai} denotes the mass ratio for climb and acceleration.

If the range attained during climb and acceleration is neglected, then the useful range of the ith stage is given by the Breguet range equation

$$R_{ci} = C_i \ln (\mu_i/\mu_{ai}) \qquad [2]$$

where C_i represents the range factor $V_i/(sfc)_i(L/D)_i$. The total useful range of an n-staged vehicle is therefore

$$R_c = \sum_{i=1}^{n} C_i \ln \frac{\mu_i}{\mu_{ai}} \qquad [3]$$

Considering each stage as constituting the payload of the preceding stage, the overall payload ratio of the vehicle can be written as

$$\Lambda = \prod_{i=n}^{n} \lambda_i \qquad [4]$$

where λ_i represents the payload ratio W_{0i+1}/W_{0i}, of the ith stage. The optimum staging relationship is the one giving the maximum value of Λ.

The requirement for the optimum solution is therefore that

$$\frac{1}{C_i}\frac{\mu_i}{\lambda_i}\frac{\partial\lambda_i}{\partial\mu_i} = -\zeta \qquad i = 1,2,\ldots,n \qquad [5]$$

Received March 6, 1961.

[1] This note is based on Technion-Department of Aeronautical Engineering Report No. 5.

[2] Senior Lecturer, Department of Aeronautical Engineering.

where ζ is a constant for all stages. If the range factor and the relationship between payload ratio and mass ratio for each stage are known, the optimum distribution of stage mass ratios is given by Eq. 5. Their absolute value depends on the total range to be covered and is obtained by solving Eq. 3.

The payload ratio of each stage is a function of μ_i, μ_{ai}, the structural weight ratio k_i, and the non-useful range that may have to be covered by the stage after separation, such as landing, return to point of takeoff, etc. The latter requirement may be expressed by the ratio r_i of the non-useful range to useful range, and would normally be between 0 and 1. Thus the payload ratio λ_i may be written as

$$\lambda_i = \lambda_i(\mu_i, \mu_{ai}, k_i, r_i) \qquad [6]$$

The structural weight ratio, k_i, expresses the stage structure weight as a function of some of the characteristic parameters of the stage. This functional relationship may depend on the aerodynamic configuration of the stage, its powerplant, and the relative weight distribution between air-frame, engine, and fuel. For the purpose of this analysis three cases will be considered

$$W_{si} = k_i W_{0i} \qquad [7a]$$

$$W_{si} = k_{si} W_{0i} + k_{fi} W_{fi} \qquad [7b]$$

$$W_{si} = \frac{k_i W_{fi}}{1 - k_i} \qquad [7c]$$

Based on these relations the following relationships between the payload ratio and the other stage parameters are obtained

$$\lambda_i = \frac{1}{\mu_i} - k_i \left(\frac{\mu_i}{\mu_{ai}}\right)^{r_i} \qquad [8a]$$

$$\lambda_i = \frac{k_{fi}\left[\frac{1}{\mu_i}\left(\frac{\mu_i}{\mu_{ai}}\right)^{-r_i} - 1\right] + \frac{1}{\mu_i}\left(\frac{\mu_i}{\mu_{ai}}\right)^{-r_i} - k_{si}}{\left(\frac{\mu_i}{\mu_{ai}}\right)^{-r_i} - k_{fi}\left[1 - \left(\frac{\mu_i}{\mu_{ai}}\right)^{-r_i}\right]} \qquad [8b]$$

$$\lambda_i = \frac{\frac{1}{\mu_i} - k_i \left(\frac{\mu_i}{\mu_{ai}}\right)^{r_i}}{1 - k_i(\mu_i/\mu_{ai})^{r_i}} \qquad [8c]$$

Substituting Eq. 8 into Eq. 5 the following relations for the optimum stage mass ratios are obtained

$$\frac{\frac{1}{\mu_i} + r_i k_i \left(\frac{\mu_i}{\mu_{ai}}\right)^{r_i}}{C_i\left[\frac{1}{\mu_i} - k_i\left(\frac{\mu_i}{\mu_{ai}}\right)^{r_i}\right]} = \zeta \quad i = 1, 2, \ldots, n \qquad [9a]$$

$$\frac{(1 + k_{fi})\left(\frac{\mu_i}{\mu_{ai}}\right)^{-r_i}\left\{\frac{(r_i + 1)}{\mu_i}\left[\left(\frac{\mu_i}{\mu_{ai}}\right)^{-r_i}(1 + k_{fi}) - k_{fi}\right] - r_i\left[\frac{\mu_i^{-(r_i+1)}}{\mu_{ai}^{-r_i}}(1 + k_{fi}) - (k_{si} + k_{fi})\right]\right\}}{C_i\left[\left(\frac{\mu_i}{\mu_{ai}}\right)^{-r_i}(1 + k_{fi}) - k_{fi}\right]\left[\frac{\mu_i^{-(r_i+1)}}{u_{ai}^{-r_i}}(1 + k_{fi}) - (k_{si} + k_{fi})\right]} = \zeta$$

$$i = 1, 2, \ldots, n \qquad [9b]$$

$$\frac{\frac{1}{\mu_i}\left[1 - k_i\left(\frac{\mu_i}{\mu_{ai}}\right)^{r_i}\right] - r_i k_i \left(\frac{\mu_i}{\mu_{ai}}\right)^{r_i}\left(\frac{1}{\mu_i} - 1\right)}{C_i\left[\frac{1}{\mu_i} - k_i\left(\frac{\mu_i}{\mu_{ai}}\right)^{r_i}\right]\left[1 - k_i\left(\frac{\mu_i}{\mu_{ai}}\right)^{r_i}\right]} = \zeta$$

$$i = 1, 2, \ldots, n \qquad [9c]$$

Eqs. 9 and 3 represent n equations in the n unknown μ_i's, allowing solution for the optimum stage mass ratios.

Nomenclature

C_i	=	$V_i/(sfc)_i(L/D)_i$, range factor in cruise of ith stage
k_i	=	structural weight ratio of ith stage
k_{fi}	=	fuel tank structural weight ratio of ith stage
k_{si}	=	structural weight ratio without fuel tanks of ith stage
$(L/D)_i$	=	cruising lift-to-drag ratio of ith stage
n	=	number of stages
R_c	=	total useful range
R_{ci}	=	useful range of ith stage
r_i	=	ratio of non-useful to useful range of ith stage
$(sfc)_i$	=	specific fuel consumption of ith stage
V_i	=	cruising velocity of ith stage
W_i	=	weight of ith stage
W_{fi}	=	fuel weight of ith stage
W_{si}	=	structural weight of ith stage
W_{oi}	=	initial weight of ith stage
ζ	=	stage constant
Λ	=	vehicle payload ratio
λ_i	=	payload ratio of ith stage
μ_i	=	mass ratio of ith stage for climb and/or acceleration, and cruise to point of separation
μ_{ai}	=	mass ratio of ith stage for climb and/or acceleration

Subscripts

a	=	acceleration and climb
s	=	structure
0	=	take off or separation
1	=	beginning of cruise
2	=	end of useful cruise

"Pinhole Camera" for Determination of Plasma Arc Rotational Speed[1]

E. A. BUNT[2] and H. L. OLSON[3]

The Johns Hopkins University, Silver Spring, Md.

AT HIGH power operation, the current density in the arc column of a plasma jet is of the order of 10^6 amp/cm^2. If one or both electrodes are of metal, serious local melting or erosion will thus occur unless the points of attachment of the arc to the electrodes are rapidly changed. This is a process normally carried out at low pressures by inducing a hydrodynamic vortex in the process gas and at high pressures by rotating the arc column in a manner similar to an armature under the action of the force F, given by

$$F = j \times B$$

where j and B are the vectors of arc current and externally imposed magnetic field strength. Such a mode of operation makes it desirable to know the mean peripheral velocity of the arc column on account of its relationship to both the electrode cooling and to other parameters which determine the arc characteristics. Although high pressure arcs are necessarily operated inside a pressure vessel, the mean peripheral velocity may be easily determined even without the use of windows. This is done by observing the arc rotation with the aid of the apparatus shown diagrammatically in Fig. 1, which also illustrates the fore-mentioned principles of arc rotation. The increased brightness of the arc column as it passes the field of view of the phototube over that of the gaseous plasma through which it is viewed is illustrated by the typical periodic output trace shown in Fig. 2. The brilliance of the source is such that the restriction of luminous flux by the "pinhole" is a considerable advantage, together with the fact that a gross rotation count does not of itself require a sharp image. Variations between successive trace amplitudes are ascribed to cyclical differences in the intensity and length of the arc presented to the field of view. This form of measurement is most satisfactory when the pressure of arc operation is high (several hundred psi), in order that the arc column be most contracted, and so yield unambiguous images. Under these conditions rotation rates are also more regular. The filter and mask shown are by no means essential and a relatively crude external optical system would suffice to enable the viewing tube to be more remotely located if desired. Since normal rotation rates are less than a couple of thousand per second, conventional recording oscillographic equipment is satisfactory.

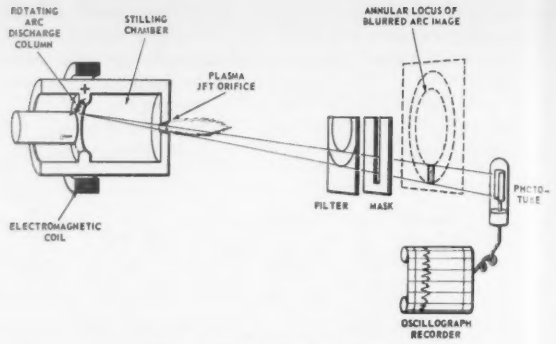

Fig. 1. Principle of operation

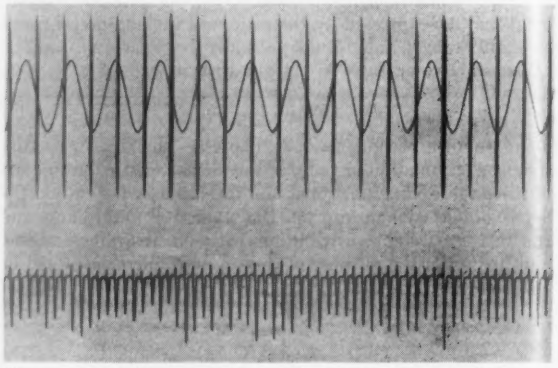

Fig. 2. Typical arc rotation timing trace (retouched for reproduction) 60 cps timing wave shown for comparison

Received April 22, 1961.

[1] This work was sponsored by the Bureau of Naval Weapons, U. S. Navy, under Contract NOrd 7386.

[2] Physicist

[3] Group Supervisor, Propulsion Facility

Contact Surface Tailoring in a Chemical Shock Tube[1]

HOWARD B. PALMER[2] and BRUCE E. KNOX[3]

College of Mineral Industries, The Pennsylvania State University, University Park, Pa.

FOR THE study of gaseous reaction kinetics using a single-pulse ("chemical") shock tube, it is usually desirable to "tailor" the driver-driven gas interface, or contact surface, to prevent multiple shock reflections or rarefactions (1).[4] Tailoring consists of making a type of acoustic impedance match between the driver gas and the shocked gas, so that the reflected shock coming off the end of the shock tube passes through the contact surface at unchanged shock strength. This can be accomplished by adjusting the composition of driver gas or driven gas. Because a single-pulse shock tube typically employs argon as the driven gas, with a few per cent added of the gas to be reacted, the most obvious procedure in tailoring is to adjust the composition of the driver.

A reasonable driver gas combination is a mixture of helium and argon. With the driver initially at room temperature, this system can produce tailored shocks in argon at reflected shock temperatures up to as high as approximately 3300 K.

Received Dec. 2, 1960.

[1] This work was supported by Project SQUID, under the Office of Naval Research, Department of the Navy, contract Nonr 1858(25) NR-098-038. Reproduction in full or in part is permitted for any use of the United States Government.

[2] Professor and Head, Department of Fuel Technology.

[3] Research Assistant, Department of Fuel Technology.

[4] Numbers in parentheses indicate References at end of paper

This is high enough for study of most reactions that are amenable to the single-pulse technique. H_2-N_2 mixtures as driver gas combinations can yield still higher temperatures under tailored interface conditions.

Since we have computed a set of tailoring conditions for changing driver gas composition, and since we have not found any previous publication of the results of such computations, our results are presented with the thought that they may be useful to others making use of single-pulse shock tubes for chemical studies. The calculations are idealized as follows:

1 The diaphragm bursts perfectly.
2 There is no shock wave attenuation.
3 The system is one-dimensional.
4 The driven gas is pure argon.
5 All heat capacities are independent of temperature.
6 Heat capacities at constant volume of H_2 and N_2 are both equal to 2.5 R/mole K.
7 Molecular weights are $H_2 = 2$, He = 4, $N_2 = 28$, Ar = 40.

These simplifications are warranted because tailoring calculations can best serve merely as a guide for setting the driver gas conditions. Achievement of tailoring can be established only by observing a pressure record, or the equivalent, in the actual experimental run. It may be noted that in our own experiments, we have found the computations to be very helpful.

The requirement for tailoring the contact surface is that the specific internal energy ratio of the gases in regions 2 and 3 (see Fig. 1) obey the following relation (2)

$$E_{32} = e_3/e_2 = (\alpha_3 + P_{25})/(\alpha_2 + P_{25}) = (\bar{C}_{v_3}T_3/\bar{M}_3)/(\bar{C}_{v_2}T_2/\bar{M}_2) \qquad [1]$$

When a noble gas mixture is driving a noble gas, $\bar{C}_{v_3} = \bar{C}_{v_2}$, $\gamma_3 = \gamma_2$, and $\alpha_3 = \alpha_2$. The requirement then leads to the condition, $E_{32} = 1$, from which $\rho_3 = \rho_2$. This is sometimes cited as an approximate rule for tailoring. From an experimental point of view, however, one wishes to know a good deal more than a simple rule of this sort. Specifically, one would like to know what driver gas composition and bursting ratio to use in order to produce a particular temperature in a tailored shock wave.

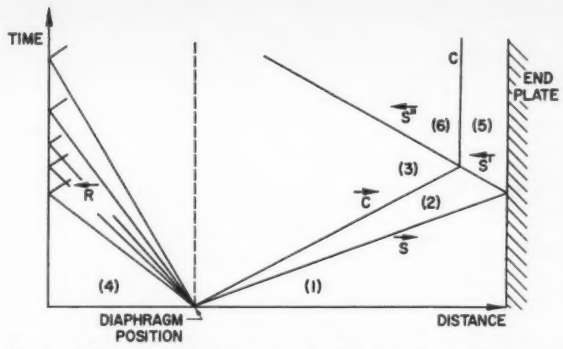

Fig. 1 Typical x-t diagram for a single pulse shock tube under "tailored" interface conditions. $\overleftarrow{R}$ = rarefaction fan; $\vec{S}$ = primary shock; $\overleftarrow{S'}$ = reflected shock; $\overleftarrow{S''}$ = reflected shock after transmission through contact surface; $\vec{C}$ = contact surface; C = stationary contact surface. The various gas regions are numbered.

Eq. 1 can be rewritten as

$$\bar{M}_4/\bar{M}_1 = (\bar{C}_{v_4}/\bar{C}_{v_1})T_{34}T_{12}(\alpha_1 + P_{25})/(\alpha_4 + P_{25}) \qquad [2]$$

Table 1 Tailoring conditions for Ar, using He-Ar or H_2-N_2 mixtures as driver gas. Initial conditions: $T_1 = T_4 = 298.2$ K

P_{21}	X_{He} (He-Ar)	P_{41} (He-Ar)	X_{H2} (H_2-N_2)	P_{41} (H_2-N_2)	ρ_{51}	T_b, deg K	$U_s \times 10^{-4}$, cm/sec
3.00	0.629	7.30	0.233	7.37	3.096	702	5.19
3.50	0.683	9.38	0.319	9.48	3.500	795	5.58
4.00	0.725	11.63	0.392	11.73	3.863	888	5.94
4.50	0.759	13.89	0.449	14.09	4.193	979	6.28
5.00	0.788	16.34	0.498	16.58	4.486	1071	6.60
5.50	0.815	18.58	0.538	19.02	4.755	1161	6.90
6.00	0.832	21.20	0.572	21.75	5.000	1252	7.20
7.00	0.866	26.45	0.630	27.05	5.435	1431	7.75
8.00	0.892	31.87	0.676	32.7	5.792	1614	8.27
9.00	0.914	37.35	0.714	38.6	6.100	1792	8.76
10.00	0.930	43.10	0.744	44.4	6.368	1973	9.22
13.00	0.968	60.48	0.811	62.2	6.997	2515	10.51
17.35	1.000	86.32	0.870	89.3	7.586	3292	12.08

P_{21}	ρ_{21}	T_{21}	ρ_{52}	P_{52}	T_{52}	T_{51}	P_{51}	$U_{RL} \times 10^{-4}$, cm/sec
3.00	1.857	1.615	1.667	2.430	1.457	2.353	7.29	3.60
3.50	2.000	1.750	1.750	2.667	1.524	2.667	9.33	3.72
4.00	2.125	1.882	1.818	2.875	1.582	2.977	11.50	3.85
4.50	2.235	2.013	1.876	3.059	1.631	3.283	13.77	3.96
5.00	2.333	2.143	1.923	3.222	1.675	3.590	16.11	4.09
5.50	2.421	2.272	1.964	3.367	1.714	3.894	18.52	4.20
6.00	2.500	2.400	2.000	3.499	1.749	4.198	20.99	4.32
7.00	2.635	2.657	2.061	3.733	1.810	4.805	26.13	4.55
8.00	2.750	2.909	2.106	3.917	1.860	5.411	31.34	4.77
9.00	2.850	3.160	2.140	4.070	1.902	6.011	36.63	5.00
10.00	2.929	3.415	2.174	4.214	1.938	6.618	42.14	5.21
13.00	3.118	4.170	2.243	4.533	2.021	8.440	58.92	5.75
17.35	3.297	5.261	2.301	4.831	2.099	11.044	83.82	6.42

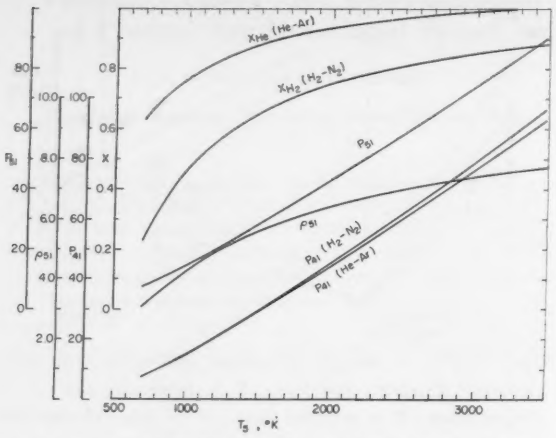

Fig. 2 Computed tailoring conditions for reflected shocks in argon, using as a driver gas He-Ar or H_2-N_2 mixtures, for the temperature range 700 K to 3500 K

where use has been made of the conditions: $\tilde{M}_1 = \tilde{M}_2$, $\tilde{M}_3 = \tilde{M}_4$, $\tilde{C}_{v_1} = \tilde{C}_{v_2}$, $\tilde{C}_{v_3} = \tilde{C}_{v_4}$, $T_{23} = T_{21}T_{14}T_{43}$, and $T_{14} = 1$. (Both driver and driven gases start at room temperature.)

Glass (2) shows that

$$T_{43} = (P_{41}P_{12})^{2\beta_4} \quad [3]$$

$$P_{25} = (1 + \alpha_1 P_{12})/(\alpha_1 + 2 - P_{12}) \quad [4]$$

$$T_{21} = P_{21}(\alpha_1 + P_{21})/(\alpha_1 P_{21} + 1) \quad [5]$$

P_{41} may be eliminated from Eq. 3 by using the ideal bursting equation

$$P_{41} = P_{21}/\{1 - (P_{21} - 1)[\beta_4 E_{14}/(\alpha_1 P_{21} + 1)]^{1/2}\}^{1/\beta_4} \quad [6]$$

E_{14} may be replaced by $(\tilde{C}_{v1}\tilde{M}_4/\tilde{C}_{v_4}\tilde{M}_1)$ since $T_{14} = 1$. The combination of Eqs. 2–6 then yields $(\tilde{M}_1/\tilde{M}_4)$ as a function of P_{21}. One can then solve for $\tilde{M}_4$ for various assumed values of P_{21}. In our computations, $\tilde{M}_4$ was expressed in terms of the mole fraction of the lighter constituent, namely He, in the case of He-Ar mixtures, and H_2 for the H_2-N_2 mixtures. Computations for He-Ar mixtures were done with a desk calculator. For H_2-N_2 drivers, a slide rule was used because further refinement did not seem justified.

Once the driver gas compositions are computed, the other shock conditions follow. Of particular interest are

$$\rho_{21} = P_{21}/T_{21} \quad [7]$$

$$P_{52} = (\alpha_1 + 2 - P_{12})/(\alpha_1 P_{12} + 1) \quad [8]$$

$$T_{52} = P_{52}(\alpha_1 + P_{52})/(\alpha_1 P_{52} + 1) \quad [9]$$

$$T_{51} = T_{52}T_{21} \quad [10]$$

$$\rho_{52} = P_{52}/T_{52} \quad [11]$$

$$\rho_{51} = \rho_{52}\rho_{21} \quad [12]$$

the incident shock velocity

$$U_s = a_1[\beta_1(\alpha_1 P_{21} + 1)]^{1/2} \quad [13]$$

and the velocity of the reflected shock relative to the laboratory

$$U_{RL} = a_1\beta_1^{1/2}\{[T_{21}(\alpha_1 P_{52} + 1)]^{1/2} - (1 - \rho_{12})(\alpha_1 P_{21} + 1)^{1/2}\} \quad [14]$$

In Table 1 are collected the results of the calculations. Fig. 2 shows some of the variables of interest, plotted over a reflected shock temperature range from 700 K to about 3500 K. It may be of interest to remark that pure H_2 at a P_{41} of 304 is computed to produce a tailored reflected shock in Ar at a T_5 of 9130 K. Ionization probably means that this shock would not in fact be tailored, but it illustrates the fact that one can indeed produce very hot shocks and retain the tailoring characteristics.

Nomenclature

X = mole fraction
$\tilde{M}$ = molecular weight
$\tilde{C}_v$ = constant-volume heat capacity per mole
e = internal energy per unit mass
α = $(\gamma + 1)/(\gamma - 1)$
β = $(\gamma - 1)/2\gamma$
ρ = density
T = absolute temperature
P = pressure
a = velocity of sound
γ = $\tilde{C}_p/\tilde{C}_v$
T_{ij} = T_i/T_j
P_{ij} = P_i/P_j
ρ_{ij} = ρ_i/ρ_j
E_{ij} = e_i/e_j

References

1 Glick, H. S., Klein, J. J. and Squire, W., *J. Chem. Phys.*, vol. 27, 1957, p. 850.

2 Glass, I. I., *UTIA Rev.* no. 12, part I, Inst. Aerophys., University of Toronto, May, 1958.

Adiabatic Nozzle Flows

R. A. A. BRYANT[1]

The University of New South Wales, Kensington, Australia

IN A RECENT note (1)[2] Snyder has discussed the problem of nonisentropic flow in nozzles to demonstrate that critical ($M = 1$) conditions can occur at the throat only if the flow is isentropic. He states that there is sometimes a misunderstanding concerning the location of the critical area; and this is certainly true, since people using one-dimensional theory to design nozzles do not worry about precise detail, nor do they often consider the adequacy of one-dimensional theory.

As it happens, the subject of nonisentropic nozzle flow is well documented: for background the reader is referred to a series of interesting arguments recorded in *Aircraft Engng.* from 1951 through 1953. More recently the present author has made a detailed study of one-dimensional nonisentropic nozzle flow theories (2) which shows that, though adequate for many practical purposes, they are far from precise.

For example, consider the adiabatic efficiency used by

Received Jan. 30, 1961.

[1] Senior Lecturer in Mechanical Engineering.

[2] Numbers in parentheses indicate References at end of paper.

Snyder as a measure of irreversibility effects. Suppose p_1, T_1, M_1 refer to some datum point in the subsonic portion of the nozzle. Subsequent states in the flow are assumed to follow an adiabatic (i.e., polytropic) state path law. Because the isentropic stagnation temperature is constant in any adiabatic flow, it is possible to relate all states on the assumed state path back to a common stagnation condition $T_{0_1} = T_0$; $M = 0$. Hence the adiabatic efficiency is defined as

$$\eta = \frac{V^2}{V'^2} = \frac{AB}{AC} \qquad [1]$$

$$\eta = \frac{T_{0_1} - T}{T_{0_1} - T'} \qquad [2]$$

where T and T' both lie on the same isobar (Fig. 1). When Eq. 2 is written as

$$\eta = \frac{1 - T/T_{0_1}}{1 - T'/T_{0_1}} \qquad [3]$$

and it is noted that T'/T_{0_1} represents the temperature ratio corresponding to isentropic expansion from p_{0_1} to p, we see that

$$\eta = \frac{1 - T/T_{0_1}}{1 - (p/p_{0_1})^{(\gamma - 1/\gamma)}} \qquad [4]$$

Clearly, if the flow is shock free, $\eta = \eta(x)$ should be a single valued function determined by the temperature and pressure distributions $T = T(x)$, $p = p(x)$ corresponding to real (adiabatic) flow conditions. For η to be of use in predicting details of real conditions it must be known in advance: and it cannot be! Almost invariably it is assumed to be of constant magnitude and this immediately puts $T = T(p)$; $p = p(x)$ or $p = p(T)$; $T = T(x)$. Thus the entropy function is given by a one-parameter law

$$S(x) = S[T(p), p(x)] \qquad [5]$$

rather than by the more general two-parameter law

$$S(x) = S[T(x), p(x)] \qquad [6]$$

necessary if a spectrum of real flows is to be covered by the mathematical model.

We can see what is implied by assuming η to be constant, by writing

$$T/T_{0_1} = (T_1/T_{0_1})(T/T_1)$$
$$= (p_1/p_{0_1})^{(k-1)/k}(p/p_1)^{(n-1)/n} \qquad [7]$$

where it is tacitly assumed that the real process follows a simple polytrope (n = constant).

Using Eq. 7 in Eq. 4 there results

$$\eta = \frac{1 - (p_1/p_{0_1})^{(k-1)/k}(p/p_1)^{(n-1)/n}}{1 - (p/p_{0_1})^{(k-1)/k}} \qquad [8]$$

and it becomes obvious that η cannot be constant if n is constant and vice versa. Hence we automatically preclude the possibility of using simple state path laws in any analysis based on constant adiabatic efficiency.

A variable exponent $n = n(x)$ is defined by each value of η. From Eq. 8 it is found to be given by

$$n(x) = \log (p/p_1) \Big/ [(\log p/p_1 + (k-1)/k \log p_1/p_{0_1} - \log \{1 - \eta[1 - (p/p_{01})^{(k-1)/k}]\})] \qquad [9]$$

where $p = p(x)$.

The entropy gradient can be found by considering an element of the expansion process and thus writing

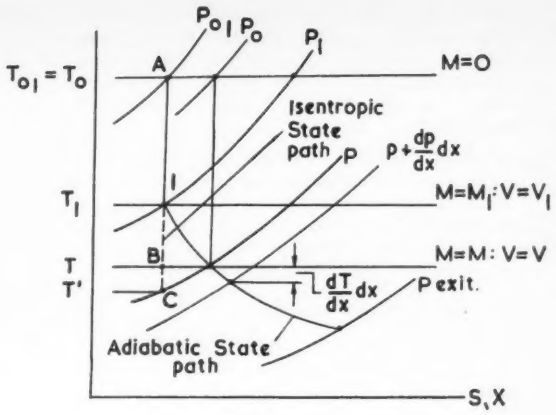

Fig 1

$$\left[\left(p + \frac{dp}{dx}\,dx\right)\Big/p\right] = \left[\left(T + \frac{dT}{dx}\,dx\right)\Big/T\right]^{n/(n-1)} \qquad [10]$$

Expanding the right-hand side of Eq. 10 as a binomial series, and neglecting small order terms, we obtain

$$\frac{d \ln p}{dx} = \frac{n}{n-1}\frac{d \ln T}{dx} \qquad [11]$$

which can be used in a statement of the second law, viz.,

$$\frac{dS}{dx} = C_P \frac{d \ln T}{dx} + R \frac{d \ln p}{dx} \qquad [12]$$

to find

$$\frac{dS}{dx} = R\left(\frac{k}{k-1} \cdot \frac{n-1}{n} + 1\right)\frac{d \ln p}{dx}$$
$$= \Phi(p(x)) \qquad [13]$$

by Eq. 9.

It should also be noted that the arithmetic of Snyder's paper can be simplified by using the local reduced velocity $N = V/(2C_PT_0)^{1/2}$ rather than the local Mach number M. The relationship between M and N is

$$M^2 = \left(\frac{2}{k-1}\right)\left(\frac{N^2}{1-N^2}\right) \qquad [14]$$

and when this is used in Snyder's Eq. 10 it is found that

$$G' = \left(\frac{2}{k-1}\right)^{1/2} \cdot \frac{N}{1-N^2}\left(1 - \frac{N^2}{\eta}\right)^{k/(k-1)} \qquad [15]$$

which is similar to a result obtained by Crocco (3) and leads to

$$N_t^2 = N^{*2}\{1 - k(1-\eta) + 0[(1-\eta)^2]\} \qquad [16]$$

An alternative demonstration that the throat velocity is subsonic can be obtained by using the concept of polytropic efficiency: although there are still inadequacies in the basic mathematical model one gets a concise result

$$M_t = (n-1)/(k-1) \qquad [17]$$

where $n < k$ is constant if the polytropic efficiency is constant. Eq. 17 is found to apply to both adiabatic and diabatic flows with constant polytropic efficiency (4).

Nomenclature

C_P = specific heat at constant pressure
G' = dimensionless mass velocity
k = ratio of specific heats
M = local Mach number
N = local reduced velocity
n = exponent of polytropic state path law
p = pressure
p_0 = isentropic stagnation pressure
R = gas constant
S = entropy
T = absolute temperature
T_0 = isentropic stagnation temperature
V = velocity
x = distance along nozzle
η = adiabatic nozzle efficiency
Φ = entropy function (see Eq. 13)

Subscripts

1 = datum point in nozzle
t = condition at throat
$*$ = values under critical ($M = 1$) conditions
$'$ = primed variables indicate values for isentropic process

References

1 Snyder, W. T., "Nonisentropic Nozzle Flow," ARS JOURNAL, vol. 30, no. 3, March 1960, pp. 270–271.
2 Bryant, R. A. A., "One Dimensional Irreversible Gas Flow in Nozzles," University of New South Wales, Bull. no. 3, 1960.
3 Crocco, L., "Fundamentals of Gas Dynamics," High Speed Aerodynamics and Jet Propulsion, vol. 3, Princeton University Press, 1958, p. 118.
4 Bryant, R. A. A. "Diabatic Nozzle Flow with Constant Small Stage Efficiency," *J. Roy. Aeron. Soc.*, vol. 64, no. 598, Oct. 1960, pp. 632–634.

Nonmatrix Formulation of an Eulerian Angle Vector Transformation

RICHARD F. LEACH[1]

The Martin Co., Baltimore, Md.

A GENERAL rotation of a coordinate system changes or transforms the numerical values of the component representation of a fixed vector. The problem of relating the components in the old (unprimed) coordinate system to components in the new (primed) coordinate system is a common engineering problem. A general rotation of a coordinate system is usually given in terms of Eulerian angles. A matrix is usually used to solve the coordinate transformation problem.

We shall assume Eulerian angles ϕ, θ, ψ where the first rotation is about the z-axis and denoted by ϕ. The second rotation is about the new x-axis and denoted by θ. The third is about the new z-axis and denoted by ψ.

Another set of Eulerian angles would lead to different equations of the same complexity.

This letter will give a nonmatrix solution of the transformation problem. In this solution, the vector will be expressed in polar coordinates r (radius), A (azimuth), C (coelevation), rather than in Cartesian coordinates. Since r is the same in the old and new systems, the problem is to express A', C' of the new system in terms of A, C of the old system.

This nonmatrix approach is based upon spherical trigonometric identities; see Fig. 1.

The azimuth and coelevation about the z-axis are denoted by A_z,C_z, and about the x-axis by A_x,C_x. Spherical trigonometry shows that

$$\cos C_z = \sin C_x \cos A_x \qquad \cos C_x = \sin A_x \sin C_z \quad [1]$$

Take the old coordinate system and the first Eulerian angle ϕ. After the rotation, the components of the vector in the rotated system are

$$C_{z1} = C \qquad A_{z1} = A - \phi$$

where the subscript z means that z is the reference axis and 1 means that the system has been rotated once. Using Eq. 1, we can express $A_{x1}C_{x1}$ in terms of $A_{z1}C_{z1}$.

The second rotation, θ, equates $A_{x1}C_{x1}$ and $A_{x2}C_{x2}$

$$C_{x1} = C_{x2} \qquad A_{x2} = A_{x1} - \theta$$

Eqs. 1 are used again and rotation is then performed. The equations of the entire process are

$$\begin{aligned} \cos C_{x2} &= \sin C \cos (A - \phi) \\ \cos C &= \sin (A_{x2} + \theta) \sin C_{x2} \\ \cos C_{x2} &= \sin C' \cos (A' + \psi) \\ \cos C' &= \sin A_{x2} \sin C_{x2} \end{aligned} \quad [2]$$

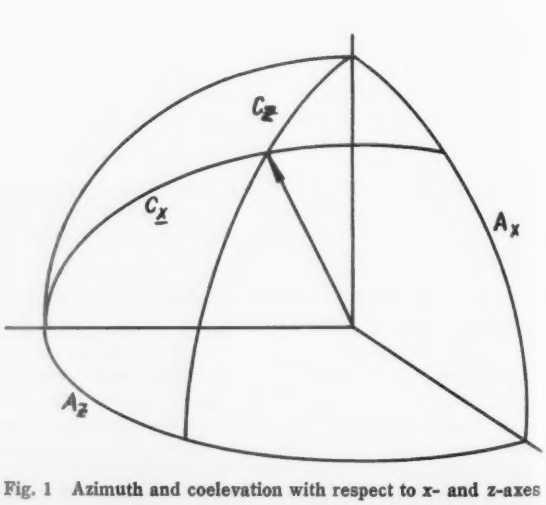

Fig. 1 Azimuth and coelevation with respect to x- and z-axes

Received March 2, 1961.

[1] Electronics Div.

Some care must be taken to ensure proper choice of quadrants of the solution of Eqs. 2.

Whether one wishes to use this transformation or the usual matrix formulation depends upon the problem and the means available for solution. It should be noted that in the matrix solution, the matrix is a function of the coordinate rotation and is independent of the vector being transformed. If many vectors are to be transformed by a fixed set of Eulerian angles, rather than by a varying set, the matrix need be calculated only once. If Eqs. 2 are used, each calculation must be completed in its entirety—whether the Eulerian angles vary or not.

In many problems, the vector is expressed originally in spherical coordinates. This means that the coordinates must be transformed into Cartesian coordinates before the matrix can be used. In some of these cases the components, after the rotation, must be changed back into spherical coordinates. If the problem is solved by machine, the fastest method and therefore the most desirable one would depend upon the speed of solution. Whether the matrix or nonmatrix solution is faster depends upon the problem statement and the specific machine used.

If calculations are to be done by hand, the nonmatrix Eqs. 2 offer certain advantages. With a log sin x table, the calculation is just a series of look-ups, additions and subtractions. If only a sin x table is available, the use of these trigonometric identities

$$2 \sin a \cos b = [\sin (a + b) + \sin (a - b)]$$
$$2 \sin a \sin b = [\cos (a - b) - \cos (a + b)]$$

simplifies the problem to table look-ups, additions, subtractions, and two divisions. If the problem is stated in spherical coordinates and analog devices are used, the nonmatrix solution is obviously much easier to implement.

The nonmatrix coordinate transformation of equations does offer a different approach to the problem, which has some advantages over the matrix solution.

Simplified Sudden-Freezing Analysis for Nonequilibrium Nozzle Flows[1]

K. N. C. BRAY[2]

University of Southampton, Southampton, England

A simplified "sudden-freezing" analysis for nonequilibrium nozzle flows is used to show that the thermodynamic state of the gas after freezing is independent of the reservoir enthalpy. The flow through a given nozzle may then be represented on a single Mollier-type diagram for a wide range of reservoir conditions. Such diagrams are presented for an ideal dissociating gas and for a simple model of air.

NONEQUILIBRIUM nozzle flows are of importance in many propulsion problems (1).[3] In principle, such problems may be solved by a step-by-step integration of the governing equations for one-dimensional flow with specified chemical reactions (2), but the computations may be very lengthy, particularly if many reactions are involved. Simplified methods of analysis are therefore required.

One such method is the "sudden-freezing" analysis (2). For flow with a single chemical reaction, this method consists of assuming that the gas remains in complete equilibrium until a particular point in the nozzle, called the sudden freezing point, has been reached. Thereafter, the flow is assumed to be frozen with constant composition. The sudden freezing point is determined from an empirical equation such as that suggested by Bray (2). This simple method cannot be expected to predict correctly all the flow variables a long way downstream in the nozzle, where the reaction has ceased. A basic error arises because it does not take account of the entropy increase occurring in the real flow due to the reaction. However, the method has been found to give results in quite good agreement with more accurate calculations, for nozzles with large area ratios. Extension to flows with many reactions has been discussed by Bray and Appleton (3).

Received Feb. 1, 1960.

[1] The research reported in this document has been sponsored in part by the Wright Air Development Div., Air Research and Development Command, United States Air Force, through its European Office, under Contract no. AF 61(052)-250.

[2] Lecturer, Department of Aeronautics and Astronautics.

[3] Numbers in parentheses indicate References at end of paper.

Sudden Freezing Analysis for an Ideal Dissociating Gas

The notation used here is that of Bray (2). An empirical equation to determine the point in the flow at which sudden freezing occurs may be written (2)

$$\left(\frac{d\alpha}{dt}\right)_e = K r_{D_e} \qquad [1]$$

where

e = equilibrium
α = dissociation fraction by mass
t = time
K = constant, expected to be of order unity
r_D = gross rate of dissociation

In terms of the dimensionless thermodynamic quantities introduced by Lighthill (4), and using Freeman's equation for the rate of dissociation (5), together with a hyperbolic distribution of the nozzle area ratio A, Eq. 1 becomes

$$\left[\frac{\sqrt{A-1}}{A}\,\frac{A(\alpha, T)}{B(\alpha)T^3 + C(\alpha)T^2 + D(\alpha)T - E(\alpha)}\right]_{ef} = 2K\Phi\left[\left(\frac{T}{T_0}\right)^{-s}\frac{\rho}{v}(1-\alpha)e^{-1/T}\right]_{ef} \qquad [2]$$

where

$A(\alpha, T) = 4\alpha T(1 + \alpha - 3T)(1 - \alpha)(i_0 - i)$
$B(\alpha) = (7 + \alpha)(4 + \alpha)(2 - \alpha) - 3\alpha(1 - \alpha)$
$C(\alpha) = 2\alpha(1 - \alpha)(1 + \alpha) - 6(2 - \alpha)(i_0 - \alpha)$
$D(\alpha) = 3\alpha(1 - \alpha)(3 + \alpha)$
$E(\alpha) = 2\alpha(1 - \alpha)(i_0 - \alpha)$

The suffix f refers to the sudden freezing point. The quantity Φ is a dimensionless dissociation rate parameter, which is related to the nozzle size and area ratio, as well as the dissociation rate constant. Using the experimental data of Mathews (6) for oxygen dissociation, Φ takes the value 3×10^{12} for the flow of oxygen through a typical nozzle 2 m in length with an area ratio of 1000. There is still some doubt about the value of the temperature exponent s in Eq. 2. Following

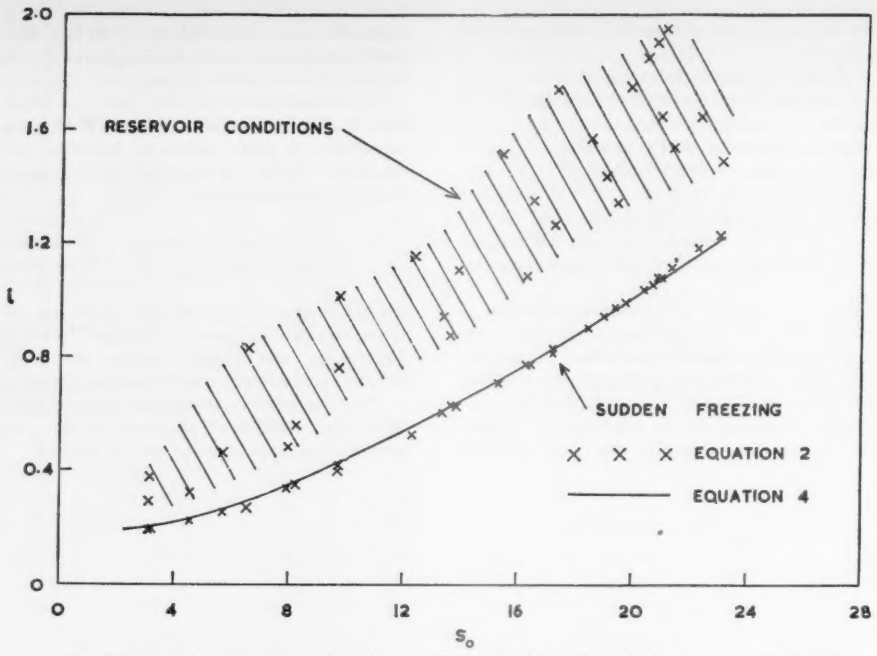

Fig. 1 Reservoir and sudden freezing conditions for ideal dissociating gas, $\Phi = 3 \times 10^{12}$

(2), it is set equal to zero in the present analysis, and the rate constant has been evaluated at 3000 K. Using the one-dimensional flow conservation equations and the equations of state for an ideal dissociating gas in equilibrum, Eq. 2 may be reduced to a complicated expression in α_f, T_f and the reservoir enthalpy i_0. If this is solved together with the equilibrium isentropic expression

$$s_0 = 3 \ln T + \frac{1+\alpha}{T} + \alpha + 2 \ln\left(\frac{\alpha}{1-\alpha}\right) + \text{constant} \quad [3]$$

where s_0 is the reservoir entropy and the constant may be set equal to zero, then numerical results may be obtained in the form $T_f = T_f(i_0, s_0)$ for given values of K and Φ. Use of the equations of state then yields the sudden freezing enthalpy $i_f = i_f(i_0, s_0)$ together with the other thermodynamic variables.

The accuracy of these results is limited not only by the approximate nature of the sudden freezing analysis but also by uncertainty as to the values of the quantities K and Φ. In order to get the best agreement with exact calculations, K must be varied by a factor of at least 3 for different reservoir conditions (7). The error in Φ arises partly from uncertainty as to the value of the rate constant, and also from lack of knowledge about the effective flow geometry. It seems likely that the total uncertainty in $K\Phi$ in Eq. 2 will be at least an order of magnitude. Eq. 2 will therefore be simplified, in order to obtain i_f more easily to within the limited accuracy of the method.

Lighthill's reduced temperature T is small under conditions of interest, so the terms in T_f^3 and T_f^2 on the left-hand side of Eq. 2 may be neglected. The left-hand side then becomes

$$\frac{\sqrt{A_f - 1}}{A_f} \cdot \frac{4T_f(1 + \alpha_f - 3T_f)(i_0 - i_f)}{3(3 + \alpha_f)T_f - 2(i_0 - \alpha_f)}$$

or

$$\frac{\sqrt{A_f - 1}}{A_f} \cdot \frac{4T_f(1 + \alpha_f - 3T_f)(i_0 - i_f)}{(1 + \alpha_f)T_f - 2(i_0 - i_f)}$$

Finally, if we neglect $3T_f$ in comparison with $(1 + \alpha_f)$, and $(1 + \alpha_f)T_f$ in comparison with $2(i_0 - i_f)$, we obtain an order of magnitude expression

$$-\frac{\sqrt{A_f - 1}}{A_f} 2T_f(1 + \alpha_f)$$

The right-hand side of Eq. 2 may be simplified by eliminating the density ρ_f using the equilibrium law of mass action (4). Then the sudden freezing condition becomes

$$\frac{\sqrt{A_f - 1}}{A_f} \frac{v_f}{K\Phi} = \frac{(1 - \alpha_f)^2}{\alpha_f^2(1 + \alpha_f)} \frac{e^{-2/T_f}}{T_f}$$

It must be recalled here that the uncertainty in evaluating the product $K\Phi$ is at least an order of magnitude. Calculations covering a very wide range of conditions show that, for given $K\Phi$, the quantity

$$v_f \frac{\sqrt{A_f - 1}}{A_f}$$

varies by a factor of no more than 2, which is insignificant in the present context. Therefore, the sudden freezing condition becomes

$$\frac{(1 - \alpha_f)^2}{\alpha_f^2(1 + \alpha_f)} \frac{e^{-2/T_f}}{T_f} = \text{constant} = G(\text{say}) \quad [4]$$

where G is evaluated from the given Φ, with $K = 1$ and a mean value of

$$v_f \frac{\sqrt{A_f - 1}}{A_f}$$

which will be taken to be 0.34 from previous calculations (2,7). Solution of Eq. 4 with the isentropic condition, Eq. 3, gives the sudden freezing point properties α_f and T_f as functions of s_0 only. Then i_f equals $i_f(s_0)$. This solution can be used to calculate a new value of G for a more accurate solution of Eq. 4. However, the corrections produced in this manner

proved to be quite negligible in the example given below.

Fig. 1, which is a plot of enthalpy against entropy, compares the results of Eqs. 2 and 4. The crosses within the shaded area all represent different reservoir conditions for nonequilibrium nozzle expansions. Below each of these will be found another cross representing the freezing point in an equilibrium isentropic nozzle expansion using Eq. 2 with $\Phi = 3 \times 10^{12}$ and $K = 1$. The full line represents sudden freezing for all reservoir conditions according to Eq. 4, again with $\Phi = 3 \times 10^{12}$ and $K = 1$. It will be seen that the agreement between the two theories is quite good, but more important for our present purpose, the prediction that i_f is independent of i_0 is very well substantiated by the more accurate calculations.

This means that, to the accuracy of the sudden freezing analysis, nonequilibrium nozzle flows may be represented as isentropes on a Mollier-type diagram, as shown in Fig. 2. Above the sudden freezing line, the flow is assumed to be in complete equilibrium for all reservoir conditions. Below this line α has the constant value α_f along a given isentrope, so the gas behaves as a perfect gas with $\gamma = [(4 + \alpha_f)/3]$. The line $T = 0$ occurs at finite enthalpy because of the energy which is stored in dissociated species even at infinite expansion ratios according to the present approximation. Fig. 2 is not a Mollier diagram in the accepted sense, as it can only be used to represent isentropic or nearly isentropic flows with specified geometry.

Step-by-step integrations (2) of the one-dimensional flow equations confirm the above conclusion, namely that nozzle flows with the same values of Φ and s_0 will pass through similar thermodynamic states, independent of the reservoir enthalpy i_0. Clearly, the reservoir entropy is a useful correlating parameter for such flows. The physical reason for this result is that an increase in reservoir pressure brings the gas closer to equilibrium, while an increase in reservoir temperature takes it further away from equilibrium. The effects of pressure and temperature changes therefore tend to cancel each other, if the reservoir state is moved along a line, such as an isentrope, in which both pressure and temperature increase.

Application to Air

The approach outlined above may also be used for flows with more complicated chemical composition. This will be illustrated using results taken from a paper (8) in which approximate solutions are obtained for the nonequilibrum flow of air in hypersonic nozzles. This work assumes a sudden freezing point for oxygen recombination, determined from a criterion (9) very similar to Eq. 1. Upstream of this point the flow is assumed to be in complete equilibrium, while the composition is completely frozen further downstream.

If these results are plotted in a manner similar to Fig. 1, it is found that once again i_f is a function of s_0 for a wide range of values. A mean sudden freezing curve has been drawn, Fig. 3, for the case in which the length l of (8) is 10 cm, and using Byron's rate constant for oxygen (10). The corresponding Φ is 2.4×10^{12}, which is very nearly the same as that considered above for the ideal dissociating gas.

A Mollier-type diagram for air under these conditions has been constructed (Fig. 3). It assumes complete equilibrium above the sudden freezing line, and constant composition

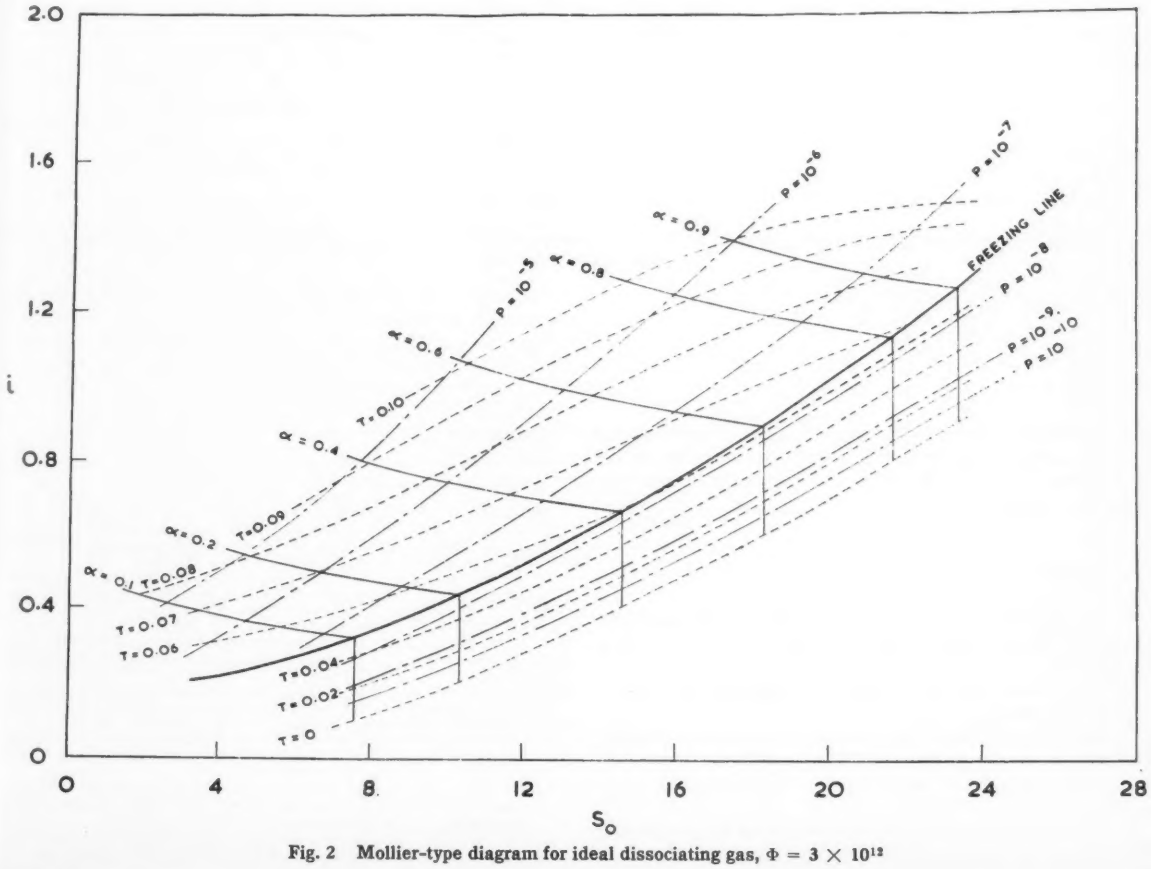

Fig. 2 Mollier-type diagram for ideal dissociating gas, $\Phi = 3 \times 10^{12}$

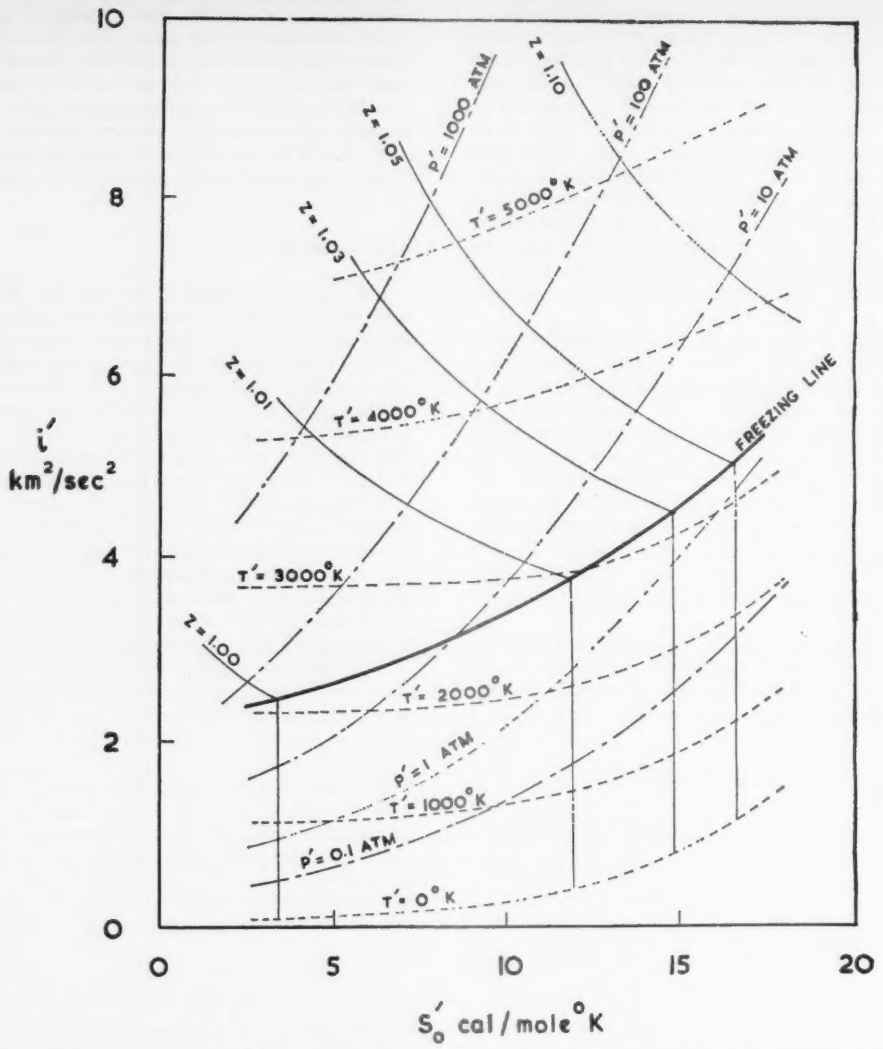

Fig. 3 Mollier-type diagram for air, using data from (8). The primes indicate dimensional quantities, and the zero of entropy has been chosen arbitrarily

along isentropes below the freezing line. The diagram shows the same general features as Fig. 2, but departure from equilibrium has a much smaller effect because of the presence of molecular nitrogen.

Conclusions

1 The reservoir entropy is a useful correlating parameter for nonequilibrium nozzle flows dominated by a single chemical reaction.

2 Such flows may be represented approximately on a Mollier-type diagram.

3 The errors involved in this very approximate analysis are likely to be no greater than those resulting from present uncertainty about the rates of many important chemical reactions.

4 Further work is required to see if similar techniques can be applied to flows with several chemical reactions.

References

1 Olsen, W. T., "Recombination and Condensation in Nozzles," presented at 2nd Int. Cong. of Aeron. Sci., Zurich, 1960.

2 Bray, K. N. C., "Atomic Recombination in a Hypersonic Wind Tunnel Nozzle," *J. Fluid Mech.*, vol. 6 part 1, July 1959, pp. 1–32.

3 Bray, K. N. C. and Appleton, J. P., "Atomic Recombustion in Nozzles: Methods of Analysis for Flows With Complicated Chemistry," Univ. Southampton Aero. and Astro. Rep. no. 166, 1961.

4 Lighthill, M. J., "The Dynamics of a Dissociating Gas, Part I, Equilibrium Flow," *J. Fluid Mech.*, vol. 2 part 1, Jan. 1957, pp. 1–32.

5 Freeman, N. C., "Nonequilibrium Flow of an Ideal Dissociating Gas," *J. Fluid Mech.*, vol. 4 part 4, Aug. 1958, pp. 407–425.

6 Mathews, D. L., "Interferometric Measurements in the Shock Tube of the Dissociation Rate of Oxygen," *Phys. Fluids*, vol. 2 part 2, March 1959, p. 170.

7 Bray, K. N. C. and Makin, B., "Recombination of Oxygen in a Nozzle; Comparison with Experimental Results for Air from General Electric Research Laboratory," U.S.A.A. Rep. no. 143, 1960.

8 Boyer, D. W., Eschenroeder, A. Q. and Russo, A. L., "Approximate Solutions for Nonequilibrium Airflow in Hypersonic Nozzles," Cornell Aeron. Lab., Rep. no. AD-1345-W-3, Aug. 1960.

9 Hall, J. G. and Russo, A. L., "Studies of Chemical Nonequilibrium in Hypersonic Nozzle Flows," Cornell Aeron. Lab., Rep. no. AD-1118-A-6, Nov. 1959.

10 Bryon, S., "Interferometric Measurement of the Rate of Dissociation of Oxygen Heated by Strong Shock Waves," Cornell University, 1958.

Irradiation of a Lunar Satellite[1]

W. LEON FRANCIS[2]

Lockheed Aircraft Corp., Burbank, Calif.

Estimations of the irradiation by the moon of a lunar satellite have been made as a function of altitude for three orbital positions using available experimental measurements of the lunar emissive and reflective power. The calculations indicate the importance of the irradiation by the moon for satellites whose orbit trajectories pass over the sunlit side of the moon. A value of 370 Btu/hr-ft² was computed for the irradiation of a surface element on the satellite which faces the subsolar point on the moon at an altitude of 100 miles.

THE RECENT emphasis on lunar satellite missions has placed a demand on determining the lunar emissive and reflective power, and the resulting irradiation by the moon of a lunar satellite. This determination is needed for maintaining a suitable thermal environment for the satellite's controls and electrical components.

In order for the lunar emissive and reflective power to be determined in the absence of an atmosphere, the temperature distribution over the surface and the surface characteristics must be known. The reflectivity of the lunar surface for solar radiation is generally given as 0.070 or slightly larger values (1,2,3).[3] Values for the emissivity of the lunar surface in the infrared spectrum, however, are largely undetermined. The computations which have been made of the lunar temperatures have usually assumed an emissivity of about unity. The computed surface temperature and assumed emissivity will then give the correct magnitude of emitted infrared radiation from the lunar surface. An assumed emissivity of unity is probably reasonable, in view of the nature of the lunar surface (3) and known characteristics of materials emitting radiation in the infrared.

Many computations of temperatures have been made from lunar radiation measurements. This radiation is partly reflected sunlight and partly direct surface emission. The separation of the reflected and direct emission for the purpose of calculating surface temperatures is accomplished by the use of a water cell. The water cell absorbs the infrared radiation and transmits most of the short wave length radiation. These measurements have been made with a reasonable degree of reliability at the subsolar point during full and half moon, at the terminator, and with less certainty of the results on the dark side of the moon, due to the low level of emission.

The most striking observations of lunar surface temperatures are those made during an eclipse of the moon. A temperature change at the same place of 270 F (from 160 to −110 F) has been observed in a period of only one hour. This fact, together with photometric and polarmetric observations, has led many observers to conclude that the lunar surface is covered with a coarse dust layer of extremely low thermal conductivity, since a high heat conducting material could not cool so rapidly. It is also concluded that the moon will have a fairly uniform, although low, temperature on the dark side, and the temperature on the sunlit side will vary by considerable amounts with increasing distance from the subsolar point because of the increasing angle between the sun's rays and the local normal to the surface. The temperature measurements tend to verify these conclusions and are summarized below for the locations previously mentioned:

Location	Temperature, °F
subsolar (at full moon)	214–264
subsolar (at half moon)	187–239
terminator (area between dark and sunlit sides)	−80
dark side	−244

On the basis of these observations and measurements, it is concluded that it is reasonable to assume that a thermal radiation equilibrium condition exists on the major sunlit portions of the moon's surface, since the amount of heat conducted into the moon's interior is probably negligible. This equilibrium condition would apply for all sunlit areas except those in the near vicinity of the terminator. Assuming a space temperature of 0 R, the surface temperature at any point on the sunlit side would be given approximately by

$$T_m = \left[\left(\frac{\alpha_s}{\epsilon_l}\right)\frac{S}{\sigma}\cos\theta_{M-S}\right]^{1/4} \qquad [1]$$

where

α_S = absorptivity in solar spectrum
ϵ_l = emissivity in infrared spectrum
S = solar irradiation normal to sun's rays
σ = Stefan-Boltzmann constant
θ_{M-S} = angle between normal to lunar surface and sun's rays

Calculations were made for the temperature distribution over the sunlit side for $(1 - \alpha_S) = 0.073$, $\epsilon_l = 1.0$, and $S = 443$ Btu/hr-ft² (value of the solar constant). These are presented in Fig. 1, where the experimental temperature measurements are also plotted. It is seen that the calculated distribution appears to agree well with the data, except, of course, at the terminator. In the region of the terminator, a linear extrapolation from $\theta = 75$ deg to the measured value at the terminator will be assumed for purposes of estimating the irradiation of a lunar satellite. A sharp drop at the terminator to a constant value of 216 R on the dark side will also be assumed.

In spherical coordinates, the irradiation of a surface element on the satellite may be computed from geometric considerations and assuming diffuse emission and reflection from

$$q_{\text{infrared spectrum}} = \frac{\epsilon_l}{\pi}\int_{\psi}\int_{\Omega} \times \frac{\sigma T_M^4 \cos\theta_M \cos\theta_P \cos\psi \, d\Omega d\psi}{(r/R)^2} \qquad [2]$$

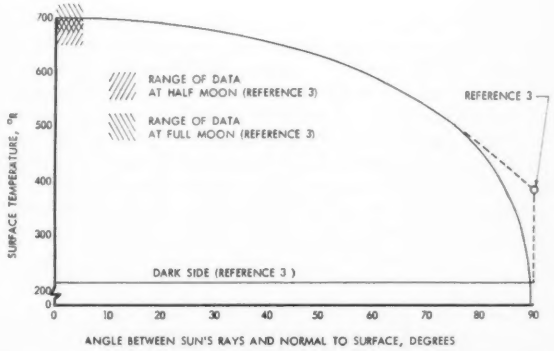

Fig. 1 Lunar surface temperatures

Received March 7, 1961.

[1] Based in part upon a thesis submitted to the University of California, Los Angeles, for the degree of M.S. in Engineering.

[2] Thermodynamics Engineer. Member ARS.

[3] Numbers in parentheses indicate References at end of paper.

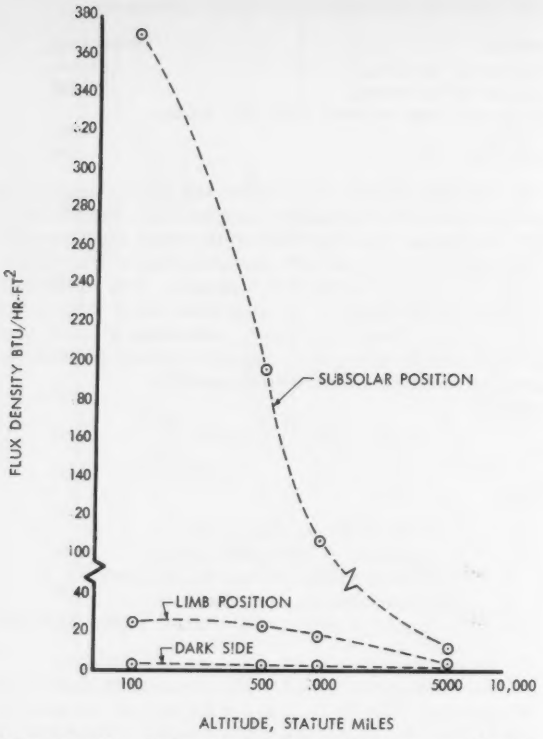

Fig. 2 Total irradiation of a satellite by the moon as a function of altitude for a surface element facing directly at the moon

$$q_{\text{solar spectrum}} = \frac{(1 - \alpha_S)S}{\pi} \int_{\psi}\int_{\Omega} \times \frac{\cos\theta_{M-S} \cos\theta_M \cos\theta_P \cos\psi d\Omega d\psi}{(r/R)^2} \quad [3]$$

$$q_{\text{total}} = q_I + q_S \quad [4]$$

where

R = radius of the moon
r = distance from satellite to element on the lunar surface (denoted as L)
θ_M = angle between normal to L and r
θ_P = angle between normal to surface element on satellite and r

Calculations were made on an IBM 7090 digital computer for a surface element on a satellite whose normal points directly at the center of the moon opposite the subsolar point, the terminator, and the dark side as a function of altitude. The results of these computations are presented in Fig. 2

These estimations serve to point out that lunar radiation will be important for lunar orbits whose trajectories pass over the sunlit side, with values of the irradiation comparable to the solar irradiation at the subsolar position, and at moderate altitudes of the order of 100 miles.

References

1 "Handbook of Chemistry and Physics," published annually by Chemical Rubber Publishing Co.
2 Forsythe, W. E., ed., "Smithsonian Physical Tables," Smithsonian Institution, 9th Rev. Edit., 1954.
3 Kiess, C. L. and Lassovsky, K., "The Known Physical Characteristics of the Moon and Planets," Georgetown College Observatory, ARDC TR 58-41, July 1958; also, ASTIA Doc. no. AD-115617.

Energy Requirements for Satellite Stabilization of the Gravitational Gradient

ROBERT R. WOLFE,[1] JOHN M. CORGAN[2] and PETER B. TEETS[3]

The Martin Company, Denver, Colo.

Satellite orientation about a gravitationally unstable reference is investigated to determine energy requirements for an attitude control system. The equations of motion are linearized and integrated to establish the natural mode of motion about the unstable axis. A limit cycle operation is established, using "on-off" reaction jets. Nomograms are provided for estimating the impulse requirements for long-term stabilization. The results are restricted to vehicle motion about the axis normal to the orbit plane, when the orbit is circular.

Received March 22, 1961.

[1] Design Specialist, Advanced Systems Analysis.
[2] Operations Research Specialist; also Instructor of Applied Mathematics, The University of Colorado.
[3] Technical Assistant, Advanced Systems Analysis.

THE GRAVITATIONAL gradient existing on a satellite is one of the major long-term disturbances experienced by a vehicle in orbit.[4] The torque producing gradient requires special attention because it acts continuously, whereas the majority of other disturbances are found to be random in nature. The motions involved are related to the body inertias and the orbit altitude. Nomograms are presented as a means of estimating the moment impulse required for stabilization about an axis normal to the orbit plane. Motion about the other axes as a result of the gravitational gradient will, in general, be stable. The results apply to rigid body motion and a satellite in a circular orbit.

The moment impulse per cycle and the cycle time required to stabilize the gravitational gradient are presented. The system is forced to lie between attitude limits by reaction jets. This defines the limit cycle operation of the control system. It is desirable to minimize the ratio of the impulse time to the total cycle time. The limit cycle is diagramed on a phase plane plot in Fig. 1.

The controlled motion is assumed to approach the asymptotes within 5% of the attitude rate, at the attitude

[4] Wolfe, R. R. and Arrow, B., "Gravitational Librations of a Satellite and The Influence on Control System Design," Space Tech. Labs., Canoga Park, Calif., AFBMD Fifth Symposium Aug. 29, 1960.

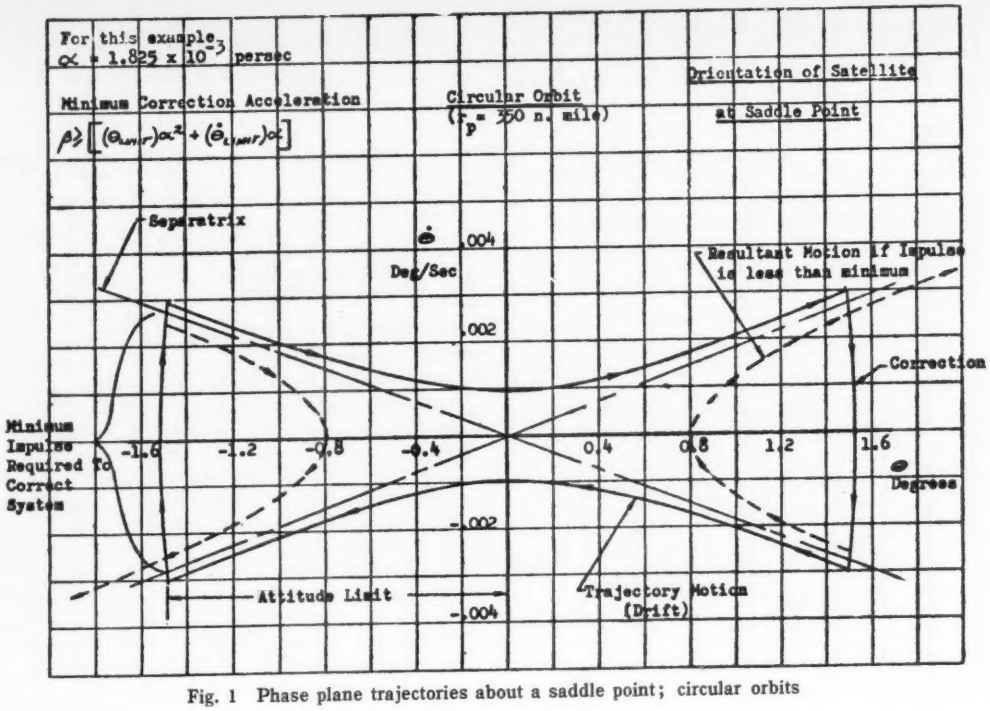

Fig. 1 Phase plane trajectories about a saddle point; circular orbits

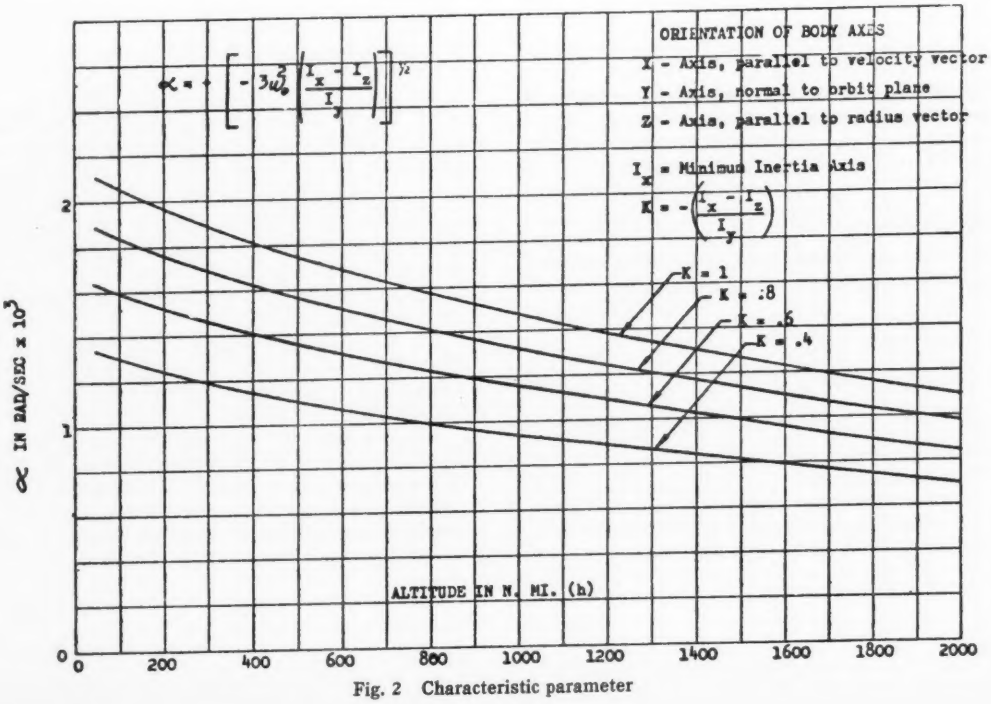

Fig. 2 Characteristic parameter

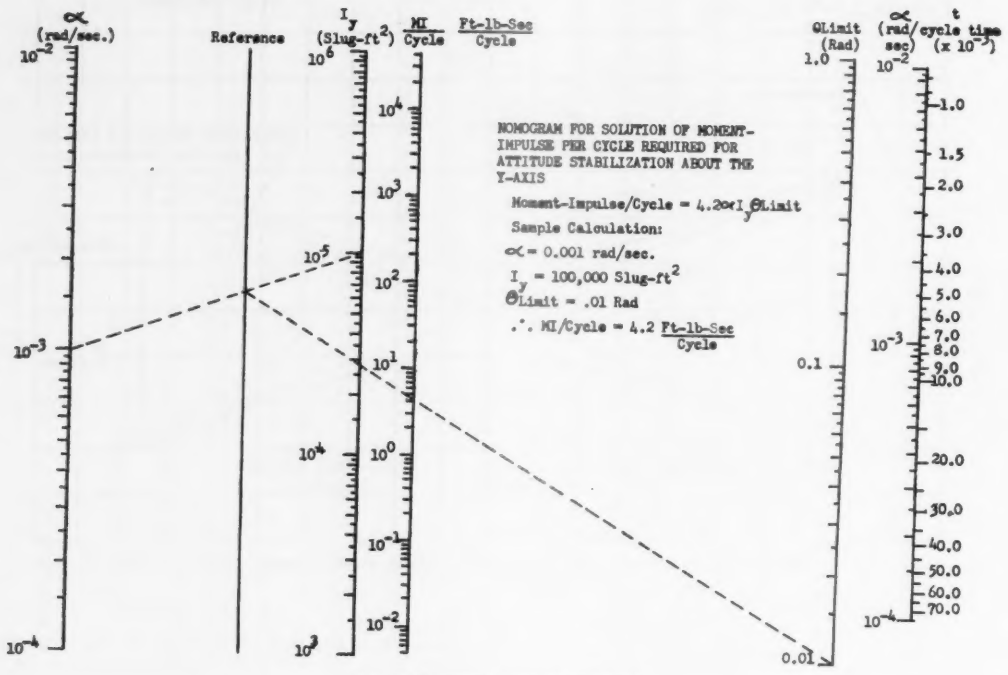

Fig. 3 Moment impulse per cycle

limit. This is felt to be a realistic value based on previous experience in satellite control system design. The assumption is necessary for estimating the energy requirements, without specifying the actual control system hardware.

Standard practice is to take the moment impulse derived from the nomograms and incorporate a safety margin of 50%. Impulse requirements to counteract random disturbances, such as solar pressure, aerodynamic moments, and torques resulting from moving masses, are to be estimated separately. The results are statistically summed with the requirements for stabilizing the gravitational gradient.

Estimation of Moment Impulse

The nomenclature and equations of motion involved in estimating moment impulses are listed as

Attitude Motion

$$\ddot{\theta}\,(t) \cong \alpha^2 \sin\theta\cos\theta - \beta \cong \alpha^2\theta - \beta$$

$$\dot{\theta}\,(t) = [(\theta(o)\alpha^2 - \beta)\sinh \alpha t + \dot{\theta}(o)\alpha \cosh \alpha t]/\alpha$$

$$\theta\,(t) = [\beta + (\theta(o)\alpha^2 - \beta)\cosh \alpha t + \dot{\theta}(o)\alpha \sinh \alpha t]/\alpha^2$$

where the reference axes system is defined as

X = local horizontal
Y = normal to orbit plane
Z = aligned with the radius vector
$\theta\,(t)$ = attitude motion about the Y-axis.
α = characteristic parameter, defined in Fig. 2
β = corrective angular acceleration applied at attitude limits
$\theta(0), \dot{\theta}(0)$ = initial conditions

The cycle time is defined as

$$t_{cycle} \cong \frac{2}{\alpha} \ln \left\{ \frac{\theta_{limit} + \sqrt{\theta^2_{limit} - \theta(0)^2 + [\dot{\theta}(0)/\alpha]^2}}{(\theta(0) + \dot{\theta}(0)/\alpha} \right\}$$

The sign associated with the radical is chosen to make the quantity in braces always positive. The time required for the impulse correction is assumed small compared with the drift time between limits.

The moment impulse required for stabilization during one limit cycle operation is

MI per cycle = $4.2\alpha IY\,\theta$ limit ft-lb-sec per cycle

The impulse, and hence the weight of the fuel required, is determined by dividing the moment impulse by the moment arm of the control torque.

Fig. 2 relates the characteristic parameter to the orbit altitude and inertia relationship of the satellite vehicle. The nomogram of Fig. 3 provides the moment impulse required per limit cycle operation and the cycle period. The total moment impulse required for a satellite vehicle is then determined by establishing the orbit lifetime.

Temperature Distribution in Couette Flow With Radiation[1]

R. VISKANTA[2]

Argonne National Laboratory, Argonne, Ill.

and

R. J. GROSH[3]

Purdue University, Lafayette, Ind.

THE STUDY of radiant heat transfer in an absorbing and emitting media is of considerable importance because of recent developments in hypersonic flight, re-entry and gas-cooled nuclear reactors. Thus, problems where radiation is combined with other modes of heat transfer, i.e., conduction, have been receiving more attention (1,2,3,4).[4] In these studies, simplifying assumptions or approximations were introduced to obtain the solution of the conservation equations or only of the energy equation; only Goulard et al. (3) presented some exact numerical results for the case of a weakly absorbing gas.

When energy transfer by combined radiation and conduction is present, the energy equation becomes a complicated nonlinear integro-differential equation (5). Since existing mathematical techniques do not disclose a general solution for this problem, simplifying assumptions or approximations are introduced to make the equation tractable. It is always of interest, therefore, to compare approximate solutions with exact solutions, when they can be found.

In this note, laminar Couette flow is considered. The radiant energy flux vector which has an integral representation, is approximated by the Rosseland approximation, which is valid for intense absorption only. The approximate solutions obtained are then compared with the solutions obtained using the exact formulations (5).

Formulation and Solution of the Problem

The complexity introduced by the radiative contribution to the energy flux is in part due to the dependence of the flux on the geometrical configuration of the system. For this reason, Couette flow, a very simple type of flow which has some remote similarity to the viscous boundary layer problem, is considered. Geometric effects are nonexistent in this problem and it is hoped that an analysis of it will contribute to the overall understanding of heat transfer in a conducting medium which absorbs and emits thermal radiation.

The conservation of energy equation at any point in the medium in steady state can be written as

$$\nabla \cdot (-k\nabla T + \mathbf{E}) = \mu\Phi \qquad [1]$$

where the radiant flux vector $\mathbf{E}$ is defined as

$$\mathbf{E}(\mathbf{r}) = \int_{\Omega=4\pi} I(\mathbf{r}, \mathbf{\Omega})\mathbf{u}\, d\Omega \qquad [2]$$

Rosseland (6) has shown that, in the limiting case of intense absorption when the emissive power of the medium varies slowly with the distance, the radiant energy flux vector can be approximated by

$$\mathbf{E}(\mathbf{r}) = -\frac{n^2}{3\kappa}\nabla(4\sigma T^4) = -\frac{16n^2\sigma T^3}{3\kappa}\nabla T \qquad [3]$$

This approximation is valid for the special case of a gray medium and only when the emissive power is nearly constant within a mean free path, $1/\kappa$.

The Rosseland approximation leads to a considerable simplification in the expression for radiant flux. The integral representation is now replaced by a simple diffusion-type equation. The simplicity is, however, offset by its approximate nature and the fact that it fails completely in the vicinity of the surface because it does not take into account radiation leaving from the surface. In spite of these shortcomings the Rosseland approximation has been used with success in a variety of problems ranging from the transport of radiation through gases at low density to the study of effects of radiation on blast waves caused by nuclear explosions (5).

Because of the approximation already introduced in the simplification of the expression for the radiant energy flux, it is usually not necessary to include the variation of the physical and radiative properties with temperature. This, however, can be done quite readily (5).

For a one-dimensional system the conservation equation reduces to a simple differential equation

$$\frac{d}{dy}\left(k_{eff}\frac{dT}{dy}\right) + \mu\left(\frac{du}{dy}\right)^2 = 0 \qquad [4]$$

where

$$k_{eff} = k + k_r + (16n^2\sigma T^3/3\kappa) \qquad [5]$$

is the effective thermal conductivity. The second term on the right-hand side of Eq. 5 can be considered as a "radiative conductivity."

A very simple solution for the temperature distribution is obtained when it is postulated that the surfaces are black, and that the temperature is constant along the wall. Thus the boundary conditions become

$$T = T_0 \quad \text{at} \quad y = 0$$
$$T = T_1 \quad \text{at} \quad y = h \qquad [6]$$

Introducing a dimensionless distance ξ, a normalized temperature Θ, and a velocity profile, $u = U_1(y/h)$, Eq. 4 becomes

$$\frac{d}{d\xi}\left[\left(1 + \frac{n^2\Theta^3}{3N}\right)\frac{d\Theta}{d\xi}\right] + \frac{\mu U_1^2}{kT_1} = 0 \qquad [7]$$

where the dimensionless parameter N determines the relative role of conduction vs. radiation term. Note that k and κ are assumed constant in the remainder of this work. The second term in Eq. 7 has a form of an Eckert number times Prandtl number in which $T_0 = 0$.

Integrating Eq. 7 twice and determining the integration constants from the boundary conditions given in Eq. 6, the equation governing the temperature distribution in Couette flow with radiation and temperature independent physical properties becomes

$$\Theta + \frac{n^2\Theta^4}{3N} = [(1-\xi)\Theta_0 + \xi\Theta_1] + \frac{n^2}{3N}[(1-\xi)\Theta_0^4 + \xi\Theta_1^4] + \frac{\mu U_1^2}{kT_1}(1-\xi)\xi/2 \qquad [8]$$

Discussion of Results

In problems where energy transport by thermal radiation is appreciable in comparison to energy transport by conduction, temperature levels will be high and viscous dissipation effects will be relatively unimportant. It is therefore permissible, as a first approximation, to neglect viscous dissipation and assume that the index of refraction is unity. The predicted temperature distributions for Couette flow with radiation is shown in Fig. 1, where the effect of varying

Received May 4, 1961.

[1] This Note is based on work performed under the auspices of the U. S. Atomic Energy Commission.

[2] Assistant Mechanical Engineer.

[3] Professor of Mechanical Engineering.

[4] Numbers in parentheses indicate References at end of paper.

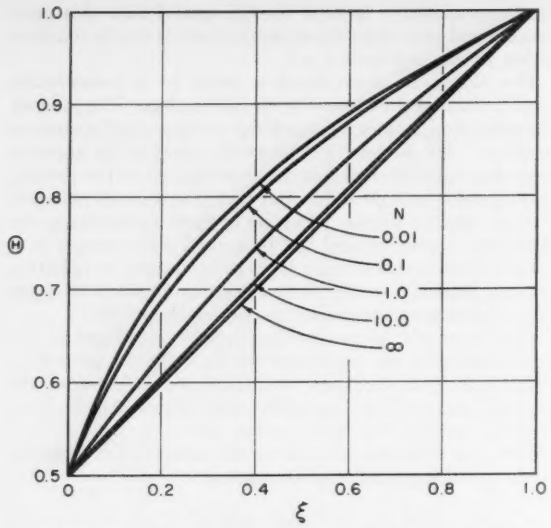

Fig. 1 Variation of the normalized temperature with the dimensionless distance

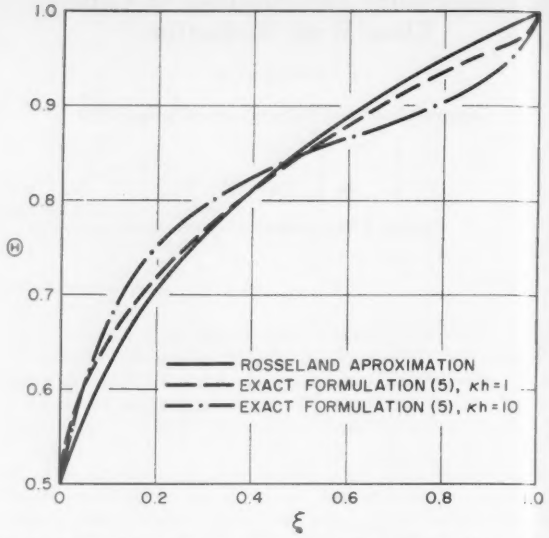

Fig. 2 Comparison of temperature distributions for $N = 0.01$

the parameter N, but holding the same temperature at the boundary, is indicated.

The physical nature of the results can be understood better when we note that the parameter N represents the relative role of energy transfer by conduction to that of radiation. Three separate cases may be considered: $N \gg 1$; $N \approx 1$; and $N \ll 1$. In the first case, conduction predominates; in the second case, energy transport by molecular conduction is of the same order of magnitude as radiation; in the last case, radiation predominates. As $N \to \infty$, the temperature profiles approach those for pure conduction, the first term on the right-hand side of Eq. 8. When $N \to 0$, the temperature distribution is governed by the second term on the right-hand side of Eq. 8. The results for the case $N \approx 1$ lie between the two limiting cases. The results show that the presence of radiation increases the temperature gradient above that for pure conduction at the cool wall and decreases it at the hot wall. This trend in the temperature gradient is expected. Since the effective thermal conductivity (Eq. 5) increases with temperature, the temperature gradient must decrease to conserve the total energy flux (conduction plus radiation).

The temperature distributions obtained from the exact formulation (5) for the value of parameter $N = 0.01$ are compared with those arrived at using the Rosseland approximation, in Fig. 2. This value of N corresponds to the case when energy transport by radiation predominates, and provides a critical check of the approximation. Since the mean free path of the photon is $1/\kappa$, the solutions for $\kappa h = 1$ and 10 correspond to the cases when the mean free path of radiation is equal to and ten times shorter than the distance between the surfaces, respectively. The agreement between the results for this latter case is better, as it should be; however, the temperature gradients at the surfaces predicted by the approximate formula are too small. This is not surprising since the Rosseland approximation fails completely in the vicinity of the surface because it does not take into account radiation leaving from the surface, and only molecular conduction insures the continuity of the temperature.

The temperature profiles for smaller values of parameter N predicted by using the Rosseland approximation are in a better agreement with those obtained from the exact formulation. Thus, the simplicity of the Rosseland approximation in comparison with the exact formulation justifies its use for problems in which the mean free path of radiation is much shorter than the distance between the surfaces in spite of the loss of accuracy.

Nomenclature

$\mathbf{E}$ = radiant energy flux vector (defined in Eq. 2)
h = distance between the planes
I = intensity of radiation
k = thermal conductivity
k_{eff} = effective thermal conductivity (defined by Eq. 5)
k_r = radiative conductivity defined as $16n^2\sigma T^3/3\kappa$
N = dimensionless parameter defined as $k\kappa/4\sigma T_1^3$
n = index of refraction
$\mathbf{r}$ = position vector
T = absolute temperature
u = velocity
U_1 = velocity of the upper plane
$\mathbf{u}$ = unit vector
y = independent variable
Θ = normalized temperature, defined as T/T_1
κ = absorption coefficient
μ = dynamic viscosity
ξ = dimensionless distance defined as y/h
σ = Stefan-Boltzmann constant
Φ = dissipation function
Ω = solid angle
$\mathbf{\Omega}$ = unit vector in the direction of the pencil of rays

Subscripts

0 = plane at rest
1 = moving upper plane

References

1 Smith, J. W., "Effect of Gas Radiation in the Boundary Layer on Aerodynamic Heat Transfer," *J. Aeron. Sciences*, vol. 20, pp. 579–580, Aug. 1952.

2 Ruminskii, A. N., "Boundary Layer in Emitting an Absorbing Media," *Izv. Akad. Nauk S.S.S.R., Otd. Tekh. Nauk, Mekhanika i Mashinostroenie*, No. 2, Mar.–Apr. 1960, pp. 47–53. (*In Russian.*)

3 Goulard, R. and Goulard, M., "Energy Transfer in Couette Flow of a Radiant and Chemically Reacting Gas," *1959 Heat Trans. and Fluid Mech. Inst.*, University of California, Los Angeles, Calif., June 1959, pp. 126–139.

4 Bird, G. A., "The Effect of Thermal Radiation on the Inviscid Flow Over a Blunt Body," *J. Aero/Space Sciences*, vol. 27, Aug. 1960, pp. 713–714.

5 Viskanta, R., "Heat Transfer in Thermal Radiation Absorbing and Scattering Media," *Argonne National Laboratory* ANL-6170, May 1960.

6 Rosseland, S., *Astrophysik auf Atom-Theoretischer Grundlage*, Springer-Verlag, Berlin, 1931, p. 42.

Meteorological Analysis of Churchill Rocket Sounding Data

SIDNEY TEWELES[1]

U. S. Weather Bureau, Washington, D. C.

Wind and temperature measurements to above 80 km taken during the International Geophysical Year by grenade, sphere accelerometer, and Pitot-static tube experiments at Churchill, Manitoba are combined with radiosonde data in time sections covering periods in July, August and December 1957 and January–February 1958. The nature of the circulation in successive layers of the stratosphere and mesosphere is suggested by this investigation. Some details of the sudden warming of the stratosphere that occurred in January 1958 are shown by means of a vertical cross section.

A REMARKABLE series of temperature and wind observations was made at Churchill, Manitoba during the International Geophysical Year by means of grenades, sphere accelerometers and Pitot-static tubes carried aloft in rocket vehicles. The grenade experiments are described, data presented, and copious references given by Stroud, Nordberg, Bandeen, Bartman and Titus (6,7),[2] while accelerometer and static tube experiments are similarly described by Jones, Peterson, Schaefer and Schulte (2,3) and Ainsworth, Fox and LaGow (1), respectively.

The results of these experiments are combined here to bring out many details of the temperature distribution and circulation of the upper stratosphere and mesosphere. In each of the four time sections presented, radiosonde information is used to determine the analysis up to the 30-km level during a two- or three-week period centered on the days of the rocket soundings. For higher altitudes, information from rocket experiments is available for two or more observations during each of the four periods. Many facets of the data and their meteorological implications have been discussed by Teweles (8) and in the cited papers by those responsible for the rocket experiments.

The reliability of the analyses is dependent upon the accuracy of the data. Stroud et al. (7) state that the errors of the grenade experiment data below 75 km are generally less than ±3 C for temperature, and ±5 m per sec and ±15 degrees for wind speed and direction, respectively. Above 75 km, the size of the errors may increase rapidly by a factor of as much as ten at the very highest points. Jones et al. (2,3) estimate the probable temperature error of the accelerometer experiment to be about 2% (4–6 C) below 75 km and 5% (10–15 C) above 75 km. Furthermore, the dependence of the acceleration upon air density and drag coefficient limits the useful range of the experiment to the layer from 25 km to 80 km. Temperatures from the static tube experiment are derived from density data having an estimated measurement error of less than 2% at 80 km, according to Ainsworth et al. (1).

The wind and temperature values given for the rocketsonde observations are averages for the layer between points at which two grenades exploded; thus, maximum and minimum values tend to be smoothed out to some extent. Furthermore, random errors will have opposite signs in adjacent layers when the source of error is difficulty in accurate timing of sound arrivals from the grenade at the boundary between the layers. In excessively thin layers, less than 3 km, errors may be greatly magnified. Where highly incompatible values suggest such errors, the effect is minimized by combining adjacent layers.

In their broad features, the time sections for July 1957 (Fig. 1) and August 1957 (Fig. 2) are remarkably similar. In the lower stratosphere, in each case, there was marked counteraction to tropospheric activity; e.g., warming occurred in this layer simultaneously with the tropospheric cooling following cold front passages.

From the 18-km level up to the stratopause (the thermal maximum at the top of the stratosphere near 50 km), the temperature increased from about −50 C to about 0 C. The double temperature maximum at the stratopause on July 29 and again on August 12, already noted by Ainsworth et al. (1), is an interesting phenomenon that might be due either to differential heating of layers or to advective processes. In the mesosphere above 50 km, the temperature decreased slightly up to 60 km but then decreased at an average rate of 4 C km^{-1} to about 80 km above which there was a small temperature increase with height. At 83 km on July 22, a remarkably low layer mean temperature of −112 C was reported.

By the end of August (Fig. 2), temperatures in the troposphere and middle stratosphere were about 5 C cooler than in July. Cooling was more marked at the stratopause where the temperature was more than 10 C lower on August 25 than on July 22. On the other hand, the temperature of the mesopause was progressively warmer in each observation from July 22 to August 25.

Murgatroyd (5) presented a vertical temperature distribution for summer at 60 deg N that is confirmed in most respects

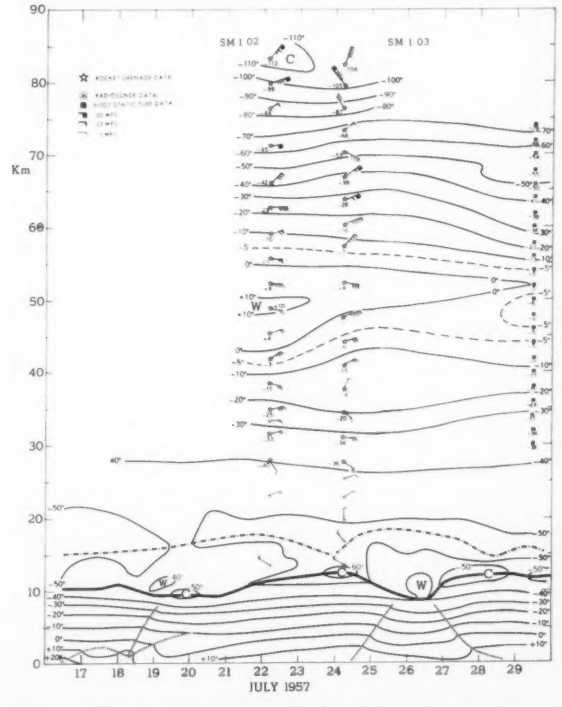

Fig. 1 Time section for Churchill, Manitoba, July 17–29, 1957, including data from rocket grenade experiments at 0416 GMT July 22 and 0530 GMT July 24, and a Pitot-static tube experiment at 2200 GMT July 29. Temperature analysis in deg C. Fronts given by dotted lines, tropopause by heavy line, thermal boundary by dash-dot line. *C* and *W* indicate cold and warm areas. Barbs representing wind speed are placed at the tail end of the wind shafts, which point in direction toward which wind is blowing, with north at top of diagram and east at the right

This Technical Note is a greatly reduced version of the paper "Time Section and Hodograph Analysis of Churchill Rocket and Radiosonde Winds and Temperatures," presented at the ARS 15th Annual Meeting, Washington, D. C., Dec. 5–8, 1960.

[1] Chief, Stratospheric Meteorology Research Project.

[2] Numbers in parentheses indicate References at end of paper.

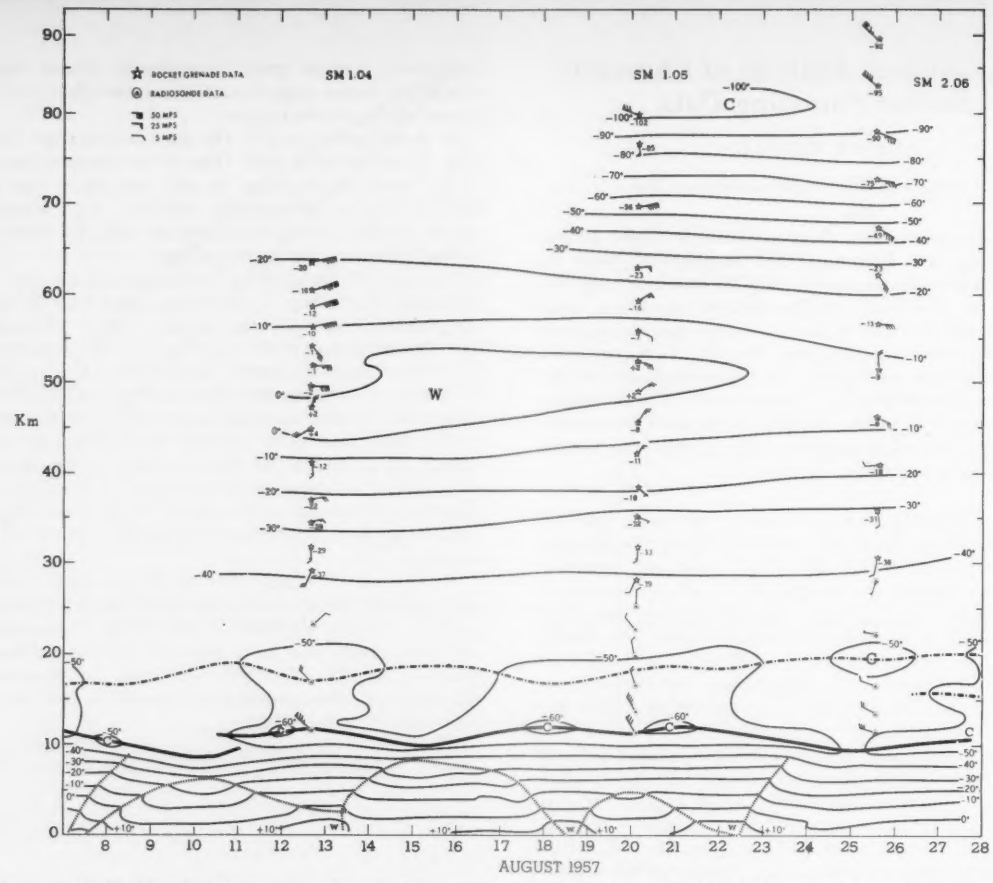

Fig. 2 Time section for Churchill, Aug. 8–28, 1957. Rocket grenade experiments are for 1600 GMT August 12, 0230 GMT August 20, and 1408 GMT August 25. (Explanation as in Fig. 1)

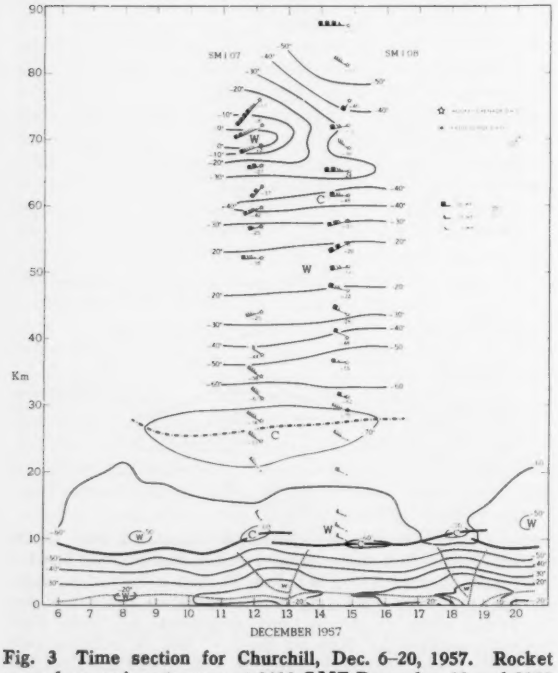

Fig. 3 Time section for Churchill, Dec. 6–20, 1957. Rocket grenade experiments were at 0400 GMT December 12 and 2100 GMT December 14. (Explanation as in Fig. 1)

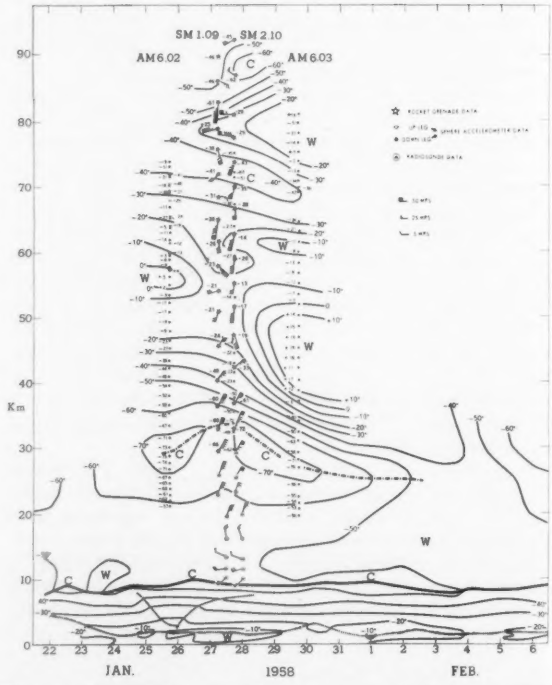

Fig. 4 Time section for Churchill, Jan. 22–Feb. 6, 1958. Rocket grenade experiments were at 0604 GMT and 1845 GMT January 27. Sphere accelerometer experiments were at 1912 GMT January 25, 1845 GMT January 27, and 1906 GMT January 29. (Explanation as in Fig. 1)

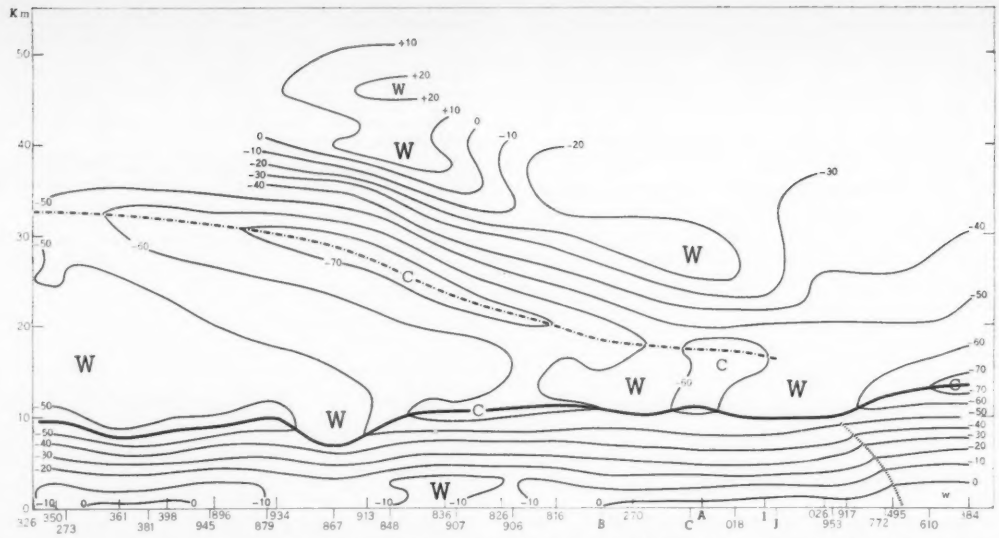

Fig. 5 Cross section, Jan. 29, 1958, near 55 deg N from Naknek, Alaska (station 326) through Churchill (station 913) to Berlin, Germany (station 384). (Explanation generally as in Fig. 1.) Temperature analysis at high levels in vicinity of Churchill is based on sphere accelerometer experiment AM 6.03. Identification numbers of radiosonde stations are shown along bottom of chart

by the Churchill summer soundings. Among the principal points of difference are his relatively high temperatures of +21 C and −93 C at the stratopause and mesopause respectively. The winds observed differ in two respects from those given by Murgatroyd for summer conditions near 60 deg N. The Churchill data indicate higher wind speeds, exceeding 25 m per sec in the 60- to 75-km layer, and a shift to west winds near 80 km elevation instead of near 90 km.

The time selection for Dec. 6–20, 1957 (Fig. 3) shows a troposphere 25 C colder than it was in summer, although the lower stratosphere cooled only 10 C. The middle stratosphere underwent more remarkable changes, the wind having increased to westerly 25 to 50 m per sec as the temperature decreased 30 C at 28 km.

Like the lower stratosphere the stratopause cooled only 10 C. The position of the stratopause at 51 km is at variance with the position near 60 km given by Murgatroyd (5) for winter at this latitude. In fact, these experiments show a remarkable temperature minimum near 60 km. The height of the stratopause in January 1958 (Fig. 4) was indefinite but somewhat closer to 60 km. The extreme temperature changes above 60 km during the December 12–14 period are in strong contrast to the regularity in temperature patterns of the summer mesosphere. Coupled with winds in the neighborhood of 100 m per sec, these temperature changes suggest the existence of violent storms in the winter mesosphere, albeit they are tempests in a near vacuum.

The wintertime temperatures of the upper mesosphere at Churchill were much warmer than those measured there in summer or at lower latitudes in winter. Although warming in the stratosphere and mesosphere is generally explainable by a reasonable amount of sinking and compression of air from higher layers, Kellogg (4) has described a process by which heat may be liberated at or above the mesopause through recombination of atomic oxygen brought down from ionospheric layers rich in this element.

The January 1958 time section (Fig. 4) benefits from the unprecedented concentration of rocket sounding data available for the period January 25 to 29. Accelerometer spheres launched by Nike-Cajun rockets on January 25 and 29 gave both up-leg and down-leg information. Down-leg information was given by a similar sphere, borne by one of two grenade-carrying Aerobee rockets launched on January 27. In the 38- to 41-km layer, these spheres gave evidence of a 4-day temperature increase of almost 70 C, greater than any ever recorded in a similar interval at lower levels of the atmosphere.

In contrast to the generally zonal flow in the three earlier cases, a strong north-south component appeared in the upper winds measured in the rocket grenade experiments of January 27. From 15 to 45 km, the winds blew from the north, with a maximum velocity near 75 m per sec at 33 km. Above 45 km, the wind direction was reversed so that equally strong winds from the south were measured at some levels above 63 km.

A vertical cross section of the atmosphere nearly along the 55 deg N latitude circle (Fig. 5) illustrates the great horizontal and vertical extent of the warming at the time of the 40-km warming at Churchill. The cooling with the advance of the cold sliver near 30 km in the lower forward portion of the system is almost as impressive as the warming in the upper rear portion. While the cooling did not produce temperatures that were anomalous for the entire hemisphere, as did the concomitant warming, it did bring anomalously low temperatures into the middle latitudes. All indications are that the stratospheric features in the cross section were slowly moving toward the west. Thus, the warmest air at 25 km crossed over Berlin on January 25, passed to the south of Greenland on January 29, and then diffused across North America in the first three days of February.

The temperature and wind observations utilized in this study were among the first to become available to great heights at such high latitudes. The large amount of information deduced from this limited number of soundings is a strong recommendation for gathering much more temperature and wind information to the highest possible levels.

That there are several layers of the atmosphere having their own characteristic types of horizontal circulation is brought out by the charts displayed here. Much about the nature of the circulation in the upper stratosphere and lower mesosphere has been revealed by these and other rocket soundings. However, if anything, the nature of the circulation in the upper mesosphere has become more of a mystery. Even though diurnal and semidiurnal effects and errors in measurement are large near the mesopause, the data presented here indicate the existence of moving disturbances in the circulation of nearby layers, particularly in winter through a deep layer at the boundary of the polar darkness.

References

1 Ainsworth, J. E., Fox, D. F. and LaGow, H. E., "Measurement of Upper Atmosphere Structure by Means of the Pitot-Static Tube," NASA TN D-670, 1961.

2 Jones, L. M., Peterson, J. W., Schaefer, E. J. and Schulte, H. F., "Upper-Air Densities and Temperatures from Eight IGY Rocket Flights by the Falling-Sphere Method," *IGY Rocket Report Series*, no. 5, IGY World Data Center A, Rockets and Satellites, Washington, D. C., Dec. 1, 1959.

3 Jones, L. M., Peterson, J. W., Schaefer, E. J. and Schulte, H. F., "Upper-Air Density and Temperature: Some Variations and an Abrupt Warning in the Mesosphere," *J. Geophys. Res.*, vol. 64, no. 12, Dec. 1959, pp. 2331–2340.

4 Kellogg, W. W., "Warming of the Polar Mesosphere and Lower Ionosphere in Winter," Abstract in *Bull. Amer. Meteorological Soc.*, vol. 40, no. 12, Dec. 1959, p. 645.

5 Murgatroyd, R. J., "Wind and Temperatures between 20 km and 100 km—A Review," *Quart. J. Roy. Meteorological Soc.*, vol. 83, no. 358, Oct. 1957, pp. 417–458.

6 Stroud, W. G., Nordberg, W., Bandeen, W. R., Bartman, F. L. and Titus, P., "Rocket-Grenade Observations of Atmospheric Heating in the Arctic," *J. Geophys. Res.*, vol. 64, no. 9, Sept. 1959, pp. 1342–1343.

7 Stroud, W. G., Nordberg, W., Bandeen, W. R., Bartman, F. L. and Titus, P., "Rocket-Grenade Measurements of Temperatures and Winds in the Mesosphere over Churchill, Canada," *J. Geophys. Res.*, vol. 65, no. 8, Aug. 1960, pp. 2307–2323.

8 Teweles, S., "Time Section and Hodograph Analysis of Churchill Rocket and Radiosonde Winds and Temperatures," *Monthly Weather Rev.*, vol. 89, no. 4, Apr. 1961, pp. 125–136. (*ARS Preprint* 1472-60, Dec. 1960).

Attitude Stabilization Using Focused Radiation Pressure

ROBERT R. HIBBARD[1]

Lewis Research Center, NASA, Cleveland, Ohio

THE UTILIZATION of solar radiation pressure for the attitude control of space vehicles appears feasible even though this pressure is less than 1 dyne per m² for surfaces normal to the sun at the Earth's orbital distance. Sohn (1)[2] has proposed the use of a weathervane-type system, and Frye and Stearns (2) have suggested that a trailing cone be so used. Sohn has calculated that 50-ft² stabilizer area would be sufficient to hold the yaw angle to 11.5 deg for a 1000-lb vehicle under the disturbing torques due to solar pressure forces. This same area would also be capable of trimming out upsetting gravitational torques in a 300-nautical-mile satellite if the moment of inertia was 30 slug-ft²; and, for a lunar shot with a moment of 300 slug-ft², it would do so after the vehicle had gone a small fraction of the way to the moon (1). Newton (3) has shown that the attitude of a spherical shell under upsetting gravitational torques can be held to within 22 deg by using an absorbing coating on the one hemisphere and a reflecting coating on the other. For any of these proposed systems the righting forces become very small at small angles of displaced attitude; they are directly proportional to the displacement at small angles. Nevertheless, this type of attitude control appears to be adequate for many systems, including those using photovoltaic power generating panels; for these the collection efficiency is proportional to the cosine of the displacement angle (e.g., 93% at 22 deg displacement).

However, if focused radiation is to be used in a space vehicle, a very close control of attitude will be required. For example, a parabolic collector driving a high temperature power conversion system may require an orientation tolerance of ±15 min (4). In general, attitude control within 2 deg will be needed with any focusing system.

Fortunately, the same concentration of radiation into a small area which makes precise attitude control so necessary with reflector systems can also serve to make radiation pressure a powerful restoring force at small displacements. This can be done by flanking the collector surface with a reflector as shown in Figs. 1a and 1b. Here the rays with proper orientation are shown as solid lines and the rays under a 2 deg misalignment as dotted lines. As shown in Fig. 1a, the misaligned radiation strikes a reflecting surface to exert a force in the direction shown by the arrow. This force will act as a correcting torque if the center of inertia of the total system is behind the correcting mirror. This would probably be the case for a space vehicle using focused solar radiation in a power system, since the capsule and much of the system mass would be in the shade of a parabolic collector.

If, however, the center of inertia is ahead of the control surfaces, the reflecting mirrors will have to face in the opposite direction (Fig. 1c) to obtain a correcting torque. The torque will be somewhat less than that obtained for the first case, since the reflected radiation cannot be directed perpendicular to the torque arm because of interference by the opposite reflector (see Fig. 1c).

In the first and more probable situation (Figs. 1a and 1b) the geometry of the reflecting surface will be dependent on the focal length to diameter ratio of the collecting system. If this ratio is large, plane mirrors set at a 45 deg angle will be effective. If this ratio is less than 1, as probable in a practical situation, a curved surface such as that shown in Fig. 1b will be required. This mirror surface can be shaped to give a beam collimated in two dimensions. The reflected radiation will fan out in the third dimension, because the focused radiation will form a spot of finite size (Fig. 1d.) (For simplicity, Figs. 1a–c were drawn for a perfect optical system and with a point source of radiation.)

The magnitude of the correcting torques is shown in the following example. Assume a 5-kw solar-driven electric generator with an overall efficiency of 10%. 50 kw of incident radiation then must be collected, which requires 50/1.35 = 37 m² of collector surface at Earth's orbital distance from the sun. (Solar flux ≅ 1.35 kw/m² at Earth's orbit.) The diameter of the paraboloid will then be 6.85 m, and, if a focal length to diameter ratio of 0.6 is used (approximately that used in Fig.

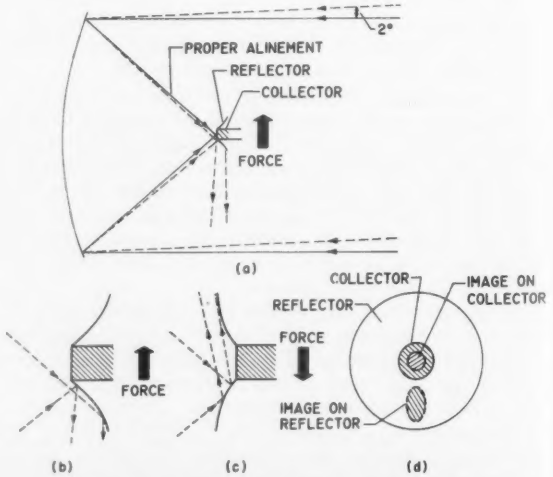

Figs. 1a, b, c, d Radiation pressure forces

Received May 11, 1961.

[1] Technical Consultant to Chief, Chemistry and Energy Conversion Div. Member ARS.

[2] Numbers in parentheses indicate References at end of paper.

1a), the distance from the mirror axis to the correcting mirror will be 4.1 m. If the payload is the shade of the collector, the center of inertia could be about 5 m from the correcting mirror. The pressure from collimated radiation is calculated from the change in momentum per unit time (i.e., mc/t). Since $mc = E/c$, $mc/t = (E/t)/c$ where E/t is the radiant power in consistent units. The pressure from 50 kw of radiant flux is then

$$\frac{50{,}000 \times 10^7 \text{ (dynes)(cm)(sec}^{-1}\text{)}}{3 \times 10^{10} \text{ (cm)(sec}^{-1}\text{)}} = 16.7 \text{ dynes}$$

The torque for the assumed system would be $16.7 \times 5 = 83$ dyne m. This value would be somewhat reduced by reflection losses and by reflected radiation not being fully collimated. However, a correcting torque of 50 dyne m should easily be realized.

Whether the above forces would be enough to counteract upsetting radiation and gravitational forces would depend on the mass and configuration of the vehicle and on the strength of the radiation and gravitational fields. While there would be little, if any, unbalance in radiation forces for a mirror system where the payload is in the shade, the upsetting gravitational forces might be appreciable. Calculations would have to be made for specific vehicles to determine at what altitude these gravitational torques would become less than the 50-dyne-m correcting torque available in this example. These calculations have not been made. In any case there would be some altitude at which the proposed system could take over and supply corrective attitude torques.

For controlling the attitude to the precision required with focused radiation systems, the proposed method should be much lighter and less cumbersome than the weather vane and trailing cone of (1 and 2). The correcting forces for the latter two are proportional to the sine of the displacement angle; for 1 deg this is only $\frac{1}{57}$. Therefore a stabilizing area about 50 times greater than the reflector area and operating on the same length arm would be required to give an equal correcting torque. These weight penalties would certainly be much greater than those involved in flanking a heat collector with a small reflecting surface.

References

1 Sohn, Robert L., "Attitude Stabilization by Means of Solar Radiation Pressure," ARS JOURNAL, vol. 29, no. 5, May 1959, pp. 371–373.

2 Frye, W. E. and Stearns, E. V. B., "Stabilization and Attitude Control of Satellite Vehicles," ARS JOURNAL, vol. 29, no. 12, Dec. 1959, pp. 927–931.

3 Newton, Robert R., "Stabilizing a Spherical Satellite by Radiation Pressure," ARS JOURNAL, vol. 30, no. 12, Dec. 1960, pp. 1175–1177.

4 Dresser, D. L., "Elements of Solar Collector Design," *IAS Paper* no. 61-24, 1961, p. 69.

Thermal Conductivity of Kerosine D.Eng. R.D. 2495 Between 15 and 325C at Pressures up to 200 Atm

H. ZIEBLAND[1]

Explosives Research and Development Establishment, Waltham Abbey, Essex, England

M. T. DUPREE[2]

Chemical Research Laboratories, Melbourne, Victoria, Australia

The thermal conductivity of an aviation kerosine, Spec. No. D.Eng. R.D. 2495, was measured with a vertical, coaxial cylinder apparatus in the temperature range 15 to 325 C at pressures between 1 and 200 atm. The trend of these results, demonstrated by the influence of temperature and pressure on the thermal conductivity, is characteristic of normal, nonassociating liquids. Smoothed graphs showing the variation of thermal conductivity with pressure and temperature were prepared.

At temperatures in excess of 280 C noticeable thermal decomposition of kerosine took place, believed to be due to the catalytic effect of the material of the receiving cylinder, a 97%/3% copper/nickel alloy. About 4% of toluene was detected after the kerosine had been exposed for approximately 7 days to temperatures between 280 and 320 C. No such decomposition took place in the same temperature interval after the receiving cylinder had been replaced by an all silver one.

Received Sept. 30, 1960.

[1] Associate Member Institute of Mechanical Engineers, Senior Principal Scientific Officer, Ministry of Aviation.

[2] Assistant Experimental Officer, Commonwealth Scientific and Mechanical Research Organization.

KEROSINES are wide-cut light petroleum fractions which for technical and economic reasons have gained considerable importance in recent years as fuels for gas turbines, ramjets and rockets. The substance investigated in this research was kerosine D. Eng. R.D. 2495, a premium grade chosen as a fuel for large, liquid propellant rocket engines in the United Kingdom.

For this latter application the fuel not only provides the thermal energy for the propulsion unit, but also serves as a coolant for the walls of the rocket motor that are exposed to the extremely hot combustion gases.

Reliable predictions of the cooling requirements will to some extent depend on the knowledge of several physical properties of the coolant over a wide range of pressure and temperature, which in the case of kerosine may include the critical region of the substance.

Even for ambient conditions, relatively little information exists on the physical and thermodynamic properties of kerosine for heat transfer calculations, namely, on the thermal conductivity, viscosity, density and specific heat, and no information can be found on some of these properties at elevated temperatures and higher pressures.

This paper gives the results of an extensive experimental investigation of the thermal conductivity of kerosine D. Eng. R.D. 2495 at temperatures from 15 to 325 C and at pressures up to 200 atm, i.e., within about 30 C of its estimated critical temperature and up to eight times its critical pressure.

The apparatus chosen for this study, a vertical coaxial cylinder conductivity cell with guard rings, and the ancillary equipment, were identical to that used by the authors in a previous study on the thermal conductivity of heavy water (1).[3] A detailed description of the apparatus, of the test procedure, and of an analysis of those phenomena that might have an adverse effect on the precision of these results can be found in that paper.

[3] Numbers in parentheses indicate References at end of paper.

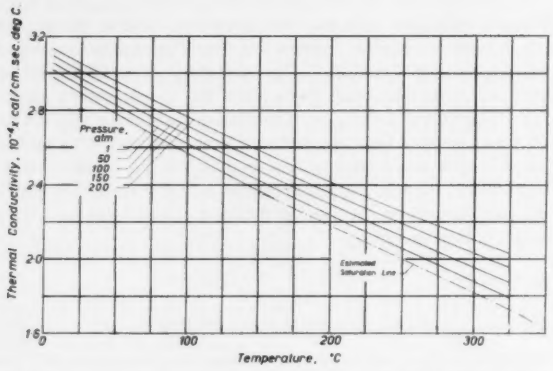

Fig. 1 **Thermal conductivity of kerosine D. Eng. R.D. 2495**

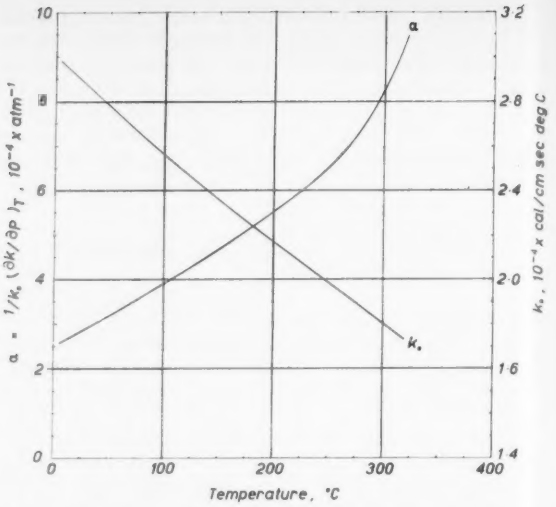

Fig. 2 **Pressure coefficient α and zero pressure thermal conductivity k_0 vs. temperature for kerosine D. Eng. R.D. 2495**

For reasons explained in the following section, two conductivity cells were employed in these experiments, the first one being constructed in silver and Hidural 5 (a 97%/3% copper/nickel alloy), the second one in solid pure silver only.

Experimental Results and Discussion

The results of this analysis are presented in Table 1.[4]

Although the method employed in this study was an absolute one, control measurements on toluene at the beginning and during the investigation were carried out in order to prove the absence of any disturbing changes in the alignment of the conductivity cell. The values found for the thermal conductivity of toluene were, within the limits of accuracy, identical with those of Riedel (2) and of Schmidt (3). Before charging the apparatus with kerosine, toluene was carefully removed from all parts of the apparatus by draining, flushing for several hours with warm nitrogen, and evacuating to a pressure below 0.5 mm Hg. This statement seems necessary in view of some observations made during the tests which are reported later in this section.

Most of the measurements were conducted at four pressures only: 50, 100, 150 and 200 atm. The results of the first series of tests from about 80 to 250 C were in all respects in conformity with the behaviour of normal liquids. The thermal conductivity decreased continuously with rising temperature, and at constant temperature the thermal conductivity increased linearly with rising pressure.

From about 250 C upwards the experimental results began to display a trend noticeably deviating from normal liquid behaviour. The gradients dk/dt of the 50 and 100 atm isobars (the only ones investigated at that time) began to fall towards zero and must have changed sign somewhere between 280 and 320 C as the thermal conductivity at 320 C was already higher than at 280 C. Within the same limits of temperature, the pressure coefficient of the thermal conductivity $(1/k_0)\cdot\left(\frac{\partial k}{\partial p}\right)_t$ increased from a value of about 0.75×10^{-3} atm^{-1} at 280 C to about twice that value at 320 C.

The most likely explanation for these anomalous results, i.e., the onset of thermal convection during these tests, was disproved by a group of experiments conducted at progressively increased temperature differences across the fluid filled annulus. Practically identical results were obtained in all cases.

Likewise it was shown by experiment that thermal diffusion and the ensuing separation of the kerosine into strata of varying composition could not have been the cause of these anomalous observations.

There remained to investigate the possibility of thermal decomposition of the substance, a supposition which became quite plausible when it was found that the earlier results at 145 C could not be reproduced. The new values were consistently lower by about 2%. It was therefore decided to open the conductivity cell and to examine the fluid.

Table 1 Analysis of kerosene D. Eng. R.D. 2495 investigated in this research

Description of test	Result
Specific gravity at 60 F	0.7836
Distillation: Initial boiling point, C	164.0
2% recovered at	173.0
5%	177.5
10%	181.5
20%	187.5
30%	192.5
40%	198.0
50%	204.5
60%	212.0
70%	220.0
80%	229.5
90%	240.0
Final boiling point	253.0
Recovery, vol %	98.0
Residue, vol. %	1.2
Loss, vol %	0.8
Recovered at, vol %	
185 C	15.5
200 C	42.0
240 C	90.0
Hydrocarbon types, FIA, vol. %	
Aromatics	3.0
Olefines	0.5
Saturateds	96.5

[4] The sample of kerosine used in this research was obtained from the Rocket Propulsion Establishment, Westcott, and was analyzed at the Research Centre of the British Petroleum Company, Ltd.

Two changes became apparent. The kerosine recovered from the cell had a light yellow color in contrast to the original specimen which was completely colorless. Further, a dark grey deposit, easily removed by wiping, was found on the surface of the receiving cylinder which was made of a 97%/3% copper/nickel alloy. No deposits were found on the silver surfaces of the emitting cylinder assembly.

Chromatographic analysis established the presence of 4 to 5% of a light fraction not present in the original sample, which by subsequent spectroscopic examination was shown to be toluene. It should be noted that the percentage of toluene detected is almost equal to the sum of the percentage of olefines and aromatics in the original samples (see Table 1). The solid deposit on the surface of the receiving cylinder was not further examined. Both color and texture seemed to suggest that it was a carbonaceous deposit. Likewise the discoloration of the fluid could have been caused by a dispersion of colloidal carbon.

From this evidence it was concluded that thermal decomposition of kerosine, catalysed on the copper alloy surface, took place at higher temperatures. The occurrence of an exothermic reaction on the surface of the receiving cylinder would well account for the anomalous results obtained at temperatures in excess of 280 C.

To substantiate these observations, some of the experiments were repeated with a new, all silver thermal conductivity cell. The results of this group of tests linked up satisfactorily with the earlier determinations. The anomalous results between 280 and 320 C were not reproduced. In fact, two sets of values obtained at 293 C and at 303 C, respectively, followed smoothly the trend predicted by the previous "normal" results. Unfortunately during the tests at a temperature of 303 C the autoclave developed a slight leak which made it progressively more difficult to operate the apparatus at higher pressures, and the last reliable determination was at 323 C at 50 atm.

After terminating the experiments, samples of the fluid were again taken from various parts of the apparatus, and subjected to a chemical examination. Neither sample showed any marked change in composition as compared with the original analysis.

In view of this evidence it seems certain that the anomalous results of the first series of tests were due to chemical reactions of some of the constituents of kerosine on the surface of the receiving cylinder. It should also be noted that catalytic decomposition can be initiated at temperatures below pyrolytic breakdown, a fact which may be of importance in the application of the substance as a coolant.

The results of this study were presented in graphical form containing smoothed isobars of the thermal conductivity.

The pressure coefficient α of the thermal conductivity was derived from a plot of the isotherms. This quantity is defined $\alpha = (1/k_0)\cdot(\partial k/\partial P)_t$ where k_0 is the thermal conductivity at zero pressure at temperature t, and $(\partial k/\partial P)_t$ is the partial derivative of the thermal conductivity k with respect to the pressure P at constant temperature t. Values for α and k_0 derived from these experiments were plotted in Fig. 2. The effect of pressure on the thermal conductivity of kerosine is considerably higher than that for water at the same temperature. At 80 C the pressure coefficient for kerosine is $0.36 \times 10^{-3}\text{atm}^{-1}$, while the corresponding value for water is only $0.076 \times 10^{-3}\text{atm}^{-1}$. It is believed that the rather high pressure coefficient for kerosine is due to its high isothermal compressibility, for which, however, no experimental data were found in the literature.

Information on the thermal conductivity of kerosine is very scarce and only one relevant publication has been found. Bridgman (4) studied, amongst other substances, the thermal conductivity of a kerosine of unspecified composition at 30 C and 75 C at pressures up to 12,000 atm. In Table 2 Bridgman's zero pressure conductivity values k_0 are compared with the corresponding values found in this research. Although

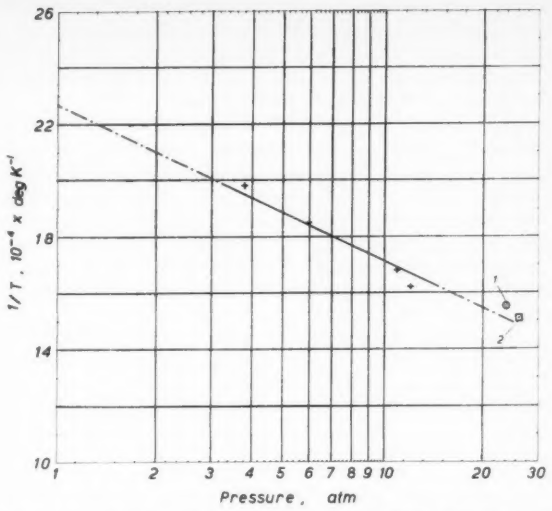

Fig. 3 Vapor pressure of kerosine D. Eng. R.D. 2495 vs. the reciprocal of the absolute temperature

1 Estimated critical point, Rolls-Royce, private communication, 1956

2 Estimated critical point, E.R.D.E., computed result

This research, experimental results

the temperature coefficient $(\partial k/\partial t)_{P_0}$ of the thermal conductivity derived from these two points is in reasonable agreement with this research, Bridgman's k_0 values, however, are about 20% higher.

The effect of pressure on thermal conductivity was expressed by Bridgman in terms of the ratio k_P/k_0, where k_p is the conductivity at elevated pressure. A direct comparison of the results of the two studies is somewhat difficult as the pressure range of this investigation extended only to 200 atm, while the lowest pressure level in Bridgman's work was 1000 kg/cm². Extrapolating graphically the latter author's k_P/k_0 values at 75 C to 200 atm (207 kg/cm²), a value of 1.05 was obtained which compares favorably with a value of 1.07 derived from this research.

Despite the good agreement between the two investigations with respect to the temperature and pressure coefficient of the thermal conductivity there is a considerable discrepancy between the absolute values of both investigations. In view of the previous statements by Riedel (2) on Bridgman's experimental technique and the fact that the data of this research were checked by control measurements on toluene, the authors are inclined to believe that the earlier work on kerosine by Bridgman is in error.

In conclusion, there are a few words to be said about the origin of the liquidus line shown in Fig. 1. As far as could be ascertained, no vapor pressure data existed for the kerosine investigated and the only relevant information, the

Table 2 Comparison with the data of Bridgman (4)

	Zero pressure thermal conductivity k_0 —10^{-4} × cal/cm s deg C—	
Temperature, C	Bridgman (4)	This research
30	3.57	2.87
75	3.33	2.67

critical pressure and temperature reported in (5) and (6), were obtained with the aid of empirical relations (7). A few crude determinations of the saturation pressure of D.Eng. R.D. 2495 were therefore made with the aid of the pressurising equipment of the conductivity apparatus.

Fig. 3 shows a plot of the experimental values of the saturation pressure vs. the reciprocal of the absolute temperature. Despite the crudeness of the tests the results obtained can be correlated with the computed critical data and also seem to be in general agreement with the first boiling point at atmospheric pressure given in Table 1. No high accuracy is claimed for these results; they were recorded here as they might be of some use in engineering practice, until superseded by accurate determinations.

Considering all factors, the overall accuracy of the thermal conductivity measurements is believed to be better than $\pm 1.5\%$ over the entire range studied.

Acknowledgments

The authors wish to acknowledge the assistance given by the Research Centre of the British Petroleum Company, Limited, in carrying out the analysis of the original sample of kerosine D. Eng. R.D. 2495, and the help given by N. J. Blay, of the Explosives Research and Development Establishment, who carried out the analysis of the various samples recovered from the thermal conductivity apparatus.

References

1 Ziebland, H. and Burton, J. T. A., *Int. J. Heat Mass Transfer*, vol. 1, 1960, p. 242.
2 Riedel, L., *Chem. Ing. Tech.*, vol. 23, no. 3, 1951, p. 32.
3 Schmidt, E. and Leidenfrost, W., *Chem. Ing. Tech.*, vol. 26, no. 1, 1954, p. 35.
4 Bridgman, P. W., *Proc. Amer. Acad. Arts Sci.*, vol. 59, 1923, p. 141.
5 Bragg, S., Rolls Royce Ltd., Derby, private communication.
6 Ziebland, H., Ministry of Supply, unpublished report.
7 Maxwell, J. B., *Data Book on Hydrocarbons*, D. Van Nostrand Co., Inc., N. Y., 1950.

Technical Comments

Thrust Termination Transients in Solid Propellant Rockets[1]

R. E. BARRY[2] and J. E. BROTHERS[3]

Hercules Powder Co., Inc., Cumberland, Md.

A solution to the differential equation relating the transient chamber pressure to time is presented for a rocket motor containing burning propellant after the terminator ports are opened.

IN AN operating rocket motor, the chamber pressure is determined by the mass rate of gas production and the mass rate of gas discharging through the nozzle. When additional discharge ports are opened (as on termination) the chamber pressure falls to a new equilibrium level. This note examines the mechanism of the pressure decay and thus is an extension of Rodean's article (1)[4] on the pressure drop in a rocket chamber after propellant exhaust cutoff.

The following assumptions are made:

1 The perfect gas relationships hold.

2 The effect of the pressure decay on the flame temperature can be neglected. (Calculations for a typical system indicate a 10% drop in temperature as the chamber pressure drops from 17 atm to 1 atm.)

3 The pressure decay is rapid enough so that the change in chamber free volume is negligible.

4 The burning rate throughout the pressure decay can be described by $r = cP^n$.

5 Sonic flow is established at the outlets.

For a well designed nozzle, the mass flow rate $\dot{m}$ depends on the throat area A_t and the chamber pressure P

$$\dot{m}_a = C_d A_t P \qquad [1]$$

Similarly, for a sonic orifice

$$\dot{m}_p = C_d b A_p P \qquad [2]$$

The total discharge rate is the sum of Eqs. 1 and 2. The rate of gas production is

$$\dot{m}\ (\text{produced}) = Srh = ScP^n h \qquad [3]$$

Therefore the change in the mass of gas contained in the chamber can be described by the following equation

$$-\frac{dM}{dt} = C_d P(A_t + bA_p) - ScP^n h \qquad [4]$$

For a perfect gas

$$M = \frac{WVP}{RT} \qquad [5]$$

and

$$dM = \frac{WV\,dP}{RT} \qquad [6]$$

Substituting in Eq. 4

$$-\frac{WV}{RT}\frac{dP}{dt} = C_d P(A_t + bA_p) - Sc\,P^n h \qquad [7]$$

Received Nov. 7, 1960.
[1] This work was performed under Air Force Contract AF04 (647) 243.
[2] Research Engineer, Ballistic Research Group, Allegany Ballistics Lab.
[3] Mathematical Analyst, Advanced Development Group, Hercules Powder Co., Magna, Utah.
[4] Numbers in parentheses indicate References at end of paper.

For convenience let

$$\frac{WV}{RT} = X \qquad [8]$$

$$C_d(A_t + bA_p) = Y \qquad [9]$$

$$Sch = Z \qquad [10]$$

The constants X, Y, Z determined by the system are assumed to be independent of pressure.
Then

$$-X\frac{dP}{dt} = YP - ZP^n \qquad [11]$$

Integrating and rearranging

$$P^{1-n} - \frac{Z}{Y} = \left[P_0^{1-n} - \frac{Z}{Y}\right]e^{-(Y/X)(1-n)t} \qquad [12]$$

where P_0 is the pressure at $t = 0$ (when the terminator ports are opened). Note that the special case of opening a pressurized chamber in which there is no burning propellant may be calculated by setting $Z = 0$ (which is equivalent to setting $S = 0$) in Eq. 11 to get

$$P = P_0 e^{-(Y/X)(1-n)t} \qquad [13]$$

The use of Eq. 12 is restricted by the fact that c in Eq. 3 is determined empirically with the pressure given in psia and r being determined in ips.

A typical case is worked below and the pressure-time relation thereof is presented.
Given:

$V = 90{,}000$ in.^{3}
$A_t = 40$ in.^{2}
$A_p = 100$ in.^{2}
$P_0 = 500$ psia
$c = 0.03$
$n = 0.4$
$h = 0.06$ lbm/in.^{3}
$W = 20$ lbm/lb-mole
$S = 2000$ in.^{2}
$T = 5000$ R
$R = 1545$ ft-lbf/mole-R
$k = 1.26$
$b = 0.83$ [sec (2)]

Then

$$X = \frac{0.0233 \text{ lbm-in.}^2}{\text{lbf}}$$

$$Y = \frac{0.7431 \text{ lbm-in.}^2}{\text{lbf-sec}}$$

$$Z = 3.6\frac{\text{lbm}}{\text{sec}}\left(\frac{\text{in.}^2}{\text{lbf}}\right)^n$$

Substituting into Eq. 12

$$P^{0.6} - 4.85 = (500^{0.6} - 4.85)e^{-19.13t}$$

Substituting values of t, the following pressure values were determined

t, sec	P, psi
0.01	380
0.02	290
0.05	136
0.10	48.7
0.2	14.0
0.0	13.9

From these values of pressure, instantaneous values of thrust and mass rate of flow can be calculated. If the total mass ejected after the ports are opened is to be determined (for sizing vacuum test equipment), this information can be obtained from graphical integration of mass flow rate vs. time.

Nomenclature

A = area
b = ratio of effective flow area to physical area in an orifice
c = constant in burning rate equation
d = differential operator
e = base of natural logarithms
g = conversion factor in Newton's Law
h = propellant density
k = ratio of specific heats
M = mass of gas
$\dot{m}$ = mass rate of flow
n = constant in burning rate equation
P = chamber pressure
p = port
R = universal gas constant
r = burning rate
S = burning surface
T = flame temperature
t = time
V = free volume
W = gas molecular weight
X, Y, Z = constants of system
C_d = discharge coefficient $\left[\frac{gkW}{RT}\left(\frac{2}{k+1}\right)^{\frac{k+1}{k-1}}\right]^{1/2}$

References

1 Rodean, H. C., "Rocket Thrust Termination Transients," ARS JOURNAL, vol. 29, no. 6, June 1959, pp. 406–408.
2 Cunningham, R. G., "Orifice Meters with Supercritical Compressible Flow," *Trans. Am. Soc. Mech. Engrs.*, vol. 73, 1951, p. 625.

Optimization of Multistage Rockets

RICHARD J. WEBER[1]

Lewis Research Center, NASA, Cleveland, Ohio

COLEMAN (1)[2] has recently presented an improved mathematical technique for optimizing the design of multistage rocket vehicles. The difference between his and previously published methods lies in the inclusion of a scaling law that accounts for variation in structural fraction with stage size. The importance of this factor varies with the mission being considered but it, in general, tends to diminish with increasing vehicle size.

Most previous authors have neglected another factor, which is usually of even greater importance than the structural variations. These authors characterize the selected mission by specifying a burnout velocity for the final stage, which is then increased by some appropriate amount to account for drag and gravity losses. (Or, alternatively, the losses are distributed in a predetermined fashion among the various stages,

Received April 10, 1961.

[1] Section Head, Mission Analysis Branch. Member ARS.
[2] Numbers in parentheses indicate References at end of paper.

ordinarily by depreciating the specific impulse of the stages.) However, these losses are themselves functions of the stage mass ratios and so cannot properly be considered as constants when the mass ratios are being varied. This criticism also applies to the technique of (1). The only paper that this writer has seen which correctly accounts for these losses is (2); however, it has the disadvantage of requiring that a number of optimum flight paths be calculated as part of the stage optimization procedure.

As an example of the importance of accounting for variable trajectory losses, a three-stage booster was optimized for the case of placing a payload into a 150-nautical-mile orbit with minimum gross weight. The assumed stage characteristics are given in Table 1. The specific impulses used are representative of two RP-LOX stages plus a H_2-LOX stage. For convenience, a constant structural-to-propellant weight ratio W_s/W_p was assumed. To include the trajectory losses in a correct fashion, the charts of (3) were used. The optimum combination of stage propellant fractions was obtained by assuming a number of first- and second-stage fractions and cross-plotting the corresponding vehicle payload fractions.

The optimum staging arrived at in this manner is shown in the table and corresponds to a total characteristic velocity increment ΔV of 32,000 fps. If this value of ΔV is presumed to pertain to all other propellant fractions, the usual mathematical optimization technique can be applied, with the results shown in the table. The payload-to-gross weight ratio W_L/W_g is seen to agree fairly well, as a result of the educated guess for ΔV. However, the propellant fractions are in serious error. The mathematical solution tends to make the upper, high specific-impulse stages big at the expense of the first stage. When doing so, however, it fails to recognize that this increases the ΔV losses of the upper stages.

Table 1 Booster staging for 150-nautical-mile orbit

Stage	F/W_G	I, sec	W_s/W_p	Opt. W_p/W_G, Constant $V = 32{,}000$	Opt. W_p/W_G, Correct solution
1	1.3	292(av)	0.08	0.30	0.67
2	1.0	305	0.08	0.48	0.35
3	1.0	425	0.08	0.81	0.72
			$W_L/W_G =$	0.0415	0.0382

Note that it would not help to distribute the ΔV losses among the stages. The greatest losses always occur in the first stage, so the mathematical solution would tend to make this stage even smaller.

The conclusion to be drawn is that mathematical optimizations of multistage rockets are valid only when all the significant variables are included. For satellite launching vehicles, an essential variable to consider is the ΔV loss due to gravity and drag. When this factor is included, straightforward cross-plotting of representative points is probably easier than mathematical optimization.

References

1 Coleman, J. J., "Optimum Stage-Weight Distribution of Multi-Stage Rockets," ARS JOURNAL, vol. 31, no. 2, Feb. 1961, pp. 259–261.

2 Chase, R. L., "Multistage Rocket Staging Optimization," preprint 60-41, *Am. Astron. Soc.*, 1960.

3 MacKay, J. S. and Weber, R. J., "Performance Charts for Multistage Rocket Boosters," NASA TN D-582, Jan. 1961.

Meteoritic Dust on the Surface of the Moon

ROY G. BRERETON[1]

Aerojet-General Corp., Azusa, Calif.

FROM a study of cosmic spherules in ocean sediments, Pettersson (1),[2] estimates that more than 5 million tons of meteoritic material actually falls to Earth every year, while Watson (2), from the observed frequency of visible meteors estimates about 24 million visible each day, and other data calculates this figure to be between 365,000 and 3,650,000 tons. These estimates of the amount of meteoritic material swept up by the Earth are necessarily crude, yet they serve to indicate that each day the Earth accretes several thousand tons of extraterrestrial material. This is a sizeable amount and represents from 10 to 50 lb of meteoritic dust annually per sq mile of Earth's surface.

Because the surface area of the moon is only about $\frac{1}{14}$ of Earth's and its force of attraction only $\frac{1}{6}$, its annual accretion of meteor material is expected to be appreciably less than for Earth. Nevertheless, calculations indicate it is at least 2 lb annually per sq mile. On the surface of the moon, this material, consisting of stoney and iron meteorites at a ratio of 3/2, would have a density of 3.5 g/cm^3. Consequently, approximately 1 cm of meteoritic dust is accreted onto the lunar surface every 100 million years.

In addition to the fine meteor material constantly raining onto the lunar surface, large meteors, ranging in weight from half a gram to many tons, are sufficiently massive to penetrate the moon's tenuous atmosphere and plunge with shattering force into the surface. Watson has shown that approximately 280,000 meteors of a mass greater than 0.6 g strike Earth's atmosphere each day. This means that millions of meteorites pulverize and bombard the lunar surface every year. These impacts pit the lunar surface and scatter debris from both lunar rocks and meteorites over a wide area.

In order to determine the present thickness of meteoritic dust covering the lunar surface, we must know the age of the moon, or at least the geological time-span since the formation of a permanent rigid crust. Present evidence suggests that the moon was formed cold by the accretion of primordial particles. After the development of a relatively cool and rigid sintered crust, gravitational compaction and radioactive heating increased the temperature of the moon's interior and triggered the super-volcanic process that formed the so-called "wet craters," and a "lava-complex" surface. Subsequently this lava cooled and now appears rugged and pitted from meteorite scars and dying volcanism.

Although the above processes reached their culmination some 3 billion years ago on Earth, and are in a sense still continuing here, calculations indicate that peculiarities of the geophysical environment of the moon delayed their full development there for about 2.5 billion years. Thus, the major

Received Dec. 22, 1960.

[1] Senior Geophysicist, Advanced Research Div.

[2] Numbers in parentheses indicate References at end of paper.

Table 1 Properties of meteor dust on the lunar surface

Thickness	On smooth uneroded surfaces—5 to 7 cm On the rough vesicular surfaces of Mares, much dust has been lost into small cracks and openings; thus it will appear thinner there—2 to 5 cm
Texture	Unconsolidated, seriated fragments, ranging in size—0.02 mm to 10 cm Some colloidal material
Composition	Meteoritic silicate plus basalt

structural and geomorphic features that are observed for the moon are approximately 500 million years old.

We may thus conclude, that in this time span, a minimum of 5 cm of meteor dust has been uniformly deposited over the lunar surface, while impact phenomena has provided 2 cm more of pulverized rock fragments. In general, this material has tended to smooth the rugged scarred surface of the moon. Accordingly, the rough vesicular surface of lava flows and small pits from impacting meteorites have been partially filled in or completely veneered by fine dust. See Table 1.

References

1 Pettersson, H., "Cosmic Spherules and Meteoritic Dust," *Scientific Amer.*, 202, Feb. 1960.

2 Watson, F. G., *Between the Planets*, Harvard University Press, 1956.

New Patents

George F. McLaughlin, *Associate Editor*

Afterburner fuel metering control (2,960,155). M. C. Bartz, South Bend, Ind., assignor to the Bendix Corp. (ARS corporate member).

Fly-weight governor connected to a constant displacement flowmeter. A spring opposes the force exerted by the governor, and means are provided for varying the force of the spring.

Liquid braking apparatus (2,960,192). H. T. Schwinge, Alamogordo, N. Mex., assignor to the U. S. Air Force.

Liquid forced through passages of varying size and number along tracks carrying a moving mass stops the mass in a predetermined deceleration-time pattern.

Rocket starter for gas turbine (2,960,824). H. Plummer, La Jolla, Calif., assignor to Rohr Aircraft Corp. (ARS corporate member).

Long mass of restricted burning solid propellant within the converging portion of the casing, ignited electrically. Hot gases are directed toward the discharge orifice.

Production of liquid oxygen (2,960,834). E. M. Kirk Patrick, Venice, Calif., assignor to the Garrett Corp. (ARS corporate member).

High pressure substance below the liquefaction temperature of the oxygen in atmospheric air is introduced to heat exchangers connected in series.

EDITOR'S NOTE: Patents listed above were selected from the Official Gazette of the U. S. Patent Office. Printed copies of patents may be obtained from the Commissioner of Patents, Washington 25, D. C., at a cost of 25 cents each; design patents, 10 cents.

Rocket nozzle with cooling means (2,962,221). H. R. Kunz, Warehouse Point, Conn., assignor to United Aircraft Corp. (ARS corpoate menber).

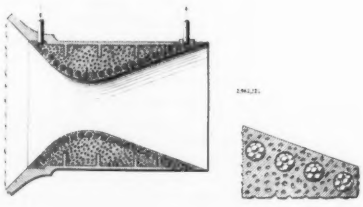

Throat cooled by transpiration of sweat cooling and cooling fluid to nozzle passage. Nozzle of porous material with coolant passages assuring flow of coolant to all portions of nozzle.

Transit-time accelerometer (2,960,872). L. M. Jones (ARS member), Ann Arbor, Mich., assignor to the U. S. Air Force.

Mass rigidly suspended within a cavity and released without imparting initial velocity. Time interval is measured between release of mass and its contact with cavity wall.

Control apparatus (2,960,875). D. F. Elwell, Columbia Heights, Minn., assignor to Minneapolis-Honeywell Regulator Co. (ARS corporate member).

Gyroscope with motor for controlling the rotor gimbal. Auxiliary holding means maintains the gimbal caged or uncaged for a predetermined time interval after the motor is rendered inoperative.

Gyroscopic instruments (2,960,876). F. Saphra, Levittown, N. Y., assignor to Sperry Rand Corp. (ARS corporate member).

Rate gyro with normally closed housing. Breakable atmospheric seal permits gas to vent when a detonator ignites a propellant grain in a chamber on the reaction-type rotor.

Gimbal system (2,960,878). S. Lees Newton, Mass.

Spherical case containing a spherical gimbal retained with complete freedom of rotation, for establishing a geometric reference.

Igniter (2,960,935). D. A. Colpitts, Ridgecrest, Calif., assignor to the U. S. Navy.

Frangible capsules within a cylinder. Some capsules are filled with oxidizer; an equal number filled with hypergolic fuel. A device in the cylinder ruptures any two adjacent capsules to cause autoignition.

Guided missile control (2,961,190). T. Miller, C. F. Conley and A. Nelkin, Pittsburgh, Pa., assignors to the USN.

Homing missile for attacking a target. Control signal varies with Doppler frequency of target signal received, steering the missile in arcuate paths.

One-star navigational director (2,961,191). R. E. Jasperson, Annapolis, Md.

Star follower for missiles continuously measures true altitude and relative bearing of a single celestial body. Controller means operate in response to bearing and handing indicators to maintain true heading.

Missile carrying aircraft (2,961,197). H. Hertel, Fontainebleau, France.

Detachable ramjet powered missiles with lift-producing annular casings, carried at the wing tips of an aircraft, and supplying additional propulsion to the aircraft.

Aircraft power plant (2,961,198). E. W. Stevens, Snyder, N. Y., assignor to Bell

Aerospace Corp. (ARS corporate member).

Turbo-jet with auxiliary reheat afterburner swingable between horizontal and vertically directed attitudes while remaining symmetrically disposed relative to the longitudinal center line.

Airborne cinetheodolite (2,961,933). F. A. Kinder and E. E. Green, China Lake, Calif., assignors to the U. S. Navy.

Method of determining course and attitude of a missile in flight from a pair of airborne camera stations flown to opposite sides of projected missile flight path.

Method of making honeycomb panels (2,962,811). T. A. Herbert Jr., Chula Vista, Calif., assignor to Rohr Aircraft Corp. (ARS corporate member).

Stainless steel sheet brazed to a core of cells and immersed to obtain nickel phosphorous alloy film 0.001 in. thick; sheet and core heated to fusion temperature.

Vehicle propulsion apparatus (2,962,934). O. R. Seidner, Alhambra, Calif., assignor to the Garrett Corp. (ARS corporate member).

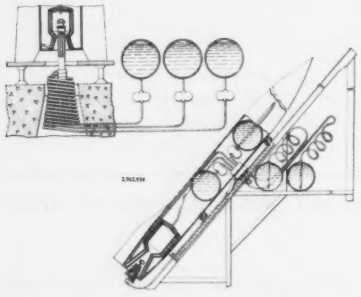

Auxiliary boost in launching rockets so fuel usually expended in getting the rocket off the ground is conserved for use in later phases. Externally supplied fuel applied from staging platform.

Gyroscopic inertial guidance for space vehicles (2,963,242). Dr. F. K. Mueller (ARS member), Huntsville, Ala., assignor to the U. S. Army.

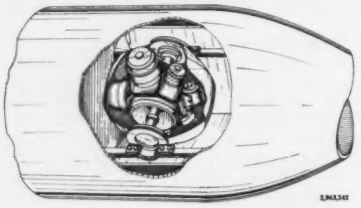

Platform stabilized relative to space and the stars, establishing a space-fixed system of three reference coordinates. Gyro gimbals located within the stabilized element.

Frictionless accelerometer (2,963,285). F. L. Fischer and E. F. Werndl, New York, N. Y., assignors to Bulova Research and Development Laboratories, Inc. (ARS corporate member).

Spherical inner and outer vessels with liquid filling space between, rendering inner vessel buoyant; photoelectric detector provides signal to indicate direction and extent of displacement between vessels.

High energy fuel (2,963,855). R. L. McLaughlin, L. O. Miller and J. W. Schick, Merchantsville, N. J., assignor to Socony Mobil Oil Co., Inc.

Trimethyl-3-cyclohexylhydrindane in wings of jet aircraft. Conventional jet fuel used up to supersonic speeds; when aerodynamic heating occurs, aircraft is operated solely from fuel in wings.

Space vehicle guidance mechanism and method (2,963,243). H. C. Rothe, Huntsville, Ala.

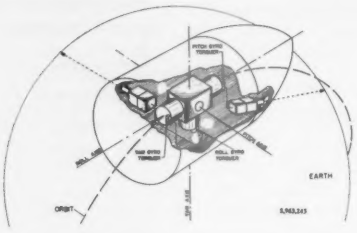

Gyroscopically stabilized inertial platform. Continuous alignment with horizon made possible by pitch-axis sensor or scanner which may be one of known types of horizon sensors.

Gyro optical system (2,963,973). R. S. Esty, North Hollywood, Calif., assignor to the U. S. Navy.

Missile adapted to home on a source of radiation. A lens and mirror system carried on a gyroscope rotor receives chop rays through a dome-shaped front window.

Monorail car design (189,461). W. H. Statler, Northridge, Calif., assignor to Lockheed Aircraft Corp. (ARS corporate member).

Bus-like configuration below which a pair of tapered legs straddles the rail at fore and aft ends of the body. (Propulsion method not disclosed.)

Steering system using thermal energy radiations (2,964,265). R. W. Ketchledge, Jamaica, N. Y., assignor to Bell Telephone Laboratories (ARS corporate member).

Two thermal energy elements having different fields of view and in alignment with each other. Electrical pulses are produced in response to energy radiation collected from each field of view.

Slaving system (2,964,266). A. M. Fuchs, New York, N. Y., assignor to the Bendix Corp. (ARS corporate member).

Antenna pointed at a target before release of a missile. Radar for determining distance between missile and target, and signals to train the antenna on target.

Missile attitude control system (2,965,334). H. S. McCullough Jr., and J. M. Hall, Huntsville, Ala.

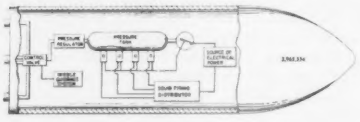

Electrically-fired squibs burning in casings containing chemicals cause pressurized gas to actuate motors controlling missile attitude.

Airplane design (189,438). E. Y. Sing and C. M. Sperazz Sr., Williamsville, N. Y., assignors to Bell Aerospace Corp. (ARS corporate member).

Pivotable shrouded ducted fans at wing tips permit vertical ascent and descent and transition to and from horizontal flight.

Jet engine muffler (2,965,190). C. W. Lemmerman (ARS member), W. Hartford, Conn.

Elongate elements mounted under tension in a housing. Exhaust gases move along the elements, some of which are divided into longitudinal independent vibratory sections.

Ommi-environment suit for high altitude flight (2,966,155). C. P. Krupp, Cuyahoga Falls, Ohio, assignor to the B. F. Goodrich Co. (ARS corporate member).

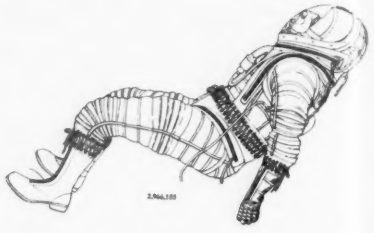

Inflatable suit carrying its own atmosphere—oxygen, pressure, and air conditioning—to overcome physiological and other hazards at 20 or more miles above sea level. Provides extensive freedom of movement.

Object detection and tracking system (2,966,591). E. J. McCartney, Rockville Center, N. Y., assignor to Sperry Rand Corp. (ARS corporate member).

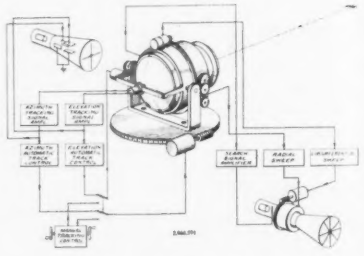

Infrared "look-through" scanning device for simultaneously tracking and searching, using single energy-collecting and focusing. Optical system uses Schmidt-like correcting lens.

Gyroscopic theodolite (2,966,744). F. K. Mueller (ARS member), Huntsville, Ala.

Compressed gas is used to form a film between concave and convex surfaces supporting a frame on which a gyrocompass is mounted.

Rocket-propelled missile (2,967,393). W. von Braun (ARS member), Huntsville, Ala., assignor to the U. S. Army.

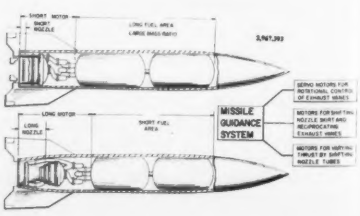

Space vehicle having short nozzle, whereby more space within shell is available for fuel. Variable thrust achieved with no variation of fuel supply. Nozzle has thrust producing bars or tubes extending across space within its wall.

Toroidal gyroscope (2,966,803). J. V. Johnston, Huntsville, Ala.

Doughnut-shaped rotor. Stator fixed at the center of a body having upper and lower spherical surfaces. Each air bearing means supports one of the surfaces on a gaseous film.

Tracking telescope with dual field optical system (2,966,823). R. H. Trimble, Culver City, Calif., assignor to Northrop Corp. (ARS corporate member).

Two real images of a point on a distant source of light lying just off the optical axis of the system are simultaneously formed on the image field over paths having different focal lengths.

Full pressure flight suit (2,967,305). R. F. White and G. J. Scott, Compton, Calif., assignors to the U. S. Navy.

Convoluted cylindrical sections at flexure joints of an occupying human body. Flexible longitudinal tubes are adjustable to length of occupant's body member length.

Technical Literature Digest

M. H. Smith, *Associate Editor*
The James Forrestal Research Center, Princeton University

Propulsion and Power (Combustion Systems)

Performance of a Low-Thrust Storable-Bipropellant Rocket at Very Low Chamber Pressure, by John P. Wanhainen, Richard L. DeWitt and Phil S. Ross, *NASA TN* D-678, March 1961, 22 pp.

Thrust with Heating at Supersonic Speeds, by K. Oswatitsch, *Deutsche Versuchsanstalt fur Luftfahrt, E. V. Bericht,* no. 90, March 1959, 29 pp.

Turbomachinery Laboratory, by Jacques Chauvin, *Training Center for Experimental Aerodynamics, Tech. Mem.* 9, Nov. 1960, 12 pp.

Factors that Affect Operational Reliability of Turbojet Engines, by *Lewis Center Staff, NASA Tech. Rep.* R-54, 1960, 211 pp.

Solid Propellant Rocket Research, a Selection of Technical Papers Based Mainly on a Symposium of the American Rocket Society held at Princeton University, Princeton, N. J., Jan. 28–29, 1960. Progress in Astronautics and Rocketry, Vol. 1, Martin Summerfield, ed., New York, Academic Press, 1960, 692 pp.

Mechanical Properties and the Design of Solid Propellant Motors, by M. L. Williams, pp. 67–100.

Solid Propellant Rocket Motors as Acoustic Oscillators, by F. T. McClure, R. W. Hart and J. F. Bird, pp. 295–358.

Heat Transfer Stability Analysis of Solid Propellant Rocket Motors, by Reuel Shinnar and Menachem Dishon, pp. 359–373.

A Theory of Oscillatory Burning of Solid Propellants Assuming a Constant Surface Temperature, by A. G. Smith, pp. 375–391.

Combustion Instability in Solid Rockets Using Propellants with Reactive Additives, by Sin-I Cheng, pp. 393–422.

The Influence of Erosive Burning on Acoustic Instability in Solid Propellant Rocket Motors, by R. W. Hart, J. F. Bird and F. T. McClure, pp. 423–451.

An Experimental Investigation of Unstable Combustion in Solid Propellant Rocket Motors, by Grant W. Brownlee and Frank E. Marble, pp. 455–494.

Experimental Investigations of Unstable Burning in Solid Propellant Rocket Motors, by E. M. Landsbaum, W. C. Kuby and F. W. Spaid, pp. 495–525.

Development Problems of Large Solid Rocket Motors, by E. R. Roberts, *Raketentechnik und Raumfahrtforschung,* vol. 5, no. 1, Jan.–Mar. 1961, pp. 6–13. (*In German.*)

Range of Application of Ramjets, by I. Sanger-Bredt, *Rakentechnik und Raumfahrtforschung,* vol. 5,n o. 1, Jan.–March 1961, pp. 18–21. (*In German.*)

Cryogenic Power—Cold Gas Actuation for Space Vehicles, by H. D. Davis, *Hydraulics and Pneumatics,* vol. 13, no. 12, Dec. 1960, pp. 83–86, 96.

The Optimum Size of a Rocket Engine, by J. E. P. Dunning, *Royal Aeron. Soc. J.,* vol. 64, no. 600, Dec. 1960, pp. 717–742.

Saturn Engine Adapted From Missiles, by R. Healy, *SAE Journal,* vol. 69, no. 2, Feb. 1961, pp. 34–37.

Propulsion and Power (Non-Combustion)

Physical Principles of Magnetohydrodynamic Power Generation, by Richard J. Rosa, *Avco-Everett Res. Lab. Res. Rep.* 69, Jan. 1960, 34 pp.

A One-Dimensional Analysis of Magnetohydrodynamic Energy Conversion, by Robert G. Deissler, *NASA TN* D-680, March 1961, 45 pp.

A Thermodynamic Analysis of Thrust Augmentation for Nuclear Rockets, by Hugh M. Henneberry, Lester C. Corrington and Roger D. Becker, *NASA TN* D-581, March 1961, 30 pp.

Spacecraft Power Generation, by Wil-

EDITOR'S NOTE: Contributions from Professors E. R. G Eckert, E. M. Sparrow and W. E. Ibele of the Heat Transfer Laboratory, University of Minnesota, are gratefully acknowledged.

CHANGE-OF-ADDRESS NOTICE

In the event of a change of address, it is necessary to include both your old and new addresses, as well as your membership number and coding, when notifying ARS headquarters in order to insure prompt service. If you are moving or have moved, send the following to to Membership Dept., American Rocket Society, 500 Fifth Ave.; New York 36, N. Y.:

Name_____

Membership Card No._____ Coding_____

Old Address_____

New Address_____

liam C. Cooley, *NATO, Adv. Group Aeron. Res. Dev., Comb. and Prop. Panel*, Pasadena, Aug. 1960, 21 pp., 12 figs.

Symposium on Magnetohydrodynamics, 4th, Lockheed Missile and Space Div., Dec. 1959, Plasma Acceleration, Sidney W. Kash, ed., Stanford University Press, 1960, 117 pp.

The Use of Plasma for Propulsion of Interplanetary Rockets, by Conrad L. Longmire, pp. 3–11.

The Electromagnetic Acceleration of a Continuously Flowing Plasma, by B. Podolsky and G. Borman, pp. 12–29.

Scaling Relations for Plasma Devices, by G. Sargent James, pp. 30–36.

Plasma Propulsion by Means of a Traveling Sinusoidal Magnetic Field, by Rudolf X. Meyer, pp. 37–46.

Acceleration of Metal-Derived Plasmas, by W. L. Starr and J. T. Naff, pp. 47–59.

Hydromagnetic Plasma Gun, by John Marshall, pp. 60–72.

Propulsion from Pinch Collapse, by S. Gartenhaus and L. M. Tannewald, pp. 73–78.

Efficiency Considerations in Electrical Propulsion, by Sidney W. Kash, pp. 79–93.

The High-Energy Electrostatic Gun, by Raymond Fox, pp. 94–117.

Conference on Properties of Elemental and Compound Semiconductors, Boston, 1959, Proceedings, Harry C. Gates, ed., sponsored by the Semiconductors Committee, Institute of Metals Div., The Metallurgical Society and Boston Section, Amer. Inst. of Mining, Metallurgical, and Petroleum Engineers, N. Y., Intersci. Pub., 1960, 340 pp.

Materials for Thermoelectric Applications, by R. W. Ure Jr., R. Bowers and R. C. Miller, pp. 245–260.

Thermal and Electrical Properties of Some Silicides, by S. E. Mayer and A. L. Miavsky, pp. 261–274.

Thermal, Electrical and Optical Properties of (In, Ga) as Alloys, by M. S. Abrahams, R. Braunstein and F. D. Rosi, pp. 275–286.

Thermoelectric Properties of Pressed Bi_2Te_3 Powders, by C. Kolm and J. J. Giacalone, pp. 287–294.

Generation and Measurement of Highly Ionized Quiescent Plasmas in Steady State, by R. C. Knechtii and J. Y. Wada, *Phys. Rev. Letters*, vol. 6, no. 5, March 1, 1961, pp. 215–217.

A Review of Republic's Pinch Engine Experimental Program, by Irving Granet and William J. Guman, *Republic Aviation Corp., Plasma Propulsion Lab., PPL*-60-15 (160), Oct. 1960, 40 pp. (AFOSR 164.)

An Analytical Approach to the Problem of Pinch Dynamics, by Boa-Teh Chu, *Republic Aviation Corp., Plasma Propulsion Lab. PPL-TR*-60-9(185), Nov. 1960, 27 pp. (AFOSR TN 19.)

Experiments on Power Generation from a Moving Plasma, by H. J. Pain and P. R. Smy, *J. Fluid Mech.*, vol. 10, part 1, Feb. 1961, pp. 51–64.

Practical MHD Generator Hinges on [illegible] **as Temperature,** by G. W. Sutton, *AE J.*, vol. 69, no. 1, Jan. 1961, pp. 58–

A 1000-KW Nuclear Powerplant for [illegible] **ce Flight,** *Luftfahrttechnik*, vol. 6, no. 12, Dec. 1960, pp. 374–377.

The Development of a Negative Ion [illegible] **state** (Presented at the ARS Electro- [illegible] **Calif.**) **Propulsion Conference, Monterey,** and R. L. R. J. Sunderland, J. R. Radbill [illegible] Gilpin (Aerojet-General Corp.), *ARS Prepr.* 1371-60, Nov. 1960.

The Duoplasmatron: Theoretical Studies and Experimental Observations (Presented at the ARS Electrostatic Propulsion Conference, Monterey, Calif.), by B. S. Burton (Convair, Fort Worth, Texas), *ARS Preprint* 1372-60, Nov. 3–4, 1960.

Multiple Beam Ion Motors (Presented at the ARS Electrostatic Propulsion Conference, Monterey, Calif.), by M. P. Ernstene, A. T. Forrester, R. C. Speiser and R. M. Worlock (Electro-Optical Systems, Inc.), *ARS Preprint* 1373-60, Nov. 3–4, 1960.

Liquid Metal Droplets for Heavy Particle Propulsion (Presented at the ARS Electrostatic Propulsion Conference, Monterey, Calif.), by V. E. Krohn (Ramo-Wooldridge Corp.), *ARS Preprint* 1375-60, Nov. 3–4, 1960.

Sputtering Due to High Velocity Ion Bombardment (Presented at the ARS Electrostatic Propulsion Conference, Monterey, Calif.), by E. T. Pitkin (Marquardt Corp.), *ARS Preprint* 1377-60, Nov. 3–4, 1960.

Neutralization of Ion Beams for Propulsion by Electron Trap Formation (Presented at the ARS Electrostatic Propulsion Conference, Monterey, Calif.), by G. C. Baldwin (General Electric Co., Res. Lab., Schenectady, N. Y.), *ARS Preprint* 1378-60, Nov. 3–4, 1960.

Transient and Steady State Behavior in Cesium Ion Beams (Presented at the ARS Electrostatic Propulsion Conference, Monterey, Calif.), by J. M. Sellen and H. Shelton, (Ramo-Wooldridge Corp.), *ARS Preprint* 1379-60, Nov. 3–4, 1960.

A New Mechanism of Neutralization of Dense Ion Beams (Presented at the ARS Electrostatic Propulsion Conference, Monterey, Calif.), by J. E. Etter, S. L. Eilenberg, M. R. Currie and G. R. Brewer (Hughes Aircraft Co.), *ARS Preprint* 1380-60, Nov. 3–4, 1960.

Present Status of the Beam Neutralization Problem (Presented at the ARS Electrostatic Propulsion Conference, Monterey, Calif.), by R. N. Seitz, R. D. Shelton and E. Stuhlinger (George C. Marshall Space Flight Center, Huntsville, Ala.), *ARS Preprint* 1381-60, Nov. 3–4, 1960.

Space-Charge Theory for Ion Beams (Presented at the ARS Electrostatic Propulsion Conference, Monterey, Calif.), by G. S. Kino and K. J. Harker (Stanford University, W. W. Hansen Laboratories of Physics), *ARS Preprint* 1382-60, Nov. 3–4, 1960.

An Electrogasdynamic Approach to the Ion Jet Neutralization Problem (Presented at the ARS Electrostatic Propulsion Conference, Monterey, Calif.), by W. D. Halverson (General Motors Corp., Allison Divison), H. M. DeGroff and R. A. Holmes (Midwest Applied Science Corp., Lafayette, Ind.), *ARS Preprint* 1383-60, Nov. 3–4, 1960.

Circular Beam Neutralization (Presented at the ARS Electrostatic Propulsion Conference, Monterey, Calif.), by P. French (Thompson Ramo-Wooldridge, Inc.), *ARS Preprint* 1384-60, Nov. 3–4, 1960.

A Three Dimensional Calculation of the Effects of Insufficient Space Charge Neutralization on Ion Rockets (Presented at the ARS Electrostatic Propulsion Conference, Monterey, Calif.), by O. von Roos (Jet Propulsion Laboratory, Calif.), *ARS Preprint* 1385-60, Nov. 3–4, 1960.

Characteristics of Porous Surface Ionizers (Presented at the ARS Electrostatic Propulsion Conference, Monterey, Calif.), by D. Zuccaro, R. C. Speiser and J. M. Teem (Electro-Optical Systems, Inc.), *ARS Preprint* 1387-60, Nov. 3–4, 1960.

The Effects of Surface Structure and Adsorption on the Ionization Efficiency of a Surface Ionization Source (Presented at the ARS Electrostatic Propulsion Conference, Monterey, Calif.), by D. G. Worden (General Electric Co.), *ARS Preprint* 1388-60, Nov. 3–4, 1960.

Theory and Application of Hot-Wire Calorimeter for Measurement of Ion Beam Power (Presented at the ARS Electrostatic Propulsion Conference, Monterey, Calif.), by L. V. Baldwin and V. A. Sandborn (National Aeronautics and Space Administration), *ARS Preprint* 1389-60, Nov. 3–4, 1960.

Beam Diagnostic Techniques (Presented at the ARS Electrostatic Propulsion Conference, Monterey, Calif.), by L. R. Gallagher, F. Barcatta, M. P. Ernstene, A. T. Forrester, D. Marlow, R. C. Speiser, D. Telec and R. S. H. Toms (Electro-Optical Systems, Inc.), *ARS Preprint* 1390-60, Nov. 3–4, 1960.

Diagnostics of the Space Charge Neutralization of Ion Beams by Electron Injection (Presented at the ARS Electrostatic Propulsion Conference, Monterey, Calif.), by D. Moore and P. Kinzie, (Convair, San Diego, Calif.), *ARS Preprint* 1391-60, Nov. 3–4, 1960.

Engineering Research in Electrostatic Propulsion Devices (Presented at the ARS Electrostatic Propulsion Conference, Monterey, Calif.), by E. N. Petrick (Kelsey-Hayes Co.), *ARS Preprint* 1393, Nov. 3–4, 1960.

Instrumentation Program for Ion Engine Testing (Presented at the ARS Electrostatic Propulsion Conference, Monterey, Calif.), by A. H. Weber, A. W. Thompson and W. J. Robinson (George C. Marshall Space Flight Center, Huntsville, Ala.), *ARS Preprint* 1394-60, Nov. 3–4, 1960.

Sputtering of Copper by Ion Bombardment in the Energy Range of 5–25 kev (Presented at the ARS Electrostatic Propulsion Conference, Monterey, Calif.), by P. K. Rol, P. M. Fluit and J. Kistemaker (F. O. M. Laboratorium voor Massaspectrographie, Amsterdam, Holland), *ARS Preprint* 1395-60, Nov. 3–4, 1960.

Diffusion of Cesium and Ionization on a Porous Tungsten Emitter (Presented at the ARS Electrostatic Propulsion Conference, Monterey, Calif.), by O. K. Husmann (Curtiss-Wright Corp., Research Division, Quehanna, Pa.), *ARS Preprint* 1396-60, Nov. 3–4, 1960.

A Coaxial Flow Reactor—A Gaseous Nuclear-Rocket Concept (Presented at the ARS 15th Annual Meeting, Washington, D. C.), by H. Weinstein and R. G. Ragsdale (National Aeronautics and Space Administration, Lewis Res. Center, Cleveland, Ohio), *ARS Preprint* 1518-60, Dec. 5–8, 1960.

Analysis of a Photoemissive Converter Using Present Materials, by R. Sheridan and R. J. Tallent, *Boeing Airplane Company* D2-3555, Sept. 21, 1959.

Materials for Astronautic Vehicles (Presented at the AGARD Symposium on Astronautics, University of Rome, Italy, May 1959), by A. J. Murphy, *College of Aeronautics, Cranfield CoA Rep.* 139, Nov. 1960.

Research Study on Plasma Acceleration, by G. Fonda-Bonardi, *Litton Industries, Beverly Hills, Calif., Final Rep.* AF 49(638)345, Sept. 30, 1959. (ASTIA AD-229, 998.)

Photovoltaic Cells, Part II: An Annotated Bibliography, by M. A. Pearcy, Compiler, *Lockheed Aircraft Corp., Mis-*

siles and Space Div., Sunnyvale, Calif., SB-60-28, Dec. 1960.

Final Technical Report: Research on High Intensity Ionic Jets, by G. L. Cann and A. Ducati, *Plasmadyne Corp., Santa Ana, Calif.* P-FR109-54, Nov. 5, 1959. (AFOSR TR-59-167; ASTIA AD-229,-902.)

The Electromagnetic Pinch Effect for Space Propulsion, by A. E. Kunen and W. McIlroy, *Republic Aviation Corp., Plasma Propulsion Lab., Farmingdale, N. Y., PPL Report* 116, Aug. 1959.

Theory of Ion Emission from Porous Media (Presented at the ARS Electrostatic Propulsion Conference, Monterey, Calif.), by G. M. Nazarian and H. Shelton (Thompson Ramo Wooldridge Inc. Cleveland, Ohio), *ARS Preprint* 1386-60, Nov. 3–4, 1960.

The Effect of Variable Plasma Conductivity on MHD Energy Converter Performance, by W. B. Coe and C. L. Eisen, *Elec. Engng.*, vol. 79, no. 12, Dec. 1960, pp. 997–1004.

Magnetohydrodynamic Generators, by S. Way, *Virginia Tech. Engr.*, vol. 34, no. 1, Nov. 1960, pp. 10, 16, 48.

A **Lunar Power Plant,** by R. H. Armstrong, J. C. Carter, H. H. Hummel, M. J. Janicke and J. F. Marchaterre, *Amer. Nuclear Soc., Trans.*, vol. 3, no. 2, Dec. 1960, p. 383.

Fluidized Bed for Rocket Propulsion, by L. P. Hatch, W. H. Regan and J. R. Powell, *Nucleonics*, vol. 18, no. 12, Dec. 1960, pp. 102–103.

Self Control of Nuclear Rocket Engines, by W. H. Esselman, P. J. Blake, L. D. Smith and L. M. Valoppi, *Amer. Nuclear Soc., Trans.*, vol. 3, no. 2, Dec. 1960, pp. 384–385.

Photovoltaic Solar Energy Converters for Space Vehicles—Present Capabilities and Objectives, by A. B. Francis and W. W. Hopp, *Applications and Industry*, no. 51, Nov. 1960, pp. 379–382.

Progress Report: Solar Energy in 1960, by J. I. Yellott, *Mechanical Engng.*, vol. 82, no. 12, Dec. 1960, pp. 41–44.

Design of a Solar-Powered Thermionic Diode, by W. J. Leovic and M. W. Mueller, *Elec. Engng.*, vol. 79, no. 12, Dec. 1960, pp. 979–986.

Experimental Solar Thermionic Converter for Space Use, by H. Oman and G. Street Jr., *Elec. Engng.*, vol. 79, no. 12, Dec. 1960, pp. 967–972.

Thermionic Reactor Systems, by R. C. Howard, *American Nuclear Soc., Trans.*, vol. 3, no. 2, Dec. 1960, pp. 382–383.

Magneto-Thermionic Power Generation, by A. Schock, *Elec. Engng.*, vol. 79, no. 12, Dec. 1960, pp. 973–978.

Thermoelectricity Application Considerations, by A. A. Sorensen, *Elec. Engng.*, vol. 79, no. 12, Dec. 1960, pp. 963–967.

Propellants and Combustion

Indirect Methods in Flame Analysis, by J. Malinowski, W. Rutkowski and S. Szymczak, *Poland (Polska) Akademia Nauk Instytut Bedan Jadrowych, Bericht no.* 110/VIII, Sept. 1959, 3 pp., 4 figs. (*In German.*)

The Measurement of Flame Temperatures by the Method of Relative Intensities of Spectral Lines, by A. P. Dronov, A. G. Sviridov and N. N. Sobolev, *The Johns Hopkins Univ., Appl. Physics Lab.* TG 230-T159 (*transl. from Optika i Spektroskopiia*, vol. 5, 1958, pp. 490–499), Nov. 1960, 15 pp.

KIWI-A THREE... the third successful nuclear rocket propulsion reactor developed by Los Alamos Scientific Laboratory for Project Rover. Testing of new designs is continuing at an accelerated pace.

Opportunities exist for engineers and scientists who have had experience in the following areas: automatic controls systems, computer simulation, electronic aspects of controls systems, reactor design and operation, fluid flow control, and cryogenics.

For employment information send resume to:
Personnel Director, Division 61-51A

los alamos
scientific laboratory
OF THE UNIVERSITY OF CALIFORNIA
LOS ALAMOS, NEW MEXICO

Adiabatic Flame Temperatures, Combustion Gas Compositions, and Expansion Ratios of Combustible Gas Mixtures at Various Pressures, by William A. Strauss and Rudolph Edse, *Wright Air Dev. Center, TN* 59–49, July 1959.

The Behavior of Explosives at Very High Temperatures, by Joseph Wenograd, *Bur. Naval Weapons Rep.* 7328, Oct. 14, 1960.

Analytical Performance Characteristics and Outlet Flow Conditions by Constant and Variable Lead Helical Inducers for Cryogenic Pumps, by John C. Montgomery, *NASA TN* D-583, March 1961.

Electric Spark Ignition in Carbon-Vane Fuel Pumps, by John A. Campbell, Richard J. Parker and Robert G. Dorsch, *NASA TN* D-589, Feb. 1961, 16 pp.

Research on the Hazards Associated with the Production and Handling of Liquid Hydrogen, by Michael Zabetakis and David S. Burges, *Wright Air Dev. Div., Tech. Rep.* 60-141, June 1960, 76 pp. *Also: Bur. Mines, Div. Explosives, Tech. Rep. of Investigations* 5707. (*ASTIA AD* 239,644.)

Handbook for Hydrogen Handling Equipment, by B. M. Bailey et al. (Arthur D. Little, Inc.), *Wright Air Dev. Center, Tech. Rep.* 59-751, Feb. 1960, 584 pp.

Solid Propellant Rocket Research, a Selection of Technical Papers Based Mainly on a Symposium of the American Rocket Society held at Princeton University, Princeton, New Jersey, January 28–29, 1960, Progress in Astronautics and Rocketry, Vol. 1, Martin Summerfield, ed., New York, Academic Press, 1960, 692 pp.

Grain Design and Development Problems for Very Large Rocket Motors, by A. B. Boyd, W. M. Burkes and J. E. Medford, pp. 3–31.

On "Poisson's Ratio" in Linear Viscoelastic Propellants, by A. M. Freudenthal and L. A. Henry, pp. 33–66.

A Method of Strength Analysis of Solid Propellant Rocket Grains, by N. N. Au, pp. 101–120.

Stress and Strain Analysis, of Cylindrical Case-Bonded Grains, by J. Vandenkerckhove and G. Lampens, pp. 121–138.

Burning Mechanism of Ammonium Perchlorate Propellants, by Martin Summerfield, G. S. Sutherland, M. J. Webb, H. J. Taback and K. P. Hall, pp. 141–182.

Some Research Problems in the Steady-State Burning of Composite Solid Propellants, by D. W. Blair, E. K. Bastress, C. E. Hermance, K. P. Hall and M. Summerfield, pp. 183–206.

A Theoretical Study of the Burning of a Solid Propellant Sandwich, by E. Nachbar, pp. 207–226.

The Role of Binder in Composite Propellant Combustion, by R. F. Chaiken and W. H. Andersen, pp. 227–249.

Combustion of Metals: Physical Considerations, by Irvin Glassman, pp. 253–258.

The Experimental Nature of the Combustion of Metallic Powders, by W. M. Fassell, C. A. Papp, D. L. Kildenbrand and R. P. Sernka, pp. 259–269.

Combustion Characteristics of Metal Particles, by Derck A. Gordon, pp. 271–278.

The Combustion of Elemental Boron, by Claude P. Talley, pp. 279–285.

Metal Combustion in Deflagrating Propellant, by William A. Wood, pp. 287–291.

Unstable Burning Phenomenon in Double-Base Propellants, by Theos A. Angelus, pp. 527–559.

Review of Experimental Research on Combustion Instability of Solid Propellants, by E. W. Price, pp. 561–602.

Resonant Burning of Solid Propellants: Review of Causes, Cures and Effects, by R. H. Wall, pp. 603–619.

The Mechanism of Ignition of Composite Solid Propellants by Hot Gases, by R. F. McAlevy, III, P. L. Cowan and M. Summerfield, pp. 623–652.

Propellant Ignition by High Convective Heat Fluxes, by A. D. Baer, N. W. Ryan and D. L. Salt, pp. 653–672.

Solid Propellant Ignition Studies with High Flux Radiant Energy as a Thermal Source, by Rodney B. Beyer and Norman Fishman, pp. 673–692.

Slotted Tube Grain Design, by Max W. Stone, ARS JOURNAL, vol. 31, no. 2, Feb. 1961, pp. 223–227.

Thermodynamic Calculations of Hydrogen-Oxygen Detonation Parameters for Various Initial Pressures, by Loren E. Bollinger and Rudolph Edse, ARS JOURNAL, vol. 31, no. 2, Feb. 1961, pp. 251–256.

An Integrated Propellant Performance Analysis Program, by Stanley F. Sarner and John F. Dollries, ARS JOURNAL, vol. 31, no. 2, Feb. 1961, pp. 257–258.

Theories of Detonation, by Marjorie W. Evans and C. M. Ablow, *Chem. Rev.*, vol. 61, no. 2, April 1961, pp. 129–178.

The Differential Thermal Analysis of Perchlorates, V. The System Lithium Perchlorate-Potassium Perchlorate, by Meyer M. Markowitz, Daniel A. Boryta and Robert F. Harris, *J. Phys. Chem.*, vol. 65, no. 1, Feb. 1961, pp. 261–266.

Oxidation of Ammonia in Flames, by C. P. Fenimore and G. W. Jones, *J. Phys. Chem.*, vol. 65, no. 1, Feb. 1961, pp. 298–303.

The Homogeneous Base-Catalyzed Decomposition of Hydrogen Peroxide, by Frederick R. Duke and Trice W. Haas, *J. Phys. Chem.*, vol. 65, no. 1, Feb. 1961, pp. 304–305.

Preflame Reactions in the Autodecomposition of Acetylenic Compounds, by U. V. Henderson Jr., *J. Phys. Chem.*, vol. 65, no. 1, Feb. 1961, pp. 309–313.

Research in Nitromonomers and Their Application to Solid Smokeless Propellants, by Carol Anderson, Roy Scott Anderson and Henry Freuer, *Purdue Univ., Dept. Chem., Progress Rep.* 23, Feb. 1961, 37 pp.

Theory of Flame-Front Stability, by Wiktor Eckhaus, *J. Fluid Mech.*, vol. 10, part 1, Feb. 1961, pp. 80–100.

Study of the Combustion of Composite Powders by Ultra-Fast Microphotography, by R. Kling and J. Brulard, *Recherche Aeronautique*, no. 80, Jan.–Feb. 1960, pp. 3–12. (*In French.*)

Erosion Losses in Solid Rocket Propellants, by W. Buschulte, *Raketentechnik und Raumfahrtforschung*, vol. 5, no. 1, Jan.–March 1961, pp. 14–17. (*In German.*)

Materials and Structures

A Differential Thermal Analysis Apparatus for Temperatures up to 1575°C, by Kenneth G. Skinner, *Naval Res. Lab. Rep.* 4942, May 1957, 12 pp. (*ASTIA AD* 134, 624.)

A Class of Solutions of the Equations of Thermoelastic Equilibrium, by Ian N. Sneddon, *Duke Univ., Dept. of Math.*, Aug. 1960, 10 pp. (*AFOSR TN* 60-1046.)

An Investigation of High-Velocity Impact Cratering into Nonmetallic Targets and Correlation of Penetration Data for Metallic and Nonmetallic Targets, by William H. Kinard and Rufus D. Collins Jr., *NASA TN* D-726, Feb. 1961, 31 pp.

A Technique for Obtaining Hypervelocity Impact Data by Using the Relative Velocities of Two Projectiles, by William H. Kinard and Rufus D. Collins Jr., *NASA TN* D-724, Feb. 1961, 14 pp.

Leading-Edge Buckling Due to Aerodynamic Heating, by E. H. Mansfield, *Gt. Brit., Aeron. Res. Council, R & M.*, no. 3197, May 1959, 20 pp.

Titanium Nitride: An Oxidizable Coating for the High-Temperature Protection of Graphite, by N. T. Wakelyn, *NASA TN* D-722, Feb. 1961, 17 pp.

Mechanical Properties of Structural Materials at Low Temperatures; a Compilation from the Literature, by R. Michael McClintock and H. P. Gibbons, *Nat. Bur. Standards Monograph* 13, June 1960, 180 pp., 104 ref.

A Compendium of the Properties of Materials at Low Temperature (Phase I) – Pt. 1, Properties of Fluids, by V. J. Johnson, *Wright Air Dev. Div. Tech. Rep.* 60-56, Pt. I, Oct. 1960, 489 pp.

Conference on Properties of Elemental and Compound Semiconductors, Boston, 1959, Proc., Harry C. Gates, ed., sponsored by the Semiconductors Committee, Institute of Metals Div., the Metallurgical Society and Boston Section, American Institute of Mining, Metallurgical, and Petroleum Engineers, N. Y. Intersci. Pub., 1960, 340 pp.

Materials Research on GaAs and InP, by L. R. Weisberg, F. D. Rosi and P. G. Herkart, pp 25–68.

Metallurgy of Some Ternary Semiconductors and Constitution of the $AgSbSe_2$-$AgSbTe_2$-PbSe-Pb-Te, by J. H. Wernick, pp. 69–88.

Use of the Electron Probe X-Ray Microanalyzer in the Study of Semiconductor Alloys, by D. B. Wittry, J. M. Axelrod and J. O. McCaldin, pp. 89–102.

Solid State Reactions of Oxygen in Silicon, by H. Reiss and W. Kaiser, pp. 103–120.

Distribution Coefficients of Impurities Distributed Between Ge or Si Crystals and Ternary Alloys or Surface Oxides, by C. D. Thurmond, pp. 121–140.

Distribution Coefficients of Various Impurities in Gallium Arsonide, by J. M. Whelan, J. D. Struthers and J. A. Ditzenberger, pp. 141–162.

Semicondutor Surfaces and Films: the Silicon - Silicon Dioxide System, by M. M. Atala, pp. 163–184.

Stoichiometry in Compound Semiconductors, by W. W. Scanlon, pp. 185–194.

Dislocations in Silicon and Germanium Crystals, by W. C. Dash, pp. 195–210.

The Effect of Elastic Strain on the Anomalous Transmission of X-Rays in Germanium, by G. E. Brock, pp. 211–224.

Etch Pits, Deformation and Dislocations in GaAs, by M. S. Abrahams and L. Ekstrom, pp. 225–244.

Uniformity of Junction in Diffused Silicon Devices, by L. E. Miller, pp. 303–326.

An Exploratory Study of Three-Dimensional Photothermoelasticity, by Herbert Tramposch and George Gerard, *J. Appl. Mech.* (*ASME Trans., Series E*) vol. 28, no. 1, March 1961, pp. 35–40.

On the Response of Linear Systems to Time-Dependent, Multidimensional Loadings, by F. P. Beer, *J. Appl. Mech. (ASME Trans., Series E)*, vol. 28, no. 1, March 1961, pp. 50–56.

Steady-State Behavior of Nonlinear Dynamic Vibration Absorber, by W. J. Carter and F. C. Liu, *J. Appl. Mech. (ASME Trans., Series E)*, vol. 28, no. 1, March 1961, pp. 67–70.

On the Stability of the Linearly Related Modes of Certain Nonlinear Two-Degree-of-Freedom Systems, by C. P. Atkinson, *J. Appl. Mech. (ASME Trans., Series E)*, vol. 28, no. 1, March 1961, pp. 71–77.

A **Nondestructive Three-Dimensional Strain-Analysis Method,** by A. J. Durelli and I. M. Daniel, *J. Appl. Mech. (ASME Trans., Series E)*, vol. 28, no. 1, March 1961, pp. 83–86.

A **Compendium of the Properties of Materials at Low Temperature (Phase I)—Pt. II, Properties of Solids,** by V. J. Johnson, *Wright Air Dev. Div. Tech. Rep.* 60-56, Pt. II, Oct. 1960, 333 pp.

A **Compendium of the Properties of Materials at Low Temperature (Phase I)—Pt. III, Bibliography of References (Cross-indexed),** by V. J. Johnson, *Wright Air Dev. Div. Tech. Rep.* 60-56, Pt. III, Oct. 1960, 161 pp.

Shielding of Partially Reflecting Stagnation Surfaces Against Radiation by Transpiration of an Absorbing Gas, by John Thomas Howe, *NASA Tech. Rep.* R-95, 1961, 38 pp., 9 figs.

Bibliography on the High Temperature Chemistry and Physics of Materials in the Condensed State Covering the Literature of Australia, Austria, Canada, Germany, United Kingdom, United States, USSR, for the Period Oct., Nov. and Dec. 1960, by N. F. H. Bright, J. J. Diamond, M. Foex, R. T. McCartney and H. Nowotny, *International Union of Pure and Appl. Chem. Comm. on High Temperatures and Refractories Sub-commission on Condensed States*, 1961, 32 pp.

Proposed Ground and Flight Program to Develop Space Age Materials, by M. A. Steinberg, J. L. Fox and B. W. Augenstein, ARS JOURNAL, vol. 31, no. 2, Feb. 1961, pp. 228–236.

Stability of Orthotropic Cylindrical Shells Under Combined Loading, by T. E. Hess, ARS JOURNAL, vol. 31, no. 2, Feb. 1961, pp. 237–245.

Technique of Evaporating Metals in a Vacuum (A Survey), by M. I. Vinogradov, *Instruments & Experimental Tech.*, no. 4, July–Aug. 1960, pp. 523–532.

Supersonic Panel Flutter of a Cylindrical Shell of Finite Length, by Maurice Holt and Sainsbury L. Strack, *J. Aerospace Sci.*, vol. 28, no. 2, March 1961, pp. 197–208.

Dynamic Airloads and Aeroelastic Problems at Entry Mach Numbers, by Garabed Zartarian, Pao Tan Hsu and Holt Ashley, *J. Aerospace Sci.*, vol. 28, no. 2, March 1961, pp. 209–222.

The Buckling of Thin Spherical Shells, by F. J. Murray and Frank W. Wright, *J. Aerospace Sci.*, vol. 28, no. 2, March 1961, pp. 223–236.

High Velocity Impact Studies Directed Towards the Determination of the Spatial Density, Mass and Velocity of Micrometeorites at High Altitudes, by J. L. Bohn and O. P. Fuchs, *Air Force Cambridge Res. Center, Bedford, Mass.* (AF 19(604)-1894), Jan. 31, 1958. (*ASTIA AD-243,106.*)

Environmental Factors Influencing Metal Applications in Space Vehicles, by J. M. Allen, *Battelle Memorial Institute,*

$$0 = \frac{d^2x}{dt^2} + \frac{x}{r^3} + \frac{\partial R}{\partial x}$$

$$0 = \frac{d^2y}{dt^2} + \frac{y}{r^3} + \frac{\partial R}{\partial y}$$

$$0 = \frac{d^2z}{dt^2} + \frac{z}{r^3} + \frac{\partial R}{\partial z}$$

PLOTTING PATHWAYS IN SPACE

A special group of engineering-oriented mathematicians (and mathematics-oriented engineers) at DSD is exclusively concerned with both theoretical and practical sides of astrodynamics and celestial mechanics. Space probes... near-earth satellites... lunar satellites and missiles... all fall within their range of interests. In addition, the statistical problems of data interpretation and mathematical techniques of vehicle guidance are under investigation.

The group operates in an informal, academic atmosphere. Staff members enjoy direct access to the best computation equipment available – including an IBM 7090, a 300 amplifier analog computer, a complete telemetry station, and the finest microwave instrumentation in the free world (MISTRAM).

Although many contracts are in progress, strong encouragement is also given to a wide latitude of independent investigations. (One of the results of this policy was the creation of GEESE – General Electric Electronic System Evaluator.)

You are cordially invited to look into the immediate opportunities in our expanding astrodynamics group... or, if you are an experienced electronics engineer interested in broad systems assignments, we'll be glad to discuss current openings in several other equally challenging program areas at DSD.

All qualified applicants will receive consideration for employment without regard to race, creed, color or national origin.

Write informally, or forward your resume to Mr. P. W. Christos, Box 6-M.

DSD DEFENSE SYSTEMS DEPARTMENT
A Department of the Defense Electronics Division

GENERAL ELECTRIC

Northern Lights Office Building, Syracuse, New York

Columbus, Ohio, DMIC Rep. 142, Dec. 28, 1960. (*OTS:PB* 151,101.)

Investigation into "More Complete Use of Structural Materials" Through a Study of the Stress-Temperature-Time Conditions of a Re-entry Vehicle, by J. E. Davis, J. E. Fischler, J. W. Lobbett, D. Saltman, J. W. Stanwood and N. A. Tiner (Douglas Aircraft Co., Santa Monica, Calif.), *Wright Air Dev. Div., WADD TR* 60-363, 1960.

The Effects of Simulated Space Environments on Cushioning Materials, by D. N. Keast and J. J. Baruch (Bolt Beranek and Newman, Inc., Cambridge, Mass.), *Wright Air Dev. Div., Materials Lab., WADC TR* 58-667, 1958. (*ASTIA AD*-229,932.)

Response of Plates to Moving Shocks, by Eric E. Ungar, *Wright Air Dev. Div. Tech. Rep.* 60-445, Aug. 1960, 33 pp. (*ASTIA AD* 247,109.)

Deformation and Thermal Stress in a Rectangular Plate Subjected to Aerodynamic Heating (for the Case of Simply Supported Edges), by Megumi Sunakawa and Masuji Uemura, *Tokyo Univ., Aeron. Res. Inst. Rep.* 359 (vol. 26, no. 10), Dec. 1960, pp. 195–213.

Time and Temperature Dependence of the Ultimate Properties of an SBR Rubber at Constant Elongations, by Thor L. Smith and Paul J. Stedry, *Calif. Inst. Tech., Jet Propulsion Lab. Tech. Rep.* 32-36, Sept. 1960, 12 pp.

American Society for Testing Materials, Symposium on Newer Metals, San Francisco, Oct. 15–16, 1959, *ASTM Special Tech. Pub. no.* 272, Philadelphia, 1960, 218 pp.

Universal High-Temperature Testing Machine for Vacuum or Controlled Atmosphere, by M. J. Manjoine, L. L. France and R. T. Begley, pp. 3–11.

Mechanical Properties of Molybdenum and Molybdenum-Base Alloy Sheet, by M. Semchyshen and Robert Q. Barr, pp. 12–35.

High-Temperature Mechanical Properties of Tantalum, by F. C. Holden, F. R. Schwartsberg and R. I. Jaffee, pp. 36–55.

Effect of Oxygen and Nitrogen on Workability and Mechanical Properties of Columbium, by R. T. Begley and L. L. France, pp. 56–67.

Tensile Properties of the Platinum-Group Metals, by F. C. Holden, R. W. Douglass and R. I. Jaffee, pp. 68–80.

Effect of Purity and Manufacturing Variables on Elevated Temperature Properties of Beryllium, by W. W. Beaver, R. G. O'Rourke and J. N. Hurd, pp. 81–94.

Stress Rupture and Creep Properties of QMV Beryllium Metal, by J. M. Hurd, R. G. O'Rourke and W. W. Beaver, pp. 95–115.

Test Methods Used for Zirconium and Zirconium Alloy in the Naval Reactor Program, by Harold L. Kall, pp. 116–123.

Effects of Heat Treatments on the Tensile and Corrosion Properties of Zircaloy, by J. G. Goodwin, L. S. Rubenstein and F. L. Shubert, pp. 124–143.

Theory of the Mechanical Properties of Yttrium and Yttrium Alloys, by O. N. Carlson, D. W. Bare, E. D. Gibson and F. A. Schmidt, pp. 144–159.

Columbium and Tantalum Fabrication, by N. M. McCullough, pp. 160–168.

Deoxidation and Denitrification Studies of Chromium and the Effect on Low-Temperature Properties, by H. L. Levingston and N. J. Grant, pp. 169–182.

Review—The Fabrication of Tungsten, by C. H. Toensing, pp. 183–194.

Solubility of Nitrogen and Oxygen in Lithium and Methods of Lithium Purification, by E. E. Hoffman, pp. 195–206.

Coulometric Determination of Tin with Electrolytically Generated Iodine: Application to Analysis of Zircaloy, by Roy D. Caton Jr. and Harry Freund, pp. 207–218.

The Ordinary Transport Properties of the Noble Metals, by J. M. Ziman, *Advances in Physics*, vol. 10, no. 27, Jan. 1961, pp. 1–56.

The Flow Stress of Metals at Low Temperatures, by P. Feltham, *Philosophical Mag.*, vol. 5, no. 62, Feb. 1961, pp. 209–216.

Thermal Expansion of Aluminum at Low Temperatures, by Eva Huzan, C. P. Abbiss and G. O. Jones, *Philosophical Mag.*, vol. 5, no. 62, Feb. 1961, pp. 277–286.

Materials in Space, by R. A. Happe, *Ordnance*, vol. 45, no. 244, Jan. 1961, pp. 578–580.

Behavior of Plastics in Re-entry Environments—Part 2, by D. L. Schmidt, *Modern Plastics*, vol. 38, no. 4, Dec. 1960, pp. 147–154, 198–200.

Materials Requirements of Hypersonic Flight Vehicles, by W. S. Pellini, *J. Metals*, vol. 12, no. 12, Dec. 1960, pp. 952–963.

Composite Material for Thermal Protection, by E. Scala, *Metals Rev.*, vol. 33, no. 11, Nov. 1960, pp. 4–9.

Fluid Dynamics, Heat Transfer and MHD

A Look at the Heat Transfer Problem at Super Satellite Speeds, by M. C. Adams, *Avco Corp., Avco-Everett Res. Lab., Everett, Mass. AMP* 53, Dec. 1960.

Electron Density Fluctuations in a Plasma, by E. E. Salpeter, *Cornell Univ. Center for Radiophysics and Space Res., Res. Rep. RS* 18 (*SR* 5), Aug. 1, 1960. (*AFCRL TN* 60-979.)

On Meteor Ablation in the Atmosphere, by F. Verniani, *Univ. of Florence, Italy, Tech. Note* 4, March 1960. (*AFCRL TN* 60-981; *ASTIA AD* 243,569.)

Air Liquefaction Effects on the Aerodynamic Characteristics of the AGARD Calibration Model B at Mach Numbers 5 and 8, by C. R. Fitch, J. D. Coats and L. L. Trimmer, *Arnold Engng. Dev. Center Tech. Note* 61-24, Feb. 1961, 32 pp.

Excitation of Plasma Waves by Bodies Moving in Ionized Atmosphere, by K. P. Chopra, *Brooklyn Polytechnic Inst., Dept. Aero-Space Engng. and Appl. Mech., Rep.* 627, Jan. 1961, 11 pp. (*AFOSR* 1.)

A Method of Solution with Tabulated Results for the Attached Oblique Shock-Wave System for Surfaces at Various Angles of Attack, Sweep and Dihedral in an Equilibrium Real Gas Including the Atmosphere, by Robert L. Trimpi and Robert A. Jones, *NASA Tech. Rep.* R-63, 1960, 141 pp.

Hypersonic Studies of Blunt Two-Dimensional Swept Wings at Zero Angle of Attack, by S. M. Bogdonoff and I. E. Vas, *Princeton Univ., Dept. Aeron. Engng. Rep.* 451, Apr. 1959, 21 pp. 17 figs.

The Structure of a Centered Rarefaction Wave in an Ideal Dissociating Gas, by J. P. Appleton, *Southampton Univ., Dept. Aeron. Astron. Rep.* 136, Apr. 1960, 43 pp. 11 figs. (*ASTIA AD* 246,453.) (*ARL TN* 60-153.)

Magnetohydrodynamic Shock Structure Without Collisions, by Cathleen S. Morawetz, *Atomic Energy Comm.*, NYO-2885, March 1960, 64 pp.

Reflection and Refraction of Shock Waves in Multicomponent Media and in Water, by G. M. Liakhov, *The Johns Hopkins Univ., Appl. Phys. Lab., TG* 230-T203, Nov. 1960. (*Transl. from Akademii Nauk SSSR Izvestiia, Otdelenie Tekhnicheskikh Nauk, Mekhanika i Mashinostroenie*, no. 5, 1959, pp. 58–63.)

Experimental and Theoretical Study of Heat Conduction for Air up to 5000°K, by Tzy-Cheng Peng and Warren F. Ahtye, *NASA Tech. Note* D-687, Feb. 1961, 38 pp.

Absorption Coefficients of Air from 6000°K to 18000°K, by Roland E. Meyerott, *Rand Corp., Res. Mem.* 1554, Sept. 1955, 11 pp.

Steady Magnetohydrodynamic Flow Through a Channel of Circular Section, by Frank Fishman, *Avco-Everett Res. Lab., Res. Rep.* 97, Dec. 1960, 19 pp.

Compressible Flow Tables, $k=1.28$ Adiabatic Flow with Friction, *Army Ballistic Missile Agency, Rep.* RA-TR-6-61, Feb. 1961, 89 pp.

Pressure Loss and Heat Transfer for Turbulent Flow, by Rudolph Koch, *Atomic Energy Comm. Transl.* 3875, Sept. 1960, 135 pp. (*Transl. from VDI-Forschungsheft*, Series B, vol. 24, no. 469, 1–44, 1958.)

Hot-Wire Heat-Loss Characteristics and Anemometry in Subsonic Continuum and Slip Flow, by Frederick W. Boltz, *NASA Tech. Note* D-773, Feb. 1961, 80 pp.

Formulation of the Theory of Turbulence in an Incompressible Fluid, by H. W. Wyld Jr., *Space Tech. Lab., Phys. Res. Lab., Tech. Rep.* 61-0000-GR 013, Jan. 1961, 33 pp.

Similarity of Near Noise Fields of Subsonic Jets, by Walton L. Howes, *NASA Tech. Rep.* R-94, 1961, 68 pp.

Several Exact Solutions to the Problem of Gas Flow in a Tube with Consideration of Friction and Convective Heat Exchange, by G. L. Grodzovskii, *The Johns Hopkins Univ., Appl. Phys. Lab.*, TG 230-T199, Nov. 1960, 5 pp. (*Transl. from Akademiia Nauk SSSR Izvestiia, Otdelenie Tekhnicheskikh Nauk*, no. 8, Aug. 1958, pp. 127–129.)

A Comparison Between Langmuir Probe and Micro-Wave Electron Density Supersonic Wind Tunnel, by L. Talbot, J. E. Katz and C. L. Brundin, *Univ. of Calif., Berkeley, Inst. Engng. Res. Tech. Rep.* HE-150-186, Jan. 1961, 19 pp., 8 figs.

Research on Compressed Plasmas at the Ionized Gas Laboratory of C.N.R.N., by B. Brunelli, *The Johns Hopkins Univ., Appl. Phys. Lab.*, TG 230-T201, Nov. 1960, 6 pp. (*Transl. from Nuovo Cimento*, vol. 16, Suppl. 1, 1960, pp. 76–81.)

Diffusion and Chemical Surface Catalysis in Flow Systems, by Daniel E. Rosner, *Aero Chem Res. Lab., Tech. Pub.* 14, Sept. 1959, rev. July 1960, 53 pp. (*AFOSR TN* 60-887.)

Recent Advances in Nonequilibrium Dissociating Gasdynamics, by Ting Y. Li, ARS JOURNAL, vol. 31, no. 2, Feb. 1961, pp. 170–178.

Shock Wave and Flow Field Development in Hypersonic Re-entry, by Ronald

F. Probstein, ARS JOURNAL, vol. 31, no. 2, Feb. 1961, pp. 185–193.

Aerodynamic Characteristics of Wedges in Low Density Supersonic Flow, by S. A. Schaaf, E. S. Moulic, M. T. Chahine and G. J. Maslach, ARS JOURNAL, vol. 31, no. 2, Feb. 1961, pp. 194–200.

Peltier Cooling of Electrical Components in Telemetering Packages, by Raymond Marlow, ARS JOURNAL, vol. 31, no. 2, Feb. 1961, pp. 263–264.

Estimation of Specific Heats at Normal Temperatures, by Fred H. Brock, ARS JOURNAL, vol. 31, no. 2, Feb. 1961, pp. 265–268.

Information Theory as the Basis for Thermostatics and Thermodynamics, by Myron Tribus, *J. Appl. Mech.* (*ASME Trans., Series E*), vol. 28, no. 1, March 1961, pp. 1–8.

Electric Breakdown of Gases at Pressures Close to Atmospheric Pressure, by I. S. Marshak, *Soviet Phys.: Uspekhi*, vol. 3, no. 4, Jan.–Feb. 1961, pp. 624–644.

Hugoniot Curve Determined by Shock Wave Detachment from an Infinite Wedge, by William A. Allen and James W. Rogers, *Bur. Naval Weapons, NAVWEPS Rep.* 7607, Jan. 1961, 46 pp.

Recent Advances in Nonequilibrium Dissociating Gas Dynamics, by Y. Li-Ting, *Rensselaer Polytech. Inst., Dept. Aeron. Engng., TR AE* 6008, Dec. 1960, 41 pp., 46 refs.

Measurement of the Flow Field of an Under-Expanded Jet in a Hypersonic External Stream (M_{∞} = 6.8), by J. G. Woodley, *Gt. Brit. Roy. Aircraft Estab. Tech. Note* Aero. 2733, Dec. 1960, 9 pp., 4 figs.

A Preliminary Study of Ionic Recombination of Argon in Wind Tunnel Nozzles, by K. N. C. Bray and J. A. Wilson, *Southampton Univ., Dept. Aeron. and Astron. Rep.* 134, Feb. 1960, 33 pp., 20 figs. (*ASTIA AD* 246,452.)

The Choice of an Optimum Set of Measurements to Study Atomic Recombination in Nozzles, by K. N. C. Bray and J. P. Appleton, *Southampton Univ., Dept. Aeron. and Astron. Rep.* 120, Nov. 1959, 40 pp. (*ASTIA AD* 233,972.)

Compressible Flow Tables, k = 1.30; Adiabatic Flow with Fricton, *Army Ballistic Missile Agency, Rep. RA-TR-7-61*, March 1961, 89 pp.

An Experimental Study of Continuous Plasma Flows Driven by a Confined Arc in a Transverse Magnetic Field, by R. L. Barger, J. D. Brooks and W. D. Beasley, *NASA Tech. Note* D-716, March 1961, 25 pp.

A Transport Equation for Magnetohydrodynamic Waves, by Marvin M. Litvak, *Avco-Everett Res. Lab., Res. Rep.* 92, Aug. 1960, 90 pp.

The Interactions Between Nitrogen and Oxygen Molecules, by Willard E. Meador Jr., *NASA Tech. Rep.* R-68, 1960, 25 pp.

Technology Reports, vol. 10, nos. 414–445, Oct. 1960, Osaka Univ., Faculty of Engineering, pp. 545–903.

Electromagnetically Driven Shock Wave in Argon (II), by Chiyoe Yamamura, pp. 553–564.

Fundamental Research on Plasma Jet and Its Application (Report 2) on the Characteristics of a Plasma Jet and Air Plasma Cutting, by Minoru Okada and Hiroshi Maruo, pp. 579–592.

Societa Italiana di Fisica Termodinamica dei processi irreversibili, Fendiconti della Scuola Internationale di Fisica "Enrico Fermi, Lago di Como, Guigno 1959," Direttore: S. R. de Groot, Bologna, Nicola Zanichelli, 1960, 317 pp. (*All papers are in English.*)

The Laws of Thermodynamics, by M. J. Klein, pp. 1–23.

Theory of Fluctuations, by A. Munster, pp. 23–130.

Nonequilibrium Thermodynamics, by S. R. De Groot, pp. 131–161.

Onsager's Relation for Vectorial Phenomena, by R. Fieschi, pp. 162–166.

On the Statistical Basis of Nonequilibrium Thermodynamics, by P. Mazur, pp. 167–197.

The Principle of Minimum Entropy Production, by M. J. Klein, pp. 198–204.

Statistical Mechanics of Transport Processes, by J. G. Kirkwood, pp. 205–216.

Statistical Mechanics of Transport Processes, by E. W. Montroll, pp. 217–261.

Irreversible Processes in Solids, by F. Henin, pp. 262–274.

On Quantum Theory of Irreversible Processes, by S. Nakajima, pp. 275–281.

On the Statistical Mechanical Theory of Irreversible Behavior, by Mazur, pp. 282–293.

Rayleigh's Problem in Magnetohydrodynamics for a Nonperfect Conductor, by D. G. Drake, *Appl. Scientific Res., Section B*, vol. 8, no. 5–6, 1960, pp. 467–472.

Diffraction of Strong Shocks by Cones, Cylinders and Spheres, by A. E. Bryson and R. W. F. Gross, *J. Fluid Mech.*, vol. 10, part 1, Feb. 1961, pp. 1–16.

Analysis of Vibrational Relaxation Regions by Means of the Rayleigh-Line Method, by N. H. Johannesen, *J. Fluid Mech.*, vol. 10, part 1, Feb. 1961, pp. 25–32.

Comparison of Exact and Approximate Methods for Analysing Vibrational Relaxation Regions, by P. A. Blythe, *J. Fluid Mech.*, vol. 10, part 1, Feb. 1961, pp. 33–47.

Gaskinetics and Gasdynamics of Orifice Flow, by Hans W. Liepmann, *J. Fluid Mech.*, vol. 10, part 1, Feb. 1961, pp. 65–79.

On a Momentum-Mass Flux Diagram for Turbulent Jets, Plumes and Wakes, by B. R. Morton, *J. Fluid Mech.*, vol. 10, part 1, Feb. 1961, pp. 101–112.

The Effect of a Very Strong Magnetic Cross-Field on Steady Motion Through a Slightly Conducting Fluid, by G. S. S. Ludford, *J. Fluid Mech.*, vol. 10, part 1, Feb. 1961, pp. 141–152.

Experiments on Heat Transport by Convection in Presence of a Magnetic Field, by Yoshinari Nakagawa and Iza R. Goroff, *Phys. Fluids*, vol. 4, no. 3, March 1961, pp. 349–354.

Stability of a Stokesian Fluid in Couette Flow, by William P. Graebel, *Phys. Fluids*, vol. 4, no. 3, March 1961, pp. 362–367.

Turbulent Flow in a Circular Pipe with Porous Wall, by S. W. Yuan and E. W. Brogren, *Phys. Fluids*, vol. 4, no. 3, March 1961, pp. 368–372.

Parametric Study of the Conical Shock Tube, by Vernal Josephson and Richard W. Hales, *Phys. Fluids*, vol. 4, no. 3, March 1961, pp. 373–379.

The Heating of Fully Ionized Plasmas by Hydromagnetic Shock Waves, by H. J. Kaeppeler and B. Mayser, *Raketentechnik und Raumfahrt forschung*, vol. 5, no. 1, Jan.–March, 1961, pp. 1–5. (*In German.*)

Flow of a Plasma into Vacuum in the Presence of a Magnetic Field, by R. V.

Wiley BOOKS

THE PHYSICAL PRINCIPLES OF

ASTRONAUTICS:

FUNDAMENTALS OF DYNAMICAL ASTRONOMY AND SPACE FLIGHT

By ARTHUR I. BERMAN, *Rensselaer Polytechnic Institute, Hartford Graduate Center.* A thorough exposition of the basic principles, covered concisely and designed for the serious student. It is the only book on the subject that is really quantitative enough beyond the level of the beginner—and yet is not highly advanced.

Emphasis is on scientific aspects and underlying principles rather than on the massive body of hardware and engineering gadgets now in use. Although all of astronautics obviously cannot be covered in a book of this scope, the hard core—weightlessness, centrifugal force and its effects, and the like—is developed fully, always in depth and with true relevance to principles.

There are a great many examples, chosen to illustrate the more important and trickier concepts. About one third of the problems are worked out numerically. *1961. 350 pages. $9.25*

ELEMENTS OF FLIGHT PROPULSION

By JOSEPH V. FOA, *Rensselaer Polytechnic Institute.* Covers the basic concepts and broad aspects of propulsion engineering. Designed as a guide for creative work rather than as a source of data on existing engines. Describes much original work and gives extensive treatment of nonsteady and steady-flow thrust generators. Existing engines are used as illustrations of methods and ideas. *1960. 445 pages. $12.50*

Send now for your on-approval copies

JOHN WILEY & SONS, Inc.

440 Park Avenue South
New York, 16, N. Y.

Polovin, *Soviet Phys.: JETP*, vol. 12, no. 3, March 1961, pp. 461–463.

Natural Oscillations of a Bound Plasma, by D. A. Frank-Kemenetskii, *Soviet Phys.: JETP*, vol. 12, no. 3, March 1961, pp. 469–475.

Structure of Low-Intensity Shock Waves in Magnetohydrodynamics, by E. P. Sirotina and S. I. Syrovat-skii, *Soviet Phys.: JETP*, vol. 12, no. 3, March 1961, pp. 521–526.

Flight Mechanics

Fast Interplanetary Missions with Low-Thrust Propulsion Systems, by W. E. Moeckel, *NASA Tech. Rep.* R-79, 1961, 29 pp.

Generalized Powered Flight Trajectory Program for IBM 704 Computer, by G. N. Gianopulos, *Calif. Inst. Tech., Jet Propulsion Lab.* 32-38, Sept. 1960, 75 pp.

Researches in Interplanetary Transfer, by John V. Breakwell, Rollin W. Gillespie and Stanley Ross, ARS JOURNAL, vol. 31, no. 2, Feb. 1961, pp. 201–207.

Ballistic Re-entries with a Varying W/C_DA, by R. V. Warden, ARS JOURNAL, vol. 31, no. 2, Feb. 1961, pp. 208–213.

Limits for Stable Near-Circular Planetary or Satellite Orbits in the Restricted Three-Body Problem, by S. H. Dole, ARS JOURNAL, vol. 31, no. 2, Feb. 1961, pp. 214–219.

Motion of a Satellite of the Moon, by Harry Lass and Carleton B. Solloway, ARS JOURNAL, vol. 31, no. 2, Feb. 1961, pp. 220–222.

Investigation of the Static Stability Characteristics of Two Stages of a Three-Stage Missile at a Mach Number of 4.00, by Ausley B. Carraway, Frederick G. Edwards and Jean C. Keating, *NASA Tech. Note* D-651, March 1961, 18 pp.

Analytical Study of Soft Landings on Gas-Filled Bags, by Jack B. Esgar and William C. Morgan, *NASA Tech. Rep.* R-75, 1960, 30 pp.

Launching of Airborne Missiles Underwater, Part IX—Statistical Missile Response Due to Wave Induced Submarine Roll, by Theodore R. Goodman and Theodore P. Sargent, *Allied Res. Associates, Inc.*, ARA-906, March 1961, 21 pp.

A Three-Dimensional Trajectory Simulation Using Six Degrees of Freedom with Arbitrary Wing, by Robert L. James Jr., **Appendix B: Damping in Pitch and Yaw for Radial Burning Solid-Propellant Rockets,** by Norman L. Crabill, *NASA Tech. Note* D-641, March 1961, 28 pp.

Parabolic Orbit Calculations on the IBM 650 (Olber's Method), by P. Herget, *Astronom. J.*, vol. 65, no. 9, Nov. 1960, pp. 491–492.

Osculating Elements Derived From the Modified Hansen Theory for the Motion of an Artificial Satellite, by A. Bailie and R. Bryand, *Astronom. J.*, vol. 65, no. 8, Oct. 1960, pp. 451–453.

Orbital Patterns for Satellite Systems, by L. G. Vargo, *J. Astronaut. Sci.*, vol. 7, no. 4, Winter 1960, pp. 78–86.

Calculating a Journey from the Earth to the Moon, by V. J. Slabinski, *Engng. and Sci. Rev.*, vol. 4, no. 1, Nov. 1960, pp. 17–20.

Formulas for Computing Perturbations in Elliptical and Hyperbolic Motion, by A. A. Orlov, *Vestnik Moskovskogo Gosudarstvenngo Universiteta, Seria Fizikii Astronomicheskii, USSR*, no. 2, March–Apr. 1960, pp. 51–60. (Abstracted in *Physics Express*, vol. 3., no. 3, Nov. 1960, pp. 28–29.)

Re-entry From Space, by J. V. Becker, *Sci. Amer.*, vol. 204, no. 1, Jan. 1961, pp. 49–57.

Analytic Solutions to Several Optimum Orbit Transfer Problems, by H. Munick, R. McGill and G. E. Taylor, *J. Astronaut. Sci.*, vol. 7, no. 4, Winter 1960, pp. 73–77.

Optimum Two Impulse Ascents to Circular Orbits, by J. P. Carstens and T. N. Edelbaum, *J. Astronaut. Sci.*, vol. 7, no. 4, Winter 1960, pp. 96–97.

Comment by D. DeBra on the Note by Carstens and Edelbaum: Optimum Two Impulse Ascents to Circular Orbts, by D. DeBra, *J. Astronaut. Sci.*, vol. 7, no. 4, Winter 1960, p. 98.

Position, Velocities, Ephemerides Referred to the Dynamical Center, by S. Herrick, *Calif. Univ., Los Angeles Astrodynamical Rep.* 7, July 1960. (*AFOSR TN* 60–773.)

Orbits From Position and Velocity, by S. Herrick, *Calif. Univ., Los Angeles Astrodynamical Rep.* 8, July 1960. (*AFOSR TN* 60–816.)

Variation of Parameters, by S. Herrick, *Calif. Univ., Los Angeles Astrodynamical Rep.* 9, July 1960. (*AFOSR TN* 60–812.)

Astrodynamical Notation and Usage, by S. Herrick, M. W. Makemson and M. P. Francis, *Calif. Univ., Los Angeles Astrodynamical Rep.* 10, July 1960. (*AFOSR TN* 60–812.)

A Study of the Accurate Re-entry and Precision Landing of an Orbital Earth Satellite, Part I, by L. R. Bush, *Cornell Aeron. Lab., CAL Rep.* VF-1351-H-1, Jun. 30, 1959. (*ASTIA AD* 245, 153.)

Nonlinear Two Point Boundary Problems with Applications to the Restricted Three-Body Problem, by R. E. Moore, *Lockheed Aircraft Corp., Missiles and Space Div.* LMSD-895025, Dec. 1960.

Oblateness Perturbations of Near-Earth Satellites, by T. W. Mullikin, *Rand Corp.*, RM-2643, Oct. 25, 1960.

Special Satellite Orbits: 1. Equatorial Orbits, 2. Polar Orbits, by J. L. Brenner, M. Weisfeld, *Stanford Res. Inst.* SRI-3163-6(F), Dec. 1960.

Vehicle Design, Testing and Performance

Landing Characteristics and Flotation Properties of a Reentry Capsule, by Victor L. Vaughan Jr., *NASA Tech. Note* D-653, Feb. 1961, 36 pp.

Low-Subsonic-Speed Static Stability of Right-Triangular-Pyramid and Half-Cone Lifting Reentry Configurations, by George M. Ware, *NASA Tech. Note* D-646. Feb. 1961, 28 pp.

Optimum State-Weight Distribution of Multistage Rockets, by John J. Coleman ARS JOURNAL, vol. 31, no. 2, Feb. 1961, pp. 259–260.

Satellite Recovery Techniques for Optimization of Touchdown Accuracy, by Daniel L. Rosamond, *J. Aerospace Sci.*, vol. 28, no. 2, March 1961, pp. 237–243.

Study of Hypersonic Aerodynamic Decelerators Incorporating Lift, by Jacques A. F. Hill, *Wright Air Dev. Div., Tech. Rep.* 60–706, Aug. 1960, 213 pp.

Busemann Correction to the Characteristics of the Two-Dimensional Hypersonic Sail, by E. A. Boyd, *Cranfield, College of Aeronautics, Rep.* 140, Nov. 1960, 7 pp.

Considerations Affecting Satellite and Space Probe Research with Emphasis on the "Scout" as a Launch Vehicle, by Jack Posner, *NASA Tech. Rep.* R-97, 1961, 146 pp.

Scientific Experiments for Ranger 1 and 2, *Calif. Inst. Tech., Jet Propulsion Lab. Tech. Rep.* 32-55, Jan. 1961, 28 pp.

USSR: Missiles, Rockets and Space Effort, *Army Dept. Headquarters, A bibliorecord 1956–1960, Pamphlet* 70-58, Sept. 1960, 49 pp.

The Ranger Spacecraft, by W. W. Hough, *Northwestern Engr.*, vol. 19, no. 4, Nov. 1960, pp. 12–13, 30.

Prediction of Transient Thermal Environment in Space Vehicles, by T. Ishimoto and B. W. Randolph, *Elec. Engng.*, vol. 79, no. 12, Dec. 1960, pp. 1019–1022.

Radiation Shielding for Space Vehicles, by J. W. Keller and N. M. Schaeffer, *Elec. Engng.*, vol. 79, no. 12, Dec. 1960, pp. 1049–1053.

Evolution and Testing of a Navigational Satellite (Transit), by M. A. Schreiber and T. Wyatt, *Elec. Engng.*, vol. 79, no. 12, Dec. 1960, pp. 1033–1040.

The Data Systems for Explorer VI and Pioneer V, by E. W. Greenstadt, *IRE Trans. on Space Electronics and Telemetry*, vol. SET-6, no. 3–4, Sept.–Dec. 1960, pp. 122–129.

Background to Dyna-Soar, by K. Gatland, *Aeroplane and Astronautics*, vol. 100, no. 2568, Jan. 6, 1961, pp. 19–22.

The Dyna-Soar Porpoise and Weathercock, by T. R. F. Nonweiler, *Aeronautics*, vol. 43, no. 3, Jan. 1961, pp. 42–44.

Around the Moon, by D. E. Smith and A. E. Smith, *Flight*, vol. 78, no. 2701, Dec. 16, 1960, pp. 941–943.

Mercury and After, by K. Owen, *Flight*, vol. 8, no. 2699, Dec. 2, 1960, pp. 867–869.

Thermal Equilibrium of Space Vehicles, by D. Bushness and A. D. Kraus, *Sperry Engng. Rev.*, vol. 13, no. 4, Dec. 1960, pp. 26–35.

Saturn Designers Tackle Advanced Cryogenic Propellants, by B. L. Brown and W. B. Smith, *Space/Aeronautics*, vol. 35, no. 1, Jan. 1961, pp. 58–61.

Solar Radiation Satellite (Transit II-A) *National Acad. Sci., IGY Bull.*, no. 42, Dec. 1960, pp. 1–5.

The Rocket-Means of Space Flight, (In "Raketoy k Lune," Moscow, 1960), by V. I. Levantovsky, *U. S. Dept. of Commerce, Off. Tech. Services, Washington, D. C., OTS:* 60–41, 473, Sept. 28, 1961. (*JPRS:* 5686.)

Ground Equipment to Support the Saturn Vehicle (Presented at the ARS 15th Annual Meeting, Washington, D. C.) by G. von Tiesenhausen (George C. Marshall Space Flight Center, Huntsville, Ala.), *ARS Preprint* 1425–60, Dec. 5–8, 1960.

Launch Area Servicing of a Fluorine Hydrogen Upper Stage, *Bell Aerosystems Co., Buffalo, N. Y., Rep.* 8031-982-003, Dec. 30, 1960.

Guidance and Control

Time-Optimal Control Systems, by P. J. Nowacki, *Poland (Polska) Akademia Nauk Instytut Badan Jadrowych, Bericht* no. 122, Nov. 1959, 15 pp., 6 figs. (*In German.*)

An Explicit Linear Filtering Solution for the Optimization of Guidance Systems with Statistical Inputs, by Elwood C. Stewart, *NASA Tech. Note* D-685, Feb. 1961, 84 pp.

Design Principles for a General Control Computer, by R. Slonso and J. H. Laning Jr., *Inst. Aeron. Sciences, SMF Paper* FF-29, Apr. 1960, 106 pp.

FORECAST

Major space age role for fluorine rocket fuel oxidizers

25,000 POUNDS OF LIQUID FLUORINE, from General's Metropolis, Ill., Works – ready for over-the-highway shipment in tank trucks of our own design to rocket and missile research centers throughout the nation.

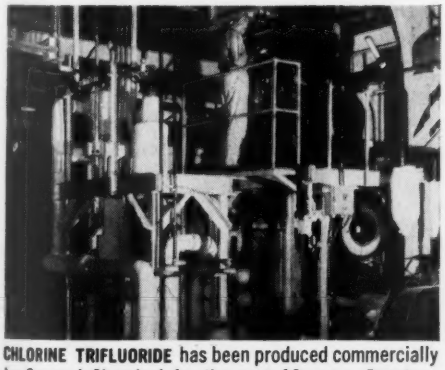

CHLORINE TRIFLUORIDE has been produced commercially by General Chemical for the past 10 years. Reactors like this one, located at General's Baton Rouge Works, have a capacity of more than 100 tons of CTF per year.

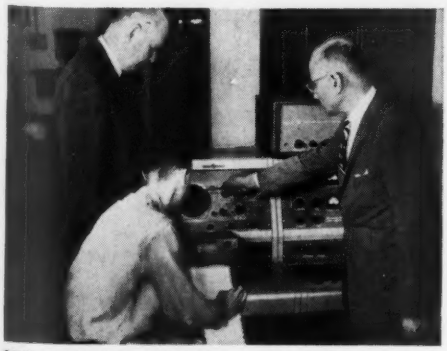

GENERAL CHEMICAL SCIENTISTS make use of the most advanced scientific equipment to investigate fluorine compounds as high energy oxidizers for solid propellants.

Potential applications for fluorine in rocketry extend over the entire propellant spectrum—from cryogenics to storable liquid to solid propellants

As America's primary producer of fluorine and halogen fluorides and leader in fluorochemical research, General Chemical helps support America's rocket and missile development programs in three key areas.

For investigation of cryogenic systems in the super-high energy range, General supplies large quantities of liquid fluorine. For investigation of advanced, high-energy storable liquid propellant systems, General supplies chlorine trifluoride (CTF) and other halogen fluorides. To serve both these areas, General has large existing production capacity, and can meet volume requirements.

In solid propellant systems, General is conducting intensive investigation under Government contract. Incorporation of the fluorine atom in the oxidizing molecule is part of this research.

If you would like technical data, we will be glad to send you our free bulletins, "Fluorine" and "Chlorine Trifluoride." Simply request them on company letterhead.

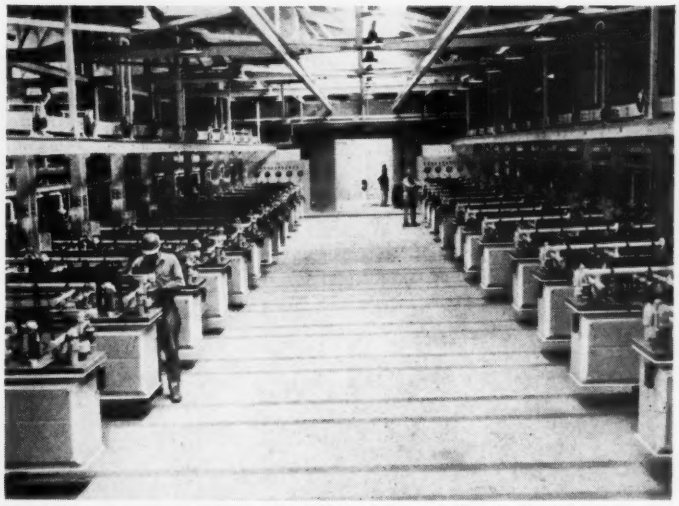

PART OF THE GIANT FLUORINE CELL ROOM at General Chemical's Metropolis, Ill., Works. This is the largest privately owned fluorine production facility in the world.

First in fluorine chemistry

Allied Chemical

GENERAL CHEMICAL DIVISION

40 Rector Street, New York 6, N. Y.

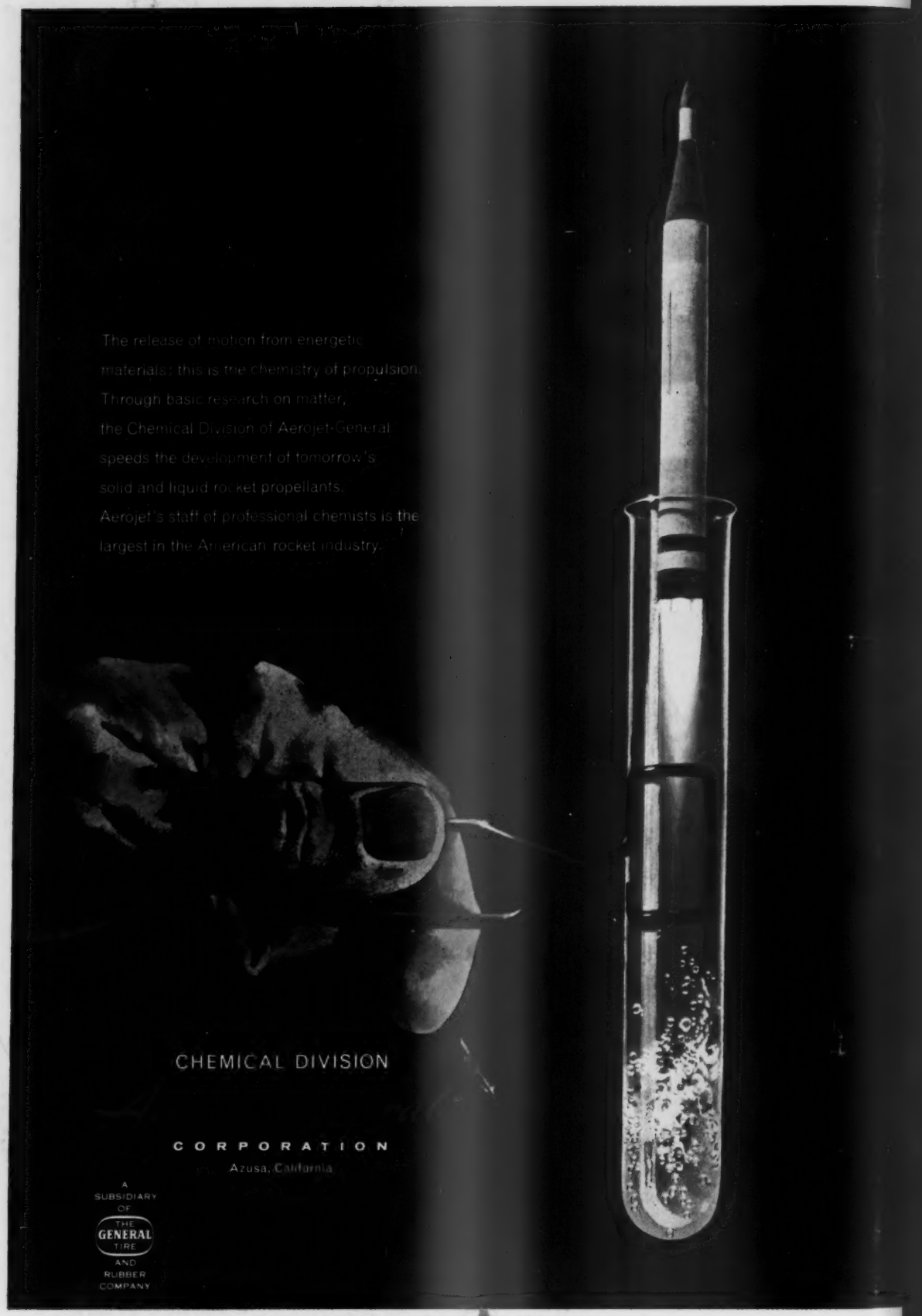
The release of motion from energetic materials: this is the chemistry of propulsion. Through basic research on matter, the Chemical Division of Aerojet-General speeds the development of tomorrow's solid and liquid rocket propellants. Aerojet's staff of professional chemists is the largest in the American rocket industry.
CHEMICAL DIVISION
CORPORATION
Azusa, California
A SUBSIDIARY OF THE GENERAL TIRE AND RUBBER COMPANY

Engineers, scientists—investigate outstanding opportunities at Aerojet